



HAL
open science

Design and realization of a 3D digital electromagnetic micro-actuator array for conveyance application

Ajinkya Deshmukh

► **To cite this version:**

Ajinkya Deshmukh. Design and realization of a 3D digital electromagnetic micro-actuator array for conveyance application. Electromagnetism. Université de Technologie de Compiègne, 2020. English. NNT : 2020COMP2546 . tel-03235396

HAL Id: tel-03235396

<https://theses.hal.science/tel-03235396>

Submitted on 25 May 2021

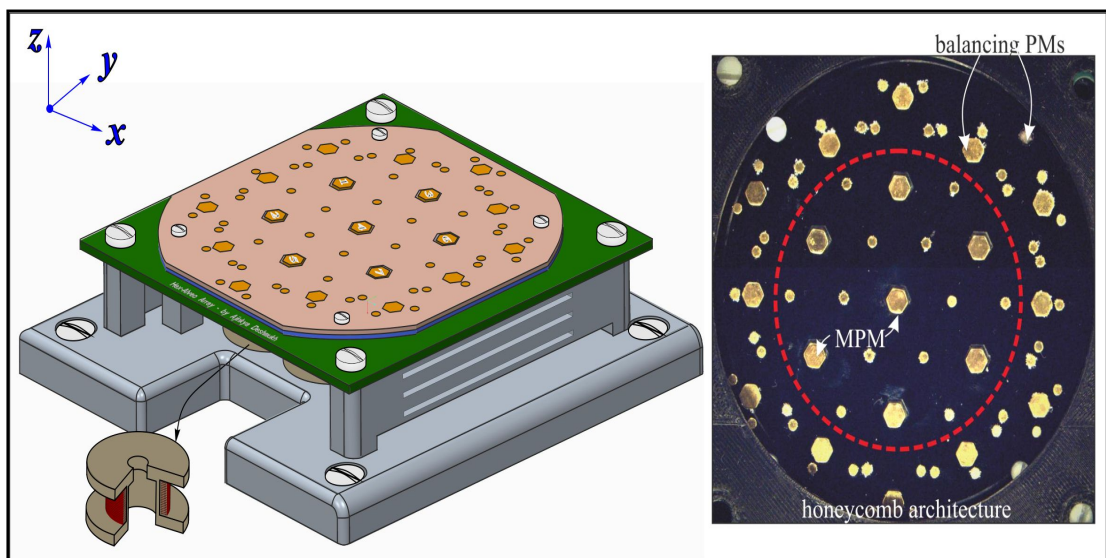
HAL is a multi-disciplinary open access archive for the deposit and dissemination of scientific research documents, whether they are published or not. The documents may come from teaching and research institutions in France or abroad, or from public or private research centers.

L'archive ouverte pluridisciplinaire **HAL**, est destinée au dépôt et à la diffusion de documents scientifiques de niveau recherche, publiés ou non, émanant des établissements d'enseignement et de recherche français ou étrangers, des laboratoires publics ou privés.

Par Ajinkya DESHMUKH

Design and realization of a 3D digital electromagnetic micro-actuator array for conveyance application

Thèse présentée
pour l'obtention du grade
de Docteur de l'UTC



Soutenue le 16 mars 2020

Spécialité : Mécatronique, Photonique et Systèmes : Unité de recherche en Mécanique - Laboratoire Roberval (FRE UTC - CNRS 2012)

D2546

Design and Realization of a 3D Digital Electromagnetic Micro-actuator Array for Conveyance Application

From the faculty of the Mechanical Engineering of the
Université de Technologie de Compiègne at Compiègne, France

Spécialité : Mécatronique, Photonique et Systèmes

16/03/2020

Dissertation

written by

Ajinkya Deshmukh

Presented on before the Jury members:

Reviewers:

Prof. Dr. Fabien Formosa Laboratoire SYMME, Université, Savoie Mont Blanc, France
Dr. Michaël Gauthier Laboratoire FEMTO-ST, Besançon, France

Examiners:

Dr. Mathieu Grossard Laboratoire CEA-List, France
Prof. Dr. Vincent Lanfranchi Université de Technologie de Compiègne, France

PhD directors:

Dr. Laurent Petit Université de Technologie de Compiègne, France
Prof. Dr. Christine Prella Université de Technologie de Compiègne, France

President of the PhD defence jury:

Prof. Dr. Vincent Lanfranchi Université de Technologie de Compiègne, France

Preface

This manuscript is the summary of my research work in the field of micro-conveyance devices. The activities performed are under a PhD program at Roberval Laboratory of University of Technology Compiègne (UTC) which is carried out as a part of ALVEO project which is funded by ANR and Region Hauts de France.

The main objective of this work is to realize a micro-conveyance device with the help of digital electromagnetic actuators. It includes development of a 3D digital actuator and then assembly of several actuators to form an array for the conveyance. This device can be used in the context of micro-factories to convey or position the objects in 3D space.

Considering the international exposure to this work, the manuscript is written in English language however, the abstract is available both in English and French languages.

Abstract

Smart Conveyance Surfaces are significantly used in many industries in accordance to the growing manufacturing demands. They are used to transfer the parts from one manufacturing station to another and can contribute to the assembly of the different parts or during the inspection and logistics operations. This technology is emerging at macro and micro levels and is the backbone to automate manipulation tasks. Several researches are in progress the industrial sector to upgrade or adapt the new trend of Industry 4.0. Miniaturization is also in high demand to obtain cost effective and high precision products with a footprint of few cubic centimetres. To realize this smart conveyance surfaces, various actuation architectures and physical principles can be used.

This thesis presents the development of a micro-conveyance device based on an array of digital electromagnetic actuators. The main originality of the proposed work lies in its hexagonal architecture and the ability of each actuator to reach twelve discrete positions distributed at two different levels along z -axis. The proposed device comprises seven actuators assembled in honeycomb architecture to realize conveyance in a collaborative or elementary manner with 4-DOF (three translation and one rotation along z -axis). Each actuator of an architecture consists of mobile part able to switch with the help of electromagnetic Lorentz force. Each actuator can be elementary controlled and exhibits different displacement strokes ranging from 0.5 mm to 1.00 mm. The overall dimension of the device is 90×90 mm and it is capable of achieving planar motion of a conveyed object due to stick-slip and lift-mode approach. The device has been designed and sized with the help of magnetic and electromagnetic force models. Several prototypes have then been realized using both rapid prototyping and micro-fabrication techniques. These prototypes have then been tested and their ability to realize conveyance tasks has been characterized.

A novel compact design of the array with 19 actuators arranged in a honeycomb architecture has also been designed.

Keywords: Micro-conveyance system, Digital actuator array, 3D digital actuators, Electromagnetic actuators, Collaborative actuation, Micro-factory.

Résumé

Les surfaces de transport intelligentes (smart surfaces) sont de plus en plus utilisées dans de nombreuses industries. Elles permettent de transférer des pièces d'une station de fabrication à une autre et de contribuer ainsi à l'assemblage de différentes pièces ou peuvent être utilisés lors d'opérations d'inspection et de logistique. Cette technologie émerge aux échelles macroscopique car elle représente un élément clé pour assurer une forte automatisation des tâches de manipulation. Plusieurs recherches sont en cours pour moderniser ou adapter cette nouvelle tendance de l'Industrie 4.0. La miniaturisation de ces surfaces est présente également un intérêt fort dans le but d'obtenir des micro-produits ayant un coût de fabrication maîtrisé et une grande précision tout en assurant un encombrement de quelques centimètres cubes. De nombreuses architectures et principes physiques peuvent être utilisés pour réaliser ces surfaces de convoyage intelligentes.

Le travaux présentés dans ce manuscrit de thèse porte sur le développement d'un système de micro-convoyage basé sur un réseau d'actionneurs électromagnétique numériques. La principale originalité du travail proposé porte sur l'architecture hexagonale des actionneurs qui leur permet d'atteindre douze positions discrètes réparties sur deux niveaux selon l'axe z. Le système proposé comprend sept actionneurs numériques assemblés dans une architecture en nid d'abeilles pour réaliser des tâches de convoyages de manière individuelle ou collaborative avec quatre degrés de liberté (trois translations et une rotation autour de l'axe z). Chaque actionneur comprend un aimant permanent mobile capable de se déplacer à l'aide d'un effort électromagnétique de Laplace et présente plusieurs courses comprises entre 0,5 et 1,0 mm. Les dimensions totales du système sont de 90×90 mm and ce dernier est capable de générer des mouvements plans d'un objet convoyé à l'aide d'un principe stick-slip. Le système a été conçu et dimensionné à l'aide d'un modèle magnétique et électromagnétique. Plusieurs prototypes ont été réalisés en utilisant différents moyens de production tels que des techniques de prototypage rapide et de micro-fabrication. Ces prototypes ont ensuite été testés et leur capacité à réaliser des tâches de convoyage a été caractérisée.

A la fin du manuscrit, une conception plus compacte du réseau comprenant 19 actionneurs organisés dans une architecture en nid d'abeilles a également été conçue.

Mots Clés: Système de micro-convoyage, Réseau d'actionneurs numériques, Actionneurs numériques 3D, Actionneur électromagnétique, Collaborative actuation, Micro-usine.

Acknowledgment

This study was conducted in the Roberval laboratory, FRE2012, UTC/CNRS, Université de Technologie de Compiègne (UTC) and it is a part of ALVEO project funded by ANR and Region Hauts-de-France. This thesis becomes a reality with the kind support of many individuals. I would like to extend my sincere thanks to all of them.

My deep gratitude goes first to my PhD supervisors, Dr. Laurent Petit and Prof. Christine Prelle. I sincerely thank you for the continuous support on my PhD study and research. Your guidance helps me all the time throughout my PhD journey. I could not have imagined having a better advisor and mentor for my Thesis.

I would also like to thank you Prof. Frederic Lamarque, Dr. Erwan Dupont, Dr. Hani Al-Hajjar, Dr. Muneeb Ullah Khan and all the staff members of the Roberval Laboratory at UTC for their immense support during my Thesis period.

I would also like to thank Dr. Swati Banerjee for sharing her PhD experiences with me throughout the period, to make sure I do not commit common mistakes and also helping me out in the my Dissertation.

My PhD journey was filled with full of fun and activities, thanks to all my colleagues and friends (Simon, Marcel, Rita, Georgina, Saly, Racha, Kong, Santiago,...). I was happy to have you guys around for a nice and cheerful environment.

Finally, I owe my deepest gratitude to my family and especially my Parents and my Sister Shweta for their support and encouragement throughout the years.

Table of contents

Preface	i
Abstract	iii
Résumé	v
Acknowledgment	vii
List of figures	v
List of tables	xi
List of abbreviations	xiii
Introduction	1
1 State of the art	3
1.1 Smart Conveyance Surfaces	3
1.1.1 Smart Conveyance at Macro-scale	4
1.1.2 Smart Conveyance at Micro/Meso-scale	7
1.2 Physical Principle for Conveyance devices	8
1.2.1 Pneumatic Principle	9
1.2.2 Electrostatic Principle	12
1.2.3 Electro thermal Principle	14
1.2.4 Piezoelectric Principle	16
1.2.5 Electromagnetic principle	17
1.2.5.1 Linear induction actuator	17
1.2.5.2 Linear reluctance actuator	18
1.2.5.3 Lorentz force actuator	20
a) Moving coil and fixed PM configuration:	20
b) Moving PMs and fixed coil configuration:	22
1.3 Actuation principles	24
1.3.1 Analogical actuators	24
1.3.1.1 Conveyance using contact actuation	25
1.3.1.2 Conveyance using non-contact actuation	25
a) Electromagnetic Levitation:	26
b) Pneumatic Levitation:	27
c) Electrostatic Levitation:	27

1.3.2	Digital actuators	28
1.3.2.1	Switching function	29
1.3.2.2	Holding function	29
a)	Magnetic Holding :	29
b)	Locking Systems:	31
c)	Compliant structures:	32
d)	Hinged mechanisms:	33
1.4	Overview of the presented conveyance systems	33
1.5	Conclusion	36
2	Principle, Modeling and Design of an elementary Digital Actuator	39
2.1	Principle of the actuator	39
2.1.1	Principle of 2D actuator	40
Actuation principle	42
2.1.2	Principle of 3D actuator	44
2.1.3	Conveyance principle	45
2.1.3.1	Stick-Slip approach	45
2.1.3.2	Lift-Mode approach	46
2.2	Modeling	47
2.2.1	Magnetic flux density distribution model	47
2.2.1.1	Cuboidal PM	47
2.2.1.2	Hexagonal PM	48
2.2.1.3	Cylindrical PM	51
2.2.2	Validation of the proposed models	52
2.2.3	Magnetic force	53
2.2.4	Electromagnetic force	55
2.2.5	Electromagnetic air-core coil	56
2.2.6	Static model	56
2.2.7	Determination of Self-returning zone and minimum Driving current (I_{min})	60
2.2.7.1	Frictional Force calculation	62
2.3	Computer-Aided-Drawing (CAD) modeling of the HDA	63
2.3.1	3D actuator with cuboidal PM	63
2.3.2	3D actuator with hexagonal PM	64
2.4	Conclusion	65
3	Realization & Experimental Characterization of the Hexagonal Digital Actuator	67
3.1	Design Layout of the prototype and component description	67
3.1.1	Mobile Part Assembly	68
3.1.2	Fabrication of the Fixed Parts	69
3.2	Measurement techniques	69
3.2.1	Fiber Optic Displacement Sensor (FODS)	69
3.2.1.1	Working Principle of the FODS	71
3.2.1.2	Calibration of the FODS	72

3.2.2	High-Resolution Camera (HRC) and Image processing	73
3.2.3	Comparison between measurement techniques	75
3.3	Assembly and Characterization of the HDA	75
3.3.1	Experimental setup and control module	75
3.3.2	Characterization of the HDA	76
3.3.2.1	Displacement in 3D space	76
3.3.2.2	Contactless Stroke measurement	77
3.3.2.3	Driving pulse duration	78
3.3.2.4	Energy consumption	79
3.3.3	Micro-positioning application using the elementary HDA	80
3.3.3.1	Positioning with Guide	80
3.3.3.2	Positioning without Guide	83
3.4	Micro-fabricated Hexagonal 3D Digital Actuator	88
3.4.1	Fabrication of Top and Second plate	89
3.4.2	Experimental characterization of the micro-fabricated HDA	91
3.4.2.1	Experimental Displacement	92
3.4.2.2	Position repeatability & Stroke measurement	93
3.5	Conclusion	95
4	Development of an Hexagonal digital actuator array for Long-range Con-	99
	veyance.	
4.1	Design Constraints and Requirements	99
4.2	Prototype validation with respect to design	
	constraints and requirements	100
4.2.1	Homogenization of Magnetic and Electromagnetic forces	100
4.3	Prototype Assembling and Working Principle	
	of HDAA	104
4.3.1	Working Principle of HDAA	106
4.3.1.1	Actuation Approaches	106
	Stick-Slip approach:	106
	Lift-Mode approach:	108
4.3.1.2	Conveyance possibilities	108
4.4	Experimental Setup and Results	110
4.4.1	Experimental prototype and Control Module	110
4.4.2	Results and Discussions	111
4.5	Micro-fabricated HDAA	114
4.5.1	Experimentation Characterization of the Micro-fabricated	
	HDAA	115
4.5.1.1	Translation of the Conveyance plate	116
4.5.1.2	Transition of the Conveyance plate between actuators	117
4.5.1.3	Rotation of the Conveyance plate	118
4.5.1.4	Realisation of Planar trajectory	120
4.6	Design of an array composed of 19 HDAs	122
4.6.1	Modeling	123
	Modeling of the elementary HDA:	123
	Magnetic interaction for the HDAA:	124

4.7 Conclusion	126
5 Conclusion and perspective	129
5.1 General conclusion	129
5.2 Perspectives	131
5.2.1 Micro-fabricated Hexagonal casing	132
5.2.2 HDA capable to reach multiple z-axis	132
5.2.3 Realisation and characterization of the array composed of 19 actuators	134
5.2.4 Modular Design concept	134
Appendix A List of publications	137
Bibliography	139

List of figures

1.1	Representation of small scaled conveyor module [Krh10].	5
1.2	Experimental setup of the multi directional transport module and view of the module matrix [Sohr 16].	5
1.3	Experimental prototype of the Celluveyor [Uria 15].	6
1.4	Electrothermal micropositioning devices: (a) Image stabilizer Lin et al. [Lin 11] (b) 2DOF MEMS nanopositioner Rakotondrabe et al. [Rako 14]. Piezoelectric micropositioning devices: (c) parallel 6DOF device Ghafarian et al. [Ghaf 18] (d) Tang et al. [Tang 17]. Electromagnetic positioning device (e) Device with 3DOF Al-Jodah et al. [Al J 19] (f) Positioning stage Zhou et al. [Zhou 19]	8
1.5	Basic principle of the pneumatic conveyance system.	9
1.6	(a) Principle of Pneumatic actuator. (b) Micro-fabricated Pneumatic actuator array by Fukuta et al. [Fuku 06].	10
1.7	(a) Cross sectional view of the module. (b) Experimental prototype. (c) Experimental setup used for the validation Guelpa et al.[Guel 17].	11
1.8	Pneumatic conveyor on aerodynamic traction principle by Laurent et al.,(a) Sectioned view (b) Global view (c) Experimental prototype[Laur 11].	11
1.9	Conveyance using soft machine table (a) Conceptualisation of the structure (b)Top view of the air chamber (c)Experimental prototype[Deng 16].	12
1.10	Principle of Electrostatic actuator (a) parallel plate actuator (b) Comb-drive actuator [Knos 09].	12
1.11	Comb drive actuator(a) Prototype of 2DOF Nanopositioner [Ji 10]. (b) Multimodule Micro transportation system [Dao 11].	13
1.12	Transparent synchronous Electrostatic actuator [Hoso 15].	14
1.13	Representation of Electrothermal actuator: Basic Principle of ETA [Wu 18].	15
1.14	(a) Actuation principle (b) Single silicon leg. (c) Micro conveyor [Ebef 99].	15
1.15	Principle of piezoelectric actuator [Wu 18].	16
1.16	Piezoelectric actuator array Tellers et al. [Tell 15].	17
1.17	Basic Principle of Linear Induction Actuator: (a) Short stator (b) Short rotor [Hamz 11] (c) Kumagai et al. [Kuma 12]	18
1.18	(a) Basic Principle of linear reluctance actuator (b) Positioning device by Santo et al. [Espr 10]	19
1.19	Hybrid LRA design (a) Andhara et al. [Andr 14] (b) Hassan et al. [Hass 17]	20
1.20	(a)Basic principle of Lorentz force actuator (b) Moving coil with fixed PMs (c) Moving PMs and fixed coil [Khan 14]	21
1.21	(a) Basic structure of a moving coil type configuration. (b) Different types of moving coil actuator, Dong et al. [Dong 16]	21

1.22 Sliding mode control conveyance system Chin et al. [Chin 13].	22
1.23 Different types of moving PMs and fixed coil actuator [Hiem 14]	22
1.24 A 2D micro-conveyor device Nakazawa et al. [Naka 97]	23
1.25 Illustration of analog and digital actuators Shutov et al. [Shut 05].	23
1.26 Planar electromagnetic conveyor Arora et al. [Aror 19].	24
1.27 Illustration of analog and digital actuators.	25
1.28 (a) Sari et al.[Sari 11] (b) Poletkin et al. [Pole 15] (c) Oda et al. [Oda 18].	26
1.29 Pneumatic levitation approaches [Vand 05].	27
1.30 Electrostatic levitation Jeon et al [Jeon 07]	28
1.31 Examples of Micro-conveyance devices based on different physical principles (a) Pneumatic Conveyance device by Deng et al. [Deng 16] (b) Electrothermal Conveyance device by Ebefors et al [Ebef 99] (c) Electrostatic Conveyance device by Hosobata et al. [Hoso 15] (d) Piezoelectric Conveyance device by Tellers et al. [Tell 15] (e) Electromagnetic Conveyance device by Arora et al. [Aror 19]	30
1.32 Representation of electromagnetic braking system (a) Staab et al. [Staa 11] (b) Kumar et al.[Ravi 17]	31
1.33 Bistable electromagnetic valve Mach et al. [Mach 19].	31
1.34 Latch-lock mechanism Gao et al.[Gao 19].	32
1.35 Self-locking micro-gripper Hao et al. [Hao 15].	33
1.36 Hinged mechanism, Wang et al.[Wang 09].	33
1.37 Electromagnetic conveyance device [Peti 09]	36
2.1 HDA design model (a) Top view. (b) Cross sectional view AA'. (c), (d) Representation of the displacement strokes along xy-plane.	40
2.2 Buildup design of the Printed Circuit Board (PCB)	41
2.3 (a) Direction of the Electromagnetic Lorentz force (Driving force) for different configurations of PM and the conductor (b) Principle of switching between discrete positions	43
2.4 (a) Representation of a 3D elementary HDA (b) Representation of twelve discrete positions with a stroke along z-axis (c) Cross sectional view of the HDA AA'	44
2.5 Representation of the different approaches for conveyance: (a) Stick-slip approach, (b) Lift-mode approach	46
2.6 Reduction of single cuboidal magnet to equivalent charge distribution and its 2D representation.	48
2.7 Distribution of hexagonal PM in to equivalent right angled triangles [Rube 13].	49
2.8 Representation of the discretization method on the Hexagonal PM.	49
2.9 Representation of Hexagonal PM in 3D space with a point outside magnet; Calculation of total flux density and the elapsed time for calculation.	50
2.10 Reduction of cylindrical PM into equivalent magnetic charge distribution and its 2D representation in reference frame.	51
2.11 Graphical representation of magnetic flux density (a) for cuboidal magnet (b) for cylindrical magnet.	53
2.12 Magnet and the illustrated coordinate system for magnetic force calculation.	53

2.13	Analytical and semi-analytical representation of electromagnetic forces for cuboidal magnet.	55
2.14	A Finite element analysis of an electromagnetic air-core coil and the representation of magnetic flux density.	57
2.15	Representation of total forces with respect to the MPM position along x -axis (Current injected in T_c). (a) Driving force (F_x) with respect to current for two different levels along z -axis. (b) Holding force (F_y) with respect to driving current values. (c) Holding force (F_y) with respect to holding current values. (d) Vertical force (F_z) with respect to driving current values. (e) Vertical force (F_z) with respect to holding current values.	58
2.16	Representation of SRZ and IZ (a) Digital actuation behaviour along xy -plane (b) Digital actuation behaviour along z -axis.	61
2.17	Representation of the generated horizontal and vertical frictional forces for MPM and the conveyance plate	62
2.18	CAD model of a 3D digital acutator with cuboidal mobile magnet. (a) exploded view to visualize arrangements of different parts. (b) Top view of the actuator;(c) Front view of the actuator.	64
2.19	CAD model of a 3D digital actuator with hexagonal mobile magnet. (a) An isometric view of the actuator with the assembly of mobile part.(b) Top view of the actuator.	65
3.1	(a) Configuration 1: Mobile part with a PMMA piece. (b) Configuration 2 : Mobile part with a z -axis retainer. (c) Geometrical design, fabricated z -axis retainer and mobile part assembly.	68
3.2	(a) PMMA deformation due to laser cutting technique for the Top plate. (b) Assembly of a 3D printed air-core electromagnetic coil.	70
3.3	(a) FODS probe (b) FODS Signal Processing Unit.	71
3.4	(a) Working principle of the FODS (b) Typical response curve of the FODS.	72
3.5	(a) FODS position with respect to different stroke displacement (b) Pre-calibration response curve for Short- x -stroke	73
3.6	Calibration Grid by Edmund optics	74
3.7	Initial and final discrete positions for different displacement strokes.	74
3.8	(a) Experimental setup (b) Control Module of the HDA.	76
3.9	Representation of twelve discrete positions distributed at two different levels along z -axis.	77
3.10	(a)Representation of minimum pulse duration required for switching with respect to driving current. (b)Representation of energy consumption for three different strokes with respect to driving current.	79
3.11	(a) An exploded view for the elementary micro-positioning device (b) Representation of the effect current values on the plate displacement. (c) Representation of the plate conveyance for the first two sequences for three major displacement strokes.	81
3.12	Representation of a plate displacement with respect to the number of sequences (a) Short- x -stroke with 0.5 mm stroke (b) Long- x -stroke with 1.0 mm stroke (c) Stroke- y with 0.86 mm stroke.	82
3.13	Experimental representation of the micro-positioning device.	83

3.14	Experimental representation of the Stick-slip and Lift-mode approaches for Short-x-stroke.	84
3.15	Maximum possible sequences for Short-x-stroke and Stroke-y with Stick-slip and Lift-mode approaches before plate goes out of limit.	85
3.16	Conveyance possibilities to all discrete positions with the help of Lift-mode and Stick-slip approaches (a) representation of experimental stroke values for planar displacement (b) representation of angles obtained for angular displacement.	86
3.17	Graphical representation of the variation in plate displacement with respect to the mass of plate for both approaches.	87
3.18	(a) Silicon substrate with Mask. (a) Isotropic etching. (c) Anisotropic etching.	89
3.19	Step-wise description of the micro-fabrication process and 3D representation of the final fabricated part.	90
3.20	(A) CAD design of the photolithography mask (b) Micro-scopic view of the hexagonal cavity for Top Plate.	91
3.21	Experimental setup for a micro-fabricated HDA with FODS contactless measurement system.	91
3.22	(a) Experimental Mobile part displacement for three different strokes. (b) oscillations on the displacement curve for Long-x-stroke.	92
3.23	Graphical representation of the position repeatability for the different displacement strokes.	94
4.1	(a) Representation of honeycomb architecture with seven HDA. (b) Magnetic force variation. (c) (d) Representation of electromagnetic force variation.	101
4.2	Representation of magnetic force variation with respect to the number of layers of balancing magnets.	102
4.3	Representation of final version of the prototype and the balanced magnetic forces for each actuator in the final array.	104
4.4	(a) 3D view of a conveyance device (b) Top view showing arrangements of seven actuators using an honeycomb architecture (c) Cross sectional view of a single actuator AA' (d) Representation of strokes and ability to reach twelve discrete positions.	105
4.5	Top & Bottom view of the PCB, buildup design and representation of soldered air-core coil	106
4.6	Principle of conveyance using Stick-slip approach.	107
4.7	Principle of conveyance using Lift-mode approach.	109
4.8	Representation of different conveyance possibilities.	109
4.9	Experimental prototype of the HDAA and the Control Module.	111
4.10	Representation of the plate displacement for stick-slip and Lift-mode approach for different driving current values.	112
4.11	(a) Representation of total time required to convey a plate with respect to driving current. (b) Representation of the number of sequences to cover 10 mm distance with respect to different current values for both the switching approaches.	113

4.12	CAD design of the photo lithography mask and figure representing the dimensions for Top and second plate	114
4.13	(a)Experimental prototype of the micro-fabricated Hexagonal digital actuator array. (b) Cross sectional view of single actuator in an array.	115
4.14	Representation of the Translation motion of the conveyance plate in xy -plane for Long- x and stroke- y	116
4.15	Representation of plate transition between the actuators (a) Representation of the transition phase. (b) Experimental transition in xy -plane using long- x -stroke and stroke- y . (c) Sectional view showing the step-by-step representation of the conveyance strategy using lift-mode and stick-slip approach.	118
4.16	Representation of the Plate rotation using different switching sequences (a) Captured images for the different rotation sequences. (b) (c)	119
4.17	Representation of the multiple rectangular profiles realized using HDAA: (a) switching sequences, (b) Rectangular profile.	121
4.18	Design of the new HDA: (a) Top view, (b) Cross sectional view, (c) (d) Representation of the different strokes.	123
4.19	Representation of the Total forces with respect to current values for short- x -stroke.	124
4.20	Representation of magnetic force variation for different configuration.	125
4.21	Representation of the final proposed prototype for 19 HDAA and the generated magnetic forces by each actuator in an array.	126
5.1	CAD view of hexagonal casing and its assembly	132
5.2	Representation of multi z -axis displacement for an HDA	133
5.3	Representation of different conveyance possibilities using 19 actuator array	134
5.4	Representation of modular design concept for long range application	135

List of Tables

1.1	Comparison between analog and digital actuators [Xu 16]	29
1.2	Characteristics of the presented Smart Conveyance systems	35
2.1	Electric current values along respective motion directions	42
2.2	Dimensional and magnetic parameters of the actuator.	42
2.3	Material properties and quantities of the components used in the assembly of digital actuator.	64
3.1	Camera Specifications	74
3.2	Acquisition Board Specifications	75
3.3	Comparison of Experimental and Theoretical strokes.	78
3.4	Comparison of Experimental and Theoretical strokes.	95
4.1	Magnetic force variation for different configurations	103
4.2	Optimized and non-optimised configurations of two sets balancing PMs	104

List of abbreviations

CAD	Computer Aided Design
HDA	Hexagonal digital actuator
PCB	Printed Circuit Board
DAQ	Data Acquisition
DOF	Degree Of Freedom
DRIE	Deep Reactive Ion Etching
EMA	ElectroMagnetic Actuator
ETA	Electrothermal Actuator
FEA	Finite Element Analysis
FODS	Fiber Optic Displacement Sensor
ICP	Inductively Coupled Plasma
LIA	Linear Induction actuator
LM	Linear Motor
LRA	Linear Reluctance Actuator
MEMS	Micro Electro Mechanical System
NS	North-South
V-I	Voltage-to-Current Converter
MPM	Mobile Permanent Magnet
FPMs	Fixed Permanent Magnets
PD	Photo Diode
PI	Proportional Integral
PM	Permanent Magnet
PMMA	PolyMethyl MethAcrylate
RIE	Reactive Ion Etching
RMS	Root Mean Square

Tc	Top wire
Bc	Bottom wire
SRZ	Self-Returning zone
I_{min}	Minimum driving current
HDAA	Hexagonal Digital Actuator Array
UTC	Université de Technologie de Compiègne
UV	Ultra violet
HRC	High resolution camera

Introduction

The era of miniaturization started in the middle of the 20th century. The need of miniaturization leads to a revolution in the production technologies to be adapted to manufacture micro-devices. Micro technologies have then been developed and are now used in many fields, for example: In our day-to-day life slim notepads, smart phones, watches, medical implants, etc.. are some common uses of micro technologies.

Precision and reliability are the backbone of micro-technologies. Nowadays micro, even nano, level precision is needed in the production of micro-systems. The difficulty in obtaining such precision is due to the amount of errors caused by human interference in the production of such micro-systems. To solve this problem, automation is a key, by ensuring automatic machining and assembly. This trend leads to the development of micro or desktop factories whose concept was firstly introduced in Japan in 1990s. Micro-factories present a high level of automation, high flexibility, reconfigurability and have a size adapted to the produced micro-parts or systems. Thus, making micro-factories more cost effective, time and energy efficient compared to standard factories.

To ensure a high automation level of such micro or desktop factories, modular design and control are needed. The micro-factories are suitable for the production of small and medium size products and their high flexibility allows them to be reorganized according to the manufacturing flow. A central element in a micro-factory that will ensure its flexibility is the conveyance device. It will ensure the part flow into the micro-factory. The existing solutions which are available for macro-level handling are not suitable at micro-level as they are difficult to be integrated and do not provide enough precision. The development of micro-conveyance device without comprising the precision and requires no or minimum human intervention is then a major challenge.

The work presented in this thesis consists of developing a new type of micro-conveyance device based on digital actuation principle and able to deliver millimeter level

strokes. In order to reach this objective, the work presented in this manuscript is divided into five chapters.

Chapter 1 provides a state of the art on conveyance devices at macro, meso and micro-levels. Various devices are presented which are classified according to their physical principle. It also describes the two functions of digital actuators and ongoing researches in that sector.

In chapter 2, the principle, modelling and design of an elementary digital actuator are presented. Magnetic and electromagnetic models of the actuator have firstly been realized and secondly a prototype has been designed.

Chapter 3 presents the realization and the experimental characterization of the designed elementary digital actuator. The manufacturing techniques and the control module are described and different experimental results are then presented. The ability of the mobile part of the actuator to reach twelve discrete positions distributed at two different levels along z -axis is presented.

Chapter 4 presents the use of several digital actuators in the form of an array to realize long-range conveyance tasks. The modeling, design, fabrication and testing of the array are detailed and its ability to realize conveyance tasks is then shown. A miniaturized version of the array is finally presented and designed.

Chapter 5 provides a general conclusion and gives some perspectives regarding the work presented in this manuscript.

The details regarding the published articles can be found in [Appendix -A](#).

Chapter 1

State of the art

This chapter provides a literature review of conveyance devices and particularly those used in the field of micro and desktop factories. An introduction to smart surface and recent advancement in the conveyance devices is firstly presented. Different actuation technologies are then discussed on their relevance to perform conveyance tasks. The main focus of this chapter is on digital actuators with their architecture and the different physical principles used for actuation. Finally, a conclusion is provided on the basis of different actuation technologies and various digital actuation principles.

1.1 Smart Conveyance Surfaces

Conveyance surfaces are mechanical handling equipments that are used in order to move objects from one place to another. These surfaces are actuated either using centralized motor system or with the help of several motors, i. e. decentralized motor system. Centralized actuation, as the name indicates, integrates one motor in order to perform the conveyance. They are dynamic and have precise motion control. However, there is a need to have constant overview of the system for the decision making, which makes the system dependant on the material flow. It also requires cooling system in order to dissipate large amount of generated heat and in case of any fault, the whole system may breakdown [Albe 05][Prab 18]. On the other hand, decentralized motor systems integrates several motors together, working elementary or in a collaborative manner. The control allows

to distribute the load homogeneously on the non-hierarchical structure, which makes it easier for decision making and task execution. If in any case, there is a failure in the working of one system, the others will still work in collaboration to perform common tasks [Vand 11][Zamo 10][Firv 18].

Decentralized motor control, when gets embedded with intelligent systems, are referred as smart conveyance surfaces. The ability to interpret position coordinates optimizes the object trajectory in terms of total time required or energy consumption and finally able to convey several objects independently are some advantages of smart decentralized motor conveyance systems [Baz 12][Bout 10][Mati 10]. Such type of conveyance surfaces are widely used at macro- and micro-scale. In this review, the main focus is on such kind of decentralised systems, as they can be easily integrated on the micro-scale and presents high flexibility.

1.1.1 Smart Conveyance at Macro-scale

In macro-scale factories, the conveyance devices are either use to convey material from the inventory store to the workspace or to sort the packages and making them ready for delivery. In the intralogistics industries, a smart conveyor is essential for an in-plant material and packages handling, that will help to speed-up the delivery process without compromising the precision in sorting.

In Fig. 1.1, a conveyance system based on actuated rollers is presented [Krh 10]. Each roller of the system, integrates a servo motor fixed at its base in order to carry out swivel drive. This swivelling roller helps to convey the object (placed on top of it), along x - and y -axis, respectively. The rollers are referred as modules and the combination of all these modules forms a decentralised conveyance system. This system provides high flexibility in terms of transfer and sorting functions. There is also a possibility to collaboratively used these modules in order to perform many operations at a time.

Another smart conveyance device has been proposed by [Sohr 16] using a multi directional transport module as shown in Fig.1.2. It consists of small scaled modules arranged in the form of a matrix with total dimension of 65×65 mm. Each module consists of a tilt

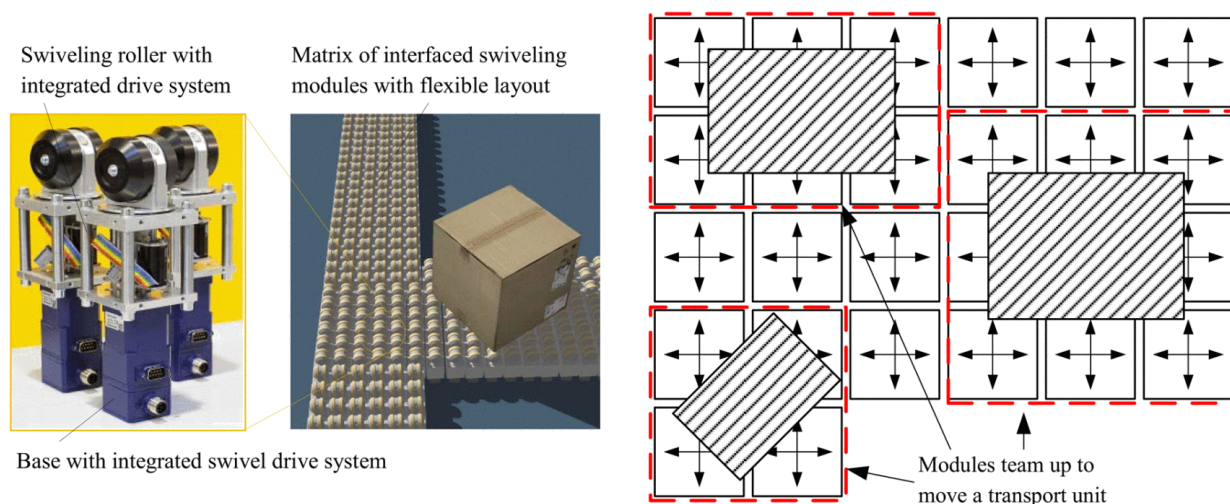


FIGURE 1.1: Representation of small scaled conveyor module [Krh 10].

disk driven by two identical collinear mounted motors. They help to vary the tilt angle and also for the conveyance. The modules are smaller than the packet sizes and therefore, several modules are then in contact with the conveyed part that ensures a collaborative actuation. The modules are decentralized systems with a 8-bit micro-controller, sensor

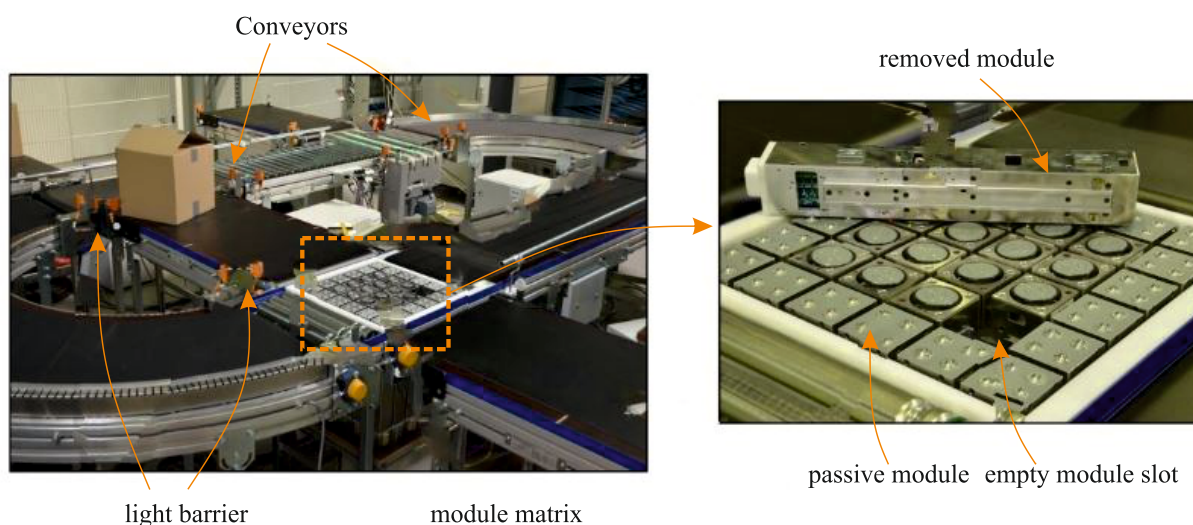


FIGURE 1.2: Experimental setup of the multi directional transport module and view of the module matrix [Sohr 16].

and servo motors. The maximum conveyance speed is around 2 m/s and carrying capacity of 125 kg/m² when used in a matrix. A light sensor fixed in each module will help to determine the location of the packet on the matrix. Each module gets the feedback from neighbouring module and it works accordingly to realize complex operations. Therefore, each module is not dependant on the size of matrix and it is not affected by the failure of

any module in a matrix as shown in Fig. 1.2. A faulty module can be easily replaced by another one.

Recently, research is going on in order to use smart conveyance devices as an omnidirectional drive system and also to obtain precision in positioning. One such example is the cellular conveyor or Celluveyor [Uria 15][Fivr 18]. It is a modular conveyor and positioning system which offers a high degree of flexibility. It consists of several hexagonal conveyor modules, each integrates three wheels. Each module is individually or collaboratively controlled which allows to move or position several objects simultaneously and independently. The three wheels enable planar motions of the conveyed objects.

The presented architecture of the macro conveyors cannot be directly miniaturized for micro-conveyance but need to be revised on a miniaturized version to have a better fit for the micro-world. The next section will talk about such devices and their different actuation technologies.

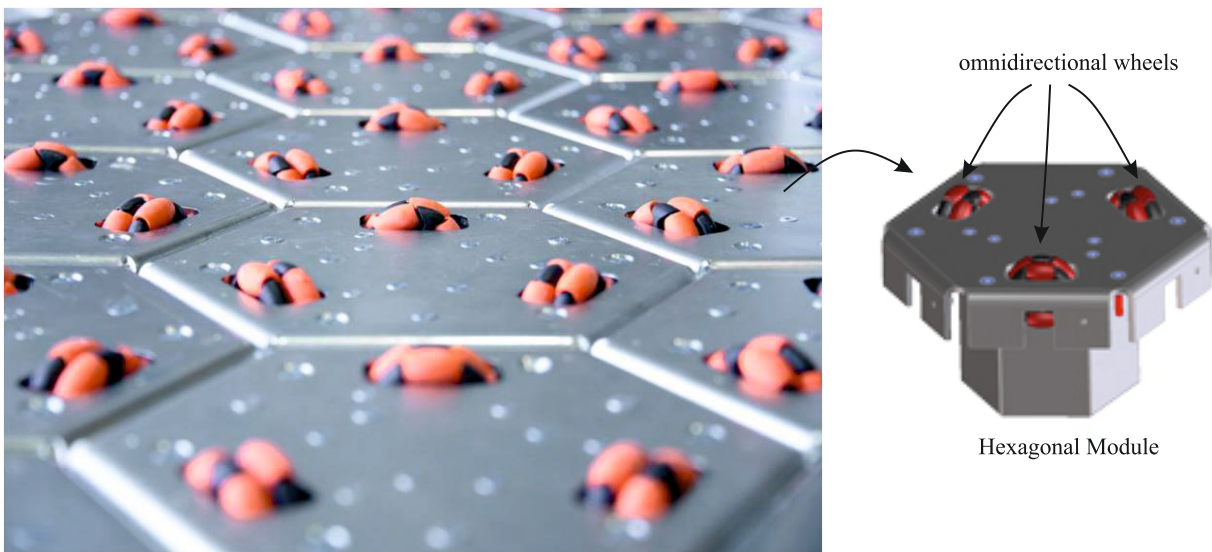


FIGURE 1.3: Experimental prototype of the Celluveyor [Uria 15].

1.1.2 Smart Conveyance at Micro/Meso-scale

The rapid growing need for miniaturized products is increasing in many domains as in aero-space, automotive, biomedical, optical, military and micro-electronics packaging industry [Koc 11]. New technologies and practices have been undertaken to meet precise and eco-friendly production requirements. Flexibility and precision can be achieved by incorporating automation in the production systems [Pere 13][Tuok 13]. Micro and desktop factories have been proposed to meet such on growing requirement. The concept of micro-factory has been first proposed by Japan in 1990's. These factories are able to realize various applications such as assembly, positioning, micro-machining, etc. As micro-factories require minimum or no human interference, smart conveyance device represents a key element and ensures to displace part/product within the micro-factory [Aror 19] [Prus 10].

In the literature, a huge number of actuators using various physical principles can be found. Nevertheless, less number of these actuators are dedicated to conveyance application or can be extended for this kind of application. However, there are several examples of actuators as micro positioning or micro-manipulation devices with a limited range. Fig. 1.4 presents some of the examples for electrothermal, piezoelectric and electromagnetic actuators. In the electrothermal principle, Lin et al. proposed a 4-axis image stabilizer based on thermal actuator to solve the anti shaking problem of the image sensor [Lin 11]. The total device is of dimension $1.49 \times 1.49 \times 0.4 \text{ mm}^3$ with a maximum actuating distance of the stage of $25 \mu\text{m}$ [Fig. 1.4(a)]. Rakotondrabe et al. [Rako 14] developed nano and micro positioning devices with a displacement range of $\pm 5 \mu\text{m}$. [Fig. 1.4(b)]. The stage is of dimension $1 \times 1 \text{ mm}$ and connected with series of beam flexures to mechanically guide the motion. The device is able to obtain a displacement range of $\pm 5 \mu\text{m}$ for both axes and a response time less than 300 ms.

The micro/nano manipulation devices using piezoelectric principle has been developed by [Ghaf 18][Tang 17], as shown in Fig. 1.4(c)(d). The device presented by Ghafarian et al [Ghaf 18] is able to obtain 6DOF but with a maximum displacement range of

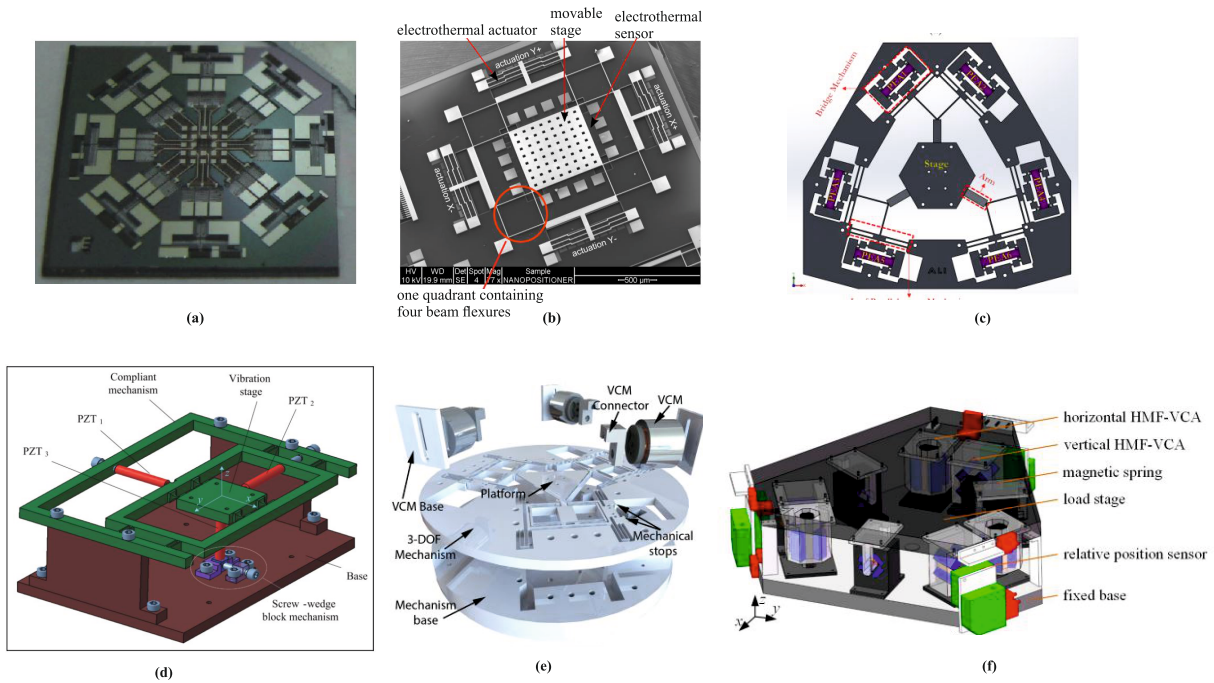


FIGURE 1.4: Electrothermal micropositioning devices: (a) Image stabilizer Lin et al. [Lin 11] (b) 2DOF MEMS nanopositioner Rakotondrabe et al. [Rako 14]. Piezoelectric micropositioning devices: (c) parallel 6DOF device Ghafarian et al. [Ghaf 18] (d) Tang et al. [Tang 17]. Electromagnetic positioning device (e) Device with 3DOF Al-Jodah et al. [Al J 19] (f) Positioning stage Zhou et al. [Zhou 19]

211.8 μm . The devices developed by [Tang 17] have a maximum displacement range of 15.55 μm . Positioning devices based on electromagnetic principles have been presented by [Al J 19] & [Zhou 19] with a translation stroke size of $\pm 2.5 \text{ mm}$ and $\pm 0.5 \text{ mm}$, respectively. The devices are capable of obtaining 3DOF during their working however, cannot be adapted for their use in the conveyance application.

The applications present above shows high precision however, they cannot be used directly to realize micro-conveyance application with millimetric/centimetric/decimetric displacements. In literature, there are some examples of conveyance devices and the following section focuses different physical principles used in such devices.

1.2 Physical Principle for Conveyance devices

The conveyance devices presented in literature are based on different physical principles. The choice between these physical principles depends on various parameters which include reliability, precision, energy consumption, etc. According to literature review,

various physical principles are listed below and described in the following paragraphs :

- Pneumatic Principle.
- Electrostatic Principle.
- Electrothermal Principle.
- Piezoelectric Principle.
- Electromagnetic Principle.

1.2.1 Pneumatic Principle

Conveyance devices based on pneumatic principle make use of compressed air, injected in small inlets (called nozzles) as shown in Fig. 1.5. This helps to simultaneously levitate and move the object. The levitation is usually obtained due to air cushion which can be controlled using pressure/pneumatic valves. A collaborative control of these valves helps to move the object. The pneumatic principle can be used for contactless actuation. It has several advantageous characteristics such as clean, non magnetic and low heat generation conveyance solution.

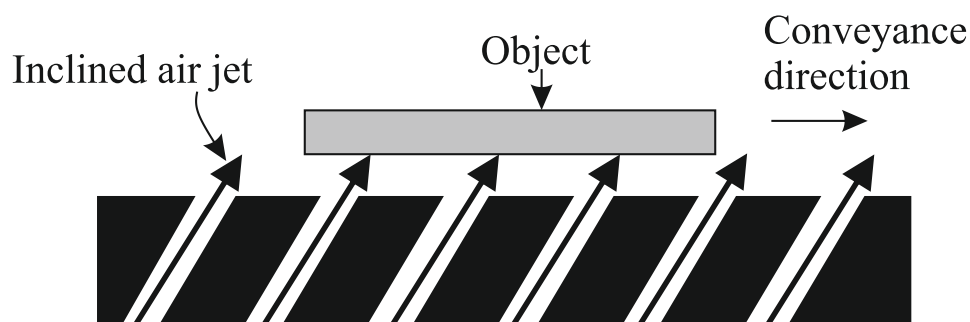


FIGURE 1.5: Basic principle of the pneumatic conveyance system.

Fukuta et al. have developed a pneumatic actuators array based on this principle [Fuku 06]. A distributed micro manipulation is realized using pneumatic principle whereas the actuation of the single nozzle, to levitate and to move the object, is based on an electrostatic principle. The mobile part of each valve consists of an electrode which is aligned with the two electrodes, one on each side, to generate the electrostatic force. When the valve is closed, a levitation force is generated using vertical air flow. To displace the object on the right side, the right electrode is turned on as shown in Fig. 1.6 (a). The total area of a single actuator is $1 \times 1 \text{ mm}^2$ and that of the array is $35 \times 35 \text{ mm}^2$ and it is

composed of 560 microactuators. Two different conveyance objects were used to characterize the velocity, air-flow force and the stability. The experiments show a conveyance velocity of this system between 0.5 mm/s and 4.5 mm/s and a maximum force is $0.37 \mu\text{N}$ with a pressure of 13.2 kPa.

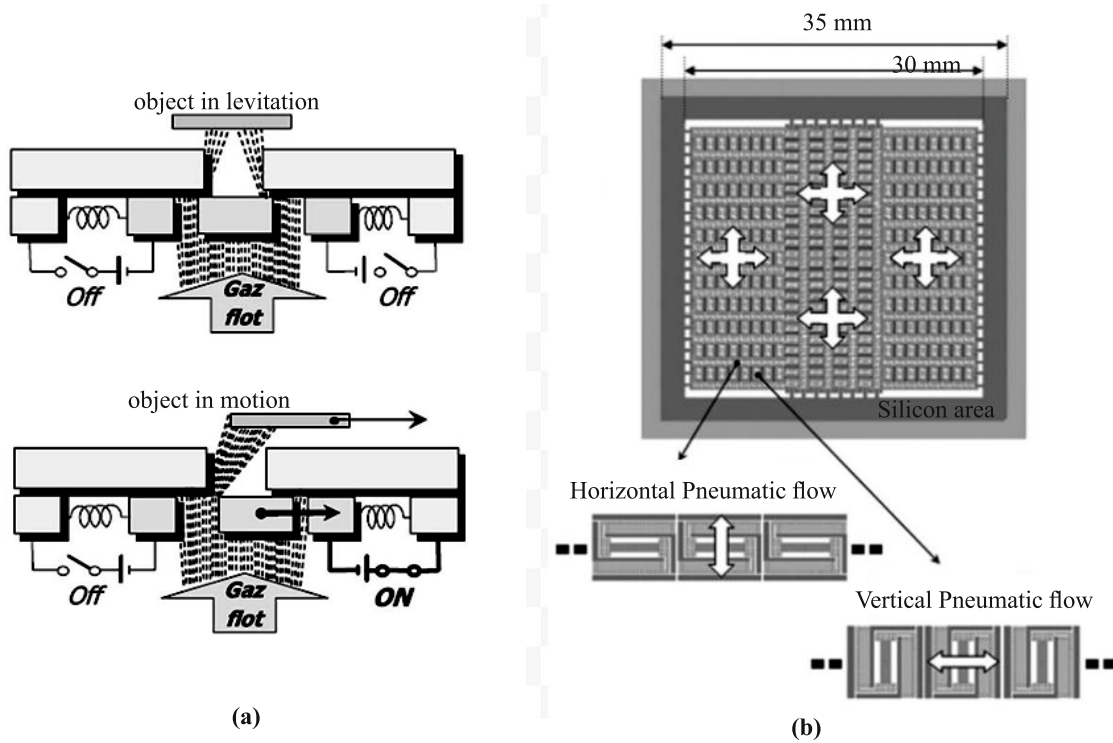


FIGURE 1.6: (a) Principle of Pneumatic actuator. (b) Micro-fabricated Pneumatic actuator array by Fukuta et al. [Fuku 06].

Another pneumatic conveyance based on an inclined air-jets technique has been proposed by Guelpa et al. [Guel 17]. The device is based on a modular concept to convey and handle fragile objects like silicon wafers. Each module/block is 3D printed with dimension of 75×75 mm. The top surface of each module consists of 128 holes with a tilt angle of 45° as shown in Fig. 1.7 (b). The blocks are fixed on a breadboard with screws and springs to obtain horizontal alignment. A combination of such blocks helps to realize conveyance operations such as displacement, positioning, rotation, etc. A L-shaped trajectory is presented in Fig. 1.7(c). The device has been able to convey with a maximal speed of 0.3 m/s in both the simulated and experimental results.

Laurent et al. have developed a pneumatic conveyance device using an aerodynamic traction principle [Laur 11]. The object is moved indirectly by the air flow which is

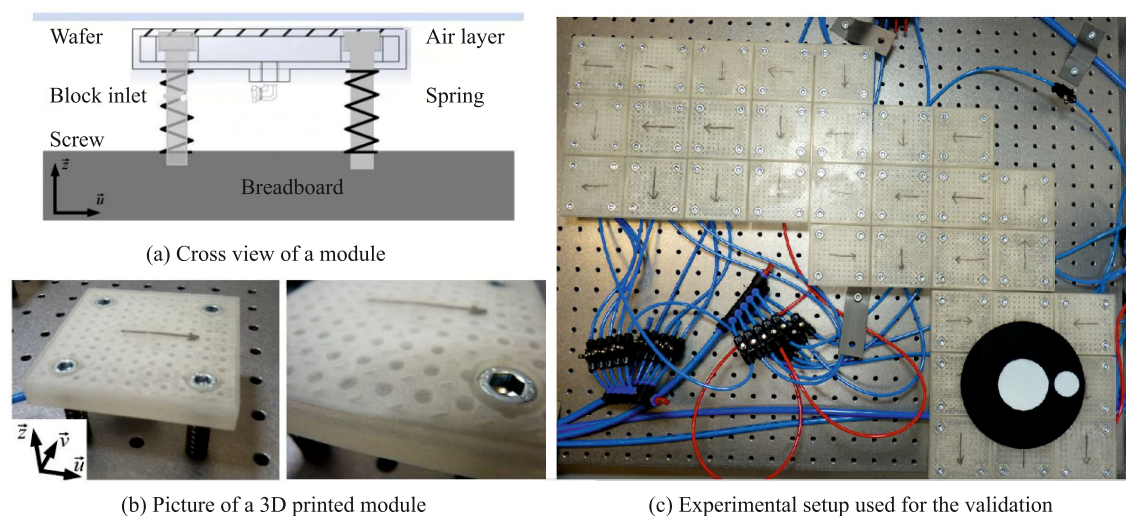


FIGURE 1.7: (a) Cross sectional view of the module. (b) Experimental prototype. (c) Experimental setup used for the validation Guelpa et al. [Guel 17].

induced by strong vertical jets. The induced air flow surface is a square profile with $120\text{ mm} \times 120\text{ mm}$ in dimensions. The device consists of an upper block of 15×15 holes (nozzles) each of diameter 0.4 mm and a lower block with 112 staggered holes. This helps to levitate and move the object. Conveyance of various objects have been realised. For a H-shaped object weighing 32.38 g , the estimated maximum velocity could reach 220 mm/s with a traction pressure of 500 kPa .

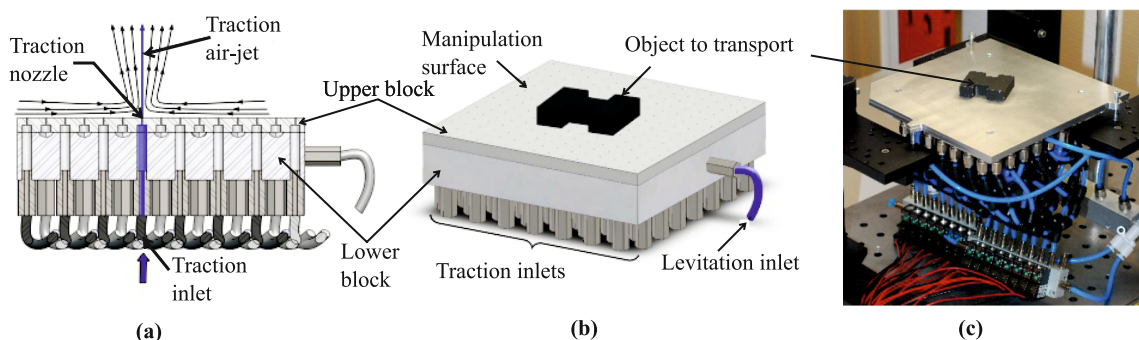


FIGURE 1.8: Pneumatic conveyor on aerodynamic traction principle by Laurent et al., (a) Sectioned view (b) Global view (c) Experimental prototype [Laur 11].

Deng et al. have developed a contact manipulation table using pneumatic principle [Deng 16]. The device is inspired by a caterpillar locomotion and realised object manipulations using the friction generated by surface deformation. The actuation is formed by the combination of inflatable soft structures as shown in Fig. 1.9. The pneumatic system (valves) helps to inflate air chambers. The prototype has 25 soft actuators in the form

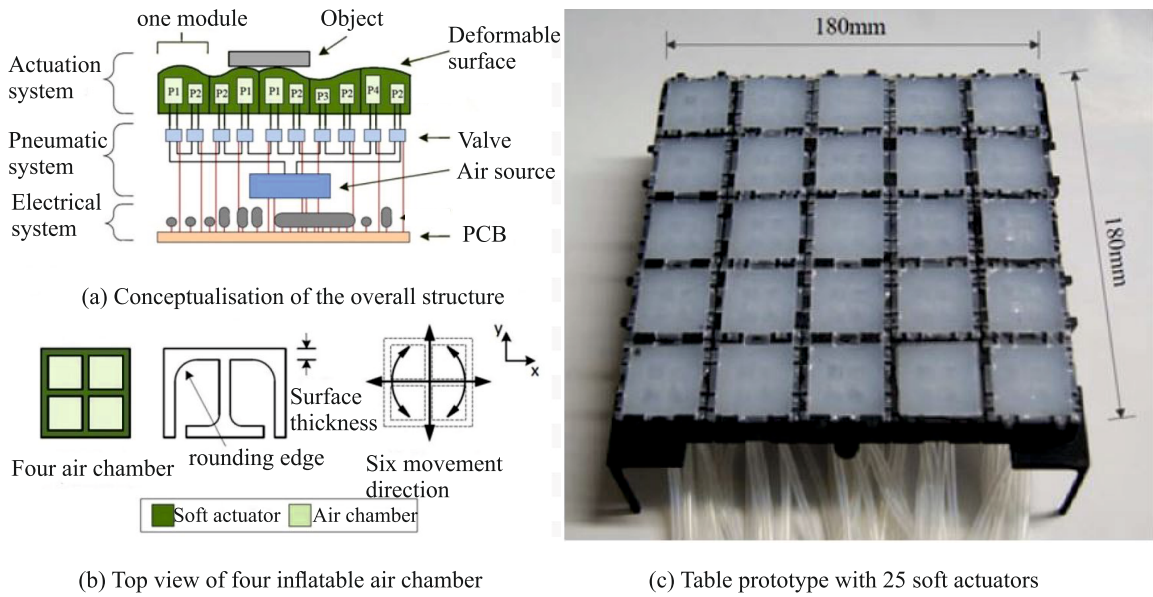


FIGURE 1.9: Conveyance using soft machine table (a) Conceptualisation of the structure (b)Top view of the air chamber (c)Experimental prototype[Deng 16].

of 5×5 square matrix. The dimensions of each actuator are $36 \times 36 \times 22$ mm with a total dimension of 180×180 mm. A smartphone has been used as conveyed object and it was moved over 21 mm with 20 motion cycles with an average speed of 30 mm/min. The device is also able to rotate the smartphone with an average speed of $1^\circ/s$.

1.2.2 Electrostatic Principle

Electrostatic actuators are based on the force between two conducting electrodes when a voltage is applied between them. The simplest electrostatic actuator consists of two parallel plate electrodes where one electrode is fixed and other is movable as shown in Fig. 1.10.

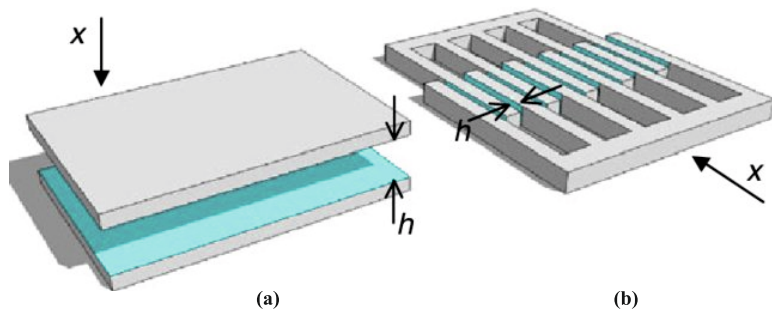


FIGURE 1.10: Principle of Electrostatic actuator (a) parallel plate actuator (b) Comb-drive actuator [Knos 09].

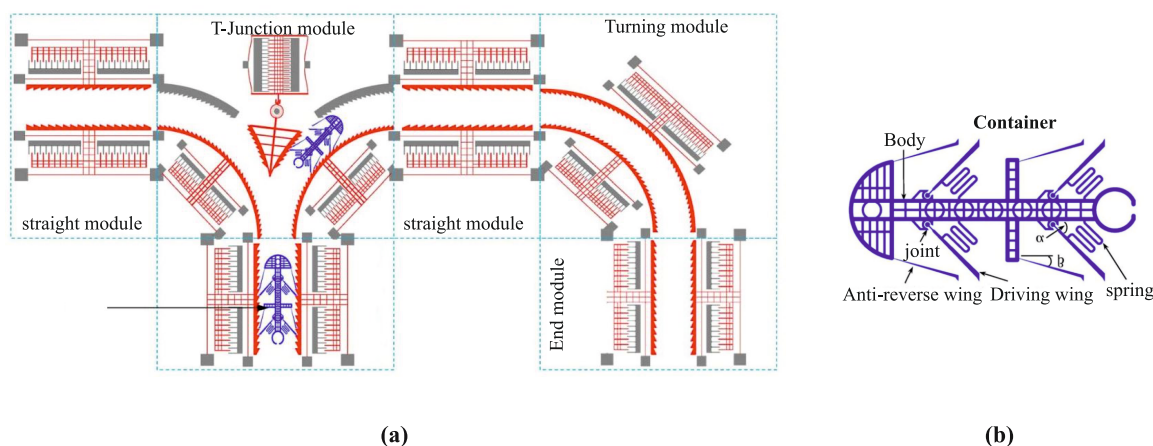


FIGURE 1.11: Comb drive actuator(a) Prototype of 2DOF Nanopositioner [Ji 10]. (b) Multimodule Micro transportation system [Dao 11].

Comb-drive structure is another widespread solution in electrostatic actuators [see Fig. 1.10 (b)]. It is typically used on micro or nano-metric level. It is composed of a static and a moving comb like structure, when the voltage is applied between them, an attractive or repulsive force is generated resulting in the motion of the mobile comb. Long range conveyance devices based on an arrangement of several comb-like structure modules together have been developed by Dao et al. [Dao 11].

The micro transportation system proposed is based on comb-drive and ratchet mechanism. Different modules are developed and attached together to obtain straight, curved and T-junction paths for the manipulation as shown in Fig. 1.11(a). The total size of mobile part is $500 \times 250 \times 30 \mu\text{m}$. The straight module is of dimension $6 \times 1.75 \text{ mm}$ allows straight displacements whereas the T junction and curved modules allow to turn right or left and also at an angle of 90° , respectively. The proposed system is able to ensure long range conveyance but the path is fixed in advance.

Hosobata et al. have developed a transparent electrostatic actuator for long stroke planar motion as shown in Fig. 1.12 [Hoso 15]. The device consists of an overlaid pair of films where the larger film is called stator and the smaller one is the slider. Glass beads are placed between them to maintain an air gap. The working is as shown in Fig. 1.12(b). The slider displacement is possible due to the generation of potential difference between the slider and the stator. The difference generates a tangential electrostatic force to exert a thrust on the slider making it to displace. The total travel range along straight or

curved paths are within 132 mm by 132 mm. This architecture is more adapted for flexible conveyance as needed in the micro-factory context.

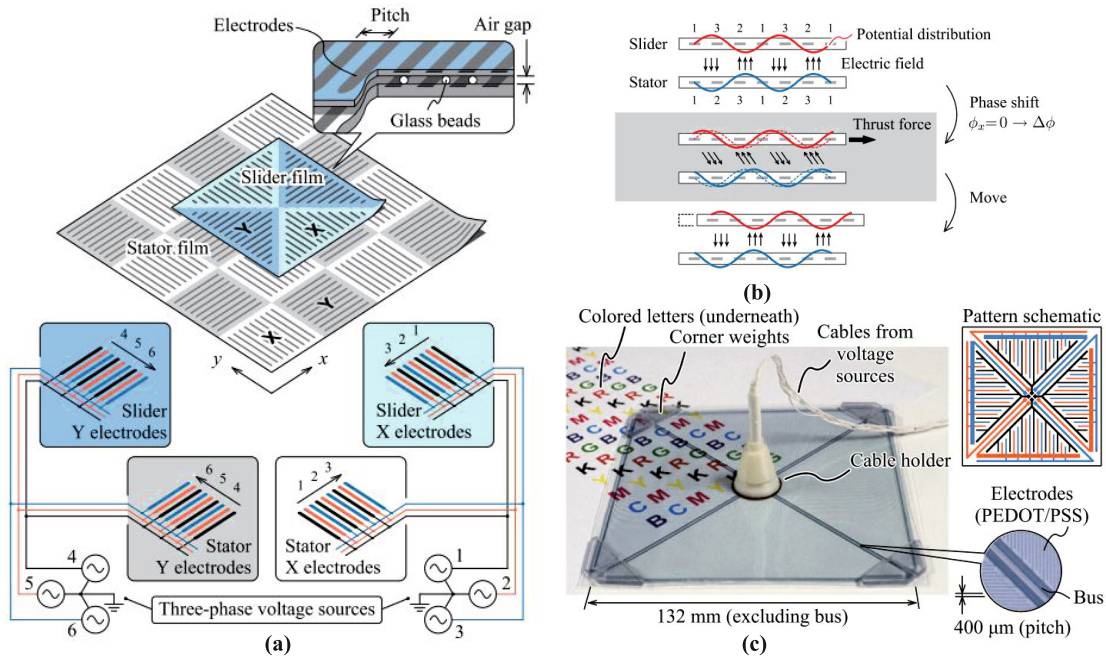


FIGURE 1.12: Transparent synchronous Electrostatic actuator [Hoso 15].

1.2.3 Electro thermal Principle

Electrothermal actuators are the kind of actuator which can be based on several physical phenomenon like material's thermal expansion [see Fig. 1.13], gas expansion, phase change (as in SMA). The examples presented in this section are based on material expansion as in literature the conveyance devices are mostly found out using this principle. The actuator works according to Ohm law based on the principle of resistive heating. When a current passes through the material, due to the presence of resistance, it generates Joule heating and then the thermal expansion of the material [Vero 17]. Based on the material expansion principle, electrothermal actuator involves three main types hot/cold arm, chevron-shaped (V-beam) and bi-morph [Pote 19].

In literature, there are not many examples of conveyance devices realized using electrothermal principle. Ebefors et al. have developed a micro conveyance device based on an array of movable silicon legs (Fig. 1.14(a)) [Ebef 99]. The array helps to realize conveyance operation by moving a flat object in horizontal direction as shown. When

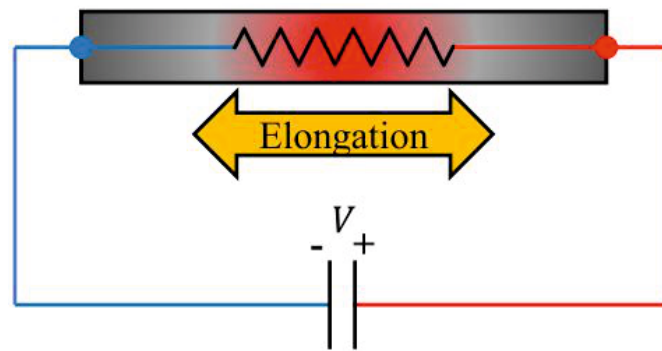


FIGURE 1.13: Representation of Electrothermal actuator: Basic Principle of ETA [Wu 18].

an electric current passes through the curved polyimide joints [Fig. 1.14(b)], it causes deformation in those joints thus creating a displacement. When the heating stops, the joint comes back to its initial position. In the work presented by [Ebef 99], they developed a platform composed of several actuators forming an array. The conveyor consists of $15 \times 15 \text{ mm}^2$ chip with 12 silicon legs each $500 \mu\text{m}$ long. It can perform translation operation to in millimetre range with a velocity of 12 mm/s .

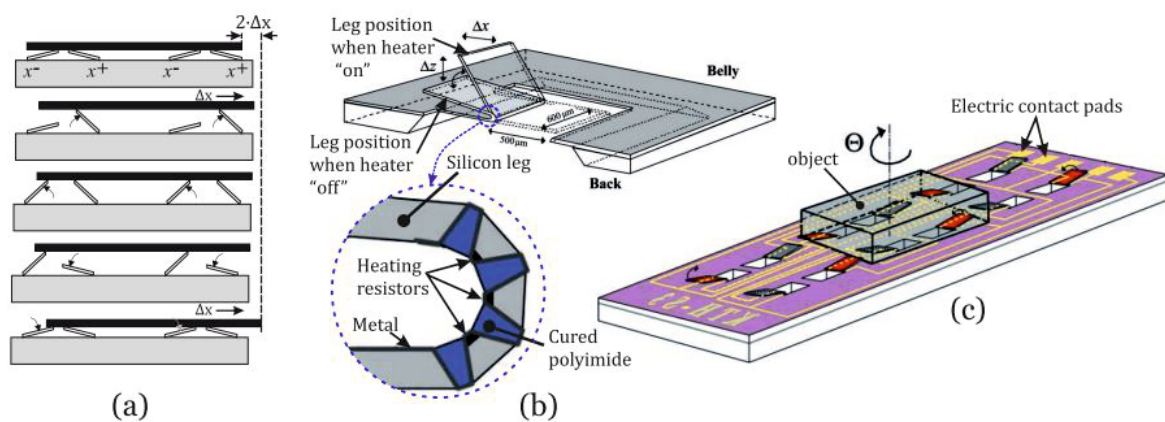


FIGURE 1.14: (a) Actuation principle (b) Single silicon leg. (c) Micro conveyor [Ebef 99].

In general, electrothermal actuators have advantages over the electrostatic ones, as they use low voltage and generate large output force. However, they are thermal dependent which generate slow actuation and therefore, limits their applications.

1.2.4 Piezoelectric Principle

Piezo electric actuators are based on piezoelectric effect which is an ability of certain materials to generate electric charge in response to applied mechanical stress. This behavior is reversible meaning that piezoelectric materials can either exhibit direct piezoelectric effect (produce electricity when applied to stress) or reverse effect that is they generate stress when subject to electric field as shown in Fig. 1.15. This reverse piezoelectric behavior can be used for actuation [Liu 18].

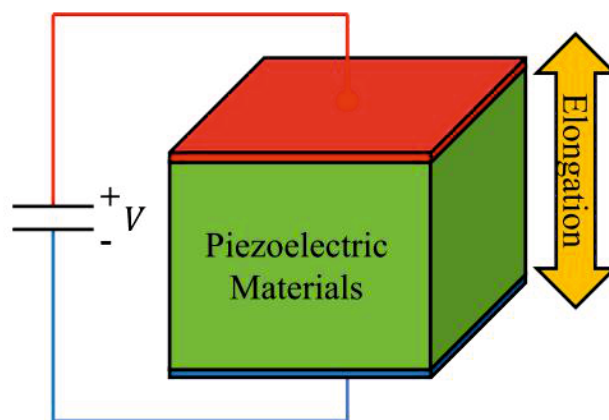


FIGURE 1.15: Principle of piezoelectric actuator [Wu 18].

Piezoelectric actuators have many actuation modes like resonance, inertial clamping, feeding actuation and direct actuation. However due to their short displacement range, they are mainly used for micro or nano level positioning devices.

In order to realize a long range conveyance, a modular design can be adapted as explained by Tellers et al. [Tell 15]. They have developed a piezoelectric actuator surface capable of conveying discrete circuit components. This surface is composed of an array which consists of several actuators each integrates a unimorph piezoelectric cantilever actuator fabricated from thin-film PZT as shown in Fig. 1.16. Two different layouts are mentioned for translation and rotation operation. The array is able to convey silicon chip ($500\ \mu\text{m}$ cube) with a maximum average velocity of $3.5\ \text{mm/s}$ and rotational speed of $31.9\ \text{rpm}$.

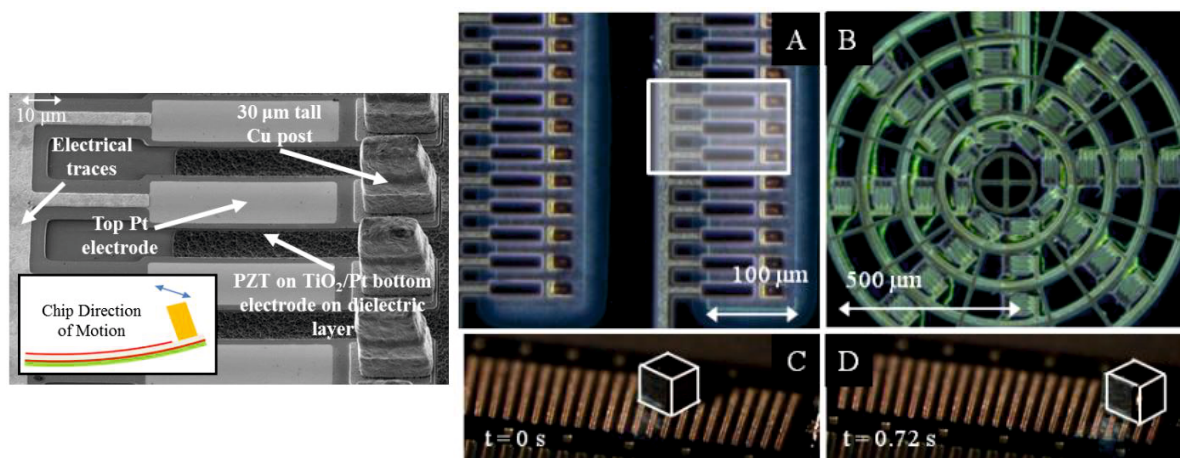


FIGURE 1.16: Piezoelectric actuator array Tellers et al. [Tell 15].

1.2.5 Electromagnetic principle

Electromagnetic actuators are based on the electromagnetic force, exerted on an electrically charged particle moving in the presence of magnetic field. The main advantages of electromagnetic actuators includes, high speed, fast response, low cost and simple design. As friction is the important parameter to be taken into account in the realisation of micro/nano positioning devices, levitation of the mobile part is a solution which can be obtained using pneumatic actuators (see section 1.2.1). Another solution to generate the levitation is by using electromagnetic effect. The electromagnetic force can be used to levitate and translate the conveyed object. The electromagnetic actuators are generally classified into three types based on the generation of electromagnetic forces: inductance, reluctance and Lorentz force [Furl 01].

1.2.5.1 Linear induction actuator

A linear induction actuator is based on the electromotive force generation. It is generally produced in a conductor or conducting material when exposed to the changing magnetic flux (Faraday law). The interaction between induced current and the changing magnetic flux generates induction (Lenz law). The linear induction actuators are either with a short stator or with short rotor as shown in Fig. 1.17(a)(b). They are used in variety of applications due to high speed, easy maintenance, low cost and simple structure. However, they require higher power consumption and have a complex control.

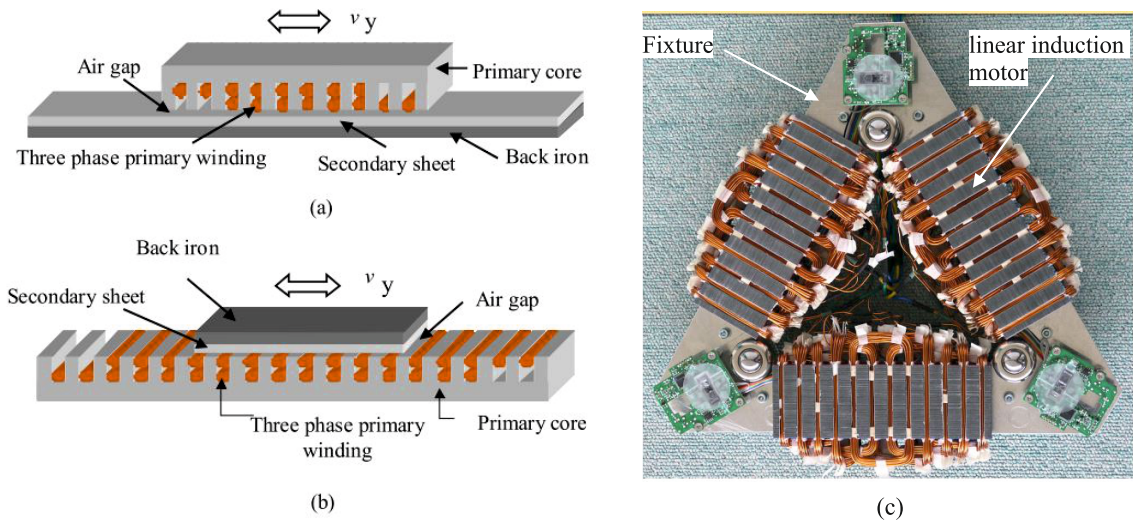


FIGURE 1.17: Basic Principle of Linear Induction Actuator: (a) Short stator (b) Short rotor [Hamz 11] (c) Kumagai et al. [Kuma 12] .

In a micro conveyance devices, this principle can be used to realize a high speed and long range device. For example, Hamz Bahmani et al. have developed an experimental model using the short stator configuration [Hamz 11]. The synchronous speed of the linear inductance actuator on a frequency of 50Hz is 13.47 m/s.

Another example is the 3DOF planar induction motor developed by Kumagai et al. (Fig. 1.17(c)) [Kuma 12]. They have used three linear inductance actuators for actuation and three laser mouse sensors for sensing. The single linear inductance motor is of dimension 150×50 mm. They are arranged in the form of delta which helps to realize three DOF (two translations and one rotation). The core material of the actuator is composed of 100 magnetic steel sheets (0.5 mm thickness each). The total diameter of the device is $\phi 180$ mm with a total weight of 4.8 kg. The actuator has a payload capacity of 60 N with a peak acceleration of 12m/s^2 .

1.2.5.2 Linear reluctance actuator

The principle of reluctance is defined as the ratio of magnetomotive force to magnetic flux and is analogous to the electrical resistance in electric circuit. The reluctance force occurs when a current carrying coil in a magnetic field is energized. It helps to reduce the overall resistance of the magnetic circuit.

Linear reluctance actuator exhibits high operation reliability and high force/weight ratio. However, there are certain drawbacks, as it requires adequate control strategy, power converters and they are noisy actuators under normal operation [Chai 06].

Santo et al. have developed a positioning device based on linear reluctance principle [Espr 10]. The device has several parts called as phases (3 are mentioned) and each parts constitute the magnetic yoke and respective coil as shown in Fig. 1.18(b). As per the experimental results, the actuator is able to develop a traction force of 150 N with a current value of 4 A.

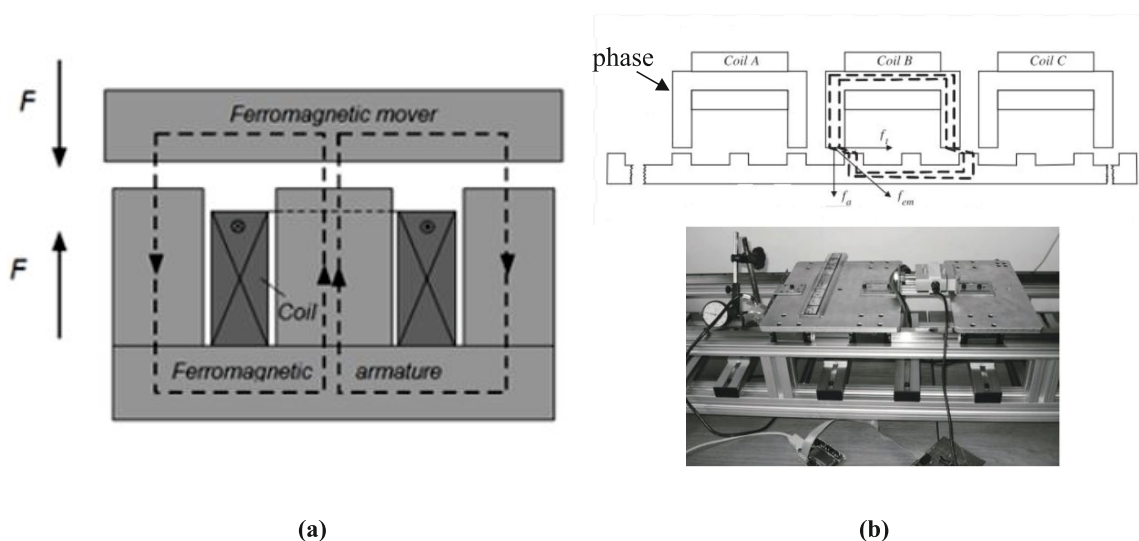


FIGURE 1.18: (a) Basic Principle of linear reluctance actuator (b) Positioning device by Santo et al. [Espr 10] .

Andrada et al. have developed an hybrid design of a reluctant actuator [Andr 14]. They placed permanent magnets (PMs) to further increase the force/weight ratio as shown in Fig. 1.19(a). Two versions have been developed, one with permanent magnets and another one without magnet. The authors are working to develop a prototype for the same.

Based on the same principle, Hassan et al. have developed an actuator in which the generated force helps to move the mobile part (called as armature) to the position where the magnetic flux faces least reluctance (see Fig. 1.19(b)) [Hass 17]. As the results presented the stroke value increases with increase in voltage inputs. The maximum stroke presented has been around ± 4.5 mm for a voltage of 35 V.

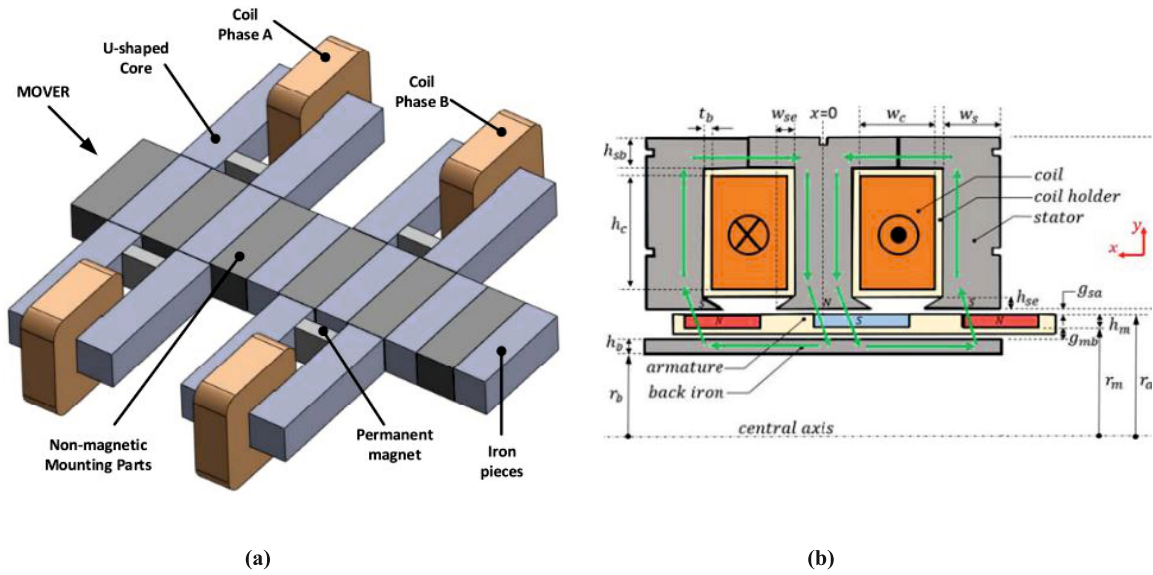


FIGURE 1.19: Hybrid LRA design (a) Andhara et al. [Andr 14] (b) Hassan et al. [Hass 17]

1.2.5.3 Lorentz force actuator

The third type of electromagnetic actuation is based on Lorentz force. It is the force on a charged particle due to electric and magnetic field. This force is generated by the interaction between the current in the conductor and the magnetic flux density around the conductor as shown in Fig. 1.20. The direction of this force is given by the Fleming's left hand rule and according to this rule, the generated Lorentz force will be oriented orthogonally to the wire. Compared to inductance and reluctance actuators, this actuators generate less noise in normal condition, can have nano-metric precision and are able to obtain a omnidirectional displacement. These actuators are mainly based on two architectures: moving coil and fixed PM configuration (Fig. 1.20(b)) and moving PM and fixed coil configuration (Fig. 1.20(c)).

a) Moving coil and fixed PM configuration: As the name indicates, in this configuration the PM is fixed on a stator part and the coil is fixed on the mover part. The main advantage of this configuration is that it allows to increase the displacement range of actuator by adding number of PMs. Gong et al. have presented a conveyance device used in photo-lithography process to obtain nano-metric precision [Gong 13]. In addition, the

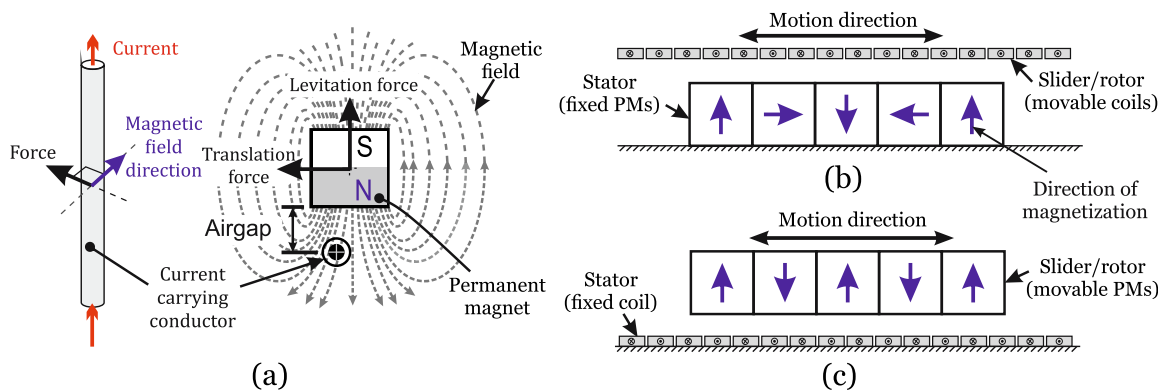


FIGURE 1.20: (a) Basic principle of Lorentz force actuator (b) Moving coil with fixed PMs (c) Moving PMs and fixed coil [Khan 14] .

stator part of this type of actuators are sometime arranged in particular fashion to enhance the magnetic field (Halbach array) as shown in Fig. 1.20(b). The basic structure of such type of configuration is shown in Fig. 1.21(a).

Based on this configuration, Dong et al. developed a device with three different types as shown in Fig. 1.21(b) [Dong 16]. The first one consists of monolithic PMs and single

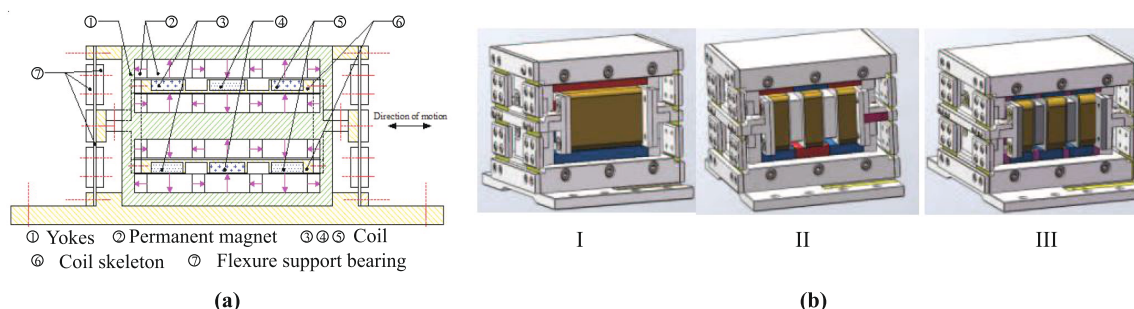


FIGURE 1.21: (a) Basic structure of a moving coil type configuration. (b) Different types of moving coil actuator, Dong et al. [Dong 16] .

coil. The second one includes common PM array and three coils while the third one integrates a Halbach PM array and three coils. All the three actuators have the same stroke size which is ± 1.5 mm. Due to the Halbach array the thrust force is increased in third configuration and also low force ripple is observed in third type. These are important parameters to be considered for these actuators as the thrust force that determines the acceleration and speed of the movement and force ripple that determines the positioning accuracy.

Chin et al. have developed conveyance device as shown in Fig. 1.22 [Chin 13]. This device consists of air core coil linear synchronous motor for the plate displacement and

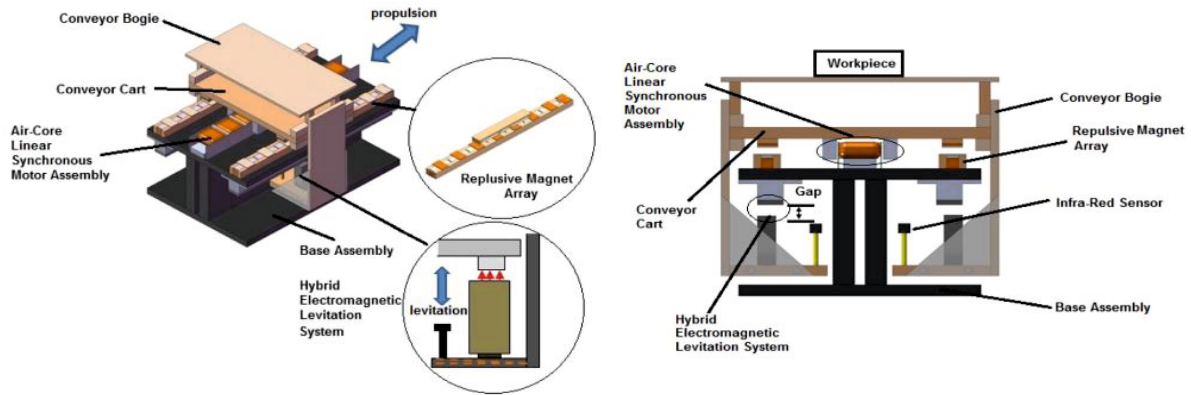


FIGURE 1.22: Sliding mode control conveyance system Chin et al. [Chin 13].

repulsive magnet array to generate levitation. The total dimension of the system is 500 mm×500 mm×300 mm and it is able to achieve maximum speed of 0.6 m/s with an acceleration of 1.2 m/s².

b) Moving PMs and fixed coil configuration: In this configuration, the PM is fixed to the mover and the coil is fixed to the stator. This configuration allows wireless actuation of the mobile part, lightweight mover and also provides enough space to integrate other devices such as sensors alongwith the actuator. This configuration can be realised with the use of these two techniques as shown in Fig. 1.23. In literature, most of the lorentz force actuators are realised using on of these two techniques.

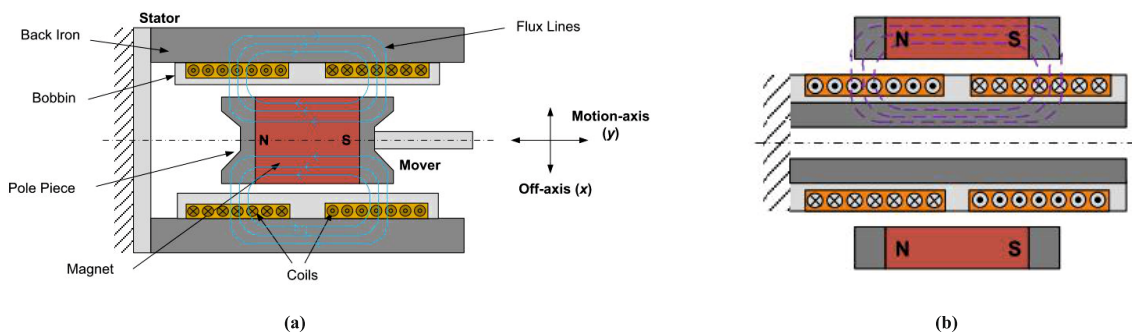


FIGURE 1.23: Different types of moving PMs and fixed coil actuator [Hiem 14] .

Nakazawa et al. have developed a 2 dimensional micro conveyor as shown in Fig. 1.24 [Naka 97]. They used an open loop system to achieve conveyance of the mover plate. The mover is of dimension 5×5×1 mm³ while the stator coil array is 40×40 mm². The NdFeB

mover is able to move a conveyed mass of 416 mg with an applied current of 0.5 A. The maximum conveyance speed without a conveyance plate is 30 mm/s.

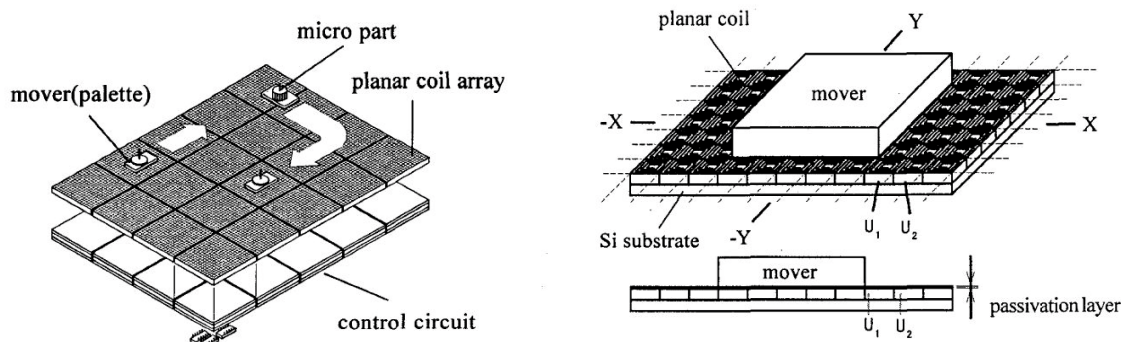


FIGURE 1.24: A 2D micro-conveyor device Nakazawa et al. [Naka 97] .

Shutov et al. have developed a linear synchronous motor as shown in Fig. 1.25 [Shut 05]. The motor consists of a translational stage made up of permanent magnet and the stator consists of microcoils. The authors presents two different configurations. First one with large permanent magnet as rotor and multiturn three phase coil as stator. Second one includes integrated magnet array as rotor and serpentine coil as stator. The device shows a long travel range of 6 cm and it has 1DOF.

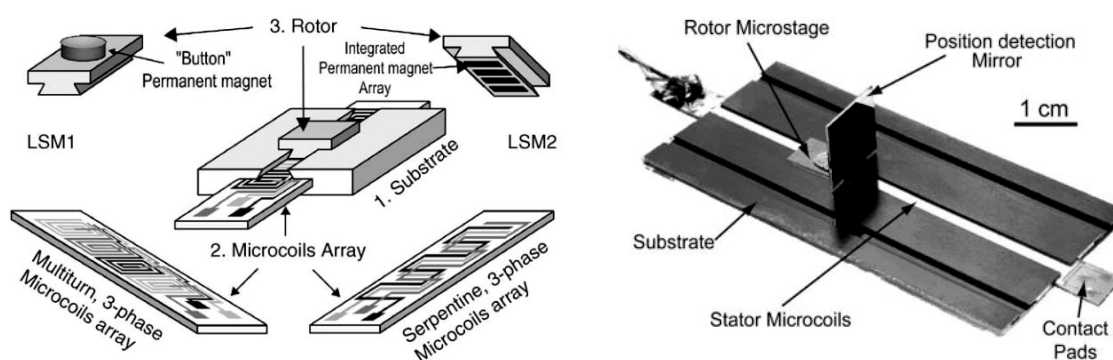


FIGURE 1.25: Illustration of analog and digital actuators Shutov et al. [Shut 05].

Arora et al. have developed a planar electromagnetic conveyor as shown in Fig. 1.26 [Aror 19]. The mobile part consists of a mechanical cross structure of dimension 68 mm×68 mm×0.5 mm and mass of 3.6 g while the stator part consists of four layer PCB having elementary cells of driving coil. There are in total 25 elementary cells arranged in a 5×5 matrix design which allow the mobile part to perform a planar motion of 70 mm

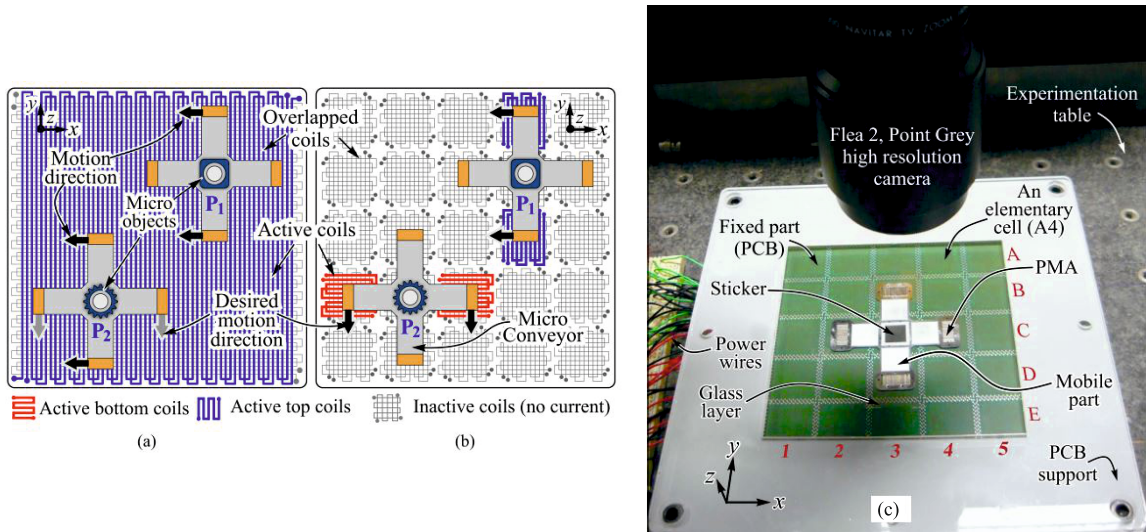


FIGURE 1.26: Planar electromagnetic conveyor Arora et al. [Aror 19].

and rotation of $\pm 12.37^\circ$. The cross structure is able to achieve a speed of 12 mm/s with a driving current value of 0.8 A.

1.3 Actuation principles

The positioning/conveyance devices based on the various physical principles described above can be categorized as analogically or digitally driven based on the displacement output they provide. Analogical actuators have continuous stroke and has the ability to reach any position within their working range. Digital actuators have discrete repeatable positions as shown in Fig. 1.27. In this figure, the mobile part of the actuator is represented as a ball and the discrete positions for digital actuator are indicated. The detailed description of the analogical and digital actuation principles is provided in this section.

1.3.1 Analogical actuators

In analogical actuators, the mobile part can reach any position between the extreme positions that define their stroke [Dudr 14]. They have high precision and the ability to realize long range continuous displacement. To obtain high precision, analogical actuators are usually controlled using closed loop system which helps to track the position of an actuator and can also help to compensate the manufacturing errors. However, at micro-level,

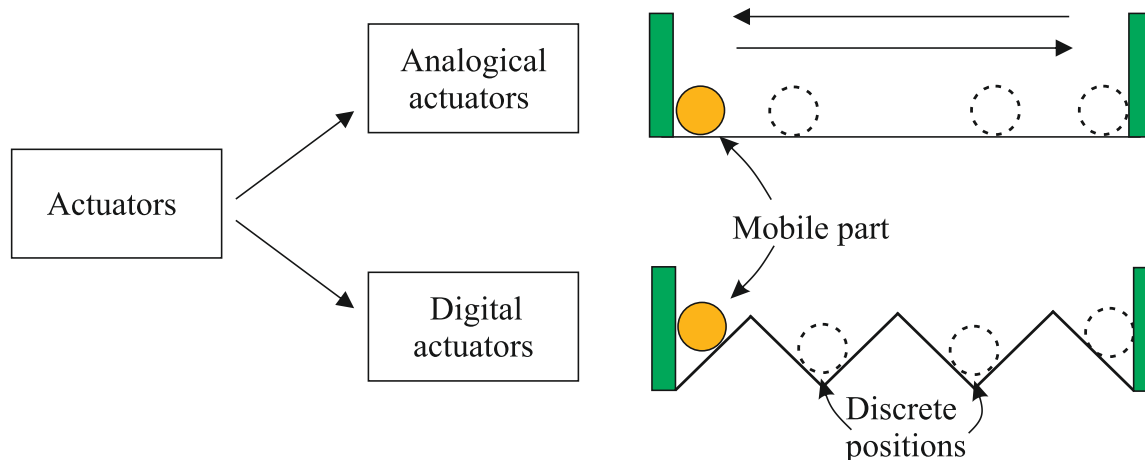


FIGURE 1.27: Illustration of analog and digital actuators.

it might be difficult to integrate sensors and it can also lead to complex control. Furthermore, to hold the mobile part at any position, analogical actuators usually require a continuous supply of energy.

1.3.1.1 Conveyance using contact actuation

In literature, there are some examples of conveyance devices in which frictional losses are observed due to contact between the plate and the mobile part of the actuator. [Ebef 99], [Aror 19], [Deng 16] are some of the examples already explained in the previous sections. These forces can also disturb the conveyance trajectory or it can damage the conveyance object which requires careful handling. To overcome such errors, levitation or non-contact actuation can be used [Guel 17] [Fuku 06]. This principle helps to reduce frictional losses during conveyance.

1.3.1.2 Conveyance using non-contact actuation

The non-contact conveyance requires two functions, firstly to levitate the object and secondly to displace the levitated object. Non-contact handling has several advantages, as it can neglect the surface forces, the friction effect is drastically reduced thus, providing high resolution and accuracy. As per literature, the most used technologies for non-contact handling include electromagnetic levitation, electrostatic levitation and pneumatic levitation [Zhu 15] [Vand 05].

a) Electromagnetic Levitation: In this type, the levitation force comes from a magnetic field which can be generated by PM, electromagnets or superconducting magnets [Sang 12].

Sari et al. have developed a levitation device as shown in Fig. 1.28 [Sari 11]. The device is based on a of hybrid principle, which includes levitation using electromagnetic induction and translation using electrostatic forces. In order to obtain levitation, an AC signal has been applied to the electrical pads of the rectangular loop. The loop consists of two tracks the outer ones are for stability while the inner ones are for levitation. The device was able to levitate a micro object of size $1 \times 1 \text{ mm}^2$ to a height of $10 \mu\text{m}$ for a current of 0.5 A. Another example of hybrid levitation have been proposed by Poletkin et

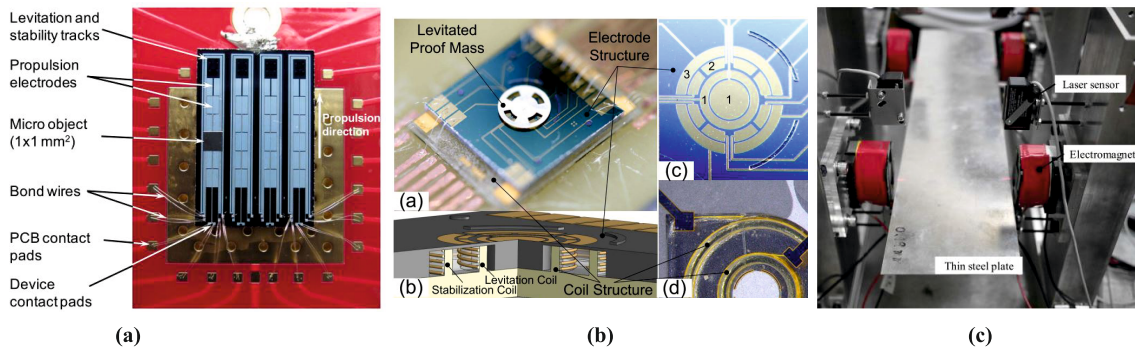


FIGURE 1.28: (a) Sari et al. [Sari 11] (b) Poletkin et al. [Pole 15] (c) Oda et al. [Oda 18].

al [Fig. 1.28] [Pole 15]. The device make use of electromagnetic force for levitation and electrostatic force for angular and vertical actuation of the disk. To obtain the electromagnetic force, a micro coil with a height of $450 \mu\text{m}$ and 18 number of windings have been used. The device is able to levitate the disk to a height from $35 \mu\text{m}$ to $190 \mu\text{m}$. The different heights have been controlled using electrostatic actuator by applying voltage to the central electrode no 1 as shown in Fig. 1.28(b).

Oda et al. have developed an electromagnetic levitation system based on maglev configuration as shown in Fig. 1.28(c) [Oda 18]. A thin steel plate have been used to levitate and translate horizontally to obtain non contact conveyance. Electromagnets have been used to levitate and laser sensors have been used to measure and control the horizontal displacement.

b) Pneumatic Levitation: Another method to obtain non contact actuation is to use pneumatic actuator where compressed air is injected in small inlets. Levitation using pneumatic principle can be obtained using two approaches: Bernoulli levitation and Air cushion [Vand 05].

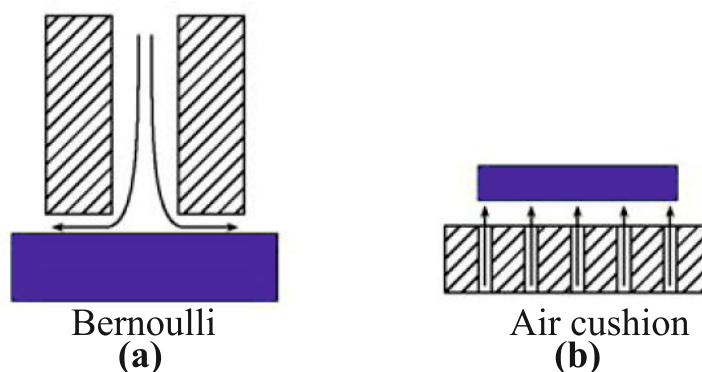


FIGURE 1.29: Pneumatic levitation approaches [Vand 05].

In Bernoulli levitation, the mover is held below the air nozzle as shown in Fig. 1.29. Compressed air flows downward through the nozzle and after in contact with component started moving radially generating an upward attraction force on the component [Walt 03] [Erzi 98].

Another approach is using air cushion as shown in Fig. 1.29(b). In this approach, the sample is held above the nozzle and pressurized air helps to levitate and translate the object to desired location as explained earlier in the previous section by [Guel 17] [Fuku 06] and [Zhon 17].

c) Electrostatic Levitation: The electrostatic principle has been used to levitate and transport object which have enough static charges on their surfaces, for example: metal, semiconductor, insulator, etc.

Jeon et al. have developed a device to transport glass panels with contactless suspension with the help of electrostatic forces [see Fig. 1.30] [Jeon 07]. The objective was to transport glass sheets (LCD screens) without any contamination or damage. The device control is divided into two parts: one for stable suspension and the second one for transportation. Voltage signals are injected in respective electrodes to obtain the stable

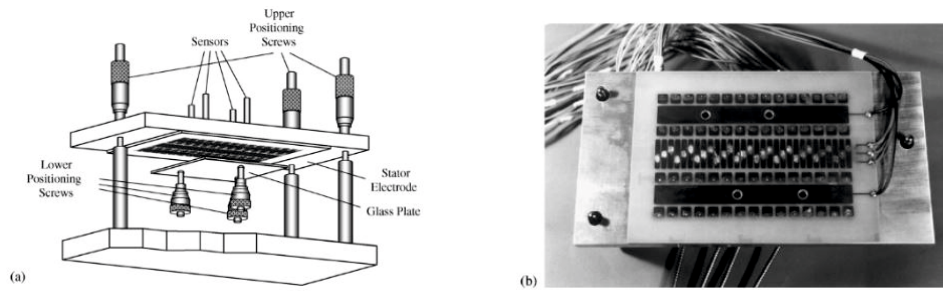


FIGURE 1.30: Electrostatic levitation Jeon et al [Jeon 07] .

suspension. The device has been able to transport a glass panel with a speed of approximately 25.6 mm/s while been suspended at gap length of 0.3 mm.

1.3.2 Digital actuators

Unlike analogical actuators, the mobile part of digital actuators can switch and be hold in a limited number of discrete positions. They can be an alternate solution to the analogical actuators to realise micro-conveyance application. The precise and repeatable discrete positions are represented in Fig. 1.27. They can be controlled in open loop that facilitates their integration in compact and highly integrated systems. They use energy in the form of pulses only for switching between discrete positions and no energy is required to hold the mobile part in discrete positions. They are then considered as energy efficient actuators [Medi 17], the control of this actuator is simple as a consequence of their functioning. However, they do not exhibit continuous displacement like that of analogical actuators. To achieve a long range displacement, several actuators need to be arranged together in the form of an array which can work collaboratively for conveyance [Abad 09] [Hadd 13]. As the discrete positions for digital actuators are defined during their manufacturing, they need to be fabricated using precised fabrication techniques and the controls cannot be used to compensate the fabrication error as of analogical actuators. Table 1.1 gives a comparison between analogical and digital actuators.

There are two essential functions in the working of digital actuators : the switching and the holding. The switching consumes external energy and is used to switch the mobile part between the discrete positions. The holding on the other hand, does not consume

Properties	Analogical Actuators	Digital Actuators
Stroke	Continuous	Discrete
Precision	High	Low
Manufacturing constraints	Low	High
Control	May be complex	Simple
Need of sensors	Yes (closed loop system)	No (open loop system)
Integration	May be complex	Simple
Energy Consumption	High (continuous supply)	Low (pulsed mode supply)

TABLE 1.1: Comparison between analog and digital actuators [Xu 16]

external energy and ensures the holding of the mobile part in the discrete positions. In the next sections, the solutions used in literature to realize these two functions are presented.

1.3.2.1 Switching function

The switching function produces a driving force, exerted on a mobile part, to switch it between the discrete positions. According to literature, it can be achieved using various physical principles such as pneumatic [Deng 18] [Roth 18], electrostatic [Ji 10] [Dao 11] [Hoso 15] [Conr 16] [Vero 18], electro-thermal [Pote 19] [Wu 18] [Khaz 10] [Lin 11] [Rako 14] [Xiuy 15] [Naki 16], piezoelectric [Lai 12] [Ding 17] [Cai 17] [Ghaf 18] [Tang 17] and electromagnetic [Xu 16] [Wang 09]. The choice between these principles is based on several parameters like speed, precision, long travel range, object material to be displaced, etc. The actuators mentioned in this section have been presented previously in this chapter. Some of these examples are presented in Fig. 1.31

1.3.2.2 Holding function

The second essential function in digital actuators is the holding. As the name indicates, this function helps to hold the mobile part at any discrete position. In literature, the holding is realized using four main solutions as magnetic holding, locking systems, compliant structures and hinged mechanisms. These solutions are detailed below.

a) Magnetic Holding : In electromagnetic digital actuators, the holding generated with the help of magnetic forces has been widely used because of its magnetic properties which can be used either for the switching or to realize holding operation. It is reliable and can

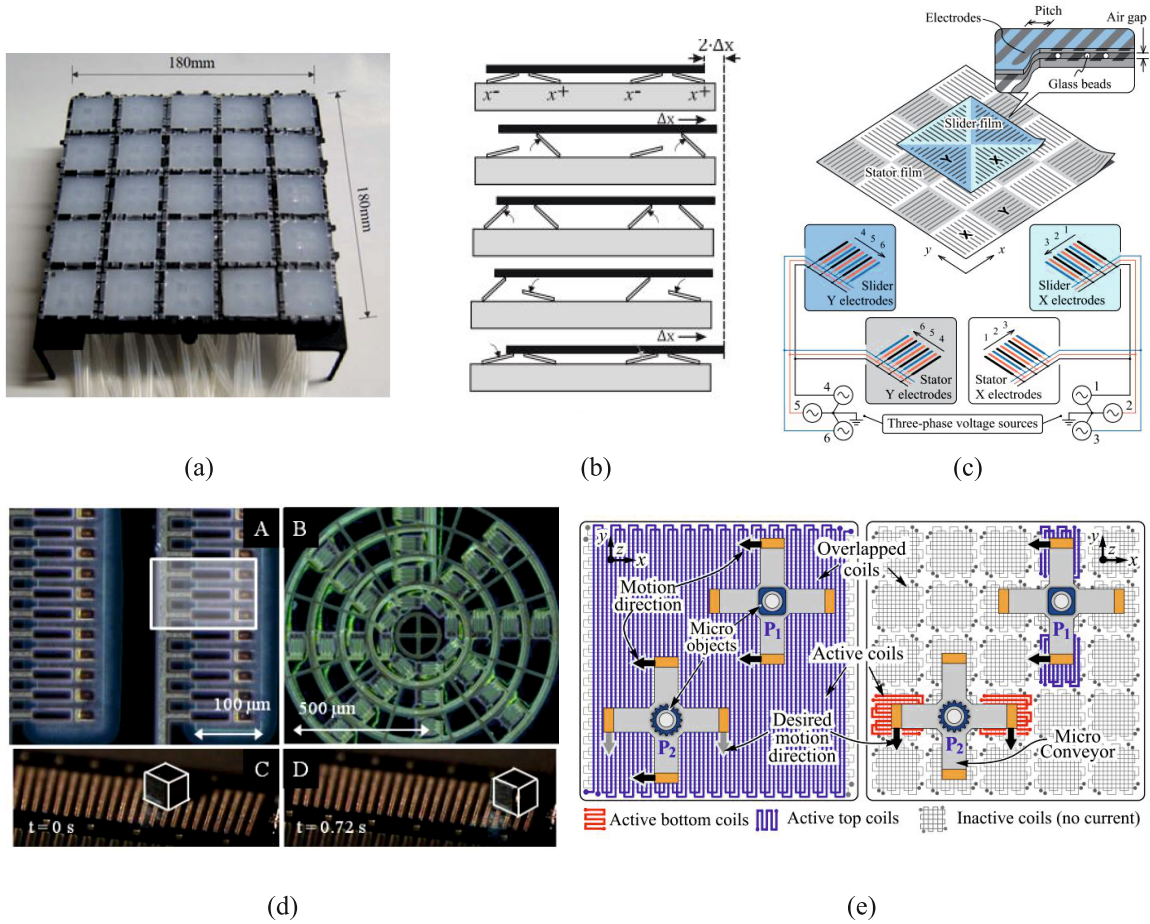


FIGURE 1.31: Examples of Micro-conveyance devices based on different physical principles (a) Pneumatic Conveyance device by Deng et al. [Deng 16] (b) Electrothermal Conveyance device by Ebefors et al [Ebef 99] (c) Electrostatic Conveyance device by Hosobata et al. [Hoso 15] (d) Piezoelectric Conveyance device by Tellers et al. [Tell 15] (e) Electromagnetic Conveyance device by Arora et al. [Aror 19] .

be used in wide variety of application. Staab et al. have developed a bistable micro relay which consists of magnetic circuit to realize holding as shown in Fig. 1.32(a) [Staa 11]. The magnetic circuit in the device is energized by several micro PMs. The nickel contact is drawn by the PMs to one of the pole shoe due to magnetic holding.

Kumar et al. have developed an electromagnetic braking system shown in Fig. 1.32 (b) [Ravi 17]. The moving part of the device is a plunger employed with springs which push the plunger to the actuator motor shaft. The figure shows the engaged mode of electromagnetic brake. When the actuator is required to be on, the brake is released and the plunger is pulled using electromagnetic force generated by coils. During holding mode the current in the coil is shut off, however the plunger stays in hold state due to the magnetic holding with PMs. The release of the plunger can be possible by sending current

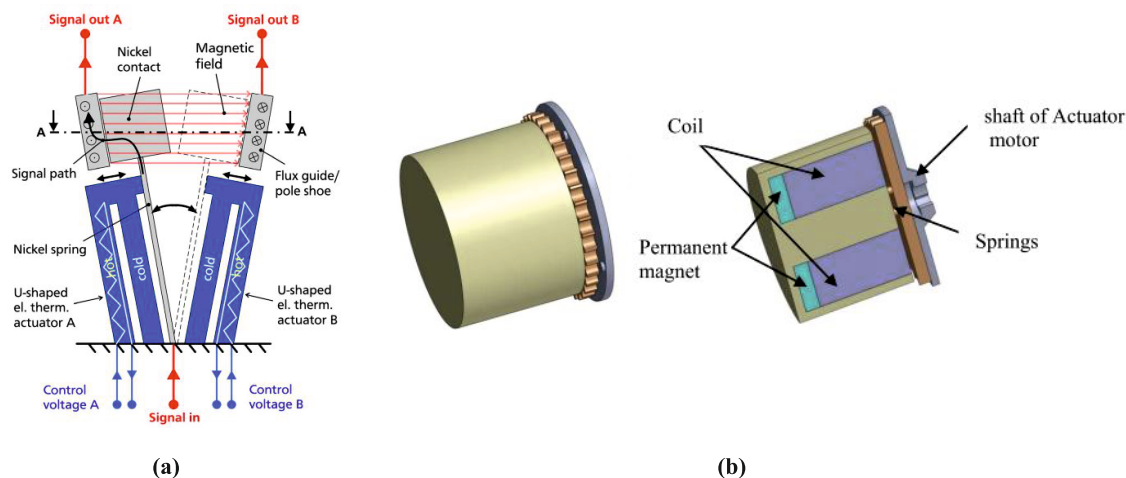


FIGURE 1.32: Representation of electromagnetic braking system (a) Staab et al. [Staa 11] (b) Kumar et al.[Ravi 17] .

in coil with reverse polarity. The PM used is 2 mm thick with flux density of 0.45 T.

Mach et al. have developed a bistable electromagnetic valve based on the same principle using a coil and PMs as shown in Fig. 1.33 [Mach 19]. The opening and closing of the valve is obtained using the coil and a ferromagnetic plunger whereas, the holding at the stable positions is obtained with the help of magnetic holding generated by PMs.

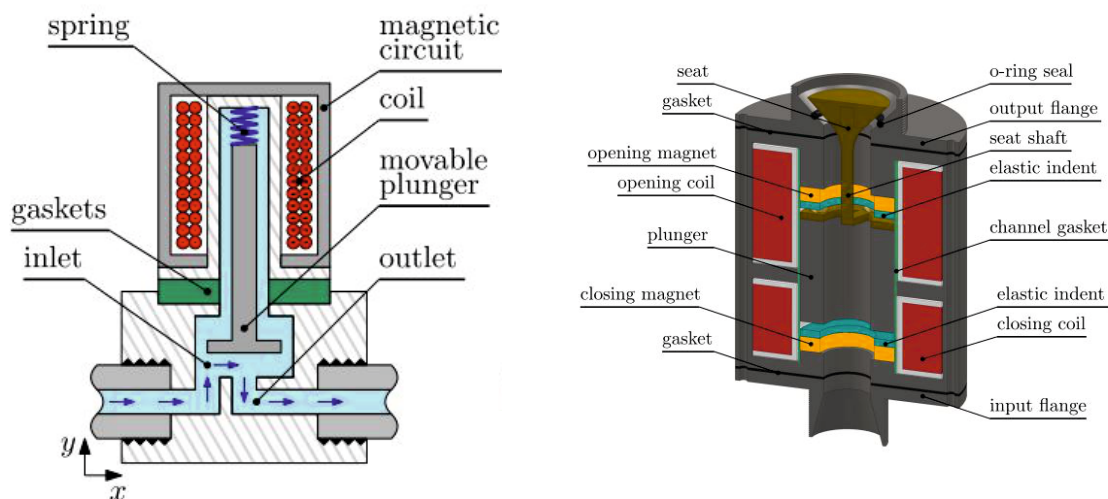


FIGURE 1.33: Bistable electromagnetic valve Mach et al. [Mach 19].

b) Locking Systems: Another solution used in literature to realize holding function is by using mechanical locking systems. In the bistable switch develop by Gao et al [see Fig.1.34], they used a mechanical latch lock mechanism [Gao 19]. Initially, the two latches are disengaged [1.34(b)]. The actuator uses electro thermal principle for its

actuation which pushes the bar and therein the angled spring. It helps to attach the two latches together as shown. The latch is thermally insulated to avoid any disturbances during working of actuator. In order to disengage the latch the push bar is used to displace the reset bar as shown.

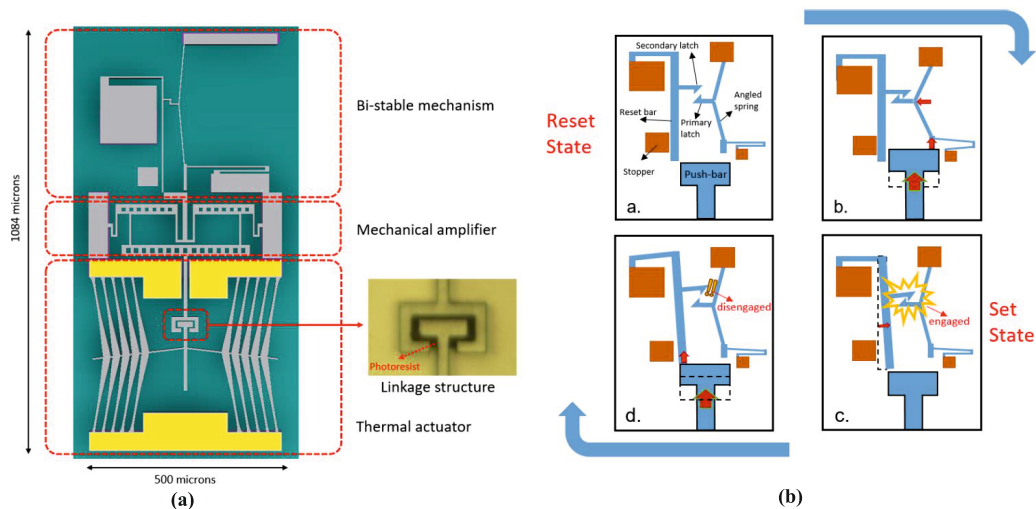


FIGURE 1.34: Latch-lock mechanism Gao et al.[Gao 19].

c) Compliant structures: The third used solution to realize the holding function is with the help of compliant structures. The ratchet mechanism is most commonly used. Dao et al. [Dao 11] have presented a digital actuator based on a comb drive structure and a ratchet mechanism. This mechanism holds the mobile part of the actuator to hold at any discrete position. The attach and detach mechanism is achieved with the help of electrostatic principle. The device has already been presented in section (1.2.2) [Fig. 1.11].

Another example has been presented by Hao et al [Fig. 1.35]. They used a ratchet self-locking mechanism to realize a micro-gripper. It consists of two main beams driven by two rotary actuators attached with the ratchet locking arrangements. Each arrangement locks the beam positions and do not allow any inverse moment. The jaws can be released by separating the ratchet pawl and tooth. The space between the jaws ranges from 0 to $100\mu\text{m}$. The gripper can grip object with a size range of $20\mu\text{m}$, $40\mu\text{m}$, $60\mu\text{m}$.

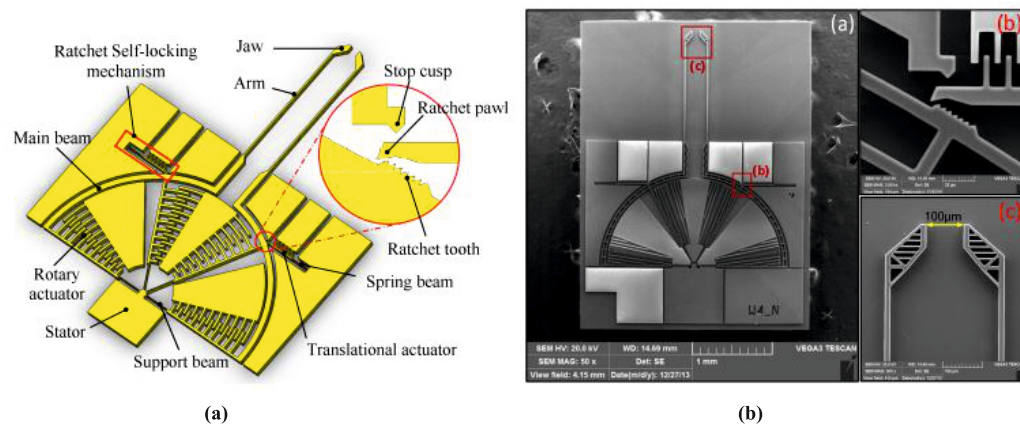


FIGURE 1.35: Self-locking micro-gripper Hao et al. [Hao 15].

d) Hinged mechanisms: Hinged mechanism is another used solution to obtain the holding function and is realized with the help of hinges. Wang et al. have developed a bistable actuator based on hinged mechanism [Wang 09]. It helps to obtain two pre-stabled states due to the combined bending and tension on the beam structure. Switching is obtained with the help of electromagnetic Lorentz force applied on the hinged beams to switch between the stable positions. The stroke of the actuator is around $90\mu\text{m}$ in both directions.

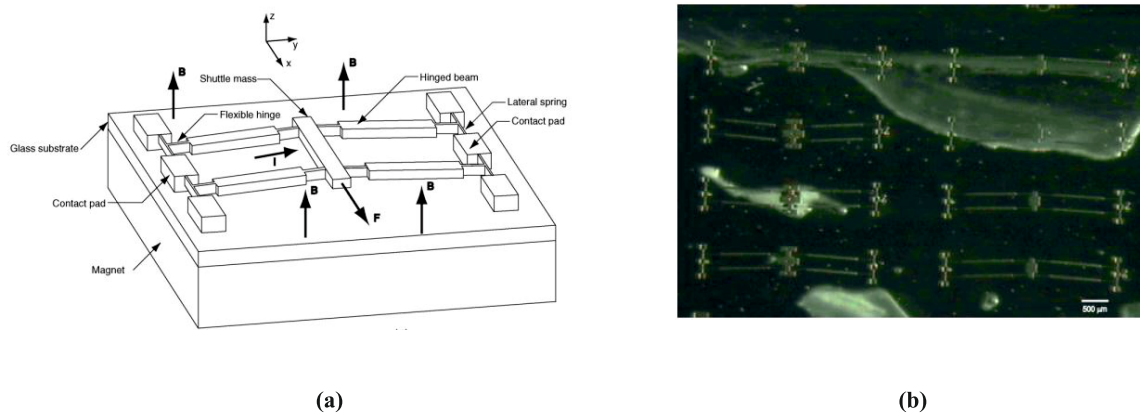


FIGURE 1.36: Hinged mechanism, Wang et al. [Wang 09].

1.4 Overview of the presented conveyance systems

In this section, an overview of the presented conveyance systems is proposed and only micro systems are considered as the present thesis is related to the conveyance at a micro-scale. This comparison is provided in Table 1.2.

Pneumatic actuators are clean, light weight and non magnetic however due to the digital control of air flow, their accuracy is limited. Moreover, downscaling of such actuators is impossible as it is difficult to fabricate complex nozzle structure at micro level.

Electrostatic actuators are simple and have fast response but this type of actuators usually requires high voltage for their working which generates an issue of reliability and safety in a system with human-machine interface. It requires large surface area for comb drive application compared to other actuators. They generally exhibit small working strokes. Their integration with other technologies (for example: electromagnetic) could be used to obtain compact size hybrid actuators as shown by Sari et al. [[Sari 11](#)].

Electrothermal and piezoelectric are material based actuators. Electrothermal presents some advantages as low voltage needed and generation of large output forces. However, they are thermal dependant actuators. Their actuation speed depends on their size which is faster at micro-scale. On the other hand, piezoelectric offers linear actuation with fast response time and also provides nano-metric displacement resolution. However, they are restricted in many applications due to their small working strokes.

Electromagnetic actuators are simple controlled and high speed actuators. As that of pneumatic actuators, non-contact actuation is possible with electromagnetic actuators due to their ability to generate levitation and translation forces. This makes them adapted for their use as micro-conveyance systems. In literature, electromagnetic actuation realized using Lorentz force technique are widely used due to low power consumption compared to linear reluctance and inductance techniques. In addition, they also provides wireless mobile part which enhances their ability as conveyance device [[Aror 19](#)] [[Pole 15](#)]. However, electromagnetic actuators are sensitive to the magnetic field environment.

The comparison between different actuators helps to choice the use of digital electromagnetic actuation principle. It is due to their simple design and control, no requirement of any feedback sensor and also the possibility to realize distributed actuation with an array. The electromagnetic physical principle is also considered as it can be well adapted

TABLE 1.2: Characteristics of the presented Smart Conveyance systems

Ref.	DOF	Dimensions	Max. Stroke	Max. vel.	A. P.
Conveyance devices based on Pneumatic Actuation Principle					
[Fuku 06]	2	35×35 mm ²	same as dimensions	0.5 mm/s	Analog
[Guel 17]	2	75×75 mm	same as dimensions	0.3 m/s	Analog
[Laur 11]	2	120×120 mm	same as dimension	220 mm/s	Analog
[Deng 18]	2	180×180 mm	same as dimension	0.5 mm/s	Digital
Conveyance devices based on Electrostatic Actuation principle					
[Ji 10]	2	3.75×3.75 mm	±6.27 μm	-	Digital
[Dao 11]	2	500×250×30 μm	6×1.75 mm	-	Digital
[Hoso 15]	2	132×132 mm	same as dimensions	250 mm/s	Analog
[Conr 16]	1	4.0 mm×26.5 μm	-	-	Digital
[Vero 18]	1	120×75 μm ²	-	-	Digital
Conveyance devices based on Electro-thermal Actuation Principle					
[Khaz 10]	2	530×60×2 μm	2.7 μm	-	Digital
[Lin 11]	2	1.49×1.49×0.4 mm ³	25 μm	-	Digital
[Rako 14]	2	3×3 mm	±5μm	-	Digital
[Xiuy 15]	2	4×5×0.5 mm ³	120.89 μm	-	Digital
[Ebef 99]	3	15×15mm ²	-	12 mm/s	Digital
Conveyance devices based on Piezoelectric Actuation Principle					
[Lai 12]	2	269×269 mm ²	41×41 μm ²	500 μm/s	Digital
[Ding 17]	3	120×120×8 mm ³	±42.31×48.56 μm ²	-	Digital
[Cai 17]	6	-	8.2×10.5×13.0 μm ³	-	Digital
[Ghaf 18]	6	243.02×223.64×24.27 μm ³	90.5×103.1×211.8 μm ³	-	Digital
[Tang 17]	3	228×158×84 mm ³	10.39×15.43×15.55 μm ³	-	Digital
[Tell 15]	3	-	-	3.5 mm/s	Digital
Conveyance devices based on Electromagnetic Actuation Principle					
[Kuma 12]	3	150×50×23 mm ³	≈ facing surface area	450 mm/s	Analog
[Espr 10]	2	2000×55 mm	-	-	Analog
[Andr 14]	2	73×71 mm ²	25 mm	0.15 m/s	Analog
[Hass 17]	2	-	±4.5 mm	-	Analog
[Dong 15]	2	-	±1.5 mm	-	Analog
[Chin 13]	2	500 mm×500 mm×300 mm	-	0.6 m/s	Analog
[Xu 14]	2	120 mm×120 mm	11 mm	-	Analog
[Naka 97]	2	40×40 mm ²	same as dimensions	30 mm/s	Analog
[Hiem 14]	2	189×26 mm ²	10 mm	1 m/s	Analog
[Zhou 19]	6	40×18×8 mm ³	5×10 ⁻⁴ m	-	Analog
[Shut 05]	1	60 mm	same as dimensions	-	Analog
[Le 18]	2	30×30 mm ²	same as dimension	-	Analog
[Aror 19]	2	68×68×0.5 mm ³	≤70 mm	12 mm/s	Analog
[Sari 11]	3	9.5×1.2×0.5 mm ³	same as dimension	3.6 mm/s	Analog
[Pole 15]	3	9.4×7.4×1 mm ³	-	-	Analog
[Oda 18]	2	400×100×0.19 mm ³	same as dimension	-	Analog
[Wang 09]	2	-	90 μm	-	Digital
[Tisn 19]	2	-	1181.9 μ	1990.4 μm/s	Digital
[Xu 16]	2	100×100 mm ²	same as dimension	-	Digital

with the digital actuators as it gives a possibility to obtain the holding and switching operations using the magnetic properties of the PM and also the previous experience of the lab in the development of digital electromagnetic actuators.

In the Roberval Laboratory, Petit [Peti 09] have developed a planar conveyance device composed of 25 elementary digital actuators as shown in Fig. 1.37. Each actuator of the array consists of four fixed PMs and one Mobile Permanent Magnet (MPM). The MPM is able to reach four discrete positions with a displacement stroke of $200\mu\text{m}$ in xy -plane. The 25 actuators are arranged in 5×5 matrix. The switching of the MPM is realized using the x - and y -axis switching wires placed beneath the square cavity as shown. This array is used to realize conveyance task. The minimum plate displacement with this configuration has been $38.3\mu\text{m}$ and the maximum driving speed is $1990.4\mu\text{m/s}$ as presented by Tisnes et al. [Tisn 19].

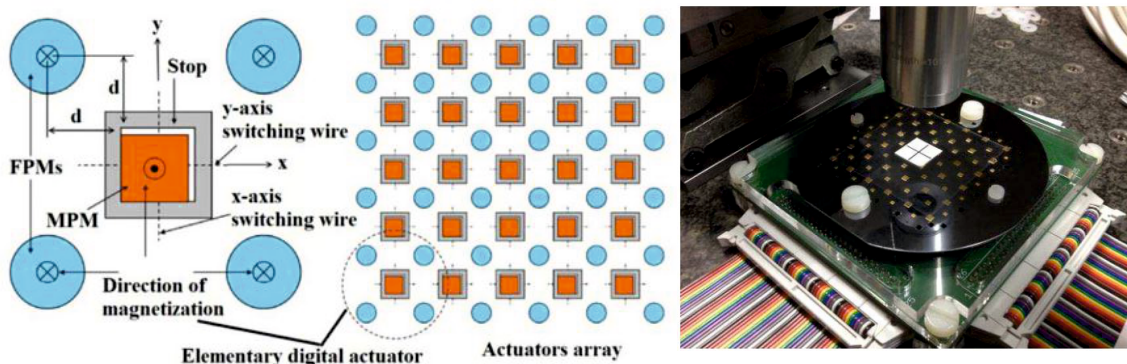


FIGURE 1.37: Electromagnetic conveyance device [Peti 09] .

1.5 Conclusion

A state of art on the micro conveyance and positioning systems has been presented in this chapter. At first, a short description about the smart conveyance devices on macro level has been presented. Various examples and their working principles have been explained. Later, the integration of smart conveyance devices at micro level with the help of actuators is presented. Different physical principles have been explained and their advantages and drawbacks are detailed. The conveyance devices presented based on different physical

principles are distributed into two different actuation principles (analogical and digital). The advantages and drawbacks of analogical and digital actuation have been shown. The analogical actuators have been further distributed into contact and non-contact actuators. The main functions of digital actuators (switching and holding) are also given. Various physical principles were presented to realize the switching and holding operation for the digital actuators.

Finally, the summary of all the presented conveyance device is given in Table 1.2. A comparison has been made between different actuation principles and an electromagnetic principle has been chosen for the proposed digital actuator. The electromagnetic principle is best suited as it gives possibility to obtain both translation and levitation in the digital actuator. The holding of the Mobile part at discrete position is considered using magnetic holding principle as it can be easily achieved using PMs and do not required any complex mechanical structure as compared with above mentioned principles.

In the roberval laboratory the digital actuators based on electromagnetic principle have already been developed [Peti 09] [Zhic 16] [Xu 16]. This work is a continuation over these previous works.

The objectives of this thesis are distributed in several steps. The first step is to design and validate a three dimensional displacement actuator with the ability to have more discrete positions to enhance the conveyance abilities. The second step includes, the validation of the proposed actuator and realization of micro-fabricated prototype. The step 3 includes, the design, modelling and validation of the conveyance device using an array of digital actuators and finally in step 4 a miniaturization of the proposed conveyance device has been designed.

Chapter 2

Principle, Modeling and Design of an elementary Digital Actuator

In this chapter, the working principle, modeling and design of a digital electromagnetic actuator are described. Firstly, the actuation is explained for a 2D actuator. Later, the same system is adapted for a three dimensional actuation. The architecture of the actuator and the solution to ensure the switching and holding functions are described. Then, a model is presented to calculate the magnetic and electromagnetic forces generated in the system. This model helps to design the actuator prototype.

2.1 Principle of the actuator

There are various actuation principles available in the literature as discussed in previous chapter. For the actuator presented in this work, an electromagnetic principle has been undertaken due to its advantages such as magnetic holding, which ensures no energy consumption at stable positions as explained in the previous chapter. This principle has also been approved by experienced research team members of Roberval laboratory. The main originality of the proposed actuator lies in its hexagonal architecture and also the ability of the mobile part to reach twelve discrete positions. The positions are divided at two different levels along the vertical z -axis. Initially, the principle of a 2D actuator is presented and later the same design is adapted for 3D actuation.

2.1.1 Principle of 2D actuator

The 2D Hexagonal Digital Actuator (HDA) includes a mobile part and fixed parts [Fig. 2.1(a),(b)]. The mobile part consists of a Mobile Permanent Magnet (MPM), placed in a hexagonal cavity. The fixed part of the HDA includes six cylindrical Fixed Permanent Magnets (FPMs) assembled around the hexagonal cavity. It also includes a four-layered Printed Circuit Board (PCB) placed beneath the hexagonal cavity which enables to switch the mobile part in xy -plane.

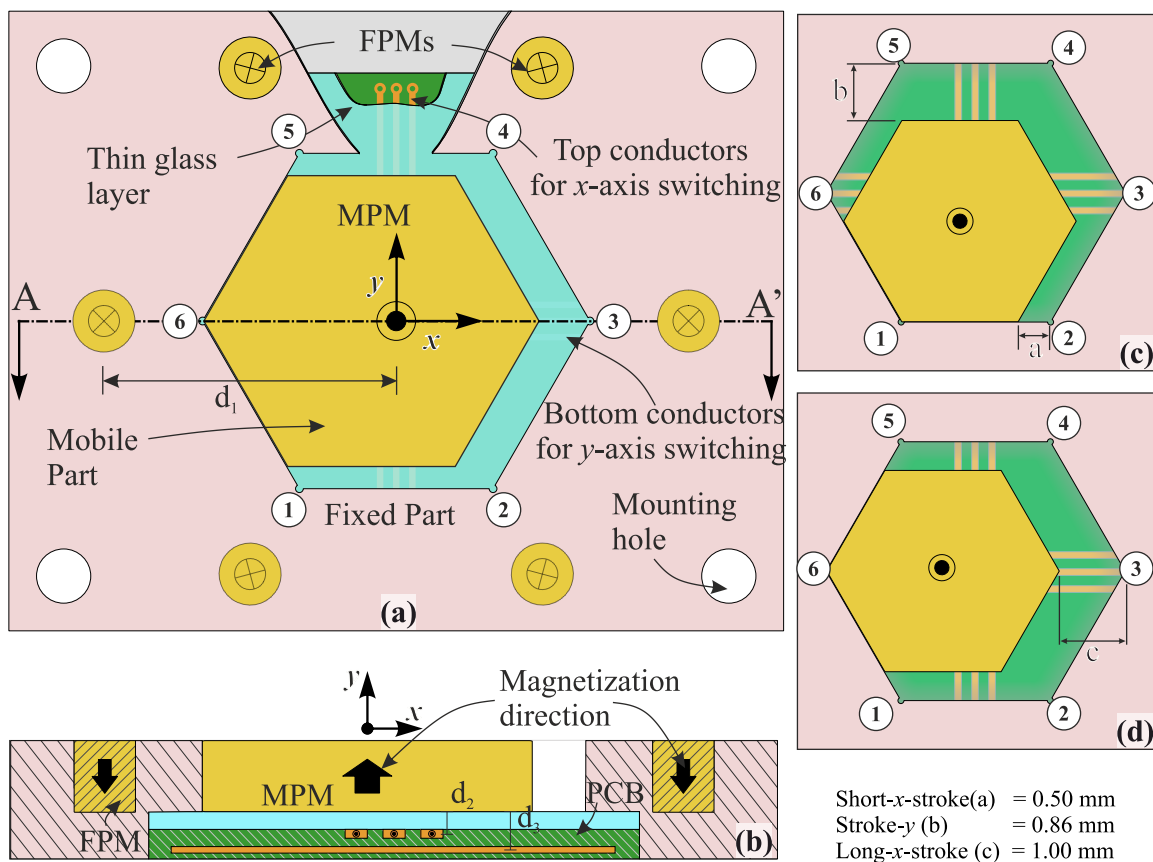


FIGURE 2.1: HDA design model (a) Top view. (b) Cross sectional view AA'. (c), (d) Representation of the displacement strokes along xy -plane.

The switching of the mobile part in xy -plane is achieved using two orthogonal sets of three serially connected electrical conductors [see Fig. 2.1(a),(b)]. One set is used to switch along x -axis and the second one along y -axis. Three electrical conductors are used to ensure the generation of enough electromagnetic forces to switch the mobile part in xy -plane. The buildup design of this PCB is shown in Fig. 2.2. It is composed of four layers of which the first and the second layer are dedicated for the two sets of driving conductors

while the third and fourth layer are used for routing purposes. The conductors printed on the first layer are called “Top conductors (T_c)” and the ones on the second layer are called “Bottom conductors (B_c)”. The distance along z -axis between these two layers is $100\ \mu\text{m}$ and the distance between adjacent conductors in xy -plane is $250\ \mu\text{m}$. The $100\ \mu\text{m}$ between the two layers is the minimum distance we can achieve considering the PCB manufacturing and using inverse PCB buildup technique. This minimum distance has been selected because it helps to lower the difference in generated electromagnetic force using B_c in comparison to that of T_c for the same current value. A thin glass layer of $170\ \mu\text{m}$ thickness [see Fig.2.1(b)] is placed between the PCB and the mobile part in order to obtain an electrical insulation. In addition, this glass layer further helps to obtain a uniform plane surface for switching the mobile part.

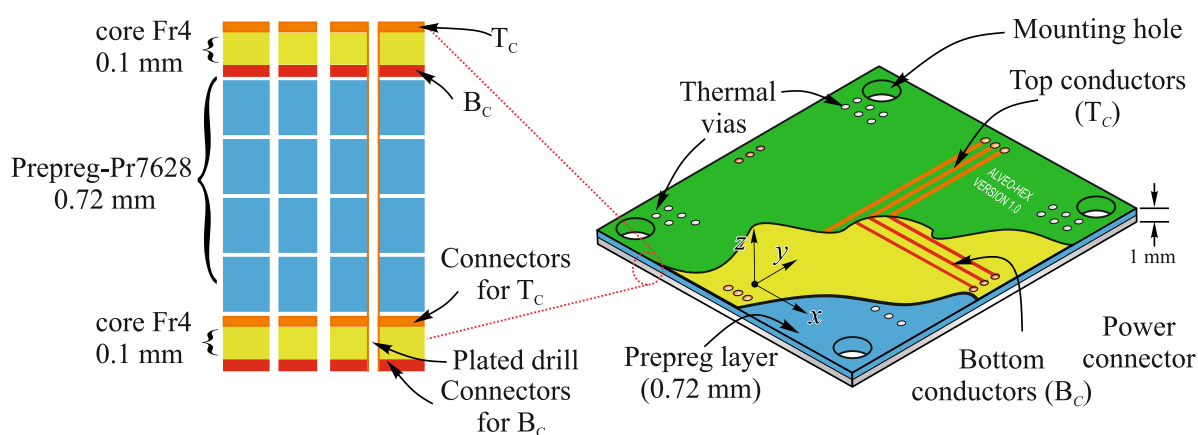


FIGURE 2.2: Buildup design of the Printed Circuit Board (PCB)

Only two sets of orthogonal conductors are used to achieve all six discrete positions which helps to limit the number of control signals and power supplies and it also helps to simplify the PCB design. Table 2.1 gives the detailed current distribution between the two sets of orthogonal wires one for each displacement direction, where I_x represents current in T_c (x -axis) and I_y represents current in B_c (y -axis). Because of the distance between T_c and B_c , the distance between the bottom side of the MPM and B_c (d_3) is higher than the distance between the bottom side of the MPM and T_c (d_2) [see Fig. 2.1(b)]. As a consequence, I_y needs to be higher than I_x in order to obtain the same electromagnetic force.

Motion Directions	Current along x -axis I_x	Current along y -axis I_y
1 \leftrightarrow 2	$\pm I_x$	0
1 \leftrightarrow 3	$\pm I_x \cos(30^\circ)$	$\pm I_y \sin(30^\circ)$
1 \leftrightarrow 4	$\pm I_x \cos(60^\circ)$	$\pm I_y \sin(60^\circ)$
1 \leftrightarrow 5	0	$\pm I_y$
1 \leftrightarrow 6	$\pm I_x \cos(120^\circ)$	$\pm I_y \sin(120^\circ)$
6 \leftrightarrow 3	$\pm I_x$	0

TABLE 2.1: Electric current values along respective motion directions

The use of standard hexagonal shape for the MPM and the cavity implies different strokes of the mobile part along each displacement axis. The stroke is defined as the displacement between two discrete positions. To clearly visualize the MPM displacement in all possible directions, the short stroke along x -axis is considered as 0.50 mm [Fig. 2.1 (c)]. Due to standard hexagonal cavity, the other obtained strokes are along y -axis as “Stroke- y , $b = 0.86$ mm” and along x -axis as a longer stroke called “Long- x -stroke, $c = 1.00$ mm” [Fig. 2.1 (d)]. The dimensional and magnetic parameters of the HDA are provided in Table 2.2.

Materials		
Permanent Magnets		NdFeB
Mechanical structure		PMMA
Components	Dimensions (mm)	Magnetic Flux Density (T)
MPM	$5 \times 5 \times 2$	1.37
FPM	$\emptyset 2.25 \times 2$	1.43
Coil	$\emptyset_{ext} 20 \times 10$ $\emptyset_{int} 9$	
Distances		
$d_1 = 1288 \mu\text{m}$	$d_2 = 200 \mu\text{m}$	$d_3 = 300 \mu\text{m}$

TABLE 2.2: Dimensional and magnetic parameters of the actuator.

Actuation principle The actuation of the HDA is based on electromagnetic Lorentz force principle which is generated when a current carrying conductor is placed in a magnetic field, here generated by Permanent Magnets (PM). It can be calculated using equation (2.1)

$$F = I \int_{wire} dl \times B_{ext} \tag{2.1}$$

where, F is the generated electromagnetic Lorentz force, I is the current passing through the conductor, l is length of the conductor and B_{ext} is the external magnetic flux density of the PM. As the conductors are fixed and the PM is mobile. In this case, the generated electromagnetic force will change the current position of the PM.

The magnitude of this generated force depends on the current amplitude, the intensity of the magnetic flux density of PM and the position of PM with respect to the conductor, whereas, the direction depends on the magnetization orientation of PM and the direction of the current. Fig. 2.3 (a), represents the direction of Lorentz force with respect to the magnetic orientation and current direction.

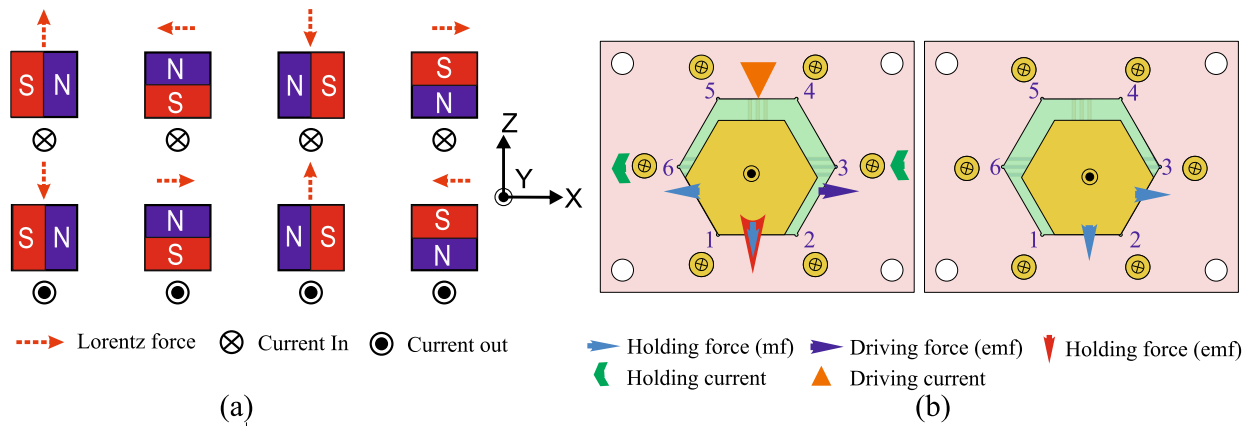


FIGURE 2.3: (a) Direction of the Electromagnetic Lorentz force (Driving force) for different configurations of PM and the conductor (b) Principle of switching between discrete positions

In the presented actuator, the conductors are fixed and the PM is mobile. In order to increase the magnitude of generated Lorentz force, three conductors are serially connected and an hexagonal PM with a magnetization of 1.40T is used. The Fig. 2.3 (b) represents the principle of MPM switching between the discrete positions. At first, the MPM is located at position 1 as shown. To switch the MPM along $+x$ (Short- x -stroke with a stroke of 0.5 mm), a current called “driving current”, oriented along the $-y$ -axis direction is injected in the Tc. It generates an electromagnetic Lorentz force on the conductors along $-x$ direction, as the conductors are fixed, the resulting driving force, oriented along

+x-axis is then exerted on the MPM. If this resulting driving force is higher than the sum of magnetic holding force and the adhesion force, the MPM switches. To switch back the MPM along -x direction, the driving current is reversed and oriented in +y-axis.

In addition, for a Short-x-stroke, a current can also be injected in the Bc called, “holding current”, in order to increase the lateral contact force between the MPM and the lateral stop. It helps to minimize the straightness error during switching.

2.1.2 Principle of 3D actuator

Similar principle has been adapted for a three dimensional displacement actuator. In order to realize a z-axis displacement, the mobile part of the digital actuator consists of a MPM fixed with a z-axis retainer at its bottom [see Fig. 2.4 (c)].

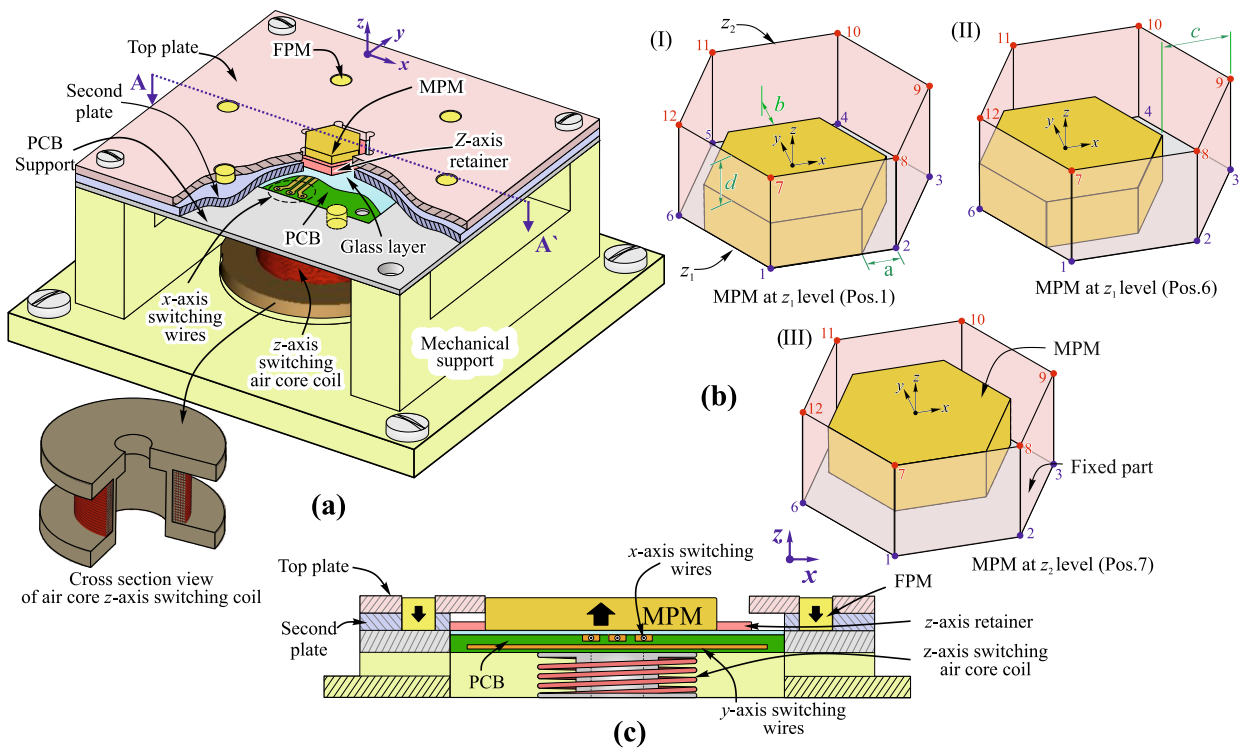


FIGURE 2.4: (a) Representation of a 3D elementary HDA (b) Representation of twelve discrete positions with a stroke along z-axis (c) Cross sectional view of the HDA AA'

The retainer serves two purposes: it defines the actuator stroke along z-direction (“Stroke-z, $d=0.40$ mm”) and it also avoid that the MPM goes out of the cavity. In order to realize it, two parts are stacked together (“Top plate” & “Second plate”). The Top plate defines the stroke whereas, the second plate is a z-axis retainer carrier. The formed

hexagonal cavity in the second plate is slightly bigger than the first one, that allows the z -axis retainer to fit inside the cavity [see Fig. 2.4 (a) (c)]. This arrangement helps to obtain MPM displacement along twelve discrete positions which are distributed at two different levels (z_1 and z_2) along z -axis where, z_2 is the upper level along z -axis and z_1 is the lower level as shown in Fig. 2.4 (b).

The switching of HDA along z -axis is possible with the help of current carrying electromagnetic air core coil placed beneath the PCB. A continuous current is required to maintain the mobile part at z_2 level. The continuous current in the coil serves as a holding current for the MPM at z_2 level. When the current is switched off, the mobile part returns back to the z_1 level due to the weight of the mobile part acting downward. Thus, the actuator shows a monostable behavior along z -axis. This configuration has been selected to simplify the architecture and the design of the proposed actuator and to ensure the access to the upper face of the MPM for its use in different applications.

2.1.3 Conveyance principle

The actuator presented in this work will be mainly used for a conveyance application. To ensure the conveyance task, two different conveyance strategies are proposed: the stick-slip approach and the lift-mode approach.

2.1.3.1 Stick-Slip approach

In this approach, the MPM is always in contact with the conveyance plate. The conveyance using this approach is possible at both the levels (z_1 and z_2) along z -axis separately.

The step-by-step conveyance based on this approach is shown in Fig. 2.5 (a). In order to switch the plate along x -direction, a low driving current is used (stick-phase). This low driving current limits the mobile part acceleration and also the sliding between the plate and the mobile part. After attending the displacement using stick-phase, the MPM needs to come back to its initial position. In order to do so, a high driving current is used to switch the MPM in the opposite direction (slip phase). High driving current is used to

increase the slipping between the MPM and conveyed plate. It will switch the MPM back to its original position with minimum disturbance to the plate. After the MPM returns back, it is ready for the next conveyance sequence.

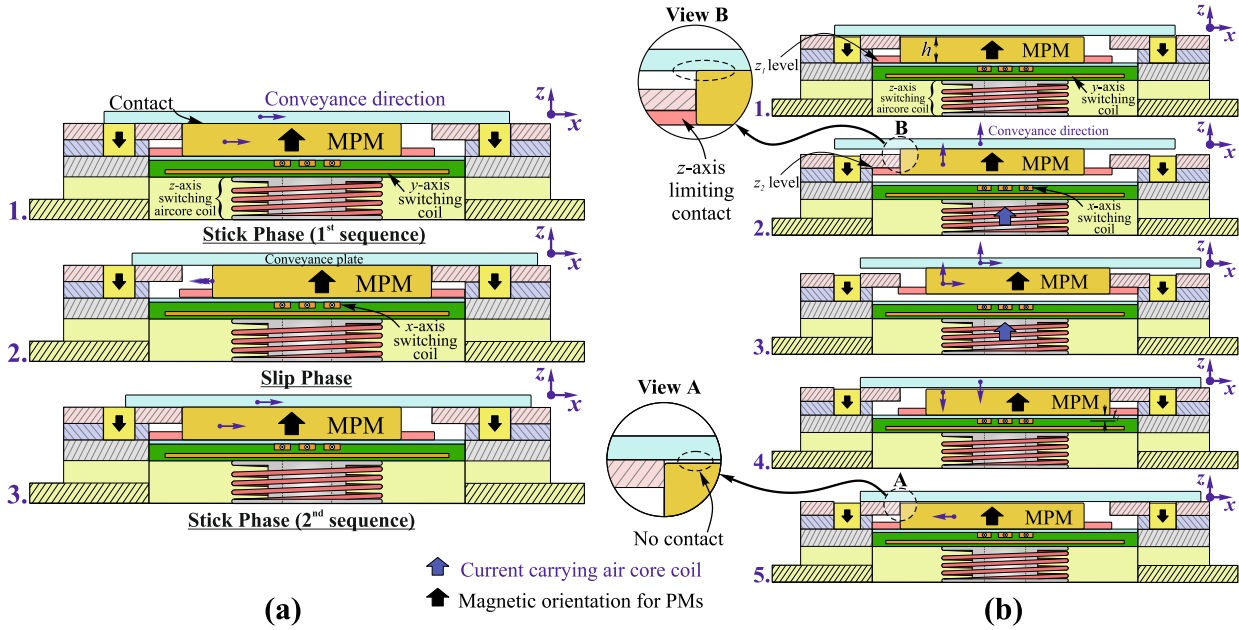


FIGURE 2.5: Representation of the different approaches for conveyance: (a) Stick-slip approach, (b) Lift-mode approach

2.1.3.2 Lift-Mode approach

In this approach, the MPM is not always in contact with the conveyance plate as shown in Fig. 2.5(b) [view A]. The conveyance using this approach is only possible with the help of the vertical axis (using level z_2). When the mobile part switches at z_2 level, it ensures a physical contact between plate and the MPM [Fig. 2.5(b)[view B]].

The working is explained using the cross sectional view presented in Fig. 2.5 (b). In the first step, the mobile part is located in one of the discrete position at z_1 level and the conveyance plate [ϕ 10 x 1 mm; mass = 0.26 g.] is placed on top of it. Initially, the mobile part is at z_1 level and there is no physical contact with the conveyance plate [see Fig. 2.5 (b) (view A)]. In order to convey the plate in x-direction as shown, the mobile part is switched to z_2 level. This step corresponds to the lift phase. In the third step, the mobile part is switched in xy-plane that ensures the plate displacement in the same direction. After that, the mobile part goes back to z_1 level that will release the contact between the plate and the MPM. In step 5, the mobile part will come back to its initial

position without disturbing the plate and then will be ready to realize next conveyance sequence.

2.2 Modeling

In this section, the modeling of the HDA is presented. This model has been used in order to design the HDA. Firstly, the magnetic flux density distribution model is presented. Later, the electromagnetic model is described. The frictional force model is also presented and taken into account to realize the conveyance application. At last, all these models are used in order to study the dynamic behaviour of the system.

2.2.1 Magnetic flux density distribution model

For the magnetic flux density model, three PMs with different shapes have been considered. It includes the analytical model for cuboidal PM, and the numerical model for hexagonal and the cylindrical PMs. As mentioned in the previous section, to realize z -axis displacement, an electromagnetic air-core coil is used. Therefore, a FEM analysis has also been done to determine the magnetic flux generated by the coil.

2.2.1.1 Cuboidal PM

Initially, a cuboidal MPM with dimension of $5 \times 5 \times 2$ mm and magnetization of 1.37 T is considered. As the PM is of finite length, the surface charge model has been used to obtain the B-field at any point $P(x,y,z)$ located outside the PM. However, in order to use this model, some assumptions were carried out. The PM is considered with perfect geometries and uniform magnetization. The proper alignment of the magnetic poles for each PMs along z -axis is also considered. In this model, the PM is reduced to a distribution of equivalent magnetic charge [see Fig. 2.6] [Furl 01].

The analytical expression of the magnetic flux density for a PM with a dimension of $(x_2 - x_1)$, $(y_2 - y_1)$ and $(z_2 - z_1)$ is given in Eq. 2.2, where, B_x , B_y and B_z are the magnetic flux density components along x -, y - and z -axis, respectively. M_s is the PM magnetization, μ_0

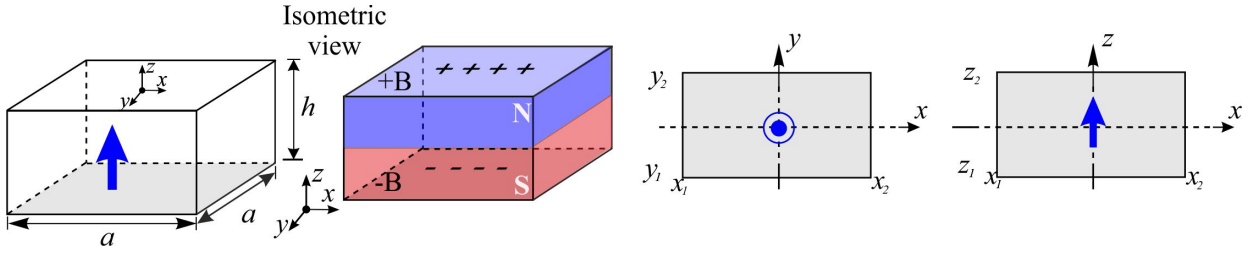


FIGURE 2.6: Reduction of single cuboidal magnet to equivalent charge distribution and its 2D representation.

is the vacuum permeability ($4\pi \times 10^{-7} \text{ Kg.m.A}^{-2}.\text{s}^{-2}$) and “m” is an index for calculation.

$$\begin{aligned}
 B_x(x, y, z) &= \frac{\mu_0 M_s}{4\pi} \sum_{k=1}^2 \sum_{m=1}^2 (-1)^{k+m} \times \ln \left(\frac{(y - y_1) + \sqrt{(x - x_m)^2 + (y - y_1)^2 + (z - z_k)^2}}{(y - y_2) + \sqrt{(x - x_m)^2 + (y - y_2)^2 + (z - z_k)^2}} \right) \\
 B_y(x, y, z) &= \frac{\mu_0 M_s}{4\pi} \sum_{k=1}^2 \sum_{m=1}^2 (-1)^{k+m} \times \ln \left(\frac{(x - x_1) + \sqrt{(x - x_1)^2 + (y - y_m)^2 + (z - z_k)^2}}{(x - x_2) + \sqrt{(x - x_2)^2 + (y - y_m)^2 + (z - z_k)^2}} \right) \\
 B_z(x, y, z) &= \frac{\mu_0 M_s}{4\pi} \sum_{k=1}^2 \sum_{n=1}^2 \sum_{m=1}^2 (-1)^{k+n+m} \times \tan^{-1} \left(\frac{(x - x_n)(y - y_m)(z - z_k)^{-1}}{\sqrt{(x - x_n)^2 + (y - y_m)^2 + (z - z_k)^2}} \right)
 \end{aligned} \tag{2.2}$$

2.2.1.2 Hexagonal PM

In the literature, the analytical expressions of the magnetic flux density components are given for cuboidal or cylindrical PMs. However, other magnet shapes must be considered as their use may improve the performance of magneto-mechanical devices [Rube 13]. In this work, a hexagonal PM is considered. As per the literature, there are articles on 3D analytical field model for triangular PMs [Jans 10] [Rube 13] and also semi-analytical models presented by Reza et al. [Reza 17]. In the article by Rubeck et al., they proposed to discretize the ‘m’ shaped polyhedral PMs into ‘2m’ shaped right-angled triangles and then calculating the B_x , B_y and B_z components [see Fig. 2.7]. However, while calculating the magnetic field in the plane of polygon, the B_x and B_y components are undefined, they manage to verify the proposed model analytically only on cuboidal magnets whereas a numerical approach have been adapted for the polygonal shapes. In addition, the numerical calculation for polygon includes division of polygon into sum of right triangles [see Fig. 2.7]. Each right angle triangle needs to be integrated to calculate the magnetic field

generated on point 'q', which adds to the complexity in calculation.

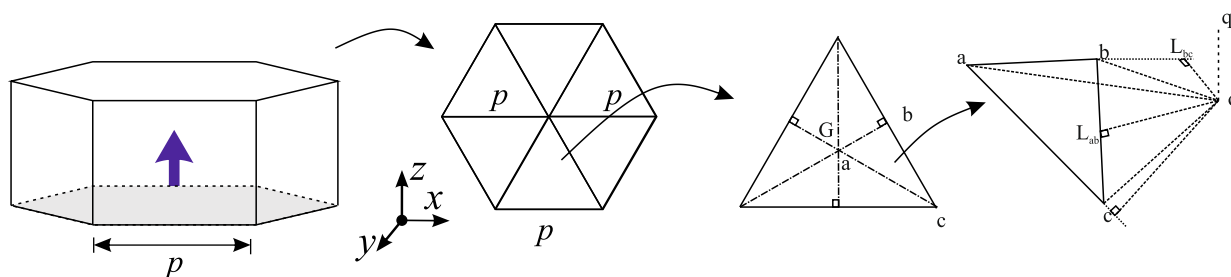


FIGURE 2.7: Distribution of hexagonal PM into equivalent right-angled triangles [Rube 13].

In order to overcome the above mentioned constraints and also to simplify the calculations, a superposition principle can be adapted as detailed by Liu et al. [Liu 17]. It includes division of hexagonal magnet into infinite number of small rectangular or cuboidal segments.

In this work, the volume of a considered hexagonal PM has been discretized into 'n' elementary cuboidal PMs and the total magnetic flux density of the hexagonal PM corresponds to the sum of magnetic flux density generated from the 'n' number of elementary cuboidal PMs [see Fig. 2.8]. The length and width are considered to be same for the elementary cuboidal shapes in order to reduce complexities. The magnetic flux density model (B_x , B_y and B_z) for cuboidal magnets is the same as the one presented in section 2.2.1.1 and given in Eq. 2.2.

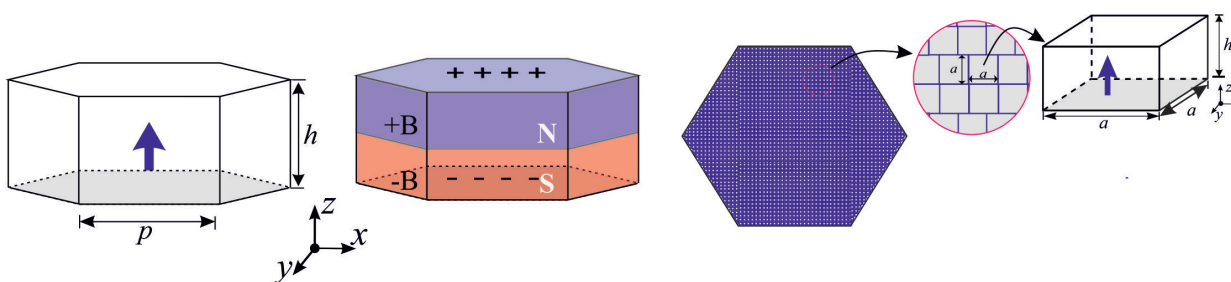


FIGURE 2.8: Representation of the discretization method on the Hexagonal PM.

A comparison has been made between the proposed discretized numerical method with the semi-analytical magnetic calculation software Radia (Mathematica add-ons) [Fig 2.9]. Radia uses boundary integral method for the force calculation. This method subdivides each object (for example: the considered PMs) of the model into number of small

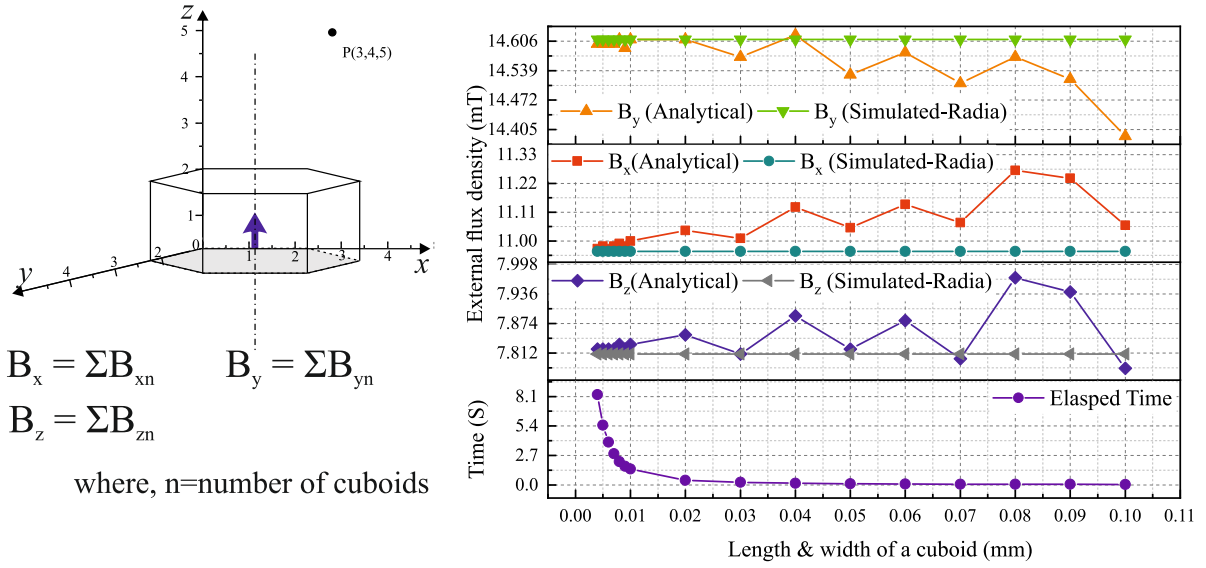


FIGURE 2.9: Representation of Hexagonal PM in 3D space with a point outside magnet; Calculation of total flux density and the elapsed time for calculation.

objects by forming a matrix and the forces are calculated by a multiplications sequence of all the small objects in a matrix. The hexagonal PM considered in this calculation is of the same dimension and magnetization to that of MPM. This figure shows the magnetic flux density components (B_x , B_y , B_z) with respect to the dimensions of the elementary cuboidal PM used for discretization from 0.004 mm to 0.1 mm. For all considered configurations, the magnetic flux density has been computed at a calculation point considered outside the MPM with the coordinates (3 mm, 4 mm, 5 mm). It has been observed that, the error between the proposed discretization and results obtained with Radia is reduced when the size of the elementary cuboidal PMs decreases. At a certain point, it starts becoming almost negligible. In addition, the time required for the calculation taking into account different cuboidal sizes has also been measured. Obviously, the calculation time increases when the cuboidal size decreases. Considering these results, a compromise has been made between the calculation error and time by considering the length and width of the cuboidal shape as 0.008 mm. In these configuration, the obtained errors are 0.19%, 0.019% and 0.08% for B_x , B_y and B_z , respectively. The model has also been tested for the coordinates (1 mm, 0.86 mm, 0.4 mm) which are within the stroke sizes of the proposed work. The errors are found to be less than 1%. As these errors are very small that validates the proposed model.

2.2.1.3 Cylindrical PM

The proposed design integrates FPM with cylindrical shape of dimension $\phi 2.25 \times 2$ mm with a magnetization of 1.37 T. A numerical model is used to calculate the magnetic flux density at any point P (r, ϕ, z) located outside the PM. Here some assumptions were carried out : the PM has an uniform cylindrical symmetry, magnetization is perfectly oriented along z -axis and uniform. Due to the considered cylindrical symmetry, the azimuthal components $B_\phi(r, z)$ equals 0 as stated by Furlani[Furl 01] and Ravaud et al.[Rava 08]. The reduction of PM into magnetic charge distribution is shown in Fig. 2.10.

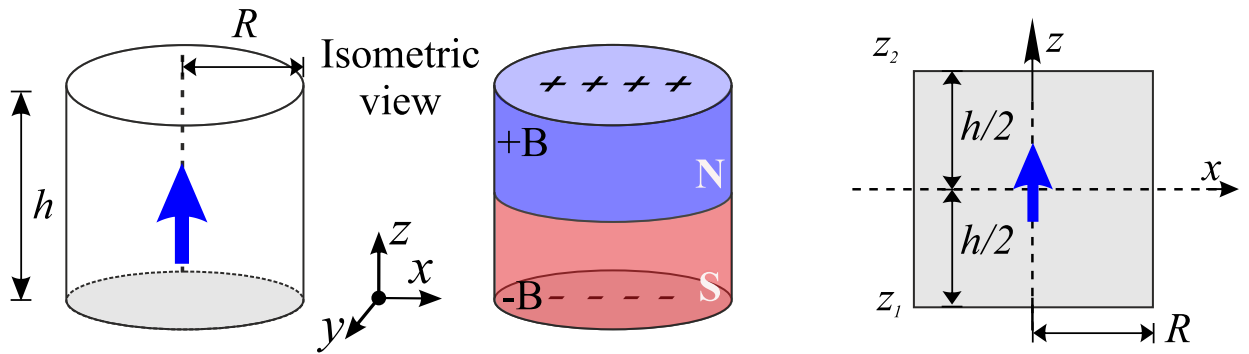


FIGURE 2.10: Reduction of cylindrical PM into equivalent magnetic charge distribution and its 2D representation in reference frame.

The analytical expressions for B_r and B_z are given in Eq. 2.3, where R is the radius of cylindrical PMs. Simpson's method is used to write the integrant ϑ' in terms of discrete sums. Let N_ϑ be the number of mesh points, the parameters $S_\vartheta(m)$ is the integration coefficients and $\vartheta'(m)$ is the value of integrant evaluated for N_ϑ mesh points [Furl 01].

$$\begin{aligned}
 B_r(r, \vartheta, z) &= \frac{\mu_0 M_s}{2N_\vartheta} \sum_{k=1}^2 (-1)^k R \times \sum_{m=0}^{N_\vartheta} S_\vartheta(m) \cos(\vartheta - \vartheta'(m)) g(r, \vartheta, z; R, \vartheta'(m), z_k) \\
 B_z(r, \vartheta, z) &= \frac{\mu_0 M_s}{4\pi} \sum_{k=1}^2 (-1)^k \times \left\{ \frac{2\pi}{N_\vartheta} \sum_{m=0}^{N_\vartheta} [S_\vartheta(m) (r \cos(\vartheta - \vartheta'(m)) - R) \right. \\
 &\quad \left. \times R \times I(r, \vartheta, z; R, \vartheta'(m), z_k)] \right\}
 \end{aligned} \tag{2.3}$$

where,

$$g(r, \emptyset, z; R, \emptyset'(m), z_k) = \frac{1}{\sqrt{r^2 + R^2 - 2Rr \cos(\emptyset - \emptyset'(m)) + (z - z_k)^2}}$$

and,

$$I \equiv \begin{cases} \frac{(z - z_k)g(r, \emptyset, z; R, \emptyset'(m), z_k)}{r^2 + R^2 - 2Rr \cos(\emptyset - \emptyset'(m))} & \text{if } r^2 + R^2 - 2Rr \cos(\emptyset - \emptyset'(m)) \neq 0 \\ \text{or} \\ \frac{-1}{2(z - z_k)^2} & \text{if } r = R, \cos(\emptyset - \emptyset'(m)) = 1, z \neq z_k \end{cases}$$

The above equation helps to calculate the M=magnetic flux density for the cylindrical magnet at a point outside or on the PM.

2.2.2 Validation of the proposed models

The analytical and numerical models proposed above have been implemented by using Matlab. To calculate the magnetic flux density analytically for cuboidal magnet, a PM with dimension $5 \times 5 \times 2$ mm - 1.37 T is used. For cylindrical magnets, dimensions are $\phi 2.25 \times 2$ mm with a flux density of 1.37 T. The magnetic flux density B_x , B_y , B_r and B_z are calculated and compared the ones obtained with the semi-analytical model Radia and also with the finite element analysis (FEA) calculation software COMSOL. A total of 8×10^5 mesh elements have been used for the calculation. Fig. 2.11 below represents the Magnetic flux density for cuboidal and cylindrical PMs. For the cylindrical PM, in order to realise numerical model, 10000 Simpson's mesh elements were used (N_ϕ)

The relative error observed with respect to the analytical and numerical model is in terms of 10^{-5} for cuboidal and 10^{-10} for cylindrical magnet. Thus, it validates the proposed model for cuboidal and cylindrical PM.

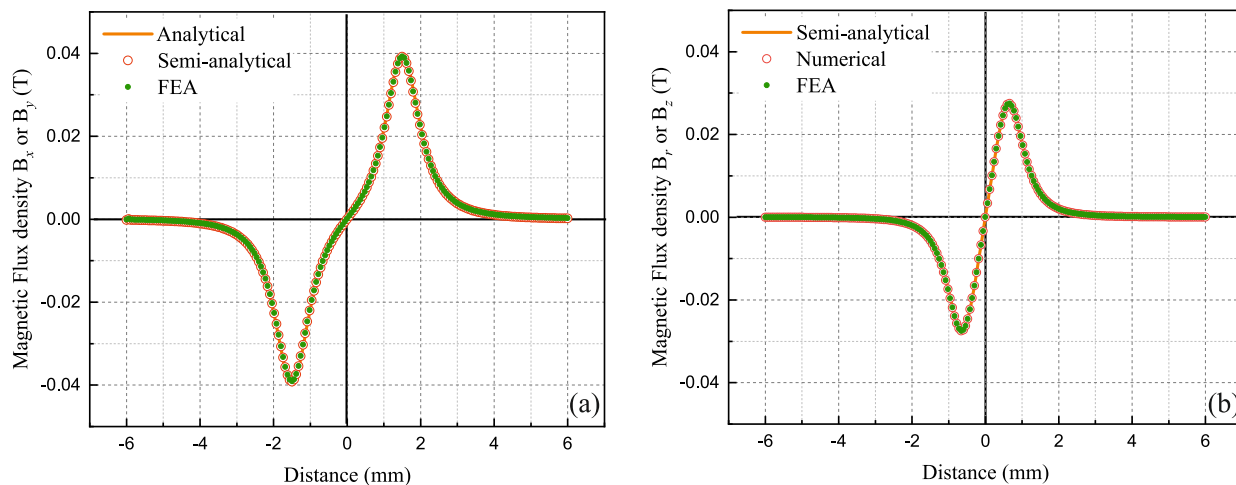


FIGURE 2.11: Graphical representation of magnetic flux density (a) for cuboidal magnet (b) for cylindrical magnet.

2.2.3 Magnetic force

The calculation of the magnetic forces exerted between the magnets (FPMs on the MPM) is described in this section. In order to determine this force, two cuboidal PMs are considered as shown in Fig. 2.12. The dimensions and magnetization considered are similar to the previous one discussed in section 2.2.2. Eq. 2.4 gives the expression to calculate the generated magnetic forces [Furl 01].

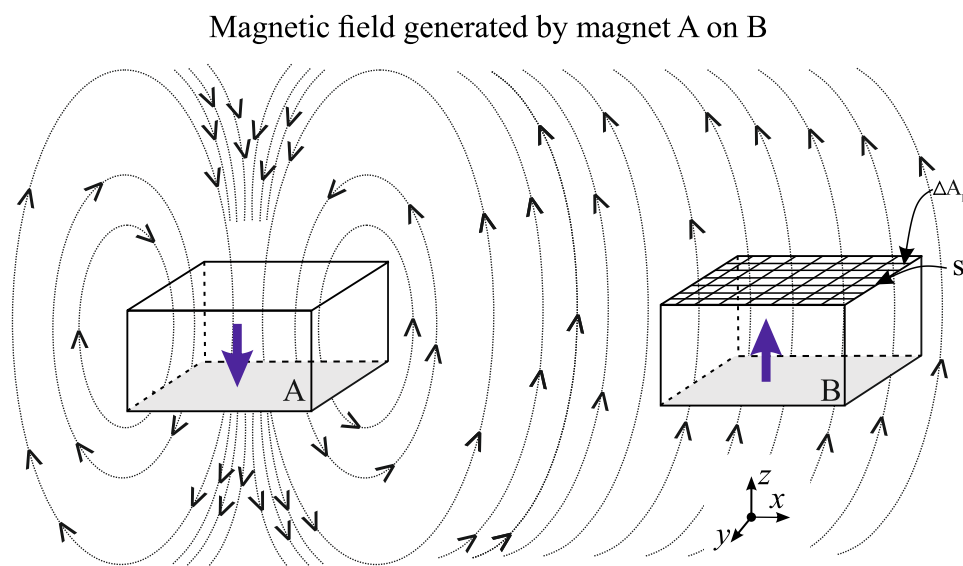


FIGURE 2.12: Magnet and the illustrated coordinate system for magnetic force calculation.

$$F_{Magnetic} = \oint_s \sigma_m B_{ext}(x, y, z) ds \quad (2.4)$$

where, σ_m is the surface charge density and B_{ext} is the external magnetic flux density generated by PM A. However, in most cases, a discretization approach is undertaken as Eq. 2.4 is not able to solve it analytically. The pole surfaces of PM B are discretize in to sub-surfaces (ΔA_p) and then the magnetic flux density is calculated [see Fig. 2.12]. Eq. 2.5 gives the expression of the magnetic force using discretized method.

$$F_{Magnetic} = \sum_p \sigma_m(x_p) B_{ext}(x_p) \Delta A_p \quad (2.5)$$

To calculate the magnetic force generated between cylindrical and cuboidal PMs, two methods can be used. Firstly, we can assume that two magnets of same volume, height and magnetization exerts the same magnetic force irrespective of their shapes. These assumptions have been verified using a semi-analytical model (Radia) and it is valid if the calculation point is not too close to the considered PM. Two PMs, one cuboidal and the other one cylindrical have been considered for the validation with same volume, magnetization and height and the magnetic forces were calculated. It has been observed that the relative error in force generated by these two magnets at a point is very small (10^{-7} T) and therefore, considered negligible. It validates the first method for the calculation.

Another method can be to convert the cartesian into cylindrical coordinates and vice versa [Eq. 2.6]. This method has also been validated using numerical model of Matlab and the semi-analytical model Radia.

$$\begin{aligned} r &= \sqrt{x^2 + y^2} \\ \Theta &= \tan^{-1}\left(\frac{y}{x}\right) \\ z &= z \end{aligned} \quad (2.6)$$

2.2.4 Electromagnetic force

In this section, the expression of the electromagnetic Lorentz force generated between a current carrying conductor and a PM is given in Eq. 2.7 with respect to current in a conductor (I), length of a conductor (l) and magnetic field generated by the PM on the wire (B_{ext}).

$$F_{Electromagnetic} = I \int_{wire} dl \times B_{ext} \quad (2.7)$$

Similarly to the magnetic flux density model, this expression has been implemented using Matlab and the results have been compared with Radia. A cuboidal PM ($5 \times 5 \times 2$ mm and magnetization of 1.37 T) with a magnetization along z -axis has been considered in order to calculate the generated electromagnetic force using a single conductor. The conductor is placed at a distance of $100 \mu\text{m}$ from the bottom of the PM. A current of 1 A flows through the conductor in T_c and the electromagnetic force is calculated from different positions of PM from -3 mm to +3 mm along x -axis. Fig. 2.13 below represents a comparison of electromagnetic force computed with the semi-analytical (using Radia) and analytical (using Matlab) model.

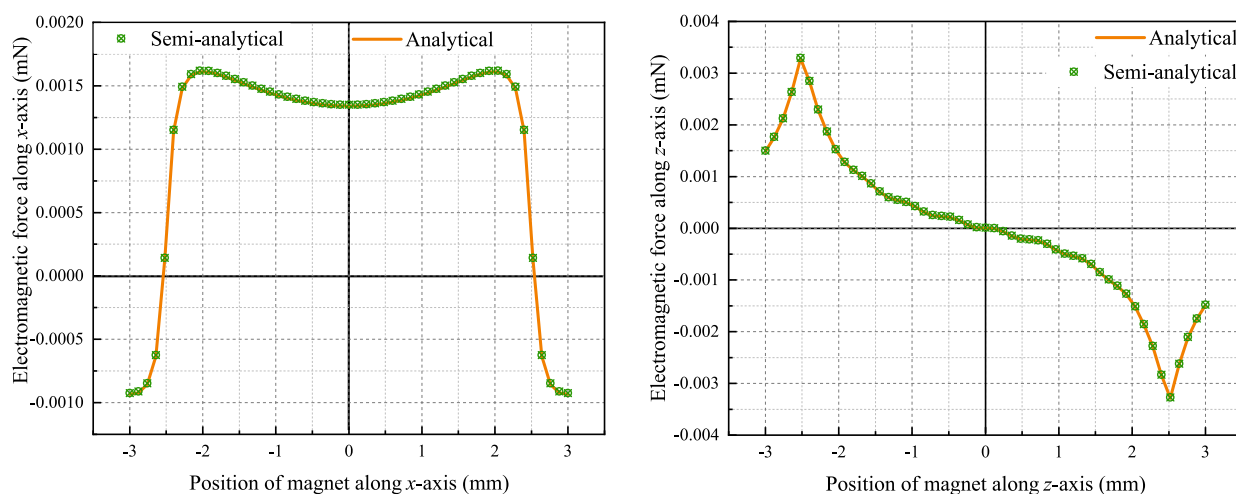


FIGURE 2.13: Analytical and semi-analytical representation of electromagnetic forces for cuboidal magnet.

Fig. 2.13(a) represents the force generated along x -axis which is maximum at the edge of the PM. This is due to the higher flux density at edge of the PM compared to the center. The electromagnetic force generated along z -axis [Fig. 2.13 (b)] tends towards zero when

the conductor is exactly at the center of PM, whereas, it starts increasing when the PM is oriented either along $-x$ - or $+x$ -axis with respect to the conductor. Both results, obtained with Matlab and Radia, are nearly superimposed with a difference of 10^{-4} between them. Thus, the proposed electromagnetic model is validated.

2.2.5 Electromagnetic air-core coil

In order to switch the mobile part along z -axis and to hold it at z_2 level, a coil is used. The magnetic field generated by the coil needs to be calculated. A FEM analysis has then been realized using Comsol (with a mesh elements of 8×10^5) to calculate the induced magnetic flux density by an electromagnetic coil (dimensions: ϕ_{ext} 20×10 mm, ϕ_{int} 9 mm). A current of 1 A is passed through the coil to generate the magnetic flux density.

The Fig. 2.14 represents the generated magnetic flux density on the top surface and at the center of an electromagnetic air-core coil. The graph represents the distribution of magnetic flux density with respect to the position along x -axis. It can be observed that, the generated flux density on the surface is uniform and ensures proper levitation of the MPM.

2.2.6 Static model

A static model of the actuator has been developed to calculate the magnetic and electromagnetic forces generated on its mobile part. In order to calculate the magnetic forces acting on the mobile part, the mobile part and six FPMs placed in a circular fashion equidistant from each other around the hexagonal cavity have been considered. The mobile part has been discretized into sub-surfaces ΔA_p as explained in section 2.2.3 and the magnetic flux density has been calculated. The resulting flux is the sum of the magnetic flux generated by six FPMs. Thus, the magnetic force is derived using equation 2.5. In addition, to calculate the electromagnetic forces generated by the current driving conductors on the MPM, Eq 2.7 has been used. The forces are calculated for top and bottom conductors as shown in Fig. 2.2.

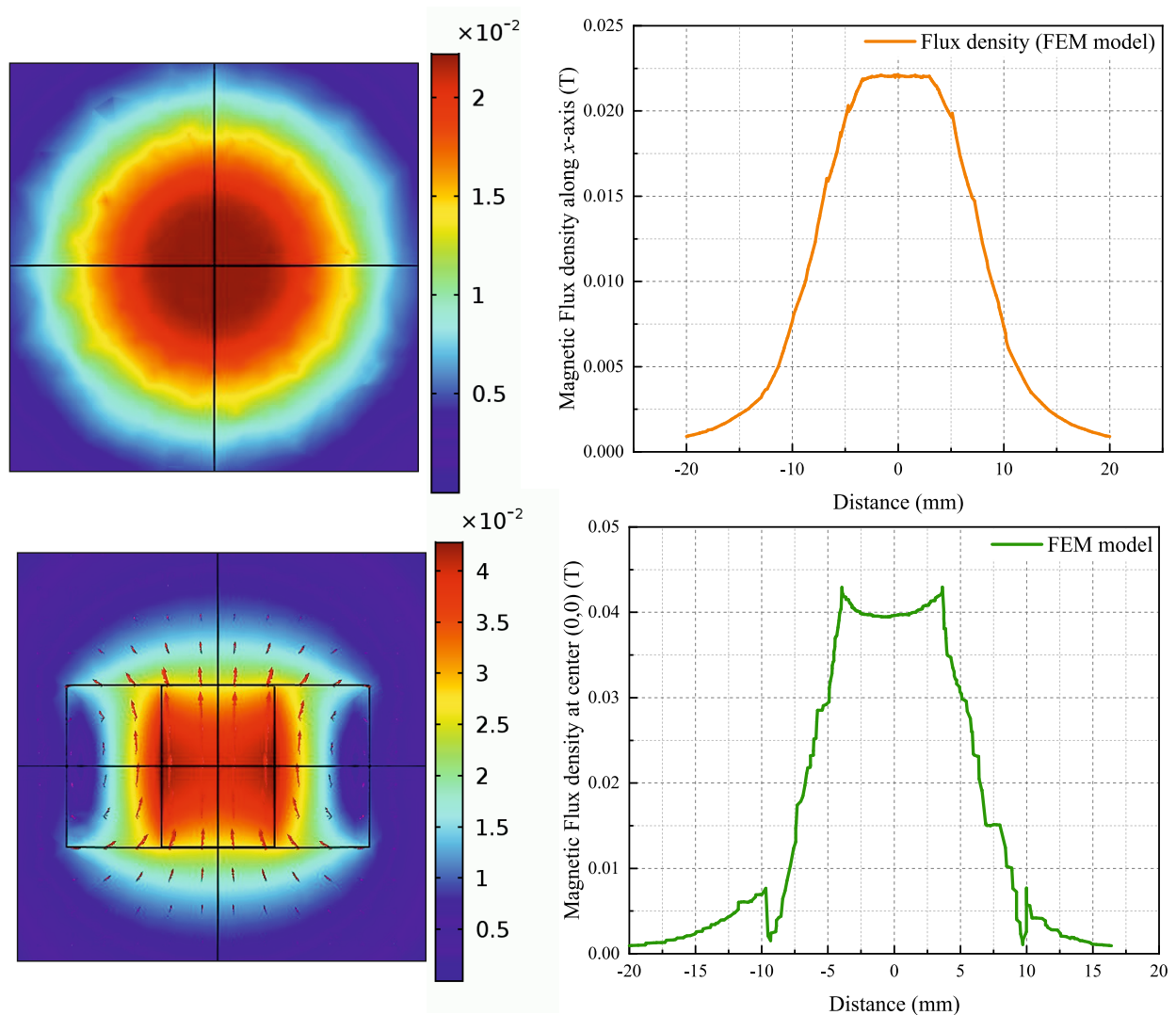


FIGURE 2.14: A Finite element analysis of an electromagnetic air-core coil and the representation of magnetic flux density.

The total forces exerted on the mobile part, is the addition of magnetic and electromagnetic forces taken into account by the static model of the HDA. The Fig 2.15 represents the total forces exerted on the MPM along x -, y - and z -axis for different positions of the MPM. In order to simplify, the total forces generated along z -axis (i.e. at z_1 and z_2 levels) are only presented for F_x , similar forces can also be observed for F_y and F_z but are not presented. The forces are calculated for three driving current values 0 A (no current), 1.5 A and 3 A, injected in the T_c of the PCB.

The Fig. 2.15 (a) represents the total force (magnetic + electromagnetic) along x -axis F_x with respect to MPM position for two levels along z -axis. When there is no current in the conductors (0A), the total force corresponds only to the magnetic holding force

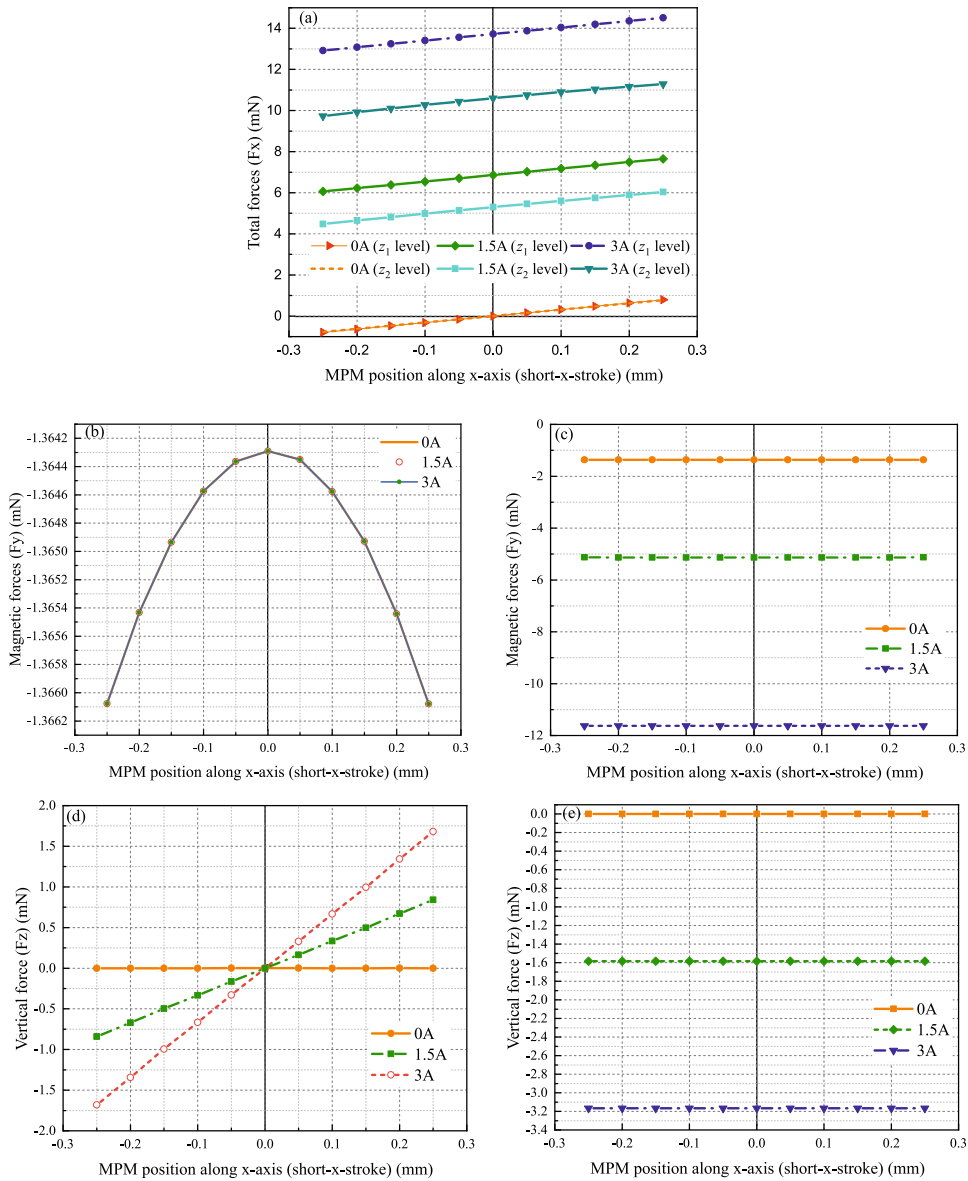


FIGURE 2.15: Representation of total forces with respect to the MPM position along x -axis (Current injected in T_c). (a) Driving force (F_x) with respect to current for two different levels along z -axis. (b) Holding force (F_y) with respect to driving current values. (c) Holding force (F_y) with respect to holding current values. (d) Vertical force (F_z) with respect to driving current values. (e) Vertical force (F_z) with respect to holding current values.

generated by the FPMs. The force generated is almost linear due to the small stroke size (0.5 mm) compared to the MPM dimension. Moreover, when an electric current is passed through the conductors, the graph shifts upward due to addition of electromagnetic forces which is proportional to the injected current value. However, for the same current values, the total forces generated for the two different levels along z -axis are different. This is due to the addition of air gap between the MPM and the conductors when

the mobile part is at upper level along z -axis (i.e. z_2 level) as shown in fig. 2.5 (b). The forces obtained along x -axis are 6.86 mN at z_1 and 5.29 mN at z_2 for a current value of 1.5 A, whereas, 13.72 mN at z_1 and 10.59 mN at z_2 for a current value of 3 A., respectively. In addition, along y -axis the forces obtained are 5.13 mN at z_1 and 3.58 mN at z_2 for a current value of 1.5 A and 11.62 mN at z_1 and 8.50 mN at z_2 for a current value of 3 A., respectively. The forces generated along y -axis are lower compared to x -axis due to the use of B_c for y -axis switching and the distance between B_c and the MPM is higher than the distance between T_c and the MPM ($d_3 > d_2$).

The Fig. 2.15 (b) represents the holding force, along y -axis F_y as a function of MPM position for three different driving current values 0 A, 1.5 A and 3 A. The three curves are superimposed as the holding is not affected by the driving current values. In the graph, the force variation is very small, its amplitude is slightly lower (1.364 mN) when the MPM is placed centrally (0,0) than that of discrete positions (1.366 mN). The magnetic holding force is higher when the MPM is indeed close to a FPM then in a discrete position. In fig. 2.15 (c), the holding force is represented for different values of holding current (injected in bottom conductors). The variation of the holding force F_y can be clearly seen for three different current values. When there is no holding current, the holding force is only due to the magnetic holding by the FPMs. But, as there is an increase in the current, magnitude of holding force also increases.

The generation of vertical force F_z is also shown with respect to MPM position (Fig. 2.15 (d)) at z_1 level. When there is no current in the conductors, no vertical force generated, but as the current is injected in the T_c , an electromagnetic vertical force is generated and is maximum at the discrete positions and it is zero when the MPM is at center. In this case, the MPM is centered relative to the supplied conductors and the vertical force is totally oriented along z -axis. The initial forces generated at the discrete positions for a current of 1.5 A and 3 A are 0.84 mN and 1.68 mN, respectively. Apart from that, the impact of holding current on the vertical force is also presented (see Fig. 2.15 (e)). It can be observed that as the current increases the magnitude is higher, it is due to the position of mobile part with respect to the B_c .

2.2.7 Determination of Self-returning zone and minimum Driving current (I_{min})

The magnetic and electromagnetic forces calculation as mentioned above helps to design the actuator especially to define the distance between the hexagonal cavity and center of the FPM (d_1) as shown in Fig. 2.1. As the distance is less, the FPM generates more holding force and a more robust behavior therein, it also increases the minimum current required to switch. Therefore, a compromise has been made between the holding force and minimum current required to switch by introducing a parameter of Self-Returning Zone (SRZ).

SRZ represents the maximum distance at which the mobile part can be placed from a discrete position while ensuring that it will return to one of its discrete positions without any external power supply. This zone is due to the magnetic holding forces generated by the FPMs on the MPM. It also provides robustness of the HDA to external disturbances that is, it provides the ability to maintain the stable positions. The Fig. 2.16 (a) below shows the distribution of hexagonal cavity into SRZ and Intermediate zone (IZ). The mobile part is represented by a circular ball and the SRZ as in inclined line. The positions A and B are the positions that defines the SRZ and IZ. An equivalent mechanical representation is also presented for clear understanding. In SRZ, the magnetic holding forces are higher than the frictional forces between the mobile and fixed parts. However, for the region located in the middle of stroke (IZ), the frictional forces are higher than the magnetic holding forces. For xy -plane motions, when the mobile part is placed at a position inside the SRZ, it will return to the nearest discrete position. If the mobile part is placed in the IZ, the magnetic force is not enough compared to frictional force and the mobile part will not return to a discrete position without any external force. For z -axis motion, the z_1 level is privileged compared to z_2 level. To hold the mobile part in z_2 level, a continuous current supply is required in the coil and when the current stops, the mobile part will return back to the z_1 level due to the weight of the mobile part acting downward [Fig. 2.16 (b)]. This configuration has been selected to simplify the architecture and design of the proposed

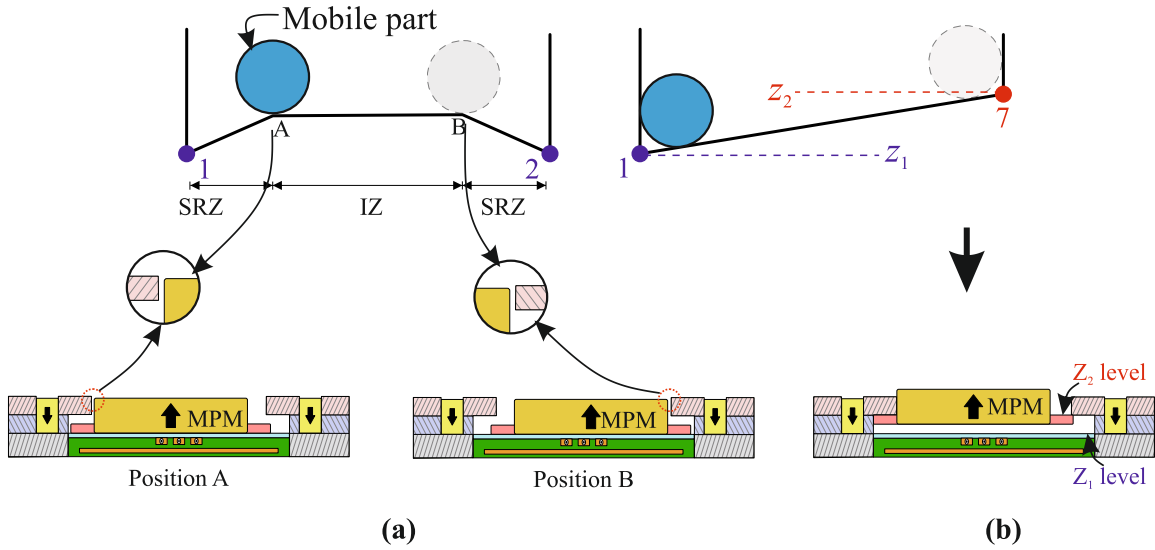


FIGURE 2.16: Representation of SRZ and IZ (a) Digital actuation behaviour along xy -plane (b) Digital actuation behaviour along z -axis.

actuator and to ensure the access to the upper face of the MPM for application.

The SRZ value can be analytically calculated. In order to do so, all the forces exerted on the mobile part have been taken into account : the magnetic forces generated by the FPMs on mobile part, the electromagnetic forces due to the current carrying conductors placed beneath the mobile part and the frictional forces. Eq. 2.8, below provides the equation to calculate the SRZ value.

$$SRZ = \frac{L}{2} \times \left[1 - \frac{F_{friction}}{F_{holding}} \right] \quad (2.8)$$

where L is the stroke of the MPM in respective direction and $F_{friction}$ is the frictional force between MPM and the cavity. The SRZ can be calculated for each stroke value.

For the considered HDA, the SRZ value is defined as approximately 10% of the stroke in order to make a compromise between the digital behaviour and the energy consumption to switch. The SRZ value depends on the distance d_1 [see Fig. 2.1] that is the distance between FPMs and center of the hexagonal cavity. The lower the distance d_1 is, the higher the holding forces and thus the high SRZ value. The high SRZ value therefore, requires more energy to switch. The minimum current required to switch the MPM (I_{min}) can be

calculated for the two sets of conductors using Eq. 2.9 as shown below.

$$I_{min}T_c = (F_{holding} + F_{friction})/F_{emfx} \quad (2.9)$$

$$I_{min}B_c = (F_{holding} + F_{friction})/F_{emfy}$$

where F_{emfx} and F_{emfy} are the electromagnetic forces generated for x - and y -axis switching, respectively.

2.2.7.1 Frictional Force calculation

The frictional forces generated between the mobile part and fixed parts are needed to determine the SRZ and I_{min} values. Two different frictional forces are considered in the model: two horizontal friction forces (named as F_{hf1} and F_{hf2}) and a vertical frictional force (F_{vf}) as shown in Fig. 2.17.

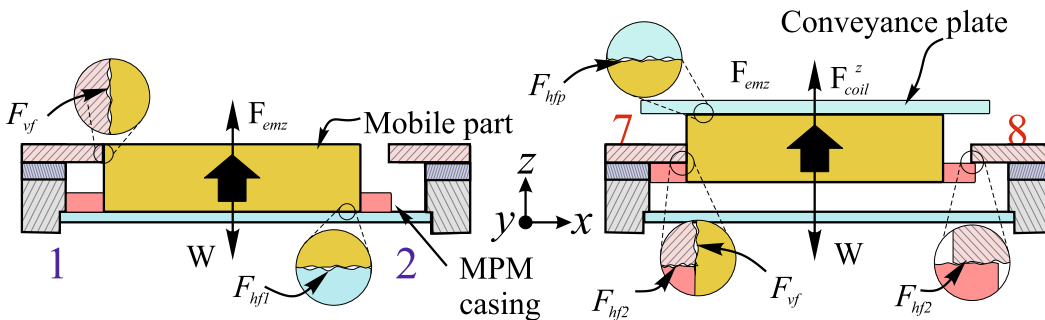


FIGURE 2.17: Representation of the generated horizontal and vertical frictional forces for MPM and the conveyance plate

The first horizontal frictional force F_{hf1} corresponds to the contact between the bottom side of the mobile part and the thin glass layer when the mobile part is at level z_1 . The second horizontal frictional force F_{hf2} appears due to the contact between the mobile part and the mechanical support at z_2 level. Moreover, the vertical frictional force F_{vf} is due to the contact between the sides of the mobile part and the hexagonal cavity. The frictional forces are calculated using Coulomb model (2.10) and (2.11). Apart from that, there is also a horizontal frictional force generated between the plate and the mobile part F_{hfp} [see Eq. 2.12], which is taken into account when the actuator is used for conveyance

application.

$$F_{hf1} = (W - F_{emz}) \times \mu_{hf} \quad (2.10)$$

$$F_{hf2} = (W - (F_{coil}^z + F_{emz})) \times \mu_{vf}$$

$$F_{vf} = F_{holding} \times \mu_{vf} \quad (2.11)$$

$$F_{hfp} = (W_p + W_o) \times \mu_{vf} \quad (2.12)$$

where W is the weight of the mobile part, W_p is the weight of the conveyance plate, W_o is the weight of the object, $F_{holding}$ is the magnetic force exerted by the FPMs on the mobile part, μ_{hf1} and μ_{vf} are the horizontal and vertical frictional coefficients which have been experimentally measured using inclined plane technique. To realize the inclined plane technique, a PM was placed on a glass slide, or on a support in silicon, and the assembly was tilted using a motorized rotation stage (Newport SR50CC) until the MPM slides. The experiment was repeated twenty times and the mean is calculated. The values obtained for μ_{hf} and μ_{vf} are 0.39 ± 0.06 and 0.48 ± 0.06 , respectively. Along with that, there are also electromagnetic forces generated due to coil and due to the current carrying wires. F_{coil}^z is the electromagnetic force generated by the coil along z -axis and F_{emz} is the electromagnetic force along z -axis generated when a current passes into the conductors.

2.3 Computer-Aided-Drawing (CAD) modeling of the HDA

In this section, a 3D CAD model of the HDA has been realized using Creo 4.0. Two CAD models are presented: one with a cuboidal MPM and another one with a hexagonal MPM. The mobile part for both types of HDA are designed in order to obtain twelve discrete positions, which are distributed at two different levels along z -axis.

2.3.1 3D actuator with cuboidal PM

The exploded view of the HDA with cuboidal PM is shown in Fig. 2.18 (a). The design integrates two mechanical supports with the defined cavities for MPM and FPMs, a PCB

support, which helps to ensure proper alignment of PCB with respect to hexagonal cavity and a base part, in order to assemble all parts together and also to fix the air-core coil. The mobile part of this HDA consists of a cuboidal MPM inserted in the hexagonal cas-

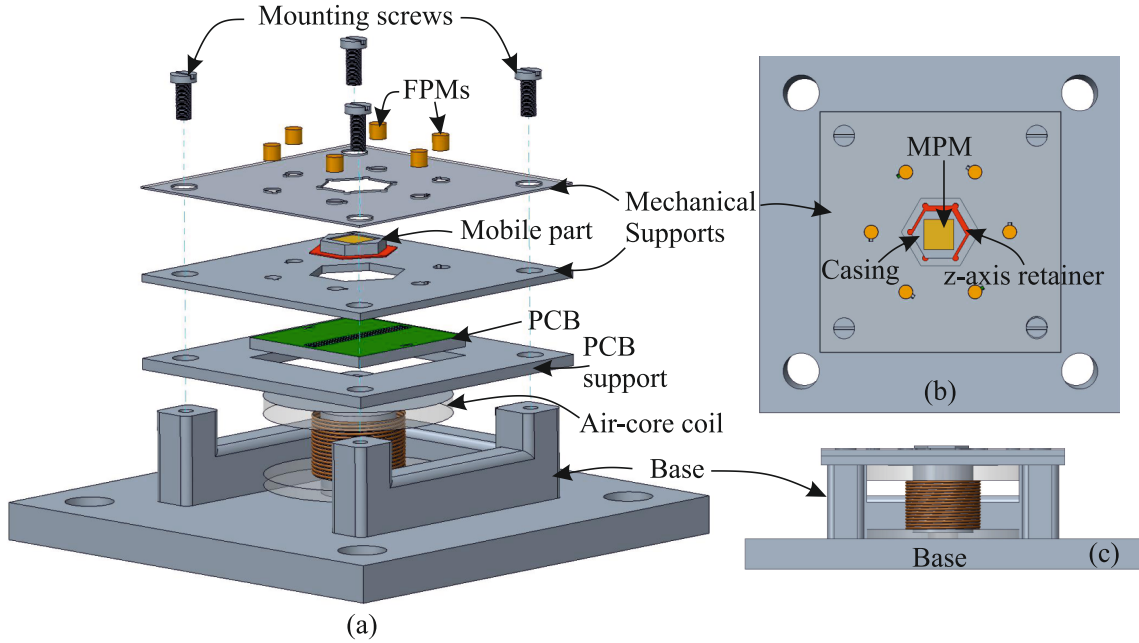


FIGURE 2.18: CAD model of a 3D digital acuator with cuboidal mobile magnet. (a) exploded view to visualize arrangements of different parts. (b) Top view of the actuator; (c) Front view of the actuator.

ing (see Fig. 2.18 (b)). The retainer is used to define the stroke along z -axis as explained in section 2.1.2. The details of all the components are given in Table. 2.3.

Components	Dimensions (mm)	Material properties	Quantities
MPM (cuboidal)	$5 \times 5 \times 2$	NdFeB-1.37 T	1
FPM	$\text{Ø}2.25 \times 2$	NdFeB-1.43 T	6
Coil	$\text{Ø}_{ext} 20 \times 10$ $\text{Ø}_{int} 9$	Cu. wire- $\text{Ø}0.654$ mm (with insulation)	1
Mechanical supports	$40 \times 40 \times 1$	PMMA	3
Hexagonal casing	$\text{Ø}4.5 \times 1.5$	PMMA	1
z -axis retainer	$\text{Ø}6 \times 0.5$	PMMA	1

TABLE 2.3: Material properties and quantities of the components used in the assembly of digital actuator.

2.3.2 3D actuator with hexagonal PM

An optimised version of the HDA has also been designed which includes, a hexagonal MPM. The mobile part in this HDA consists of a hexagonal MPM with a z -axis retainer

fixed at its bottom (dimensions- $\text{Ø}3.50 \times 0.5$; Material -PMMA). The design is composed of similar components (electromagnetic air-core coil, mechanical supports, PCB) to that of the cuboidal PM (not shown in fig.). The Fig. 2.19 provides the CAD model and top view of the HDA.

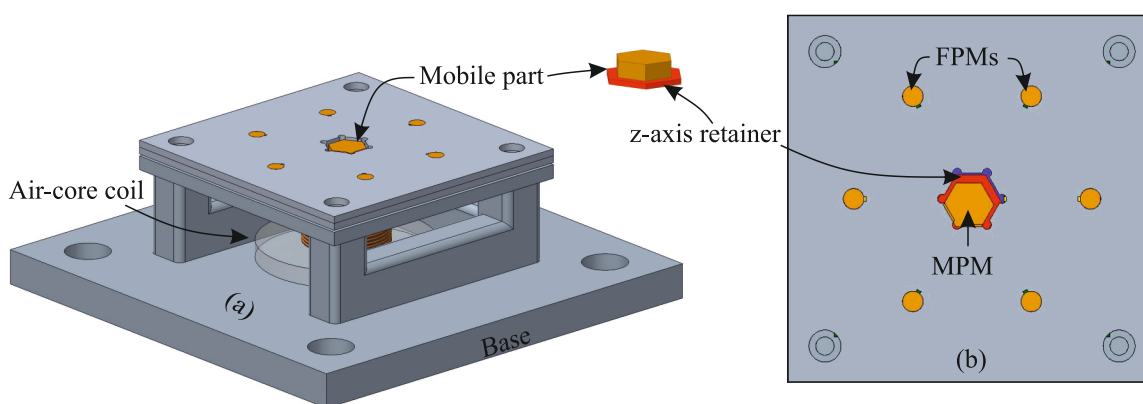


FIGURE 2.19: CAD model of a 3D digital actuator with hexagonal mobile magnet. (a) An isometric view of the actuator with the assembly of mobile part.(b) Top view of the actuator.

2.4 Conclusion

In this chapter, a 3D HDA based on the electromagnetic Lorentz force principle is presented. The mobile part of the actuator is able to reach twelve discrete positions, distributed at two different levels along z -axis. The HDA architecture makes it possible to have two conveyance strategies for the plate displacement using a single actuator: stick-slip and lift mode approaches.

In the first part of the chapter, the design of a 2D HDA has been explained then the actuation principle have been described. Two important principles are used for this actuator and are detailed: switching with the help of Lorentz force and holding with the help of magnetic forces. Initially, a cuboidal shaped MPM has been used to validate the proposed concept. Later, it has been replaced by an hexagonal shaped MPM in order to optimize the working of the digital actuator. An analytical model has been proposed for cuboidal PMs, whereas a numerical model have been proposed for cylindrical and hexagonal PMs in order to design two version of the HDA. A FEM analysis of an electromagnetic air-core

coil is also detailed in this chapter, in order to calculate the magnetic flux generated for z -axis levitation of the mobile part.

In the second part, static model have been proposed to design the HDA. The static model takes into account the total forces exerted on the mobile part. It also includes, SRZ calculation which is an important parameter to characterize the dynamic behavior of the HDA. Lastly, with the defined dimensions, CAD models of the HDA have been proposed in order to realize prototypes which will be presented and characterized in the next chapter.

Chapter 3

Realization & Experimental Characterization of the Hexagonal Digital Actuator

In this chapter, experimental prototypes of the HDA and their characterization are presented. In the first part of this chapter, the detailed design layout of the HDA and its different components are presented. Moreover, the different manufacturing processes for the fabrication of the prototypes are described. In the second part, the experimental characterization of the prototypes is presented. This characterization includes: the experimental validation of the HDA and its application as a positioning device.

3.1 Design Layout of the prototype and component description

The design layout of the HDA is as explained in the previous chapter. The HDA consists of two main parts: the mobile part and the fixed part. The mobile part has been realized by assembling the z -axis retainer with the MPM. Two different plates are fabricated (Top & Second) in order to define the stroke along z -axis and also in xy -plane. In addition, a square cavity has been realized to center-align the PCB with respect to the hexagonal

cavity. A thin glass layer is also placed in the square cavity of the PCB. The detail illustration of the design parameters and the development of each component is explained in the following sections.

3.1.1 Mobile Part Assembly

The mobile part of the HDA is designed in order to obtain displacement along x -, y - and z -axis direction. Two different configurations have been proposed as shown in Fig. 3.1 (a) (b). In the first configuration, the top side of the bracket is used to limit the MPM stroke along z -axis, a PMMA piece is then attached on top of the MPM for the conveyance application. The z -axis stroke in this configuration is the difference between top side of the MPM and the bracket. However, only a small surface (of the attached PMMA piece) comes in contact with the conveyance plate. A second configuration has been proposed with a z -axis

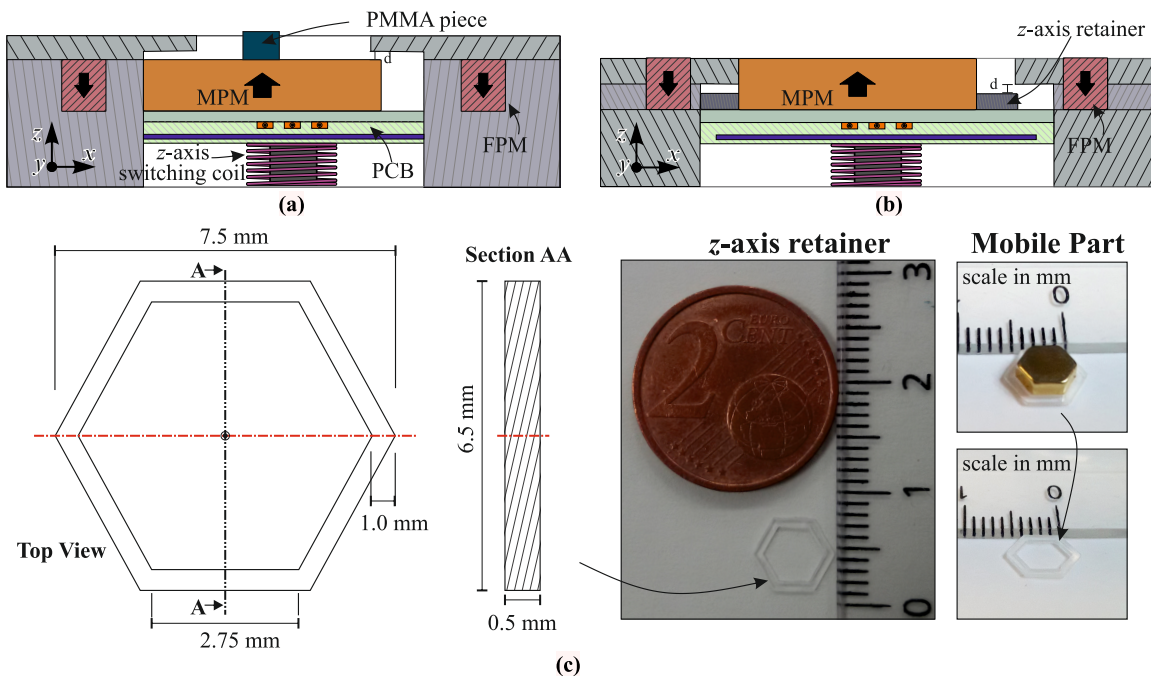


FIGURE 3.1: (a) Configuration 1: Mobile part with a PMMA piece. (b) Configuration 2 : Mobile part with a z -axis retainer. (c) Geometrical design, fabricated z -axis retainer and mobile part assembly.

retainer which is fixed at the bottom side of the MPM as shown in Fig. 3.1 (b). A thin layer of cyanoacrylate glue is applied to the assembly area for a proper fixation of the retainer on MPM. The retainer is made of PMMA material with a mass of 0.007 g and is fabricated using a laser cutting technique. The overall dimensions of the retainer was selected in

order to minimize its weight, which will add to the weight of mobile part. The fabricated z -axis retainer can be clearly seen in Fig. 3.1 (c). An assembled mobile part is also shown and a coin is placed for size estimation.

3.1.2 Fabrication of the Fixed Parts

The fixed parts are essential components of the HDA as the stroke is defined during its manufacturing process. Initially, a laser cutting technique is used to fabricate all the fixed parts. PMMA material has been used for the manufacturing. However, the main idea of this first prototype was to validate the proposed concept, the ability of mobile part to reach twelve discrete position at two different levels along z -axis and also to initially characterize the HDA. To verify the stroke of PMMA version prototype, a stereomicroscope (Leica DFC400) has been used Fig. 3.2 (a).

The electromagnetic air-core coil has been manufactured at Roberval Laboratory due to the unavailability of such compact size air-core coil in the market. The dimensions were determined using the FEM analysis explained in the modeling section and as per that, a 3D printed core has been manufactured as shown in Fig. 3.2 (b). Then, a Copper wire of 0.6 mm diameter (0.654 mm with insulation) has been rolled over the 3D part as shown in Fig. 3.2.

3.2 Measurement techniques

Different measurement techniques have been used to characterize the performances of the developed prototypes and are described in this section. In order to do so, non contact measurements technique have been selected because they avoid any disturbance in the functioning of HDA. The two non contact measuring technique used are a Fiber Optic Displacement Sensor (FODS) and a High Resolution Camera (HRC).

3.2.1 Fiber Optic Displacement Sensor (FODS)

The FODS used during experiments has been initially developed in the Roberval laboratory of UTC by Dr. Damping Wang [Wang 99]. It is composed of three main components,

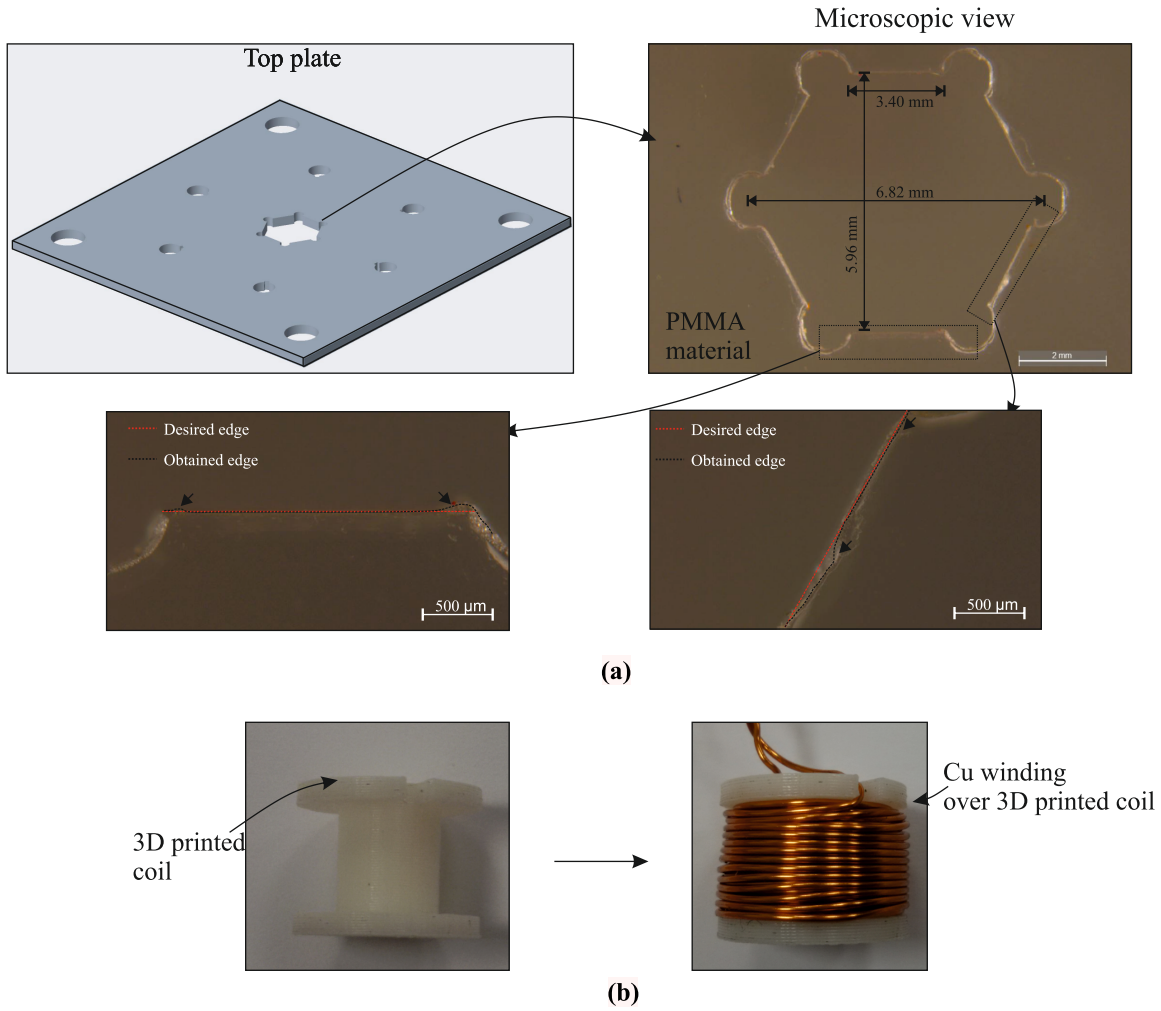


FIGURE 3.2: (a) PMMA deformation due to laser cutting technique for the Top plate. (b) Assembly of a 3D printed air-core electromagnetic coil.

the signal processing unit, a FODS probe [see Fig. 3.3] and a reflective surface (e.g. mirror). The FODS probe consists of a ferrule, corresponding to the measurement head of the sensor, in which there are five optical fibers: one for emission and four for reception as shown in Fig. 3.4(a). The probe transmits and collect reflected light whereas, the signal processing unit consists of an electronic circuit which interprets the light into voltage and vice versa.

The probe has small dimensions ($\phi 2$ mm, length= 10 mm). Only the ferrule is required to be placed close to the mobile part of actuator while the electronic unit is deported from the optical fiber. The ferrule of FODS is composed of non magnetic material, which is essential in order to avoid any magnetic disturbance in the working principle of the HDA due to sensor. In terms of performance, this sensor has a measurement range

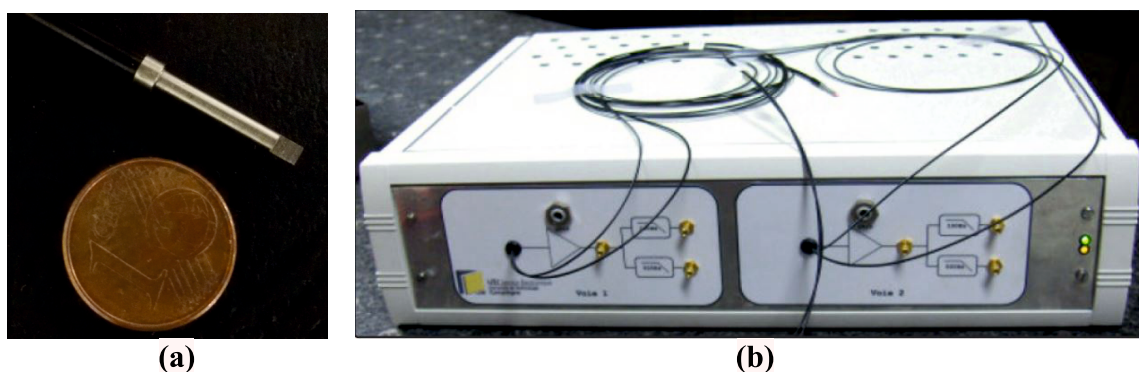


FIGURE 3.3: (a) FODS probe (b) FODS Signal Processing Unit.

of several millimeters and is therefore suitable to measure the entire stroke of the mobile part. The maximum stroke is indeed limited to 1 mm. The resolution depends on several parameters such the reflection coefficient of the used mirror, the positioning and the distance of the ferrule relative to the mirror, etc.. Its value will be indicated for each experimental measurement. In the best case, it can reach values in the order of a few nanometers [Prel 06].

3.2.1.1 Working Principle of the FODS

The FODS is composed of one emission fiber and four reception fibers as shown in Fig. 3.4 (a). A LED is used as a light source, which is injected in the emission fiber and transmitted to the end of ferrule. A reflecting mirror is placed in front of the ferrule and reflects the emitted light which is collected by the reception fibers. The captured light is then routed to the photodiode in the FODS signal processing unit. The photodiode converts the collected light into electrical voltage. The amount of light reflected is directly linked to the displacement between the probe and the reflecting mirror. The change in position of the mirror with respect to the probe, leads to an output voltage variation. The acquisition of this voltage is carried out using a National Instruments data acquisition board.

The typical response curve of the FODS is shown in Fig. 3.4 (b). The curve is composed of four different zones. Zone 1 corresponds to the dead zone, where no light is collected by the reception fibers due to the small distance between the ferrule and the reflecting mirror. After this zone, the output voltage starts increasing almost proportionally to the

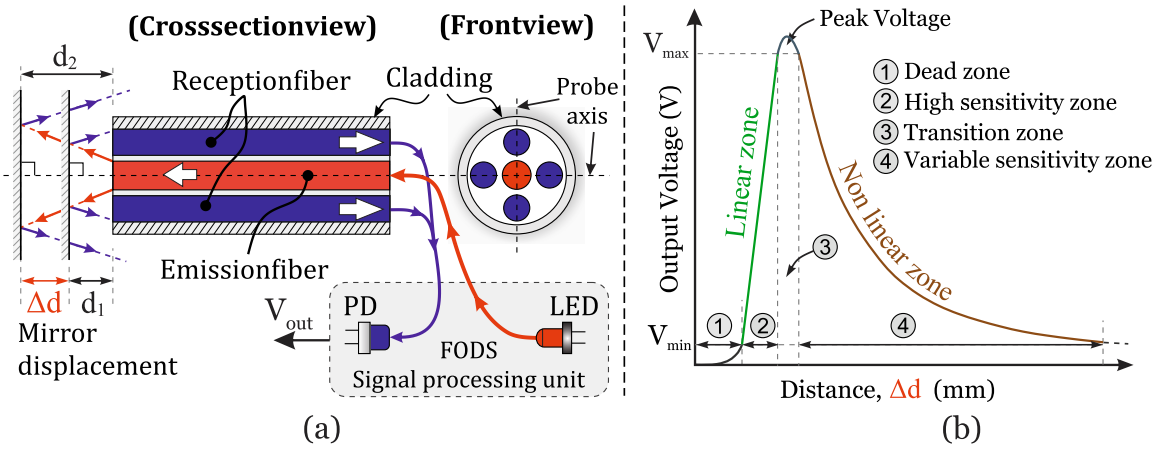


FIGURE 3.4: (a) Working principle of the FODS (b) Typical response curve of the FODS.

distance between the ferrule and the mirror as the amount of light collected by reception fibers increases. This zone exhibits linear response and presents the maximum sensitivity compared to the other zones. Upon further increase in the distance between the mirror and the ferrule, the output voltage goes through a maximum as shown in zone 3, that integrates a peak voltage. This zone is also called transition zone between the linear and non-linear zones. The fourth zone is non-linear zone. This zone is used for long-range displacement measurements. However, in this zone the sensitivity of the FODS decreases with respect to increase in the displacement. For our experiment, we are using zone 4 due to the long range displacement measurement.

3.2.1.2 Calibration of the FODS

The FODS used during the experiment needs to be calibrated in order to obtain the output voltage as function of the position of mobile part. At first, current is injected in the conductors to place the mobile part at the required position. A mirror is fixed on top of the mobile part as shown in Fig. 3.5(a). A calibration process has been undertaken to obtain the FODS response curve. It is obtained by moving the FODS probe relative to the mirror in successive steps using a translation stage (Newport MFA-CC) and by acquiring the output voltage of sensor at each step. Fig. 3.5 (b) shows the obtained calibration curve for the Short-x-stroke configuration.

The calibration is performed in the same direction as in which the mobile part is moving as shown in Fig. 3.5 (a). The non-linear zone (fourth zone) is considered for the stroke

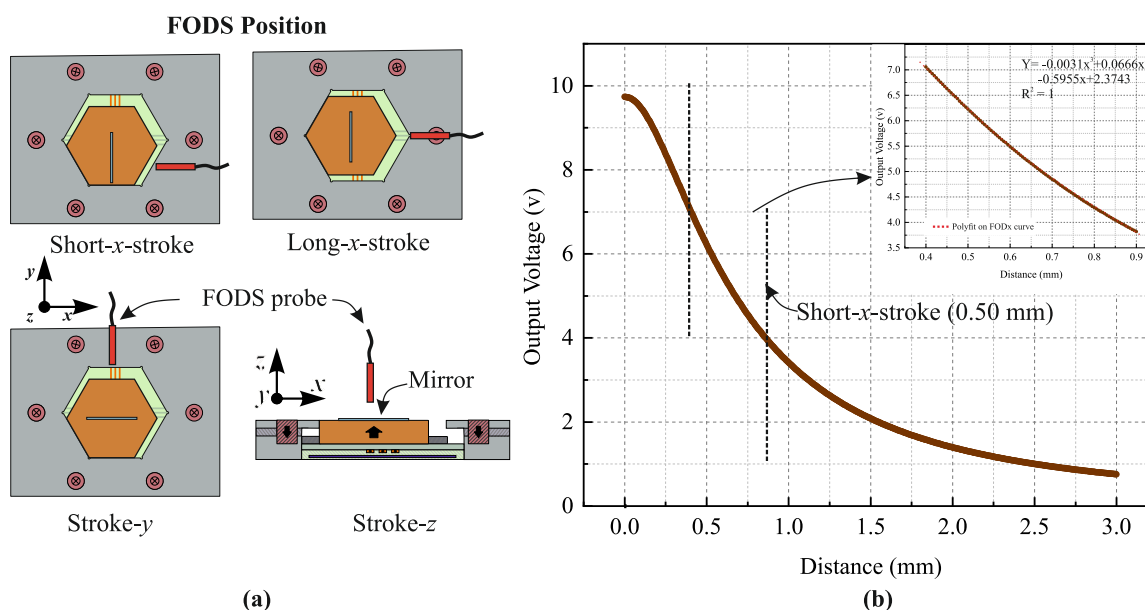


FIGURE 3.5: (a) FODS position with respect to different stroke displacement (b) Pre-calibration response curve for Short-x-stroke .

measurement due to the stroke size between 0.5 mm (short-x-stroke) and 1 mm (Long-x-stroke). From the calibration curve, a least square regression polynomial is determined and its equation is used to calculate the mobile part displacement or position of the mobile part from the recorded voltage values. However, during the displacement measurements, the mirror (fixed on the mobile part) is in motion and the FODS probe is fixed. Different curves are obtained for different displacement strokes due to their position as shown in Fig. 3.5(a).

3.2.2 High-Resolution Camera (HRC) and Image processing

During experiments, another measurement method based on a HRC and image processing has been used. It captures images of the mobile part during its displacement between discrete positions and from the images, the image processing determines the mobile part displacement. The properties of the camera are as given in Table 3.1.

Before doing experiments, the camera has to be calibrated and to do so, a calibration grid has been used [see Fig. 3.6]. The grid represents matrix of dots, where the distance between center of two dots is $125 \mu\text{m}$. With the help of this grid, the pixel size is calculated and it is found to be $0.6935 \mu\text{m}$ for a given position of the camera.

Camera	FLIR ORX-10G-C-51S5C
Resolution	2448 x 2048
Number of pixels	5.0 MP
Frame rate	162 FPS
Sensor reference	Sony IMX250
Sensor type	CMOS
Analog to digital converter	12-bit ADC

TABLE 3.1: Camera Specifications

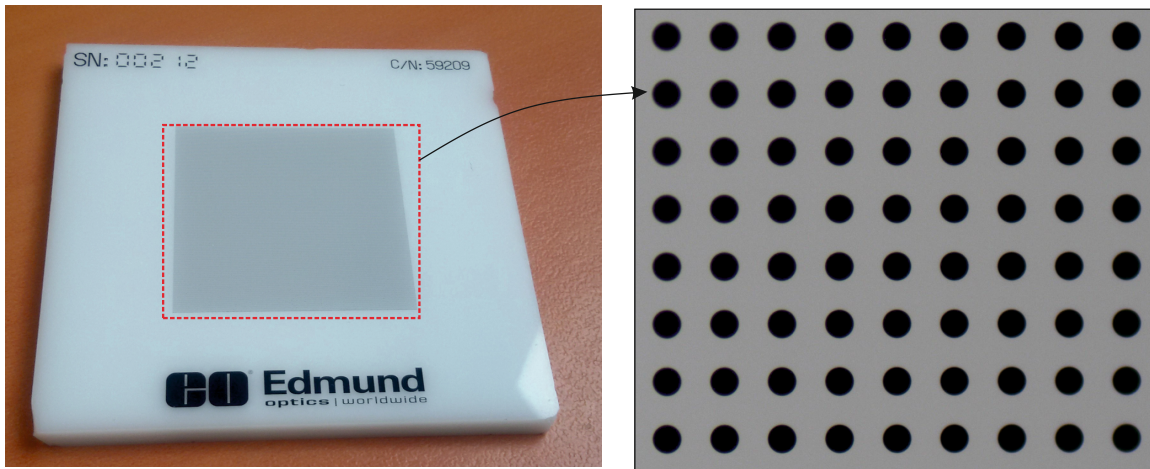


FIGURE 3.6: Calibration Grid by Edmund optics .

During the experiments with the HDA, a sticker which represents a white plus sign on a black background is placed on top of the mobile part (see Fig. 3.7) to measure displacement with the camera. After that, with the help of calibrated pixel size, the mobile part displacement is determined.

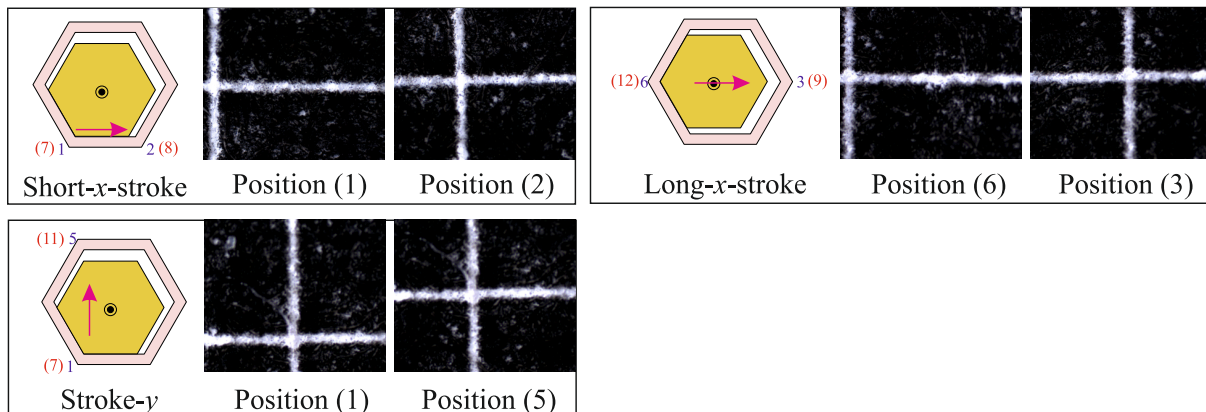


FIGURE 3.7: Initial and final discrete positions for different displacement strokes.

3.2.3 Comparison between measurement techniques

The two measuring techniques discussed above have certain advantages and limitations. The FODS has a high acquisition frequency (500 Hz) compared to HRC (maximum Frame rate of 162 FPS), but only for short range displacement. The HRC can be used for long range displacement upto certain limit. The FODS needs to be calibrated separately for different displacement direction and the orientation of the mobile part during its displacement could highly disturb the FODS results compared to that of HRC. It is also difficult to place the vertical mirror on top of the MPM perpendicular to its surface without any error. Thus, it helps to use the HRC to determine the plate displacement during the conveyance or positioning application and the FODS to measure the stroke sizes of the HDA.

3.3 Assembly and Characterization of the HDA

This section describes the assembly of all the parts of HDA (fixed and mobile part), the control module and the detail characterization of an HDA. A micro-positioning application has also been tested using this prototype.

3.3.1 Experimental setup and control module

The fabricated mobile and fixed parts are assembled together as shown in Fig. 3.8(a) (b). It includes a top view (a) showing the assembly of the MPM and FPMs in their respective cavities. An air-core coil is assembled as shown in side view (b). In order to control the mobile part displacement, a control module has been used and is detailed in Fig. 3.8(c). It consists of a data acquisition board National instruments(NI)-PCIe 7841 module integrated in a computer and controlled using a LabView program. The specifications of the data acquisition board are given in Table 3.2.

Acquisition Board	Analog input/output	Resolution input/output	Max. Sampling rate per channel
NI-PCIe 7841	8 I/O	16 bit	200 kS/s

TABLE 3.2: Acquisition Board Specifications

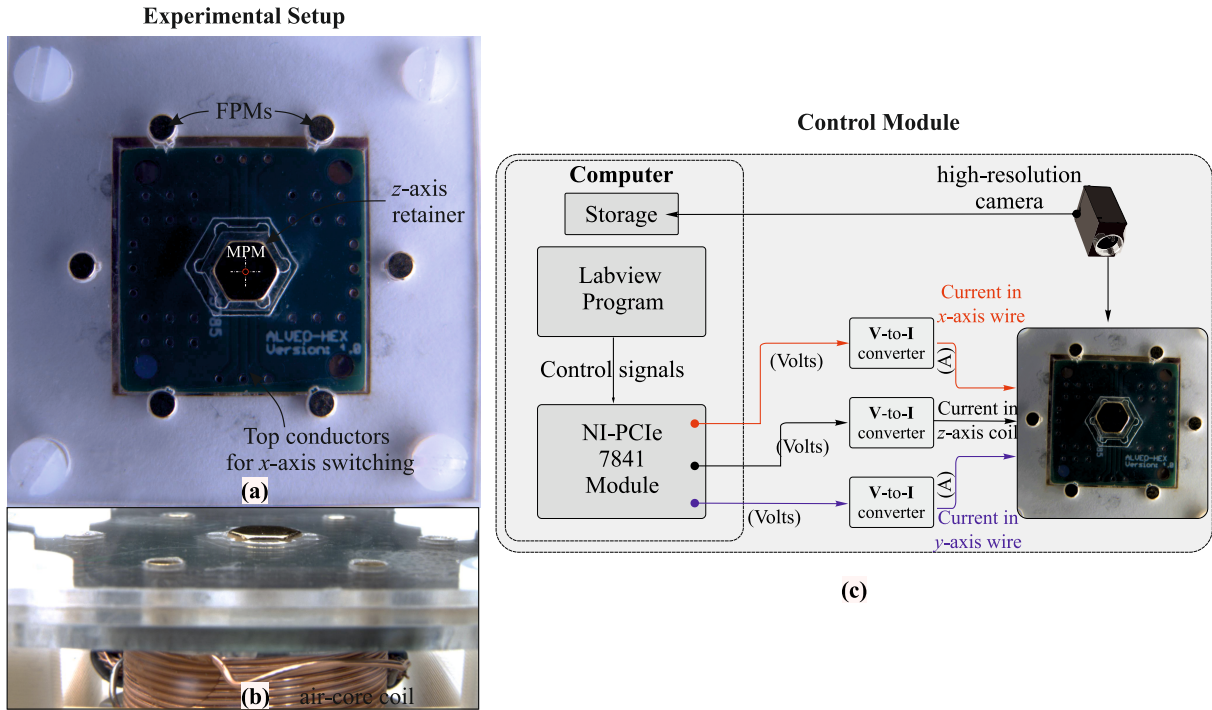


FIGURE 3.8: (a) Experimental setup (b) Control Module of the HDA.

Three analog outputs of data acquisition board are used to generate output voltages. Three different voltage values are generated, which then passes to the three different Voltage-to-current converters (V-I) (linear conversion, 50kHz sampling rate [± 10 V; ± 10 A]). These converters convert these values into respective currents and that are injected into the conductors for switching along xy -axis and in the coil (continuous current) in order to switch along z -axis.

3.3.2 Characterization of the HDA

To experimentally validate the proposed concept, several experiments have been undertaken with the first prototype and are listed below.

3.3.2.1 Displacement in 3D space

At first, the ability of the actuator to switch the mobile part along the three-displacement axes has been experimentally verified. In order to observe the displacement, the HRC has been used. For this experiment, current is injected in the conductors either to switch along x -axis or y -axis switching directions or both to obtain the displacement between discrete positions in xy -plane. In addition, the ability to switch along z -axis has been

proved by injecting current in the z -axis coil. Fig. 3.9 shows firstly the switching of the mobile part in xy -plane from position 1 to 6 and then realization of short- x -stroke from position 7 to 8 at z_2 level. A continuous current of 0.5 A is injected in the coil for z -axis displacement and a pulse of 1.5 A to realize x -axis stroke of 0.5 mm. The mobile part is able to switch at any position in xy -plane on both the levels along z -axis with the help of Tc or Bc.

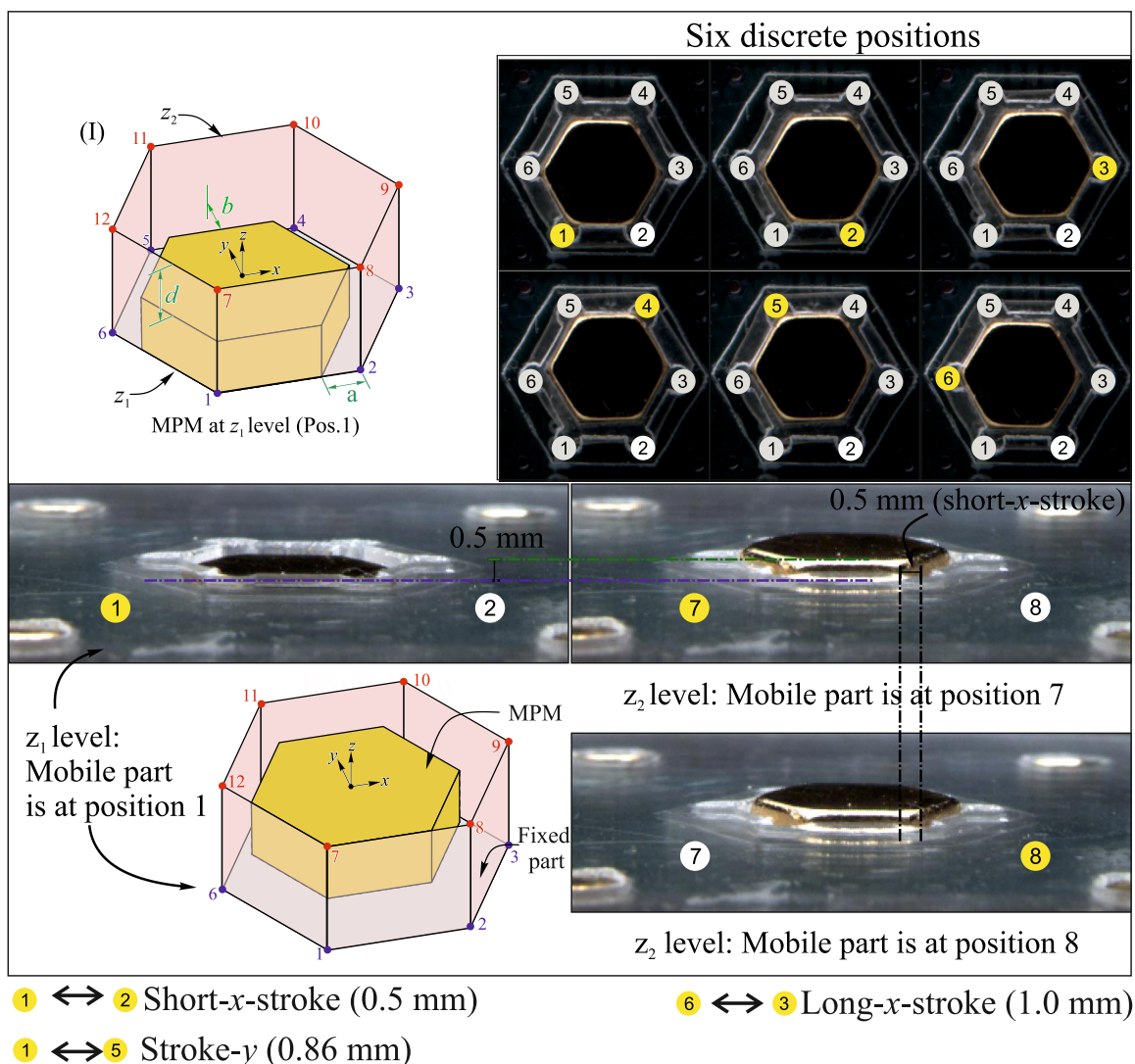


FIGURE 3.9: Representation of twelve discrete positions distributed at two different levels along z -axis.

3.3.2.2 Contactless Stroke measurement

After the validation of the ability to switch along the three displacement axes, the experimental measurement of the different strokes has been carried out. For this initial

prototype, the HRC is used and the experimental strokes have been determined using the image processing technique. For each displacement direction, the strokes were measured 5 times and the standard deviation has been determined [see Table 3.3]. For this prototype, due to the fixed thickness of the PMMA plate (top and bottom plate with 1 mm thickness each), the stroke along z -axis is considered to be 0.5 mm.

TABLE 3.3: Comparison of Experimental and Theoretical strokes.

Displacement directions	Theoretical stroke (mm)	Experimental stroke (mm)	Absolute error (mm)	Relative error
Short- x -stroke	0.500	0.635 ± 0.004	0.135	27%
Long- x -stroke	1.000	1.216 ± 0.003	0.216	21.6%
Stroke- y	0.8660	1.072 ± 0.006	0.212	24.65%
Stroke- z	0.500	0.545 ± 0.002	0.045	9%

The absolute and relative error on the stroke size are indicated in Table 3.3. A huge difference is observed between the theoretical and experimental stroke sizes due to the manufacturing tolerances in laser cutting technique and also due to the tolerances in the fabrication of the MPM. However, in a digital actuator, the stroke is not the only important characteristics, the position repeatability is also important. As this is the first prototype, the objective is to validate the architecture and its parameters like position repeatability, stroke size are characterized in the second version of actuator.

3.3.2.3 Driving pulse duration

As the switching along xy -plane is obtained with the help of current in the form of pulses (detail explanation in section 2.1.1.1), the minimum driving pulse duration required to obtain a proper switch between two discrete position has been experimentally measured for different driving current values [see Fig. 3.10 (a)]. The determination of pulse duration for each driving current values ensures smooth switching of the mobile part between discrete positions and it also helps to minimize the backlash effect. It also economize the energy consumption. In order to measure it, the mobile part has been displaced with a particular driving current value and the minimum required pulse duration has been experimentally determined for each particular driving current ranging from

1.5 A to 7 A and for three different strokes: Short-x-stroke, Stroke-y and Long-x-stroke. It can be observed that, the pulse duration reduces when the driving current increases for all the three strokes. The average pulse duration for Long-x-stroke is observed to be 8.8% higher to that Short-x-stroke as the stroke size is double to that of Short-x. However, Stroke-y, requires higher pulse duration, the average increase is 26.6% compared to Short-x-stroke. This is due to the use of Bc for y-axis switching as shown in Fig. 2.1. The use of Bc generates less electromagnetic force for the same current value compared to Tc. Apart from that, there is also an influence of the stroke value, which is higher (0.86 mm) for stroke-y compared to short-x-stroke (0.5 mm).

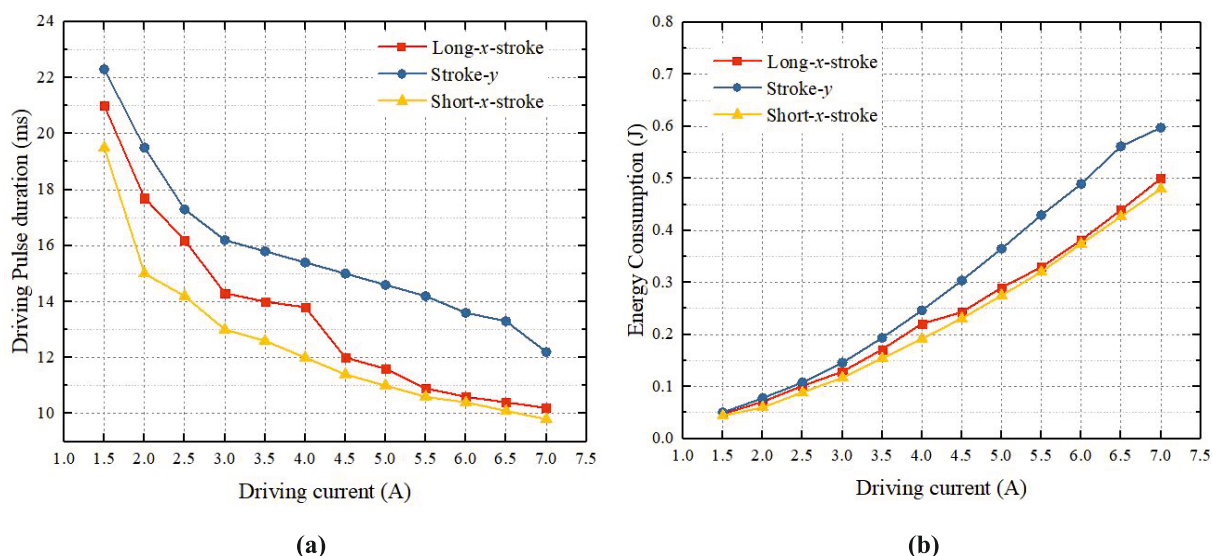


FIGURE 3.10: (a) Representation of minimum pulse duration required for switching with respect to driving current. (b) Representation of energy consumption for three different strokes with respect to driving current.

3.3.2.4 Energy consumption

After the experimental determination of optimal pulse duration to ensure proper switch, the energy consumption to switch the MPM between the discrete positions has been studied. In order to calculate it, the pulse duration, the measured voltage and the driving current values have been taken into account and Eq. 3.1 has been used.

$$E = U \times I \times t \quad (3.1)$$

where, E is the energy consumed, U the measured voltage, I the current and t is the pulse duration. This expression involves the values of the voltage and current generated by the convertors. These values have been experimentally measured using a multimeter. The pulse duration is obtained from above results and the energy consumption has been determined by considering the minimum pulse duration value. Fig. 3.10 (b) represents the energy consumption for the three different strokes as function of the driving current value. It can be observed that the energy consumption increases when the driving current increases. Moreover, due to the difference between the generated electromagnetic force for the two displacement axis, the energy consumption is more important to switch along y -axis than along x -axis.

3.3.3 Micro-positioning application using the elementary HDA

The elementary HDA has been tested for micro-positioning application. The idea behind this experiment was to validate the ability to realize a displacement task using an elementary HDA.

3.3.3.1 Positioning with Guide

The first test has been conducted with the help of a mechanical guide to control the trajectory of the conveyance plate and limit the straightness error as shown in Fig. 3.11 (a). In the first test, only the stick-slip approach (described in section 2.1.3) has been undertaken to validate the proposed idea.

In order to observe the plate displacement, the HRC has been used. Images of the plate displacement in xy -plane have been captured in order to determine the distance travelled by plate with respect to each sequence [see Fig. 3.11 (c)]. During this test, the driving currents used during the stick and slip phases are 2 A and 6 A, respectively. In Fig. 3.11 (c), the initial and final plate position for the first two sequences for Short- x -stroke, Long- x -stroke and Stroke- y are shown. Due to the stick-slip approach, there is also backlash effect which occurs when the mobile part is going back to its initial position to realize next sequence. This backlash effect is also observed but not shown in figure. Thus, this experiment helps to validate the conveyance using single actuator.

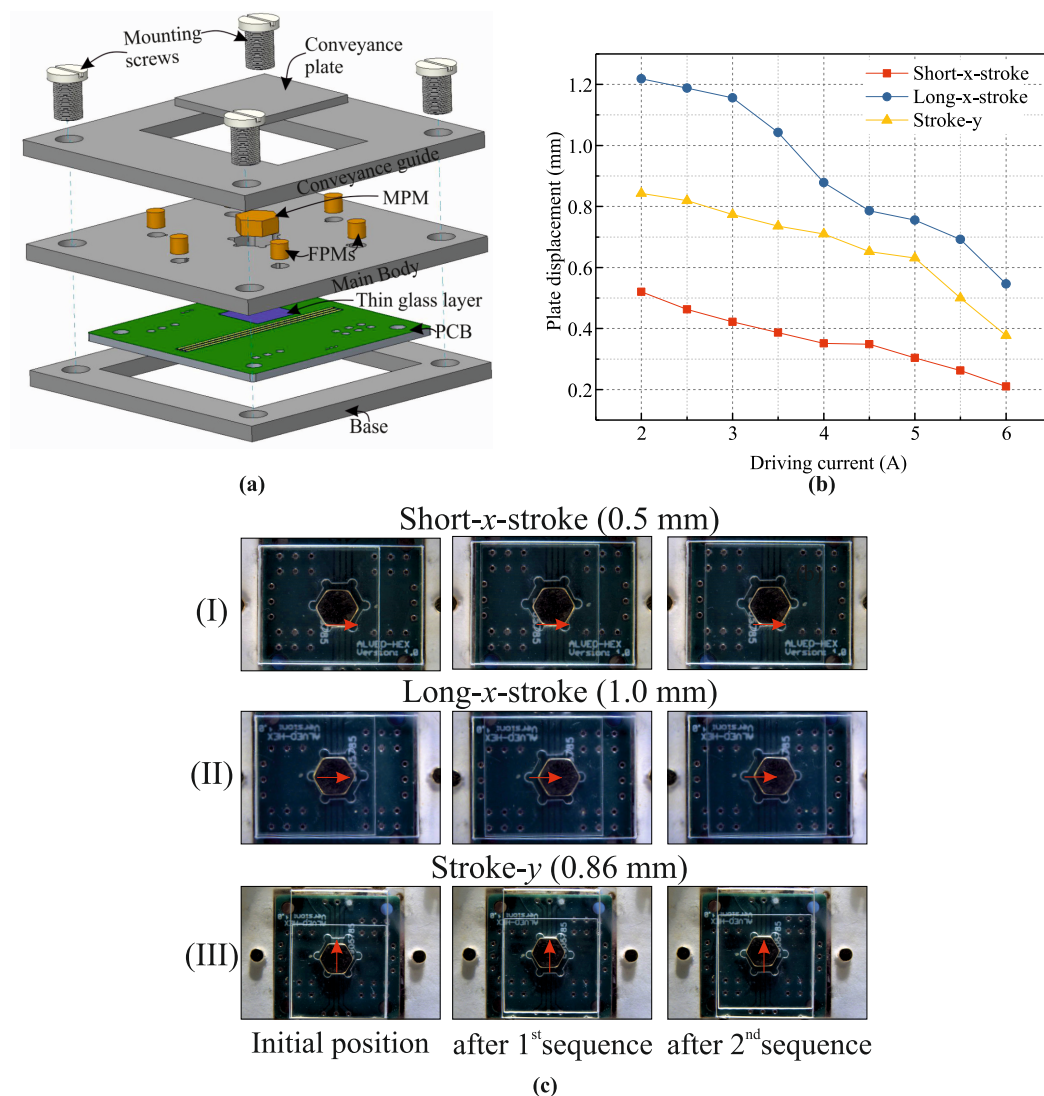


FIGURE 3.11: (a) An exploded view for the elementary micro-positioning device (b) Representation of the effect current values on the plate displacement. (c) Representation of the plate conveyance for the first two sequences for three major displacement strokes.

Experimentally, the effect of the driving current values on the plate displacement has been studied and is presented in Fig.3.11 (b). The experiment has been realized for the three different strokes and considering a current range from 2 A to 6 A. It has been observed that the plate displacement is reduced when the driving current is increased. Indeed with a high driving current, there is an increase in the MPM acceleration compared to the low current value, which generates a high sliding between the MPM and the plate. An increase in sliding between the MPM and the plate will help the MPM to return to its original position (slip phase) with minimum backlash effect [see Fig.3.11 (b)]. Thus, to realize the stick phase, low driving current must be used and on a contrary, high current

help to realize optimal slip phase as shown.

Furthermore, several sequences have been studied and the plate displacement with respect to the number of sequences in shown in Fig. 3.12 (a),(b),(c). The experiments have been carried out for the three displacement strokes. A driving current of 2 A is used for the stick phase and 6 A for the slip phase. For each sequence, the plate displacement is plotted as well as the backlash effect. Five sequences have been realized for each displacement stroke. It has been observed that, the plate displacement values for all three

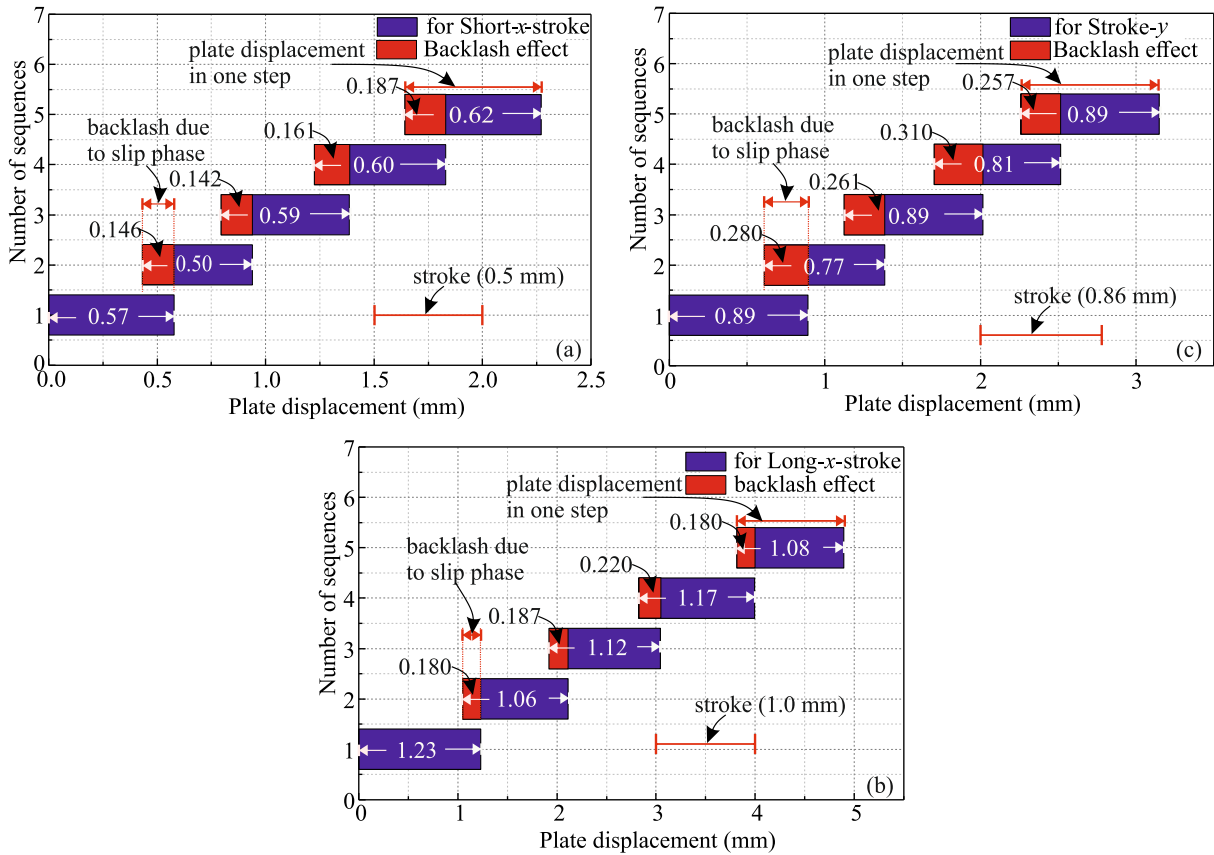


FIGURE 3.12: Representation of a plate displacement with respect to the number of sequences (a) Short-x-stroke with 0.5 mm stroke (b) Long-x-stroke with 1.0 mm stroke (c) Stroke-y with 0.86 mm stroke.

strokes, Short-x-stroke, Long-x-stroke and Stroke-y are 0.58 ± 0.04 mm, 1.13 ± 0.06 mm and 0.85 ± 0.05 mm, respectively. The average plate displacement is higher than the theoretical MPM stroke value, this is due to the experimental strokes values which are different than the theoretical ones as shown in Table 3.3 and also due to the sliding between the MPM and plate. During the stick phase, the MPM switches from a discrete position to another one and this switch generates the displacement of the conveyed part

by friction. However, when the MPM reaches the final position, the conveyed object continues to move until it stops due to friction.

The backlash effect of the conveyed part for all the three displacement strokes is also clearly visible. For the same current value (6 A), a noticeable backlash of 0.27 mm for Stroke-y is obtained which is more than that of Short-x-stroke (0.15 mm) and Long-x-stroke (0.19 mm). This is due to the use of Bc for y-axis switching and Tc for x-axis. The air-gap between Bc and the mobile part is more compared to that between Tc and the mobile part. This generates lower electromagnetic force, which thereby increases the backlash effect.

3.3.3.2 Positioning without Guide

The HDA with guide helps to validate the positioning application using stick-slip approach. Another approach that is the Lift-mode has also been tested using 3D displacement actuator. For this prototype, the guide is also removed from the device and the prototype is shown in Fig. 3.13. Experiments have been performed using the Short-x-stroke to validate the Lift-mode approach.

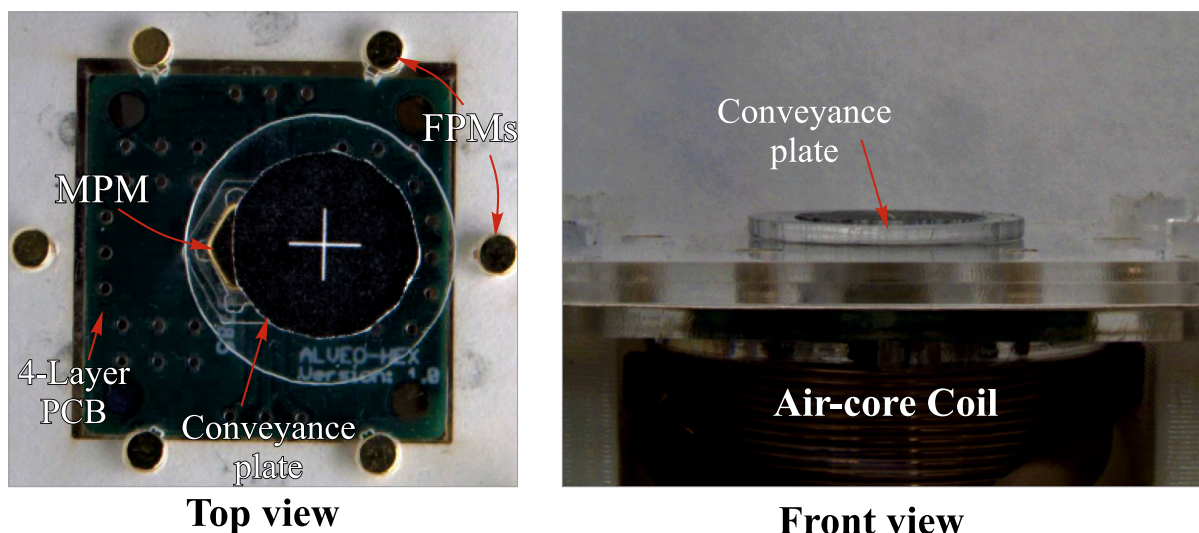


FIGURE 3.13: Experimental representation of the micro-positioning device.

The experimental plate displacement for Short-x-stroke is represented taking into account both the approaches, Lift-mode and Stick-slip [see Fig. 3.14]. Images of the initial plate position, after 1st sequence, after the backlash and after the 2nd sequence are shown.

It can be observed that, for the same current value (2 A), the plate displacement in the first sequence is slightly more for Stick-slip compared to Lift-mode approach. This can be justified due to the increase in airgap between the PCB and bottom surface of the mobile part in Lift-mode approach (at z_2 level) compared to Stick-slip. However, in order to realize a long range conveyance, the mobile part must return to its initial position, which therein generates a backlash effect in Stick-slip approach. This effect is not observed in Lift-mode due to the detachment of a mobile part from the conveyance plate (use of z_1 level to detach the plate and come back to its initial position).

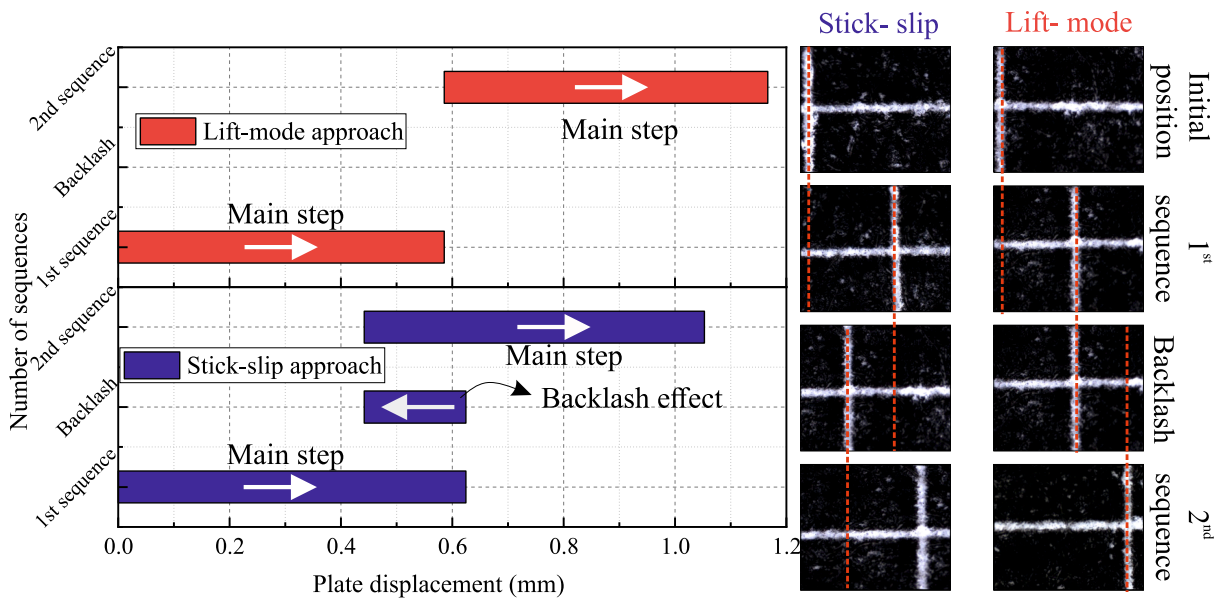


FIGURE 3.14: Experimental representation of the Stick-slip and Lift-mode approaches for Short-x-stroke.

As the positioning application using an elementary actuator is observed, after a given number of sequences, the conveyance plate goes out of limit due to plate dimension ($\phi 15 \times 1$ mm) and it becomes impossible to move it back on the top of mobile part without human intervention. To determine the maximum possible sequences, experiment has been performed (see Fig. 3.15). This limit is different along the different displacement directions. Here, two directions are considered (Short-x-stroke and Stroke-y) for a driving current value of 2 A. Initially, the plate is placed exactly at the center of the MPM. It has been observed that, for short-x-stroke, initially there is a noticeable difference for the plate displacement between the stick-slip and lift-mode approach. This is mainly due to the backlash as discussed in stick-slip approach section. However, when the number of

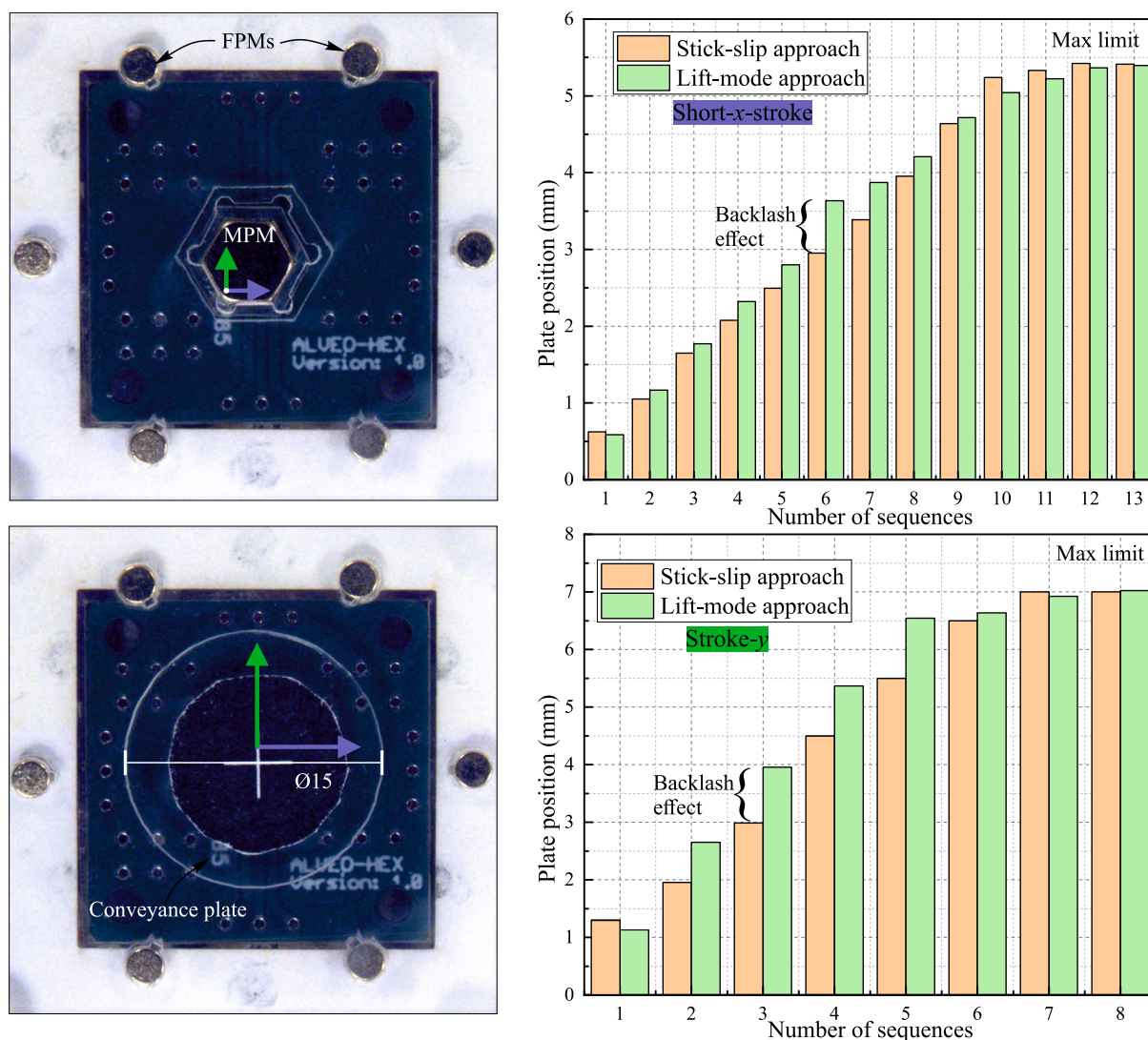
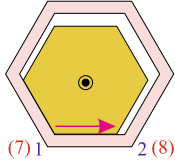
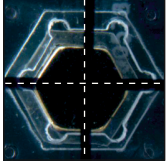
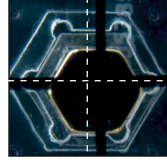
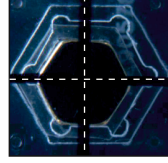
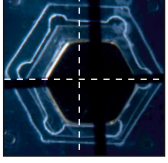
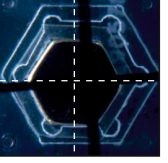
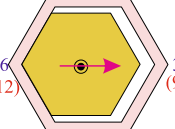
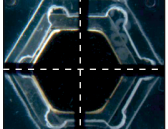

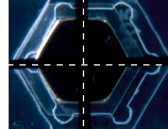
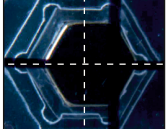
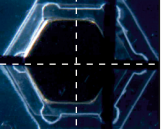
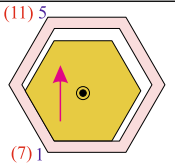
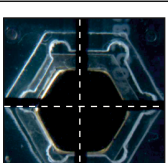
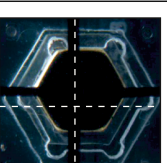
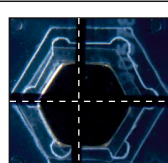
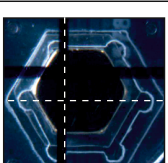
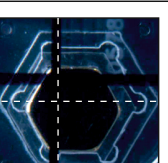


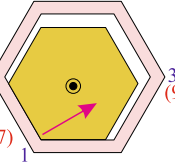
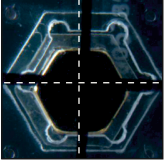
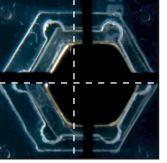
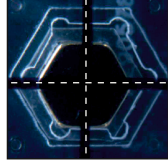
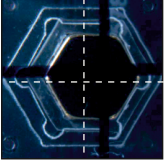
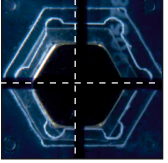
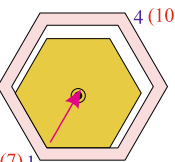
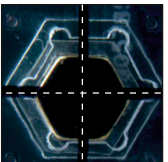
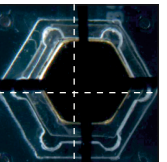
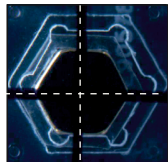
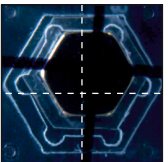
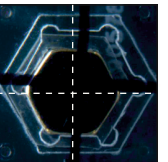
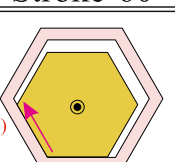
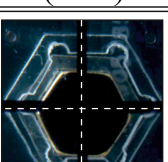
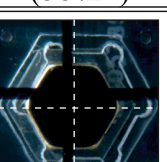
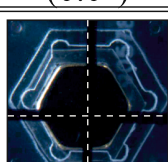
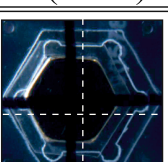
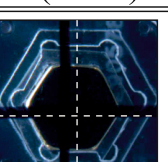
FIGURE 3.15: Maximum possible sequences for Short-x-stroke and Stroke-y with Stick-slip and Lift-mode approaches before plate goes out of limit.

sequences increases, there is reduction in backlash effect as less plate surface is in contact with the magnet and at certain point the plate displacement stabilizes thus, it reaches the maximum limit of conveyance. Similar effect has also been observed for stroke-y but with less number of sequences due to the different stroke sizes (0.5 mm for short-x-stroke and 0.86 mm for stroke-y). Thus, the optimal positioning range is determined which is ± 5.40 mm along short-x-stroke and ± 7.05 mm along y-stroke.

In order to clearly show the ability to realize positioning of the plate in all the directions provided by hexagonal architecture, images of the plate displacement were captured for the two different approaches and are presented in Fig. 3.16. To understand the position of mobile part while switching, an enhanced view is presented. A circular plate with

	Lift-mode		Stick-Slip		
	Initial	1 st sequence	Initial	1 st sequence	Comeback
 Short-x-stroke					
	(0.00,0.00)	(0.61,0.00)	(0.00,0.00)	(0.64,0.23)	(0.44,0.31)
 Long-x-stroke					
	(0.00,0.00)	(1.22,0.12)	(0.00,0.00)	(1.56,0.00)	(1.35,0.05)
 Stroke-y					
	(0.00,0.00)	(0.07,1.07)	(0.00,0.00)	(0.08,1.39)	(0.12,1.28)

(a)

	Lift-mode		Stick-Slip		
	Initial	1 st sequence	Initial	1 st sequence	Comeback
 Stroke-30°					
	(0.0°)	(30.5°)	(0.0°)	(29.6°)	(27.7°)
 Stroke-60°					
	(0.0°)	(55.2°)	(0.0°)	(62.7°)	(51.9°)
 Stroke-120°					
	(0.0°)	(121.8°)	(0.0°)	(128.9°)	(135.1°)

(b)

FIGURE 3.16: Conveyance possibilities to all discrete positions with the help of Lift-mode and Stick-slip approaches (a) representation of experimental stroke values for planar displacement (b) representation of angles obtained for angular displacement.

the same dimensions but with a printed plus sign is used. As there is no backlash effect in the Lift-Mode, only the first sequence and the initial position are presented. The mobile

part and the plate displacement along different directions can be clearly visible. It has been observed that, for the stick-slip approach, there is major influence of sliding effect on the conveyance plate after the mobile part reaches discrete position. A rotation effect is also observed in stick-slip approach as during switching along x -axis, there is a slight displacement along y -axis as shown. This can be overcome with the help of an array of digital actuators as the array will increase number of contact points between the plate and the mobile part.

The influence of conveyed mass has also been studied [see Fig. 3.17]. An experiment has been carried out where the conveyed mass has been increased by adding a thin piece of glasses each weighing 0.015 g and the displacement has been measured. In this test, the plate displacement has been realized with the help of Short- x -stroke for the two approaches. The influence of the conveyed mass on the plate displacement has been mea-

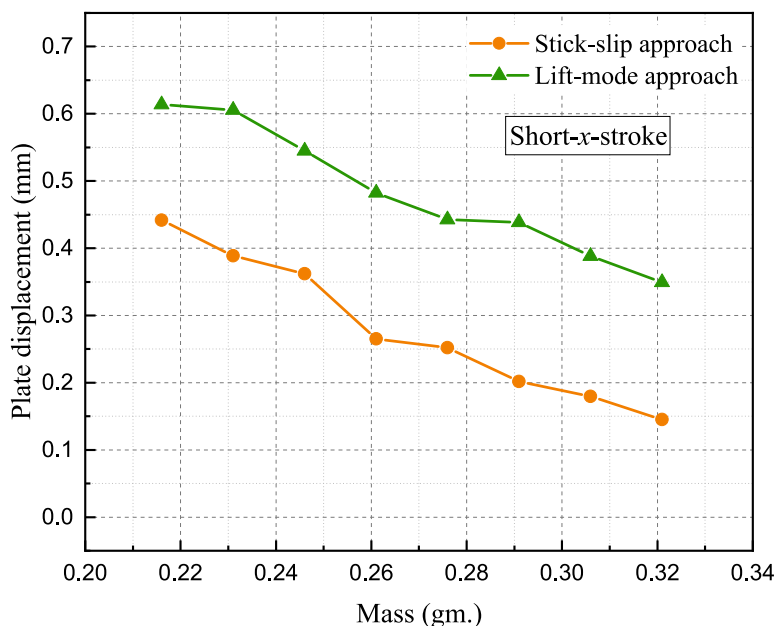


FIGURE 3.17: Graphical representation of the variation in plate displacement with respect to the mass of plate for both approaches.

sured. For that, a driving current pulse of 2 A is used to switch along x -axis for both the approaches, and a continuous current of 0.5 A is used in order to switch along z -axis for the Lift-mode approach. The reduction in plate displacement is clearly observed with an increase of the mass. The maximum mass displaced by the mobile part with a current of 2 A is also measured, which is found to be 1.15 g. In the graph, the results are only

shown till 0.32 g as it was difficult to stack thin pieces of glasses on top of each other. To determine maximum displaced mass, another plate with defined weight has been used.

The characterisation of the HDA and its application as a micro-positioning device has been presented and validates the proposed concept. However, it has been observed that the manufacturing process have major influence on the difference in the experimental and theoretical stroke values. To overcome this difference a silicon micro-fabrication technique has been adapted to manufacture the fixed parts. The detail about the micro-fabrication process and final prototype for the elementary HDA is described in the following section.

3.4 Micro-fabricated Hexagonal 3D Digital Actuator

This section explains the micro-fabrication technique used, It has been selected as other conventional machining techniques are not able to reach the required precision due to the manufacturing constraints.

Micro-fabrication technique originated from the micro-electronics industry and it is widely used in semiconductor processing, microelectronic fabrication, integrated circuit technology, etc.,[Khan 14]. It mainly uses silicon material for fabrication. It is basically a collection of different technologies used in making micro-devices such as lithography, etching, polishing,... The micro-fabrication process includes several steps such as depositing a photoresist film, patterning of it with desired micro features, removing (etching) portions of the film. These processes requires dust free environment known as "clean rooms", to avoid any contamination during fabrication. In order to meet these standards, the microfabrication of our proposed actuator design has been carried out in collaboration with ESIEE Paris.

For our actuator design, we used a silicon wafer. Micro-machining of silicon usually includes chemical process also known as "etching" of the unprotected parts. The silicon wafer is structured with protected parts known as "etch mask and unprotected parts from where the silicon material is removed from the substrate as shown in Fig. 3.18. Etching of silicon material can be possible with wet or dry etching process. Among the available

etching methods, the "Deep reactive ion etching (DRIE)" is used for the fabrication of plates. It has been chosen, as it enables the fabrication of deeper and narrower structures with a higher etch rate [Sain 09] and it is also an anisotropic etching process, which avoids the undercut produced during isotropic etching as shown in Fig. 3.18 (b),(c).

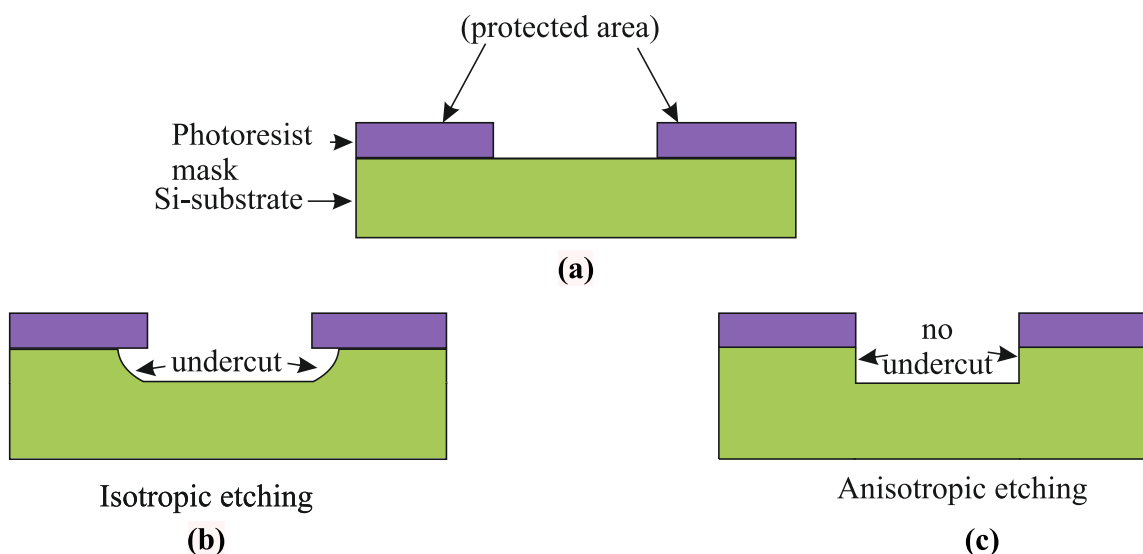


FIGURE 3.18: (a) Silicon substrate with Mask. (a) Isotropic etching. (c) Anisotropic etching.

3.4.1 Fabrication of Top and Second plate

The mechanical parts that define the actuator strokes are micro-fabricated which includes fabrication of top and second plate. They are fabricated in order to obtain micro-metric tolerances in the stroke sizes and also to have straight edges. The step-by-step process is shown in Fig 3.19. This process includes six steps and it has been applied on both the plates. Initially, the silicon wafer (dimensions: $\phi 100 \times 0.90$ mm) is cleaned and spin coated with photoresist (AZ4562) on top of it (see step 2.). In step 3, the photolithography mask is used to expose the photoresist layer to Ultra violet (UV) light for 8 s. After the exposure, the wafer was developed in a developer solution as shown in step 4. In step 5, the silicon wafer is etched in Inductively Coupled Plasma (ICP) etching machine. During this process, the remaining photoresist acts as a etching mask and the plasma in the ICP machine reacts with the unprotected silicon layer. The silicon layer was etched until the structure was through etched. Upon finishing, the photoresist from the protected silicon layer is removed using acetone and ethanol solution and later the wafer is rinsed with

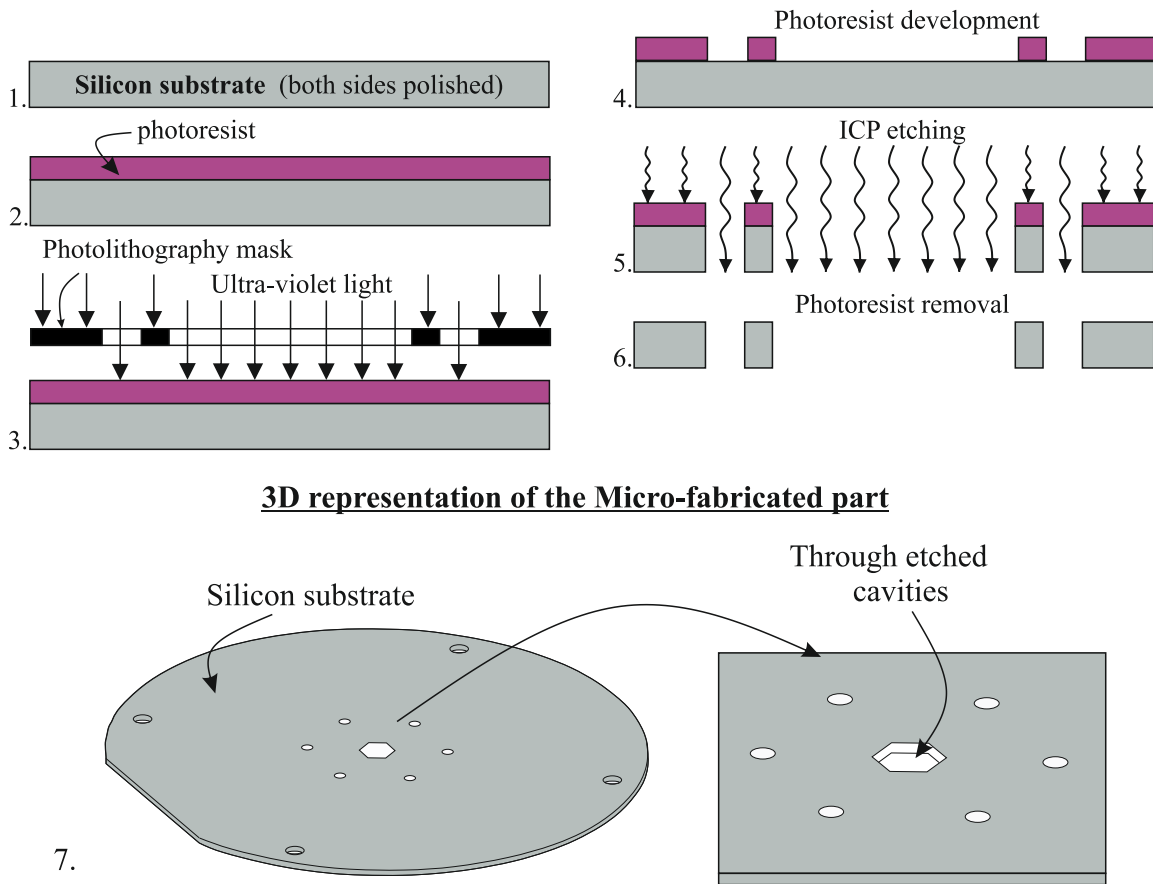


FIGURE 3.19: Step-wise description of the micro-fabrication process and 3D representation of the final fabricated part.

di-ionized water and dried out. An isometric view of the obtained wafer is shown in Fig. 3.19(7). It represents the final shape of the micro-fabricated plate.

Fig. 3.20 represents the microscopic view of the hexagonal cavity fabricated using silicon micro-fabrication technique for Top plate. It also shows a CAD view of the mask used for the photolithography process. It can be observed that, compared to the laser cutting technique, the micro-fabrication helps to obtain more precise hexagonal cavity with non visible deformation and waviness on the edges as shown. The measured dimensions for the hexagonal cavity have on an average error of $9 \mu\text{m}$ with the theoretical ones.

Thus, the objective of obtaining precise hexagonal cavity is completed. However, it is necessary to verify the stroke size obtained for the three displacement strokes. It is determined in the next section.

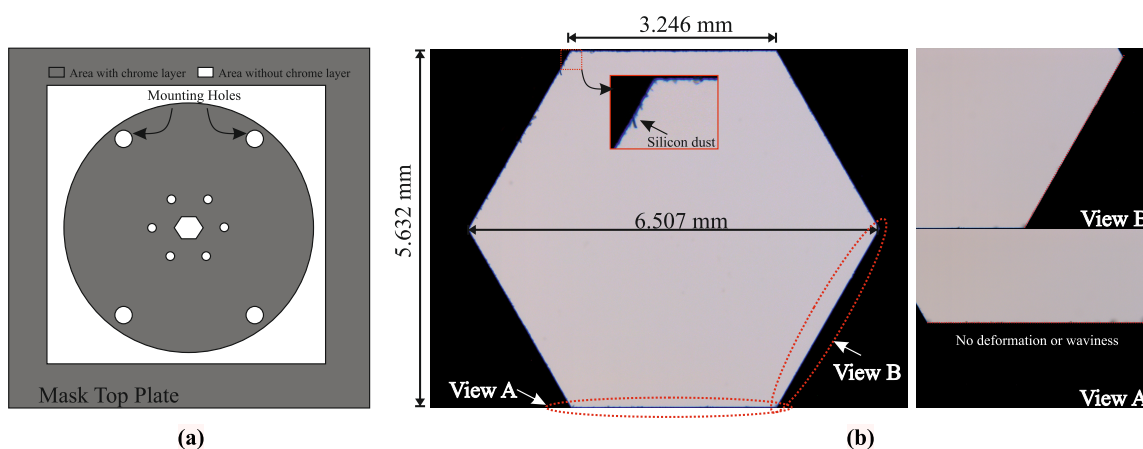


FIGURE 3.20: (A) CAD design of the photolithography mask (b) Micro-scope view of the hexagonal cavity for Top Plate.

3.4.2 Experimental characterization of the micro-fabricated HDA

After the fabrication of fixed parts using silicon micro-fabrication technique, the actuator has been assembled as shown in Fig. 3.21. The objective is to obtain precision in the stroke sizes and also to compare it with the previous obtained results. To determine that, a FODS has been used for the stroke measurement due to its precise measurement ability compared to HRC. For the measurements with the FODS, a vertical mirror is fixed on top of the mobile part as shown in Fig. 3.21. A calibration process has been performed

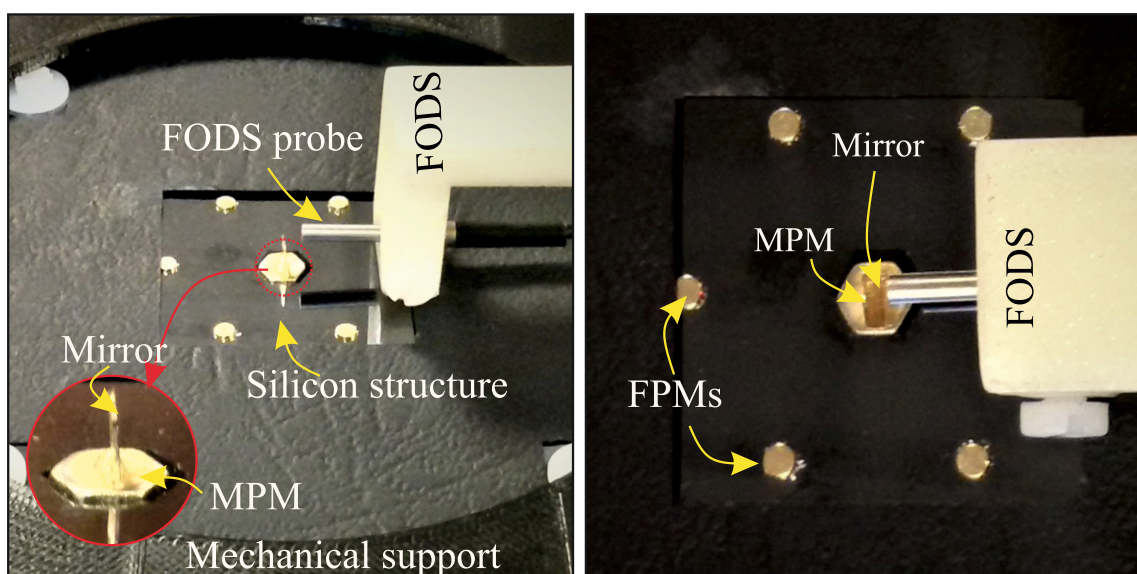


FIGURE 3.21: Experimental setup for a micro-fabricated HDA with FODS contactless measurement system.

separately for each displacement axes which results in a resolution limit of less than

0.1 μm and an acquisition frequency of 500 Hz. Firstly, the experimental displacement is observed and various phenomenon are discussed to characterize the HDA. Later the position repeatability and stroke dimensions for Short- x -stroke, Long- x -stroke, Stroke- y and Stroke- z are experimentally measured as shown in following section.

3.4.2.1 Experimental Displacement

The Fig. 3.22 represents the experimental mobile part displacement for the three displacement axes. A driving current of 2 A and holding current of 1.5 A are used for the displacement along Short- x -stroke and Stroke- y at z_1 level. No holding current is required for the displacement along Long- x -stroke. The theoretical values are marked on the graph using dotted lines. It has been observed that, for the same driving current value, the time required to switch along Short- x -stroke (13 ms) is less compared to Long- x -stroke (29 ms) and Stroke- y (25 ms). This is due to the different stroke size (0.5 mm for Short- x -stroke and 0.86 mm and 1.00 mm for Stroke- y and Long- x -stroke, respectively). The Short- x -stroke switching represents less oscillations due to the presence of lateral support during

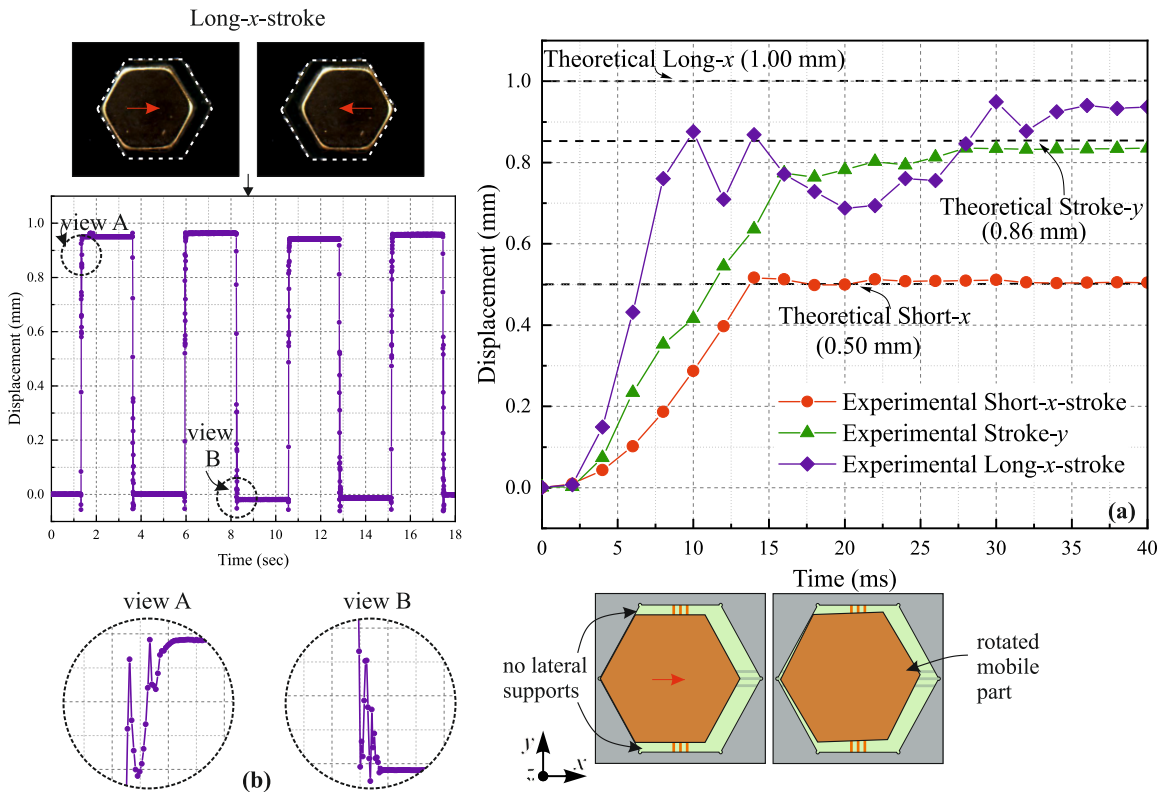


FIGURE 3.22: (a) Experimental Mobile part displacement for three different strokes. (b) oscillations on the displacement curve for Long- x -stroke.

overall displacement compared to Long- x -stroke and Stroke- y . However, oscillations on the displacement curve can be observed on Long- x -stroke and stroke- y , as both the displacement direction do not have any lateral support during the mobile part switching. For the displacement along y -axis (stroke- y), the oscillations are rather controlled due to the use of holding current in the top conductors. The holding current helps to switch the mobile part at the desired position, absence of the holding force will make it impossible to arrive at the required position. However, for a Long- x -stroke, the use of holding current is impossible. To clearly visualize the oscillations, the experiment are repeated several times for Long- x -stroke and are presented in Fig. 3.22 (b).

The errors are shown in view A and view B. The errors can be due to the oscillations as visible before the mobile part reaches its discrete position and are due to the absence of lateral support. Moreover, the oscillations can be also due to the rebound effect which occurs due to the contact between the lateral support of hexagonal casing and the MPM or it can be due to the rotation of mobile part. It disturbs the orientation of MPM which therein affects the amount of light collected by the sensor and represents it by variation in the displacement. Both the displacement errors are clearly visualised in figure above.

3.4.2.2 Position repeatability & Stroke measurement

The position repeatability of the MPM has been measured in order to characterize the digital behavior of the HDA. It has been measured using the FODS and with a driving current of 2 A for Short- x -stroke, Long- x -stroke and Stroke- y . For Stroke- z , a 0.5 A driving current has been used. The stroke along z -axis is 0.4 mm rather than 0.5 mm (PMMA version) due to the dimensional constraints (thickness of z -axis retainer = 0.5 mm; thickness of silicon wafer = 0.90 mm). For all the displacement axes, the experiment has been repeated 50 times and the results are presented in Fig. 3.23. The average stroke value is mentioned for respective axes. It can be observed that, there is difference between the measured and theoretical strokes. The observed strokes errors along x - and y -axis are: 0.59% for Short- x -stroke, 3.13% for Stroke- y and 8.50% for Long- x -stroke. This difference is mainly due to the manufacturing tolerances for the MPM. The MPM

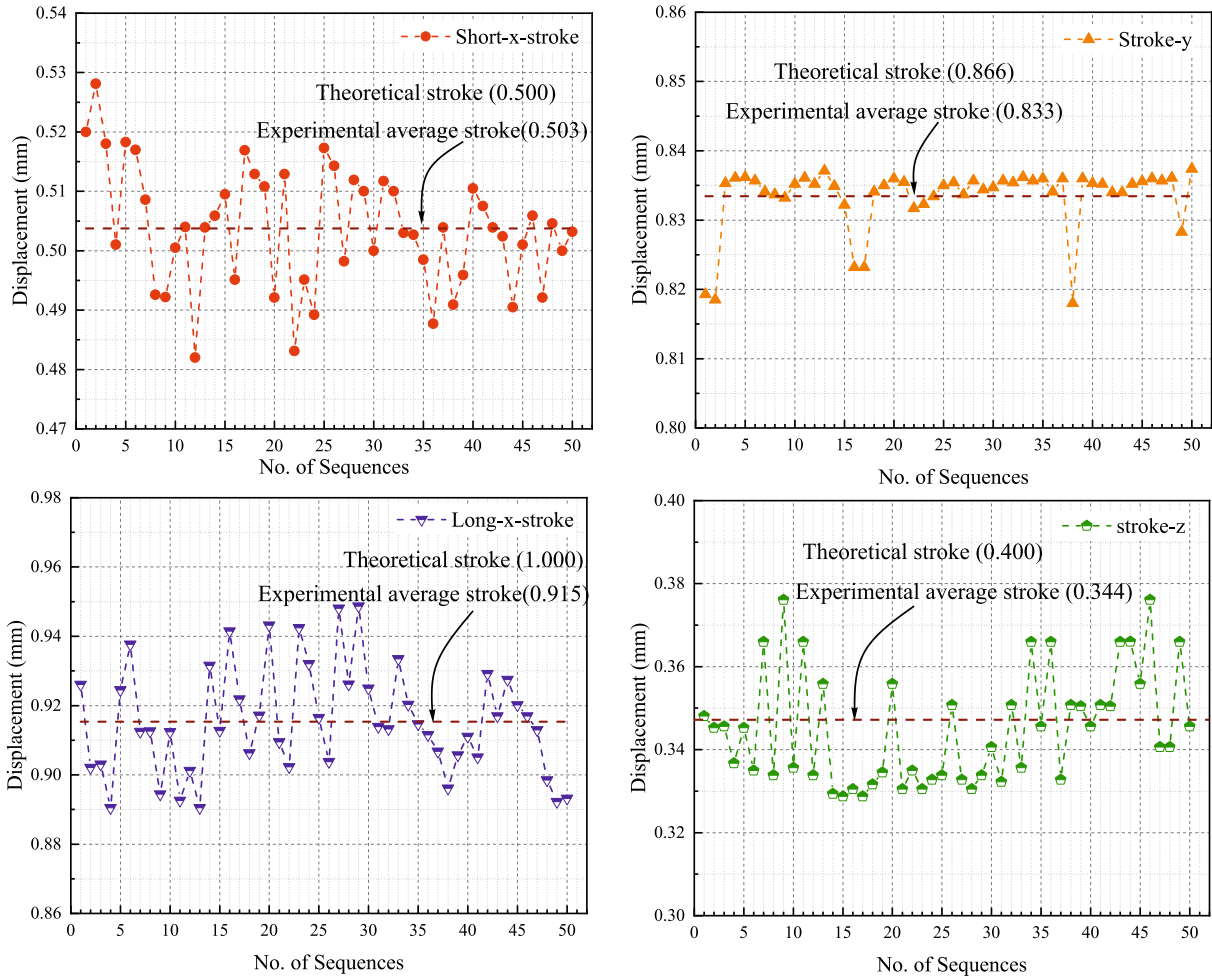


FIGURE 3.23: Graphical representation of the position repeatability for the different displacement strokes.

is manufactured from HKCM, a German based company and the tolerances are set according to ISO 2768-1m standards. It represents the length/width tolerance of ± 0.1 mm, edge roundings of ± 0.2 mm and angle tolerance of $\pm 0.1^\circ$. However, along z -axis, a major difference of 14% has been observed between the measured and theoretical stroke values. As the z -axis retainer is manufactured using laser cutting technique, the deformation of PMMA due to the laser cutting, the manufacturing errors and the tolerances in the PMMA thickness causes the stroke difference. These errors could be reduced by using micro-fabrication techniques for the z -axis retainer and that represents a perspective for this work. For the four strokes, the positioning repeatability errors are between $5\mu\text{m}$ and $16\mu\text{m}$. These repeatability errors represents 2.0% (Short- x -stroke), 1.8% (Long- x -stroke), 0.6% (Stroke- y) and 9.4% (Stroke- z) of the stroke values.

The Table 3.4 gives a comparison between theoretical and experimental stroke values

for the different displacement strokes for PMMA and silicon micro-fabricated versions. Based on the results presented in Fig. 3.23, the standard deviation for the stroke values for micro-fabricated version is calculated for the 50 sequences. Whereas, the influence of the z -axis retainer affects the repeatability along z -axis.

TABLE 3.4: Comparison of Experimental and Theoretical strokes.

Displacement directions	Theoretical stroke (mm)	PMMA		Silicon	
		Experimental stroke (mm)	E_R	Experimental stroke (mm)	E_R
Short- x -stroke	0.500	0.635	27.0%	0.503 ± 0.010	0.6%
Long- x -stroke	1.000	1.216	21.6%	0.915 ± 0.016	8.5%
Stroke- y	0.8660	1.072	24.6%	0.833 ± 0.005	3.13%
Stroke- z	0.500(PMMA) 0.400(Silicon)	0.545 -	9% -	- 0.344 ± 0.014	- 14%

(E_R) Relative error

A huge difference is observed between the obtained strokes using both the fabrication techniques. The maximum error obtained using micro-fabrication version is 8.5% whereas, using laser cutting technique it is 27%. Apart from that, a 14% relative error is obtained for a stroke along z -axis, as the retainer is fabricated using rapid-prototyping technique. The deformation and wavyness formed due to the use of this fabrication technique defines the error. On comparing both the fabrication techniques, it is decided to use the micro-fabricated version for further experimentations and testing as a conveyance device.

3.5 Conclusion

In this chapter, two experimental prototypes of a single HDA have been presented and various experiments have been carried out to validate and characterize the proposed designs. Initially, the components have been described which includes the mobile part and the fixed part of the actuator. For the mobile part, the retainer is fabricated using laser cutting technique however, for the fixed parts two different manufacturing techniques: the rapid-prototyping (laser cutting) and silicon micro-fabrication have been used and the obtain results with these two prototypes have been discussed and compared. In order

to observe and characterize the prototypes, contactless measurements techniques have been introduced. Two different methods were proposed: a high-resolution camera and a fiber optic displacement sensor. The control module of the prototypes is also explained to control the working of an HDA.

To experimentally validate the proposed concept, the PMMA version of the HDA has been initially used. Various experiments have been performed to characterize the HDA. The ability to reach the twelve discrete positions, distributed at two different levels along z -axis has been validated. The strokes have also been measured and compared with the theoretical values. As the HDA uses current in the form of pulses to switch in xy -plane, an experiment to determine the optimal driving pulse duration has been performed which helps to minimize the energy consumption. The average pulse duration is 8.75% and 26.60% higher for Long- x -stroke and Stroke- y compared to the Short- x -stroke.

The HDA has also been tested for micro-positioning application. At the initial stage, a conveyance guide is placed at the top of HDA to control the conveyance trajectory. The plate displacement with respect to driving current values has been determined. The Stick-slip and Lift-mode conveyance approaches have been validated. For a displacement sequence, the Lift-mode is determined to be more efficient compared to Stick-slip approach due to the absence of backlash effect. In addition, the maximum mass displaced using single actuator for a particular current value has been determined and it has been observed that 1.15 g can be displaced using a current of 2 A. As single actuator is used to realize micro-positioning application and as the dimension of conveyance plate is fixed, the conveyance stroke has been determined and is also found out, which is ± 5.40 mm for Short- x -stroke and ± 7.05 mm for Stroke- y . The HDA actuator can switch between six discrete positions on each level along z -axis and it includes three axial strokes and remaining three angular strokes. To experimentally visualize it and also to experimentally measure the displacement and angles, images were captured and presented in this chapter.

Finally, a micro-fabricated version has been introduced and various experiments have been performed. The total switching time has been measured for different strokes and found out approximately to be 13 ms for Short- x -stroke, 25 ms for Stroke- y and 29 ms

for Long- x -stroke for a given current value of 2 A. Position repeatability has also been measured and the errors are found out to be between $5\mu\text{m}$ and $16\mu\text{m}$. These repeatability errors represents 2.0% (Short- x -stroke), 1.8% (Long- x -stroke) and 0.6% (Stroke- y) of the HDA strokes. At last, experimental strokes have been measured and compared with the theoretical and the PMMA version ones. Obviously, the strokes obtained using micro-fabrication technique are more precised.

As explained, this chapter validates and characterized the proposed HDA. A positioning application has been studied and two approaches have been tested. In order to realize more complex tasks, an array of HDA will be proposed, designed and experimentally tested in the next chapter.

Chapter 4

Development of an Hexagonal digital actuator array for Long-range Conveyance.

This chapter presents the design of an Hexagonal Digital Actuators Array (HDAA) and its characterization in order to validate the conveyance application. The HDAA consists of seven elementary controlled HDA arranged in a honeycomb architecture. The objective is to test the ability to realize conveyance tasks using a distributed actuation strategy. At first, the detailed design layout of the HDAA and the different components used in the assembly are presented. In order to ensure an homogenous behavior of all the HDA, the magnetic and electromagnetic force interactions between the HDA have been studied and an optimal array design has been proposed. The two conveyance approaches proposed in chapter 3 (Stick-slip and Lift-mode) have been undertaken. The advantages and drawbacks of Lift-mode approach and Stick-slip are then detailed. Secondly, the experimental conveyance possibilities have been tested to qualify the performance of HDAA.

4.1 Design Constraints and Requirements

In the designing of HDAA, some constraints have been taken into account in terms of dimension of the HDAA and size of the elementary modules. A total of seven modules

are used in the HDAA. They are identical and have the same dimensions as mentioned in chapter 2 (total dimension of each module : 25.76×22.30 mm). These HDAs are arranged in a honeycomb architecture and the FPMs are shared between the HDA to obtain a compact array.

This constraints helps to fabricate the conveyance device using micro-fabrication technique as the usual dimensions of silicon wafer is fixed (100 mm). Larger silicon wafers are also available, but fabrication using them was not possible with our partner ESIEE Paris as special settings need to be realized. The final proposed design takes into account all this constraints and requirements.

4.2 Prototype validation with respect to design constraints and requirements

In order to validate the proposed design and its ability to realize conveyance tasks, the same prototyping steps, as the ones used for the elementary HDA, have been selected. A first version realized with rapid prototyping techniques has then been studied. The main idea was to validate the proposed concept. Then, a micro-fabricated version has been realized.

4.2.1 Homogenization of Magnetic and Electromagnetic forces

The first step in the validation of HDAA design deals with the calculation of magnetic and electromagnetic force interaction. These forces have been calculated in order to verify that the behavior of the seven HDA are almost identical which represents an important property of an actuators array. To determine that, the semi-analytical software Radia has been used. The honeycomb architecture composed of seven HDAs is shown in Fig. 4.1 (a). There are seven MPMs (as numbered) and 24 FPMs used in this design. To calculate the magnetic force variation, all the mobile parts are in the same discrete position as shown in Fig. 4.1 (a). In this considered configuration, a huge magnetic force variation is observed as shown in Fig. 4.1 (b). The average magnetic force difference along x- and y-axis

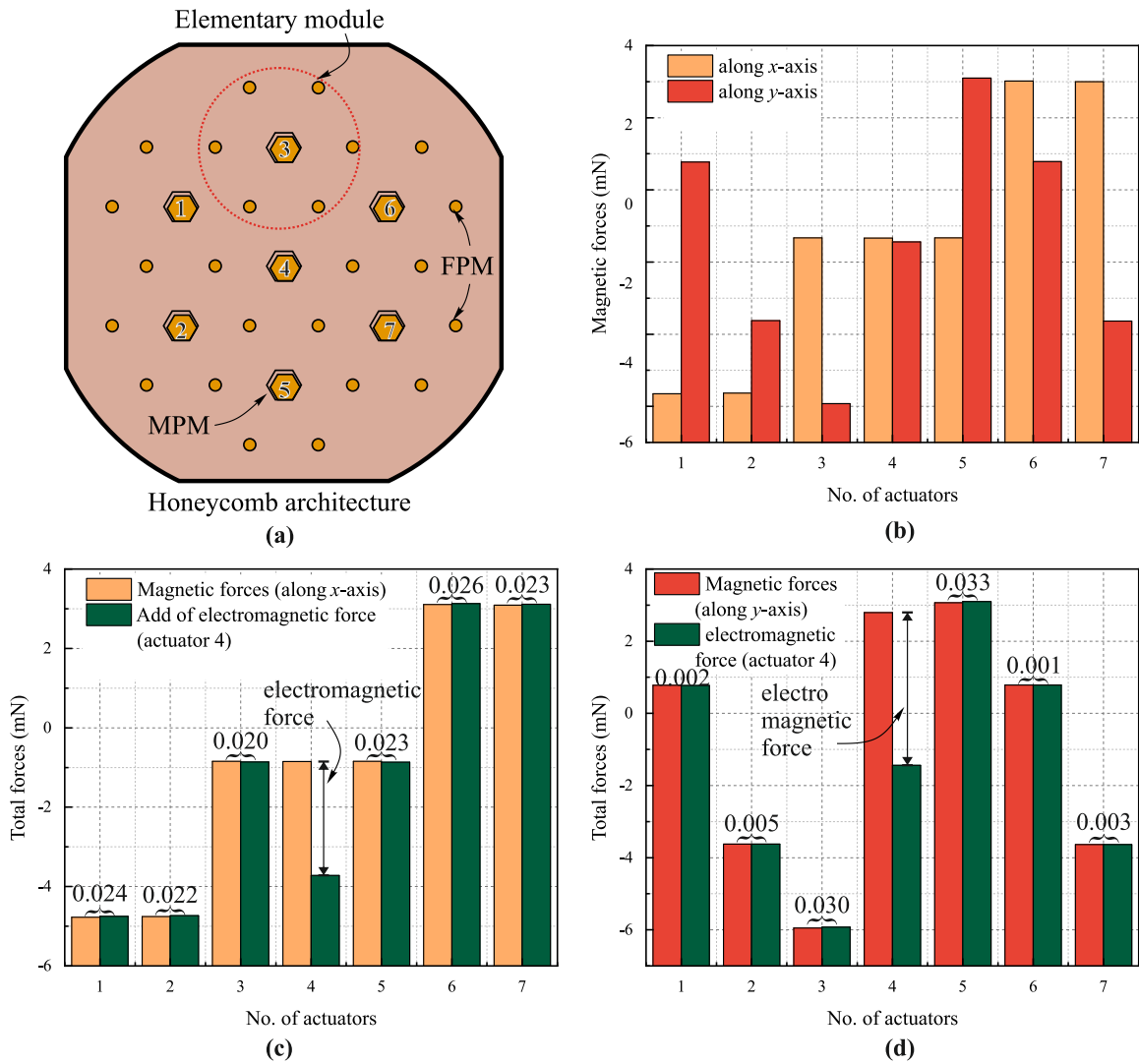


FIGURE 4.1: (a) Representation of honeycomb architecture with seven HDA. (b) Magnetic force variation. (c) (d) Representation of electromagnetic force variation.

is found to be 7.87 mN and 9.02 mN, respectively. This difference will generate a non homogenous behavior between all the HDA. The origin of this difference is mainly due to the magnetic interaction between the MPMs. The conveyance with this observed variation is rather impossible. A need to reduce this non homogeneity is then necessary. The generation of such non-homogeneity was not observed for electromagnetic forces (see Fig. 4.1 (c) (d)). The results presented in these figures have been obtained considering, a current of 1 A injected in the Tc (x-axis switching) placed behind MPM number 4 and the variation on other MPMs has been calculated. It has been observed that (Fig. 4.1 (c)), the average electromagnetic force generated on other MPM variation is around 0.023 mN, which is very low in comparison to the magnetic forces. Similar variation has also been

observed using Bc (y-axis switching), and an average value of 0.016 mN has been obtained. These disturbing electromagnetic forces are not enough to change the position of other neighbouring actuators because it is very low compared with the magnetic force and can then be neglected.

As explained previously, the magnetic force variation needs to be reduced to obtain homogeneity in the proposed conveyance device. To do so, a set of balancing PMs are placed around the array. The balancing PMs helps to reduce the variation observed as shown in Fig. 4.2 because they compensate the absence of PM for the HDA placed at the periphery of the array. According to the graph, the highest force variation was observed

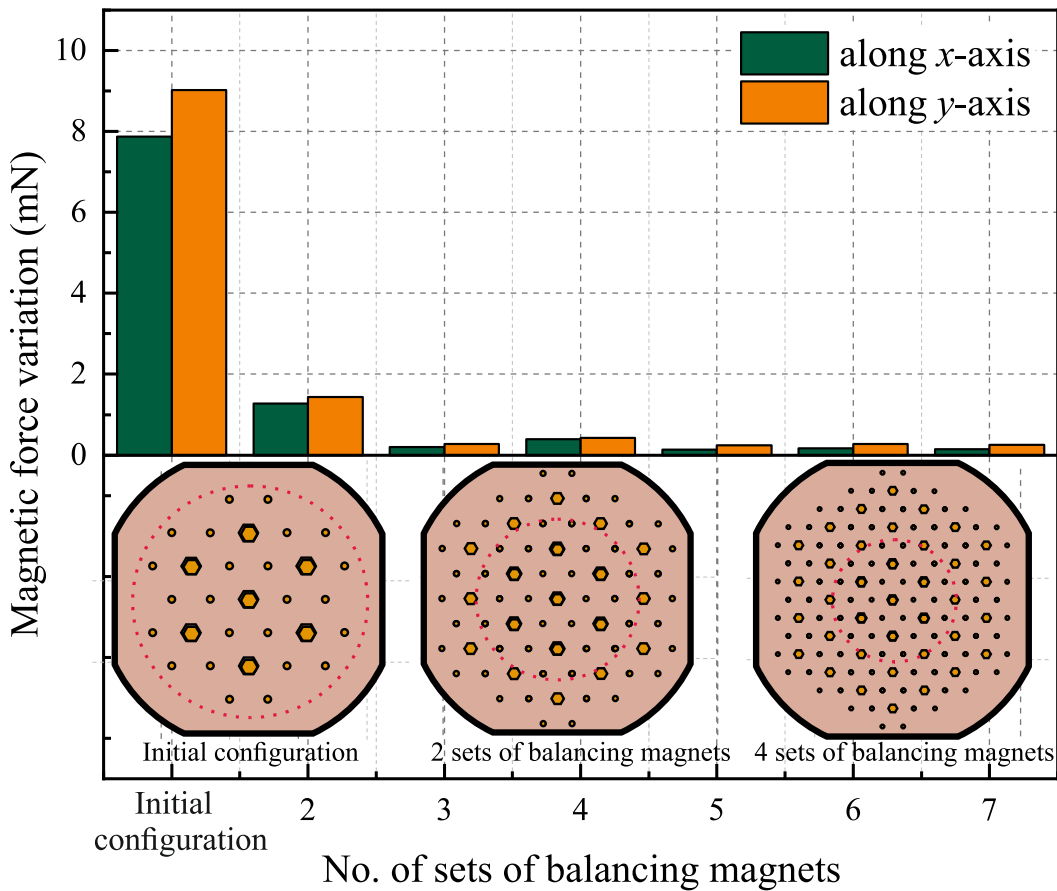


FIGURE 4.2: Representation of magnetic force variation with respect to the number of layers of balancing magnets.

to be for initial configuration (i.e. without balancing PMs), and it gradually decreases with the addition of balancing layers around the seven HDA. There are two types of balancing PMs considered (hexagonal and cylindrical) for MPM and FPM, respectively. The balancing hexagonal PMs have the same magnetization orientation and same volume to

that of MPM whereas, the balancing cylindrical PMs have orientation like that of FPMs. In the graph, total of seven layers have been added and with a 7th layer of balancing magnets, the average variation has been highly reduced compared to the initial configuration and are 0.143 mN and 0.249 mN along x - and y -axis, respectively. Table 4.1 provides the magnetic force variation for each considered configuration.

Configuration	along x -axis mN	along y -axis mN
Initial	7.8771	9.0206
1 sets	2.3215	2.9758
2 sets	1.2789	1.4389
3 sets	0.2001	0.2772
4 sets	0.3930	0.4266
5 sets	0.1365	0.2456
6 sets	0.1662	0.2794
7 sets	0.1439	0.2493

TABLE 4.1: Magnetic force variation for different configurations

However, the addition of balancing layers increases the array size and make it impossible to fit inside a 100 mm silicon wafer. Therefore, a compromise has been done between the array dimension and the homogenous behavior by selecting the second configuration (with two layers of balancing PMs). An optimisation of this second configuration has then been done in order to further reduce the magnetic force variation along x - and y -axis. It has been observed that, on further adapting the position of balancing PMs, the variation can be reduced and it can also reduce the size of an array but, after a certain limit of reduction in size, the magnetic variation again increases. Taking both the aspects into consideration, the final configuration has been obtained as shown in Fig. 4.3 and the obtained magnetic force variation is also given in the figure. This structure has been considered for the final version by compromising the behavior homogeneity with the array dimension. The final array dimensions is 77.68×84.09 mm which fits with a $\phi 100$ mm silicon wafer. Table 4.2 below represents the comparison in size of the HDAA and the

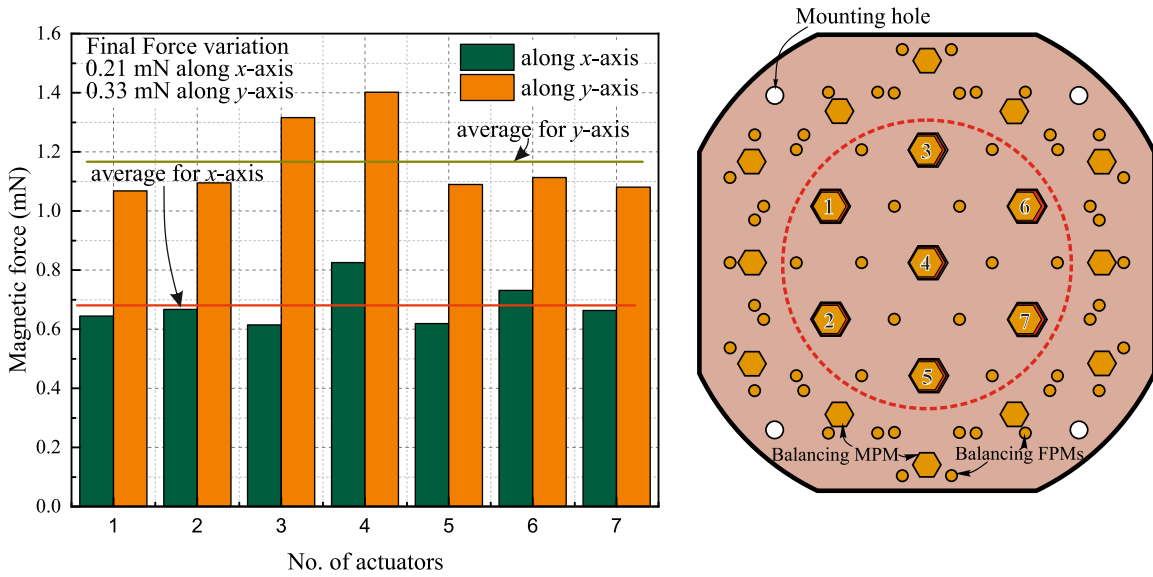


FIGURE 4.3: Representation of final version of the prototype and the balanced magnetic forces for each actuator in the final array.

magnetic force variation for the optimised and non-optimised configuration consisting of two sets of balancing PMs.

Configuration	Size	Magnetic force variation
Two sets of balancing PMs (without optimisation)	103.04 mm × 111.54 mm 11533.23 mm ²	1.28 mN(x-axis) 1.44 mN(along y-axis)
Two sets of balancing PMs (With optimisation)	77.68 mm × 84.09 mm 6532.11 mm ²	0.21 mN(along x-axis) 0.33 mN(along y-axis)

TABLE 4.2: Optimized and non-optimised configurations of two sets balancing PMs

4.3 Prototype Assembling and Working Principle of HDAA

The proposed HDAA has then been manufactured to experimentally validate the homogeneous behavior of PMs and the working principle for a conveyance application. Fig. 4.4 (a) represents the CAD model of the HDAA. The mobile part of each HDA consists of a hexagonal MPM glued at the bottom with a z-axis retainer as shown in the cross sectional view. (Fig. 4.4 (c)). Each mobile part of the actuator is able to switch between twelve discrete positions distributed on two different levels along z-axis. The representation of these twelve discrete positions is shown in Fig. 4.4 (d) along with the stroke sizes. As

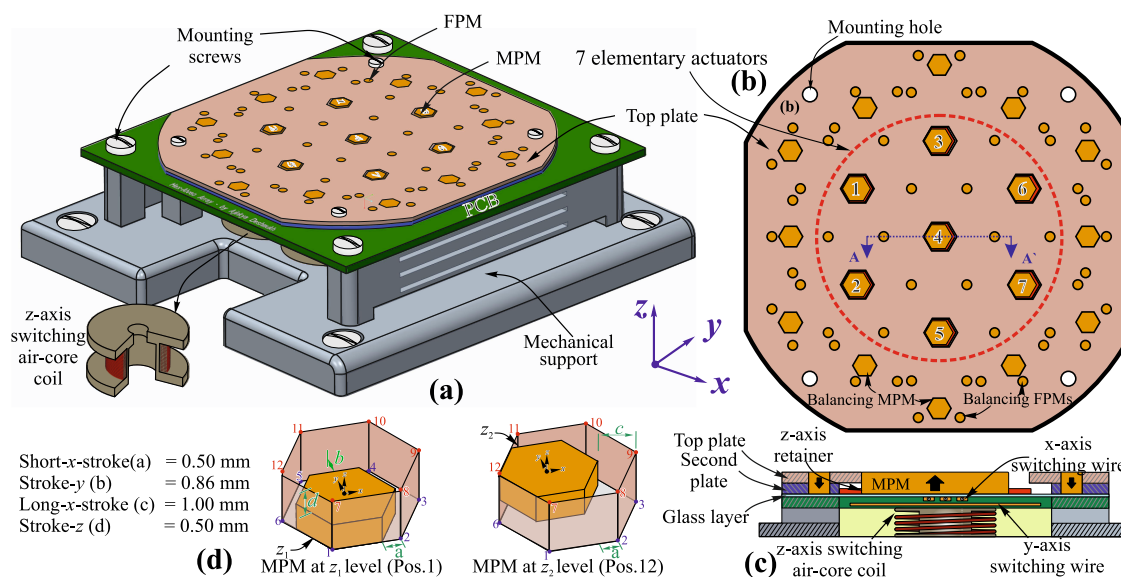


FIGURE 4.4: (a) 3D view of a conveyance device (b) Top view showing arrangements of seven actuators using an honeycomb architecture (c) Cross sectional view of a single actuator AA' (d) Representation of strokes and ability to reach twelve discrete positions.

described in the design of an elementary actuator (see Chapter 3), the prototype also consists of two plates, ("Top and Second") needed to obtain the stroke displacement along z -axis for each HDA. Seven electromagnetic air-core coils (one for each HDA) have been used for the z -axis switching. Each coil has been verified using an LCR meter (RLC100 Digimess) and the resistance is found out to be in the range of $0.27\ \Omega$ to $0.45\ \Omega$. The switching in the xy -plane is obtained using a 4 layers PCB which integrates two sets of orthogonal conductors printed for each HDA. To avoid direct contact between the PCB and mobile parts, a thin glass layer is placed beneath them as described in chapter. 2.

The PCB developed for the array has been designed using the software by Cadsoft-Eagle. The fabrication is outsourced from the Eurocircuits company to ensure proper manufacturing taking into account the design rule check. Fig. 4.5 represents the top and bottom views of the PCB. As in chapter 3, a reverse design has been used in order to obtain an airgap of $0.1\ \text{mm}$ between the first two layers that will lower the difference in electromagnetic force generation between B_c and T_c as explained in chapter 2. There are seven different orthogonal sets of conductors for displacement in xy -plane for all the seven actuators. At the bottom side, there are separate SMD solder connections for the soldering of x -, y - and z -axis switching conductors, respectively. The SMD facilitate the

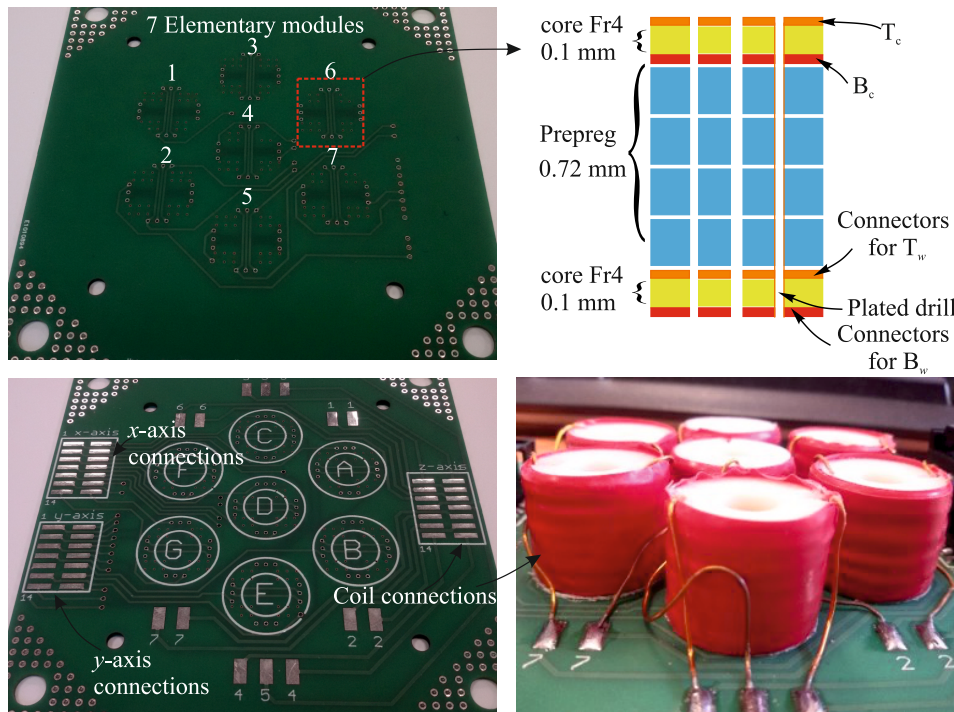


FIGURE 4.5: Top & Bottom view of the PCB, buildup design and representation of soldered air-core coil

connection process. Dedicated SMD connections are also integrated in the fourth layer for the electromagnetic coil connection. Fig. 4.5 also represents the assembly of coils on the PCB.

4.3.1 Working Principle of HDAA

4.3.1.1 Actuation Approaches

The two proposed approaches: Stick-slip and Lift-mode, tested for the positioning application using single HDA have been adapted and used with this array. Fig. 4.6 and 4.7 represent the working principle using both the approaches for the considered array. The principles are applied on all the seven actuators but in order to facilitate the understanding, only two actuators are represented in this section.

Stick-Slip approach: The basic principle of this approach is similar to the one explained for the elementary actuator in chapter 2 and is based on a stick phase during which the plate is displaced and slip phase during which the mobile part returns to its initial position. Fig. 4.6 represents the stick-slip approach for the HDAA. In this first

prototype, to always ensure a physical contact between the MPM and the conveyance plate, a small PMMA piece is fixed on top of the MPM as shown in Fig 4.6. As only two actuators are shown, the approach includes four different steps. In the first step, all the

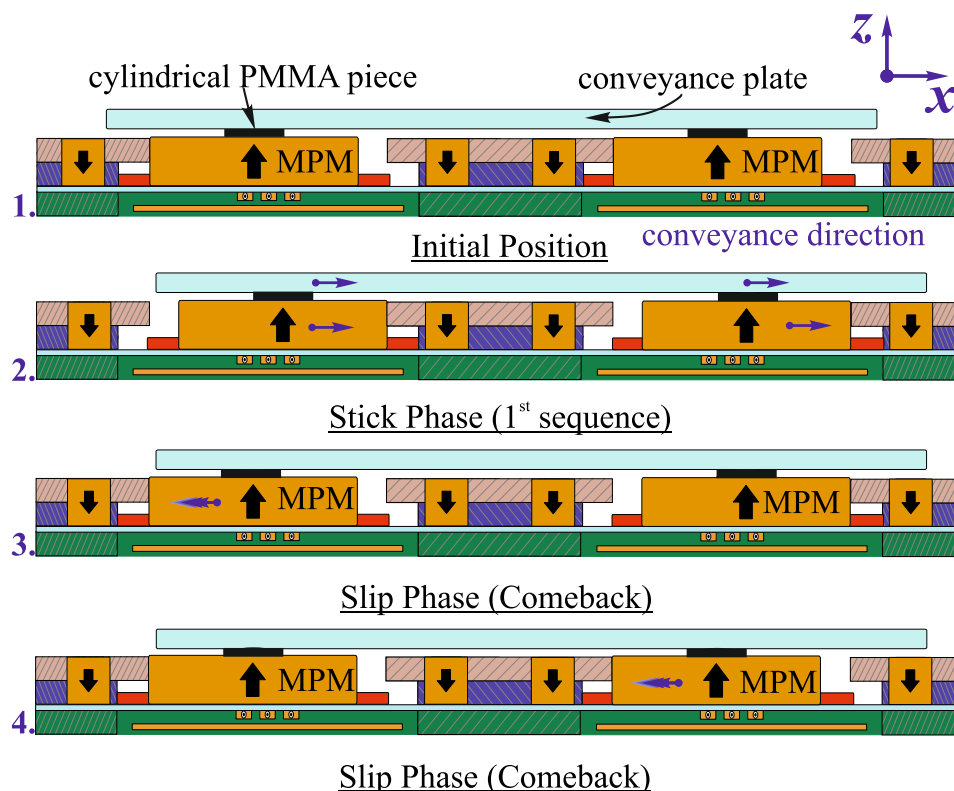


FIGURE 4.6: Principle of conveyance using Stick-slip approach.

mobile parts are at same discrete positions and the conveyance plate is placed on top of them as shown. In the second step also called as the stick phase, a low driving current is used for switching of all mobile parts simultaneously. It generates enough force to switch MPMs then the conveyance plate (along x -axis in this case) [Fig. 4.6 (2)]. The frictional force generated between the conveyance plate and the PMMA piece ensures the plate displacement. As the MPMs velocity is low, the sliding between the MPMs and the plate is then minimized and the plate is conveyed on a long distance. After this step, the MPMs need to return to their initial position to realize next switching sequence. If all the MPMs will return to their initial positions at a time, it will move back the conveyance plate thus generating the backlash effect. To reduce this effect, firstly a higher driving current is used to increase the slipping between the MPM and the conveyance plate (called as slip phase) and secondly, the MPMs are switched back one by one. The switching is as

shown in Fig. 4.6 (3) (4). After this sequence, a second displacement step can be realized. To perform a long range displacement, the stick and slip phases are repeated until the desired conveyance distance is achieved. This approach can be used both at z_1 and z_2 levels. However to maintain the mobile part at z_2 level, a continuous current need to be injected in all the seven air-core coils which are placed beneath the mobile parts.

Lift-Mode approach: Unlike the stick-slip approach, this approach cannot be used independently on both levels along z -axis. At z_2 level, there is contact between the plate and the mobile parts and at this level, the mobile part displacement ensures the plate displacement. At z_1 level, there is no contact between the plate and the mobile part and this level is used to ensure a return of the mobile part in their initial position [see Fig. 4.7 (1) (2)]. In Fig. 4.7 (1), no current is injected into the coil, the MPMs are then not in contact with the conveyance plate. In Fig. 4.7 (2), a continuous current is injected through the coils to switch the MPM from z_1 level to z_2 level and to ensure the contact with the plate. Then, the MPMs are switched along x -axis to move the plate with a low driving current to move the plate as for the stick phase with the Stick-slip approach Fig. 4.7 (3). To ensure the return of the MPMs, the current through the coils is stopped and the MPM return to their initial position simultaneously. In comparison to the Stick-Slip approach, here all the MPMs can return to their initial positions at a time and no disturbance to the plate is observed in xy -plane. For long range conveyance, it reduces the time required to switch but therein increases the energy consumption as high current is required to generate enough electromagnetic force at z_2 level. To validate this two approaches and to study their experimental behavior, they have been tested on the device and results are presented in the upcoming sections.

4.3.1.2 Conveyance possibilities

The two approaches discussed above can be used to realize different conveyance possibilities. They presents some advantages and drawbacks about energy consumption, conveyance velocity, presence of backlash,.. and the choice of one approach depends on the context. Fig. 4.8 represents the different conveyance possibilities. As the seven HDAs

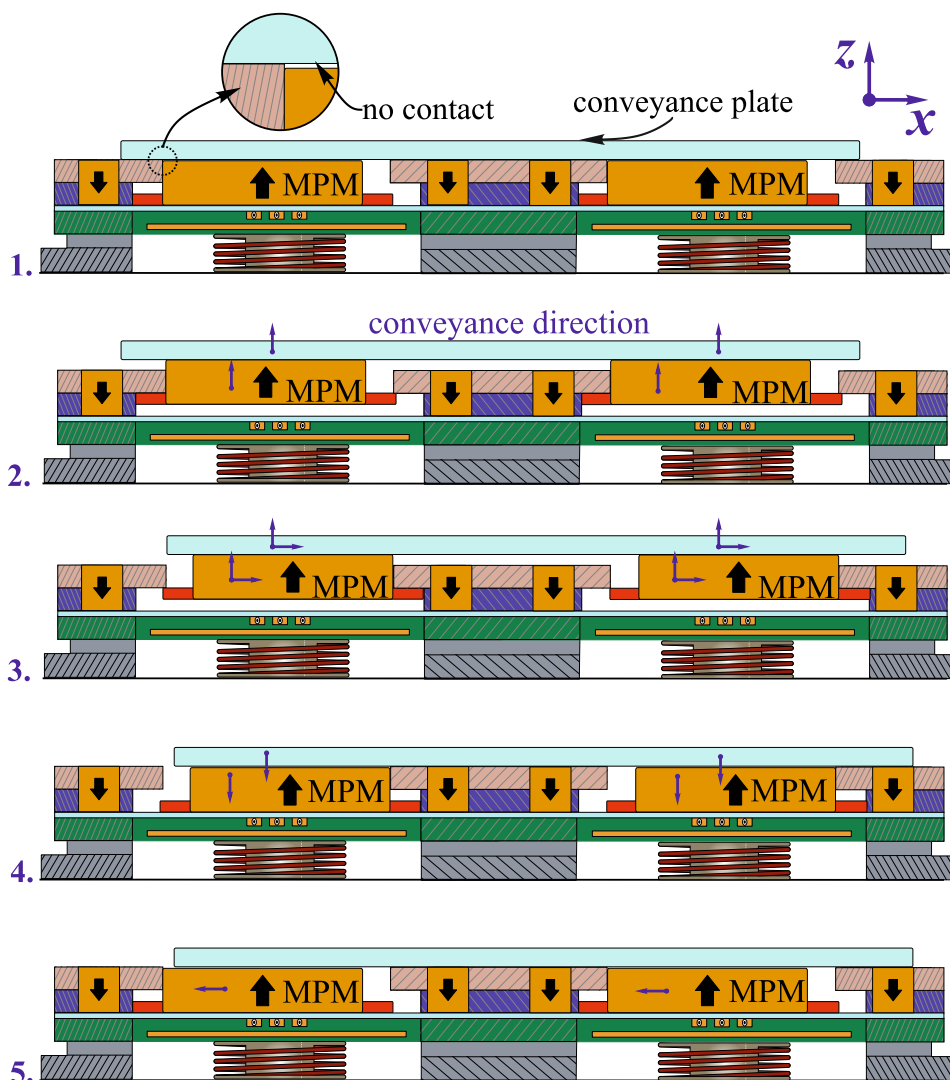


FIGURE 4.7: Principle of conveyance using Lift-mode approach.

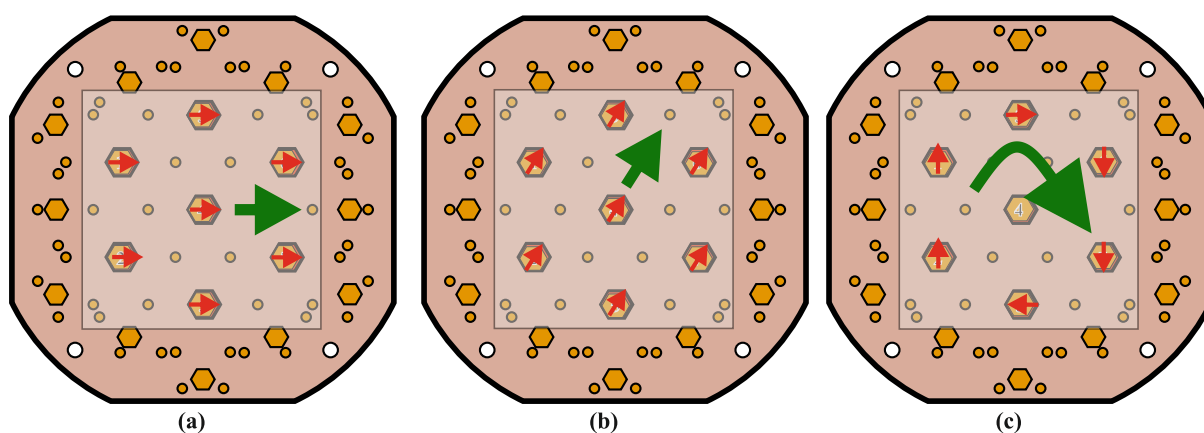


FIGURE 4.8: Representation of different conveyance possibilities.

present in an array can be individually controlled, it will optimise the energy consumption by limiting the switching of only required actuators. Translations along x - and y -axis

or combination of xy (diagonal) is possible with the help of all the seven actuators. The rotation possibility is also shown in figure, which can be achieved by controlling the six HDA's in a particular manner while the middle HDA remains at idle state.

4.4 Experimental Setup and Results

This section details the assembly of the experimental prototype, the control module and the experimental characterization of the HDAA.

4.4.1 Experimental prototype and Control Module

To validate the proposed concept of HDAA, a rapid prototyping i.e. laser cutting techniques has been used. The base of the array is 3D printed with cylindrical bars and screw holes to fix the seven air-core coils and the PCB. The two plates, Top and second plate, have been fabricated using laser cutting technique and are fixed on the PCB. To avoid a direct contact between the PCB and the MPM, a thin glass layer ($50.00 \times 50.00 \times 0.17$ mm) is placed between them. As in chapter 3, a z -axis retainer has been used and glued at the bottom of MPM to obtain the z -axis stroke. The formed cavities for the MPM and FPMs helps to assemble the array. The top and front view of the array is as shown in Fig. 4.9.

The control module is identical to the one presented in the previous chapter. However, the addition of extra V-I converters to realize switching along x -, y - and z -axis is needed to control the array. If the totally independent control is desired, 21 V-I converters are required to elementary control each HDA in all the three axis. But for this initial prototype, we minimize the number of converters by connecting the actuators in series column by column. It reduces the number of converters to seven. To observe the plate displacement on a longer range, the same HRC presented in previous chapter (FLIR ORX 10G-51s5c) has been used.

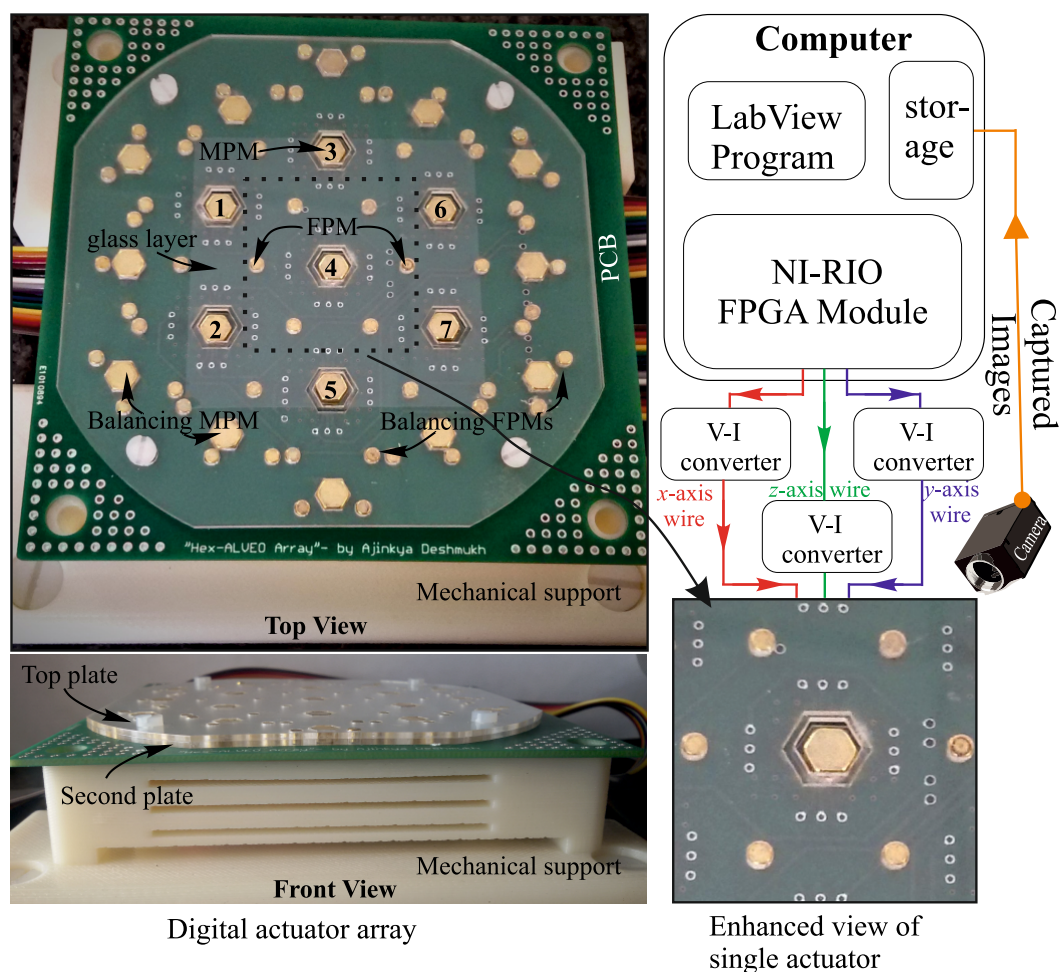


FIGURE 4.9: Experimental prototype of the HDAA and the Control Module.

4.4.2 Results and Discussions

In this section, various results are presented and discussed to characterize the array prototype. It is mostly observed for x -axis displacement as the idea was just to validate the prototype. At first, the ability of the array to convey a plate along x -axis using Long-stroke for different current values has been tested and is shown in Fig. 4.10. In order to measure the plate displacement with the HRC, a sticker with a printed plus mark has been placed on top of the conveyance plate. In this test, a PMMA plate is used for the conveyance with dimension of $50 \times 50 \times 2$ mm and mass of 5.56 g. In the Fig. 4.10, it can be observed that the plate displacement is reduced when the driving current is increased. This is due to the sliding between the plate and a MPM which is high for high driving current values and inversely. This effect is observed for the two conveyance approaches.

When the driving current values increases from 1.5 A to 7.5 A, the plate displacement is then reduced from 1.18 mm to 0.25 mm, for the Lift-mode approach and from 1.35 mm to 0.10 mm, for the Stick-slip approach. The difference in the plate displacement between the two approaches is due to the use of two different configurations for the conveyance. For the Stick-slip approach, there is a horizontal friction between the PMMA part fixed on the top of the MPM and the conveyance plate. However, in a Lift-mode approach, there is a direct contact between the MPM and a conveyance plate.

The total time and the number of sequences (displacement steps) required to reach a particular distance (10 mm) for the conveyed part has also been experimentally characterized. For that, again the same driving current values (1.5 A to 7.5 A) have been used with the two proposed approaches. The graph representing the total time required to switch is shown in Fig. 4.11 (a). For this experiment, the required pulse duration is determined for each driving current value to reach the defined discrete position as shown in Fig. 3.10 of chapter. 3. Taking into account, the current value and its respective pulse duration, the total time required to cover 10 mm is determined. The measurements have been repeated five times and the error bars represents the standard deviation for each measured point.

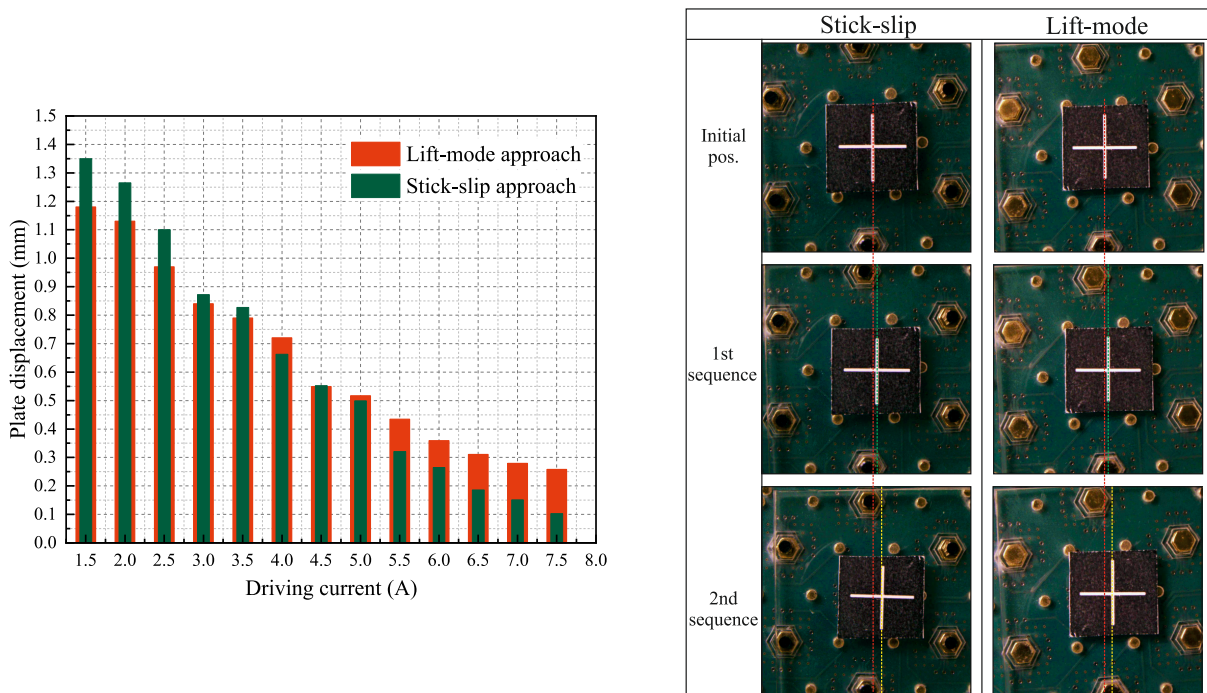


FIGURE 4.10: Representation of the plate displacement for stick-slip and Lift-mode approach for different driving current values.

It can be observed that the time required to convey the plate over 10 mm, increases when the current rises from 1.5 A to 7.5 A. However, there is sudden decrease in plate displacement after 5.5 A for Stick-slip approach. This leads to the increase in total required time to cover a distance of 10 mm. This decrease for higher current value can be due to the generation of force along z -axis and also due to increase in slipping effect. The maximum velocity have also been determined for both the approaches. For stick-slip, the device is able to convey object at a speed of 3.33 mm/s for 1.5 A and 1.14 mm/s for 7.5 A. Whereas for lift-mode approach, the device is able to achieve speed of 4.76 mm/s and 1.58 mm/s for 1.5 A and 7.5 A, respectively. Secondly, the required number of switching

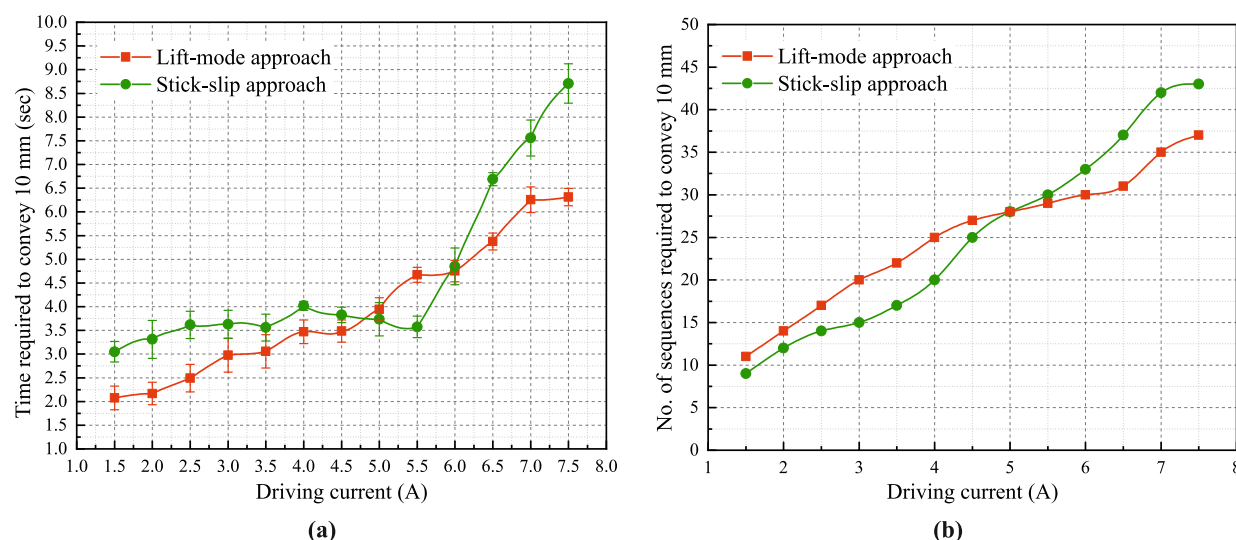


FIGURE 4.11: (a) Representation of total time required to convey a plate with respect to driving current. (b) Representation of the number of sequences to cover 10 mm distance with respect to different current values for both the switching approaches.

sequences to reach the distance of 10 mm with different driving current values are also determined [see Fig. 4.11 (b)]. In accordance with the results presented in Fig. 4.10, the number of sequences required to reach a distance of 10 mm has been determined and is found to be small for low current values and it increases with the current. The increase in the number of sequences is then visible for both the approaches.

The presented results, validates the proposed concept of a conveyance device. It also presents the comparison between the two conveyance approaches in terms of plate displacement, no. of sequences and time. Thus, it also validates the ability of an array to realize conveyance using both the conveyance approaches: Stick-slip and Lift-mode.

4.5 Micro-fabricated HDAA

After the validation of the HDAA design using rapid prototyping technique, the next phase is to realize the HDAA prototype using micro-fabrication techniques. As for the elementary HDA, a DRIE process has been used for the micro-fabrication of the two plates.

Fig. 4.12 shows the mask used for the fabrication of Top plate. Two separate masks have been used for the fabrication of Top and Second plate. In this process, at first, the masks are aligned on respective silicon wafers ($\phi 100\text{ mm} \times 0.90\text{ mm}$ each). The details of this process can be found out in section 3.2. as the same process is used. Fig. 4.12 also represents the total dimensions of Top and second plate.

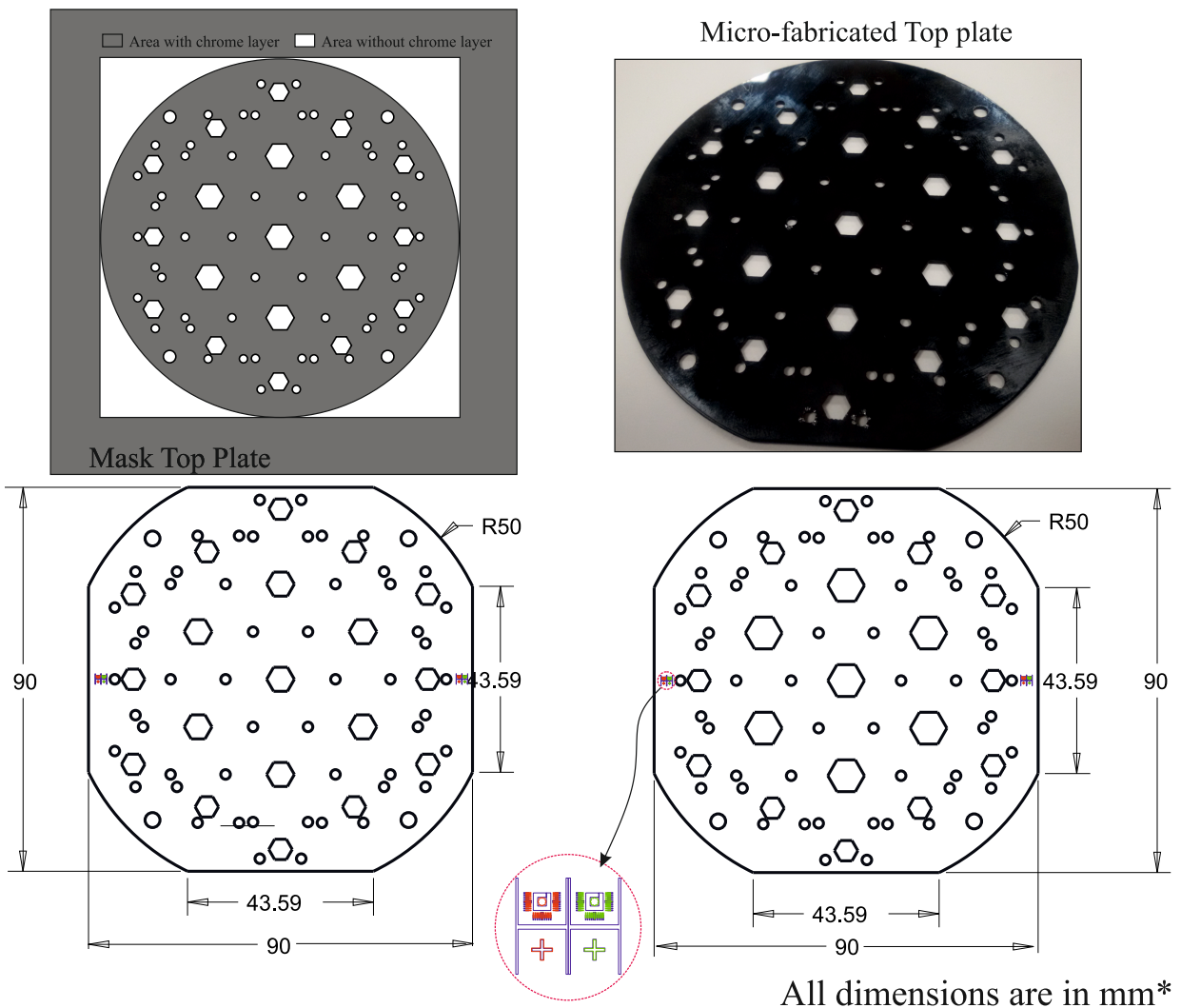


FIGURE 4.12: CAD design of the photo lithography mask and figure representing the dimensions for Top and second plate

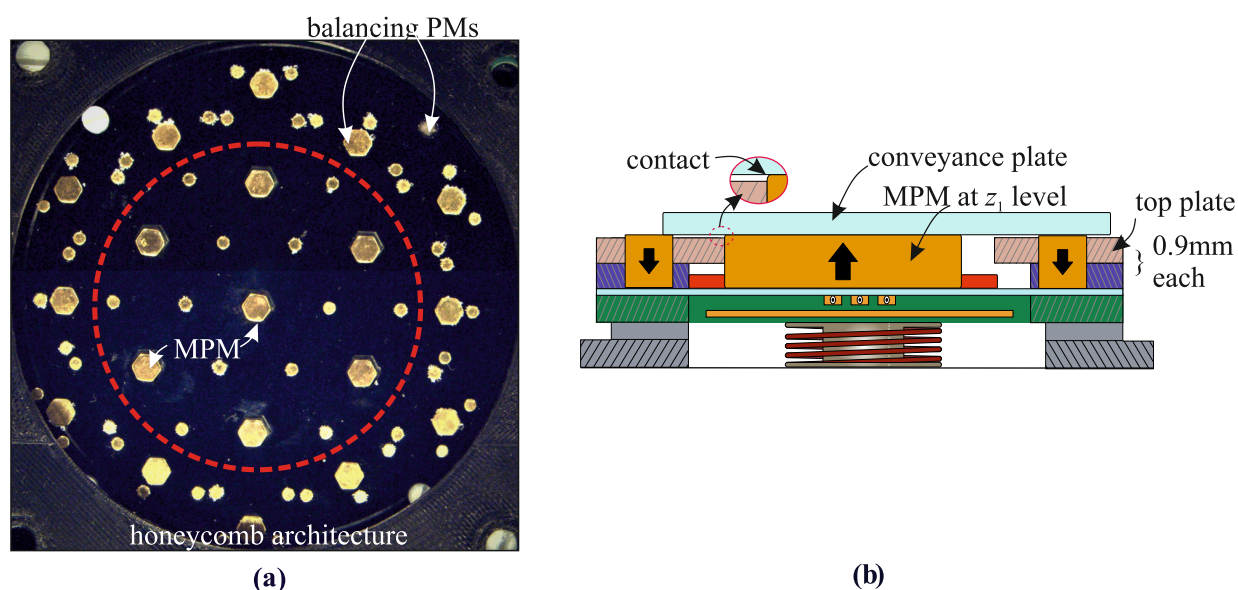


FIGURE 4.13: (a) Experimental prototype of the micro-fabricated Hexagonal digital actuator array. (b) Cross sectional view of single actuator in an array.

These two plates are stacked together and then assembled on the PCB. The mobile part, FPMs and the balancing PMs are placed in the provided cavities as shown in Fig. 4.13 (a). The z -axis retainer used in the mobile part is made up of PMMA material and fabricated using laser cutting technique. The top and second plate used in the micro-fabricated version are of thickness 0.9 mm each [see Fig. 4.13(b)]. Thus, there is no need of any cylindrical PMMA piece on the MPM to realize conveyance using Stick-slip approach as for the PMMA version. The 0.9 mm thickness of each wafer allows the upper 0.2 mm of the magnet height (Total height of MPM = 2 mm) outside the cavities and helps to obtain a proper surface contact between the MPM and conveyance plate. This arrangement also helps to compare the two approaches using the same configuration in the conveyance which was rather impossible in the PMMA version.

4.5.1 Experimentation Characterization of the Micro-fabricated HDAA

This section presents the experimental characterization of the micro-fabricated HDAA. As in the previous version of the HDAA, the advantages of both conveyance approaches have been experimentally determined. In the micro-fabricated version, different conveyance

abilities of the HDAA have been characterized as translation of the conveyance plate in xy -plane, translation of the plate on long strokes with transition between different actuators, rotation of the plate around z -axis. The conveyance plate used for these experiments is made up of glass with a dimensions of $50\text{ mm} \times 50\text{ mm} \times 100\text{ }\mu\text{m}$ and mass of 0.72 g .

4.5.1.1 Translation of the Conveyance plate

To observe translation of the conveyance plate in xy -plane, the HRC has been used. A sticker is placed on top of the conveyance plate as shown in Fig. 4.14. In this test, the

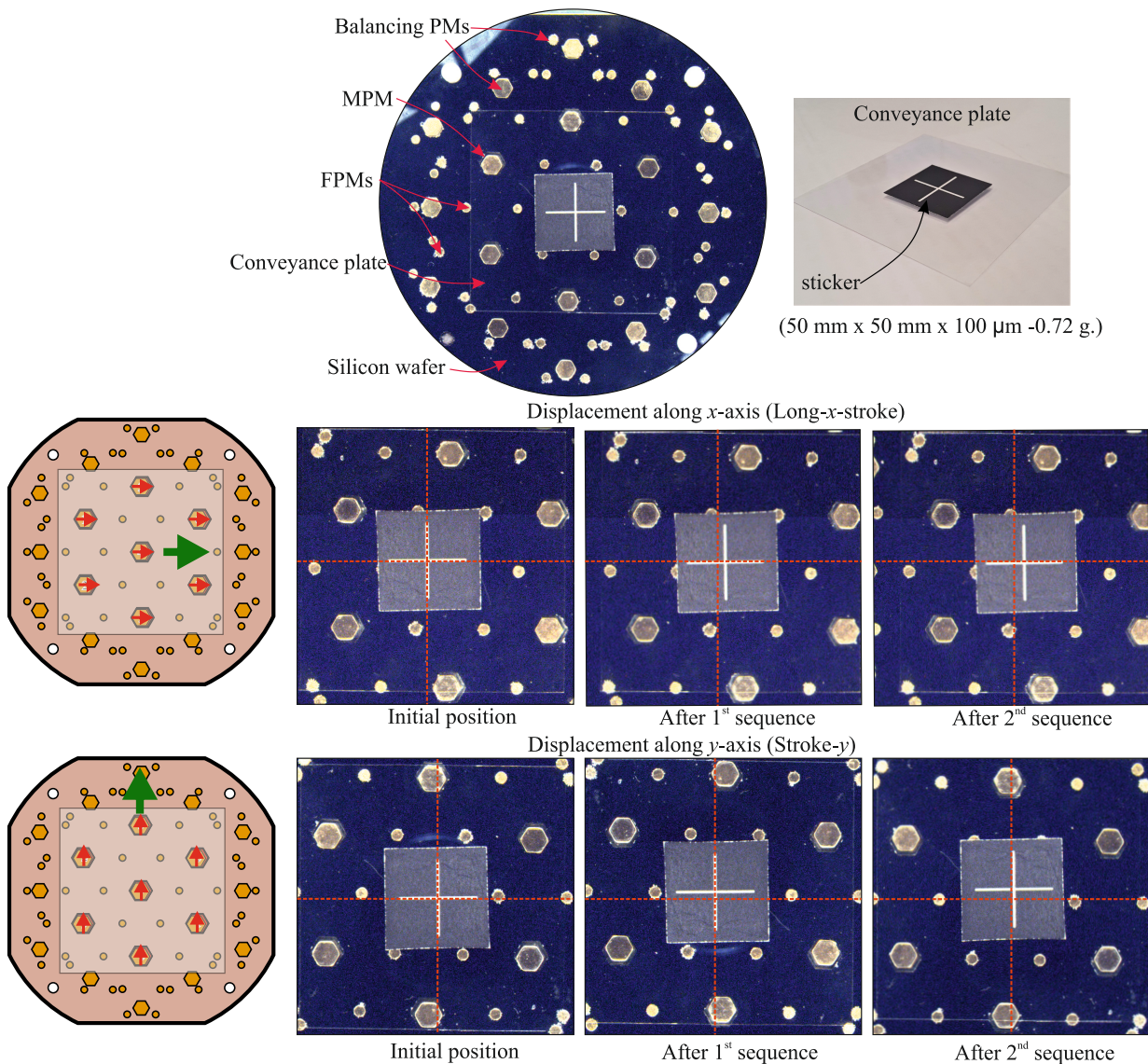


FIGURE 4.14: Representation of the Translation motion of the conveyance plate in xy -plane for Long- x and stroke- y .

Stick-slip approach has been used and the two different displacement strokes Long- x -stroke and Stroke- y have been used to obtain conveyance along x - and y -axis, respectively.

The plate displacement with respect to mobile part switching is clearly visible in the pictures taken from the HRC. The plate is observed to be displaced on an average of 1.17 mm for the Long- x -stroke in the two sequences.

To realise plate conveyance along y -axis, same arrangement has been used with Stroke- y . The images presented in Fig. 4.14, represents the plate displacement using first two switching sequences of the mobile part. The average displacement along y -axis is observed to be 0.89 mm.

4.5.1.2 Transition of the Conveyance plate between actuators

In this section, the long conveyance ability is shown by a transition of the plate between the actuators of the array. The transition has been realised along x -axis using Long- x -stroke and along y -axis using Stroke- y . A driving current of 2 A is used for the switching whereas, 6 A is used to realize the slip effect to minimize the backlash effect. The transition along x and y axes can be clearly seen in the Fig. 4.15(a) and (b). Four sequences are shown to visualize step-by-step plate transition from one actuator to the next one. Due to the tolerance in manufacturing, it has been observed that, when the plate is at the edge of an actuator during transition phase, the actuator pushes back the plate causing a huge impact in the plate conveyance trajectory. This impact can generate an unpredictable backlash effect as shown in Fig. 4.15 (c). In order to avoid the disturbance caused in the plate conveyance due to impact, the Lift-mode approach has been used. The step-by-step conveyance strategy is explained in Fig. 4.15 (d). It consists of three different steps as shown from step 1 to 3. In step 2, the conveyance plate is at the edge of actuator no. 3. If the next switching sequence is realised directly, an impact may appear between the plate and the mobile part. To avoid that, actuator no.1 and 2 are lifted upward at z_2 level using a lift-mode approach. A continuous current of 0.8 A is then used through the coils to obtain a stability of the plate at z_2 level. This lift generates enough gap between the plate and third actuator. Thus actuator no.3 first comes back to its initial position. After that, in step. 2 the mobile parts of actuator no. 1 and 2 return back at z_1 level. Then one-by-one they return to their previous position as shown in step 2 and 3. When all the actuator return to their initial position, they are ready for next switching sequence. This

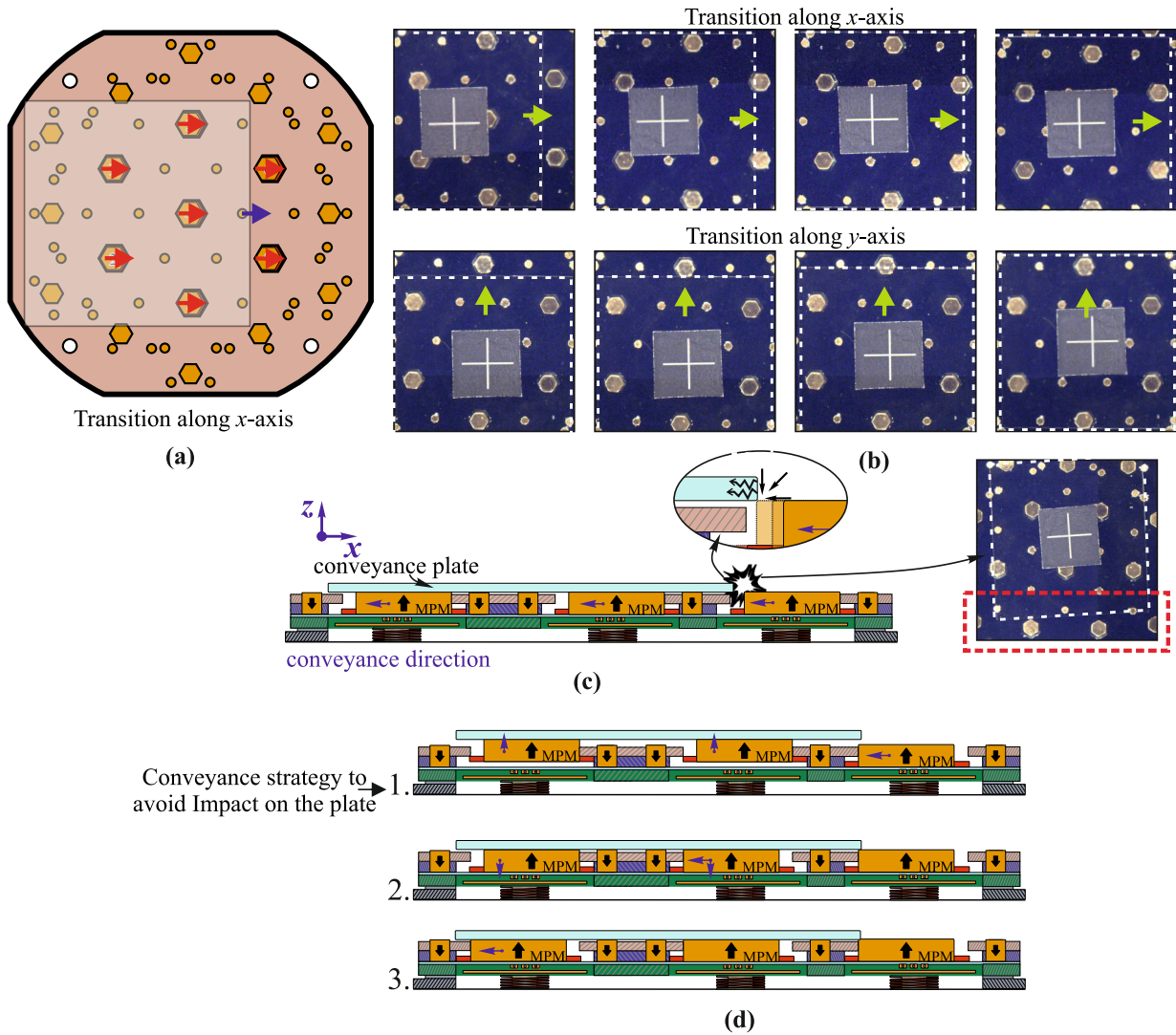


FIGURE 4.15: Representation of plate transition between the actuators (a) Representation of the transition phase. (b) Experimental transition in xy -plane using long- x -stroke and stroke- y . (c) Sectional view showing the step-by-step representation of the conveyance strategy using lift-mode and stick-slip approach.

strategy is only needed when the plate is at the edge of transition actuator and apart from this transition, the plate can be conveyed using either Stick-slip and Lift-mode strategies as explained in previous sections.

4.5.1.3 Rotation of the Conveyance plate

The proposed actuators array is theoretically able to realize rotation of the conveyed plate as explained before. This ability has been tested and characterized in this section. For that, the actuators have to be elementary controlled. The used displacement pattern is shown in Fig. 4.16. The total of six working actuators are required to perform rotation.

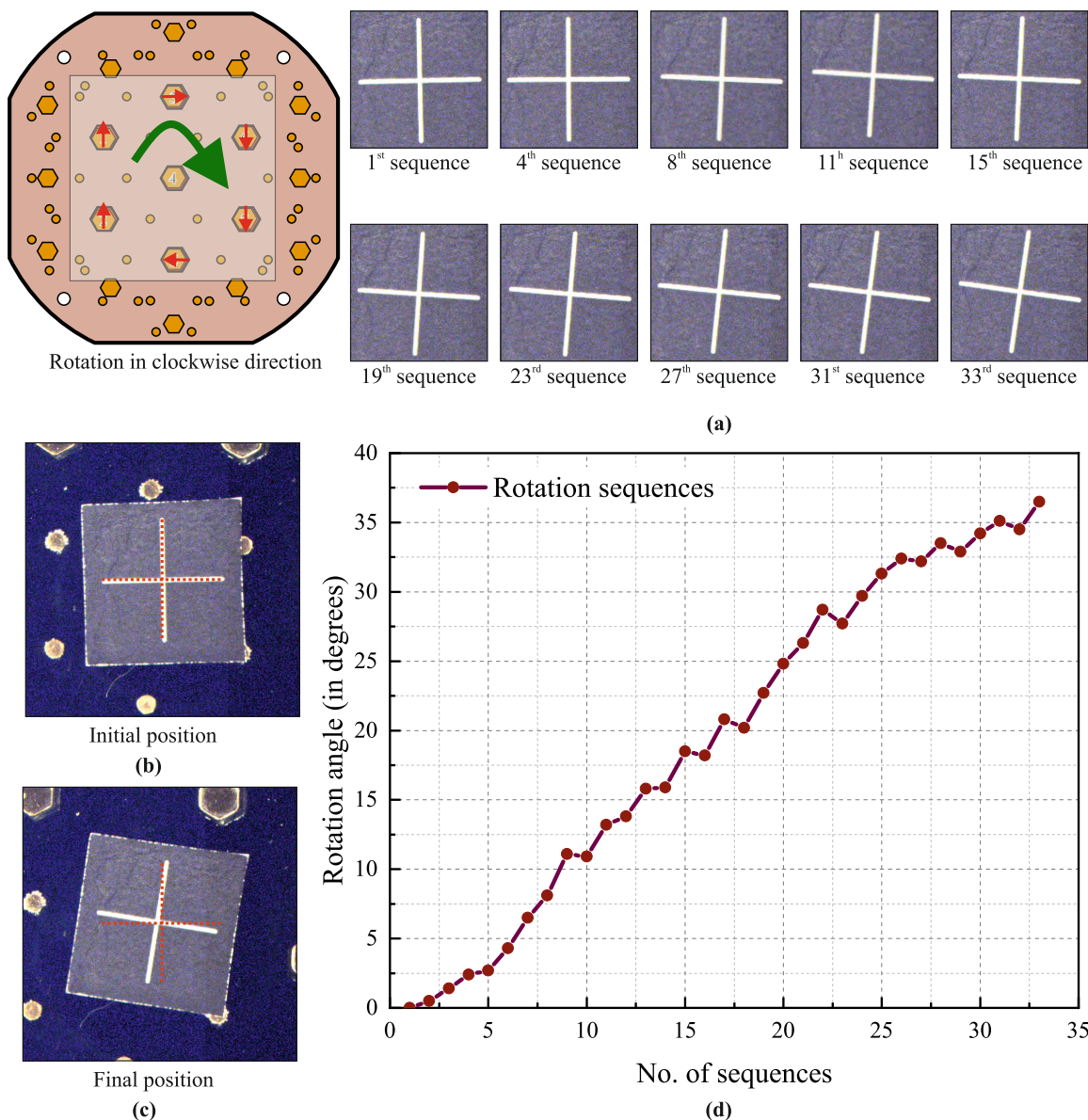


FIGURE 4.16: Representation of the Plate rotation using different switching sequences (a) Captured images for the different rotation sequences. (b) (c)

The actuator at the center of the HDAA (i.e. actuator 4) remains in its idle state, whereas actuator on the sides are controlled along y-axis in either forward or backward manner with respect to their sides and the actuators at top and bottom observe stroke along x-axis also in forward and backward manner, respectively. The Long-x-stroke has been used for displacement along x-axis in order to reduce friction losses which are caused by contact between lateral side of hexagonal cavity and the mobile part. The captured images of the plus sign placed on the conveyance plate are shown in Fig. 4.16 (a). In order to better understand the rotation trajectory, only few sequences are presented. However, the detailed switching trajectory has been graphically shown in Fig. 4.16 (d). A total of 33

switching sequences have been realized and a rotation of 0° till 36.4° has been observed. As the stick-slip mode has been used to realize rotation, a driving current of 2 A is used in stick phase and 6 A in the slip phase. Fig. 4.16 (b), (c) show the initial and final positions where, at the initial position the plate is at 0° and at final it is at 36.4° as mentioned earlier. The average rotation is observed to be 1.103° .

4.5.1.4 Realisation of Planar trajectory

After the validation of translation, rotation and transition between HDA's, the ability to realize planar trajectory has been tested. For that, a simple rectangular profile has been used. To realize this trajectory, all the HDAs are switched in the respective pattern as shown in Fig. 4.17 (a). The pattern is divided into four sequences starting from position 6 and then coming back again to the same position. The total pattern includes two displacements using Short-x-stroke and then two displacements using Stroke-y alternatively. The switching pattern is repeated three times to characterize the repeatability. The Fig 4.17 (b) represents the obtained trajectory. To observe the trajectory repeatability, initial point of each trajectory has been superimposed. As the array is controlled in open loop and also due to frictional inhomogeneity, a shift is visible on the trajectory especially at its end between the initial and final position which should be theoretically same. The shift can be mostly due to the sliding effect between the plate and the mobile part. In an open loop system, the absence of trajectory correction and generation of sliding after each switching sequence displaces the rectangular pattern each time from its initial position. This can be minimized by predicting the sliding behavior of the plate with respect to the driving current value. It can be determined by repeating the experiments several time and finding an average sliding in each displacement direction. The sliding can also be reduced by reducing the velocity before the impact using the reverse current in the conductors. It can be generated by sending another driving pulse in reverse direction when the actuator reaches the SRZ of desired discrete position. This reverse driving current pulse will generate electromagnetic force in opposite direction between the plate and mobile part, which will lower the plate velocity then the sliding. This principle has not yet experimentally tested on the proposed array but can be an objective for future work. Apart from the slid-

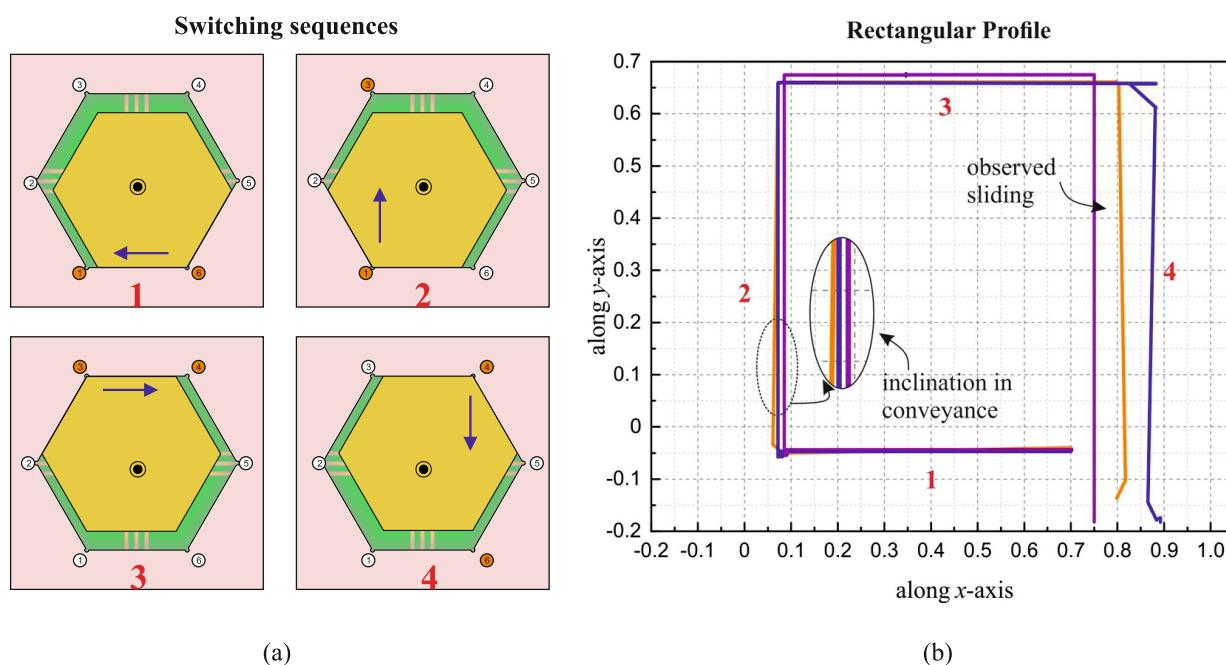


FIGURE 4.17: Representation of the multiple rectangular profiles realized using HDAA: (a) switching sequences, (b) Rectangular profile.

ing, it can be observed that the plate displacement trajectory for Short- x -stroke is almost straight compared to that for stroke- y . This can be due to the presence of lateral support to the mobile part during switching along x -axis using Short- x -stroke. The lateral support is indeed not available during switching along y -axis. To overcome the above mentioned errors which are caused due to open loop system and frictional inhomogeneity, a closed loop control can help.

The proposed array design based on seven actuators has been validated and experimentally characterized. Its ability to ensure conveyance tasks has been shown. In the following section, an array composed of more compact HDAs is proposed and designed. The interest of this new array is to obtain a higher actuator density that will help to obtain more precise conveyance tasks (translation, rotation) and a higher charge capacity. To achieve this objectives, an array composed of 19 HDAs is proposed and presented in the following section.

4.6 Design of an array composed of 19 HDAs

This section describes the design of a HDAA with a reduced stroke size compared to the previous one and an increased number of actuators always arranged in an honeycomb architecture. For this a new array, a new HDA has been designed and is shown in Fig. 4.18(a) and (b). The proposed design is initially limited for 2D motion but it can easily be adapted for 3D motion by adding air-core coils below the cavity. The design is similar to previous HDA presented in chapter 2 with one MPM surrounded by six FPMs. The total dimension of this HDA is $17 \text{ mm} \times 14.72 \text{ mm}$ which is reduced compared to the previous one ($25.76 \text{ mm} \times 22.30 \text{ mm}$). The selected MPM in the actuator is having smallest possible dimension (side: 2.5 mm, height: 1 mm) as per the supplier standards for hexagonal shaped PM. The dimensions for the MPM and FPM is given in Fig. 4.18. The FPMs used are smaller in height (0.8 mm) compared to that of MPM. This configuration has been considered to avoid any contact between the FPMs and the conveyance plate when it is in contact with the MPM. This configuration will simplify the conveyance device architecture as there will be no need to use a PMMA piece on top of the mobile part to realise stick-slip approach as explained in section 4.3.1.1.

Two pairs of orthogonal conductors each having three serially connected conductors are used like that in previous HDA. The PCB designed for this prototype also consists of four layers with first two layers for the x -axis and y -axis switching conductors and third, fourth layer for the routing purpose. An inverse PCB technique is also used to reduce the airgap between the first two layers.

The stroke sizes are shown in Fig. 4.18 (c), (d) and are 0.40 mm, 0.80 mm and 0.69 mm for Short- x -stroke, Long- x -stroke and Stroke- y .

The use of 19 actuators rather than 7 increases the number of contact points between the plate and the mobile parts. To design the HDA and also the array, it is necessary to determine the magnetic and electromagnetic forces using the models presented in chapter 2. The modeling is explained in the following section.

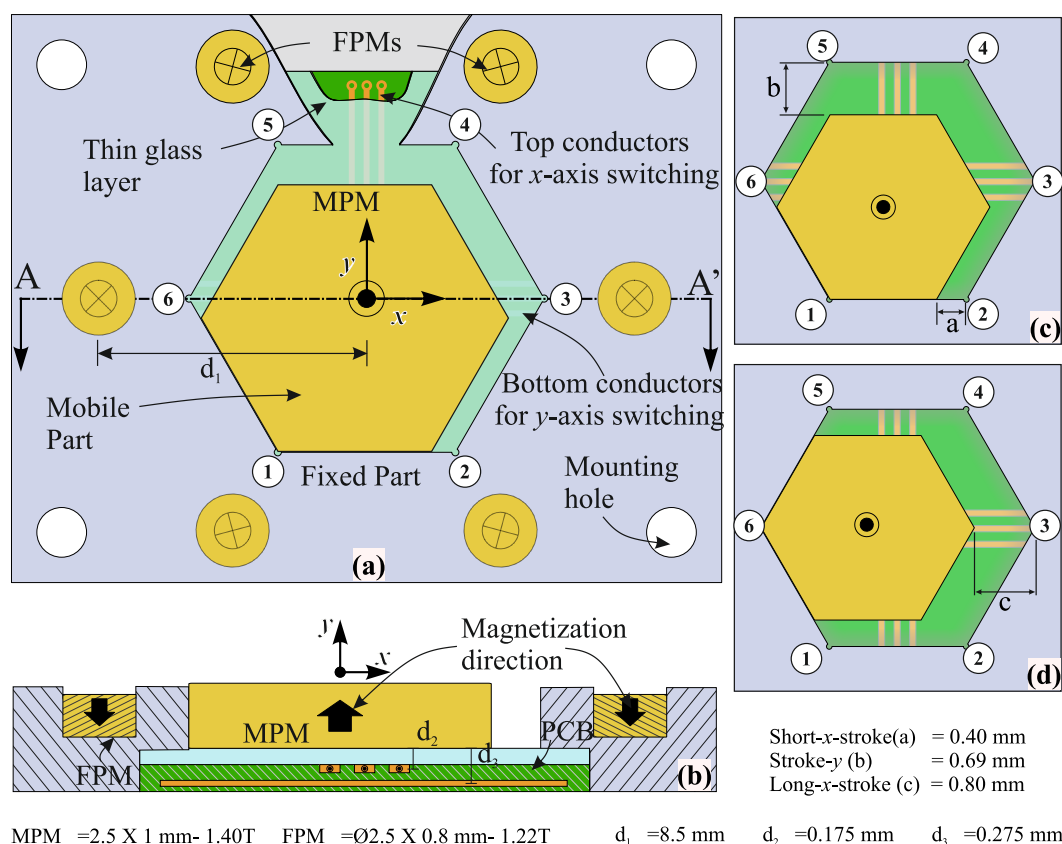


FIGURE 4.18: Design of the new HDA: (a) Top view, (b) Cross sectional view, (c) (d) Representation of the different strokes.

4.6.1 Modeling

This section details the modeling of the HDA and also the study of magnetic interaction between the different actuators in the array. The model has been used for the actuator as already explained in chapter 2. The modeling of the HDA is necessary to compute the magnetic and electromagnetic forces and to verify the actuator behavior. After the designing of a single actuator, the next important thing is to study the magnetic interactions between different actuators in the array.

Modeling of the elementary HDA: The numerical model of the previous HDA has been used to determine the magnetic forces generated by the FPMs on the MPM. These forces helps to define the distance d_1 (see Fig. 4.18) between the center of FPM and the center of hexagonal cavity. As already mentioned, the size of MPM is fixed because of the manufacturing limitations. Therefore, different FPM sizes have been considered to obtain

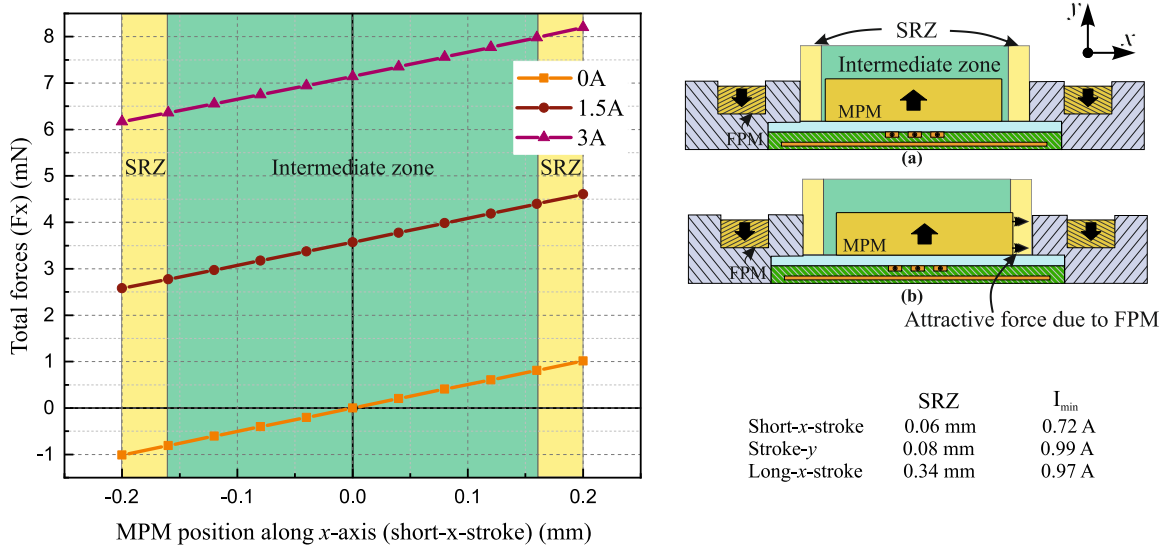


FIGURE 4.19: Representation of the Total forces with respect to current values for short-x-stroke.

a HDA with smallest possible dimensions taking into account a 10% SRZ and the minimum current required to switch which should not exceed more than 1.5 A. Considering all these aspects, the FPM dimensions (indicated in Fig. 4.18) and a distance d_1 of 8.5 mm have been selected. The SRZ and I_{min} have also been determined as explained before. Fig. 4.19 provides a graphical representation of total forces (magnetic + electromagnetic) generated on the MPM for different current values. The forces mentioned in the graph are for x-axis switching precisely using Short-x-stroke. As per graph, the force behavior of the actuator is similar to that of the previous one with different values. When there is no current, the force plotted represents only the magnetic forces generated by FPMs on the MPM whereas addition of current generates the electromagnetic force which shifts the graph upward. In the figure, the intermediate zone and SRZ are represented and their values indicated. The details about SRZ and I_{min} calculations are given in section 2.2.7.

Magnetic interaction for the HDAA: A standard size of silicon wafer ($\phi 100$ mm) has been selected for the HDAA and it has been a challenge to integrate maximum number of HDA in a standard wafer. Total of nineteen actuators are present in the array which are selected due to their integration in standard size silicon wafer. However, as for the previous array, to use it as a conveyance device, homogenous behavior is needed. Initially, only the nineteen HDA arranged in a honeycomb architecture have been considered using

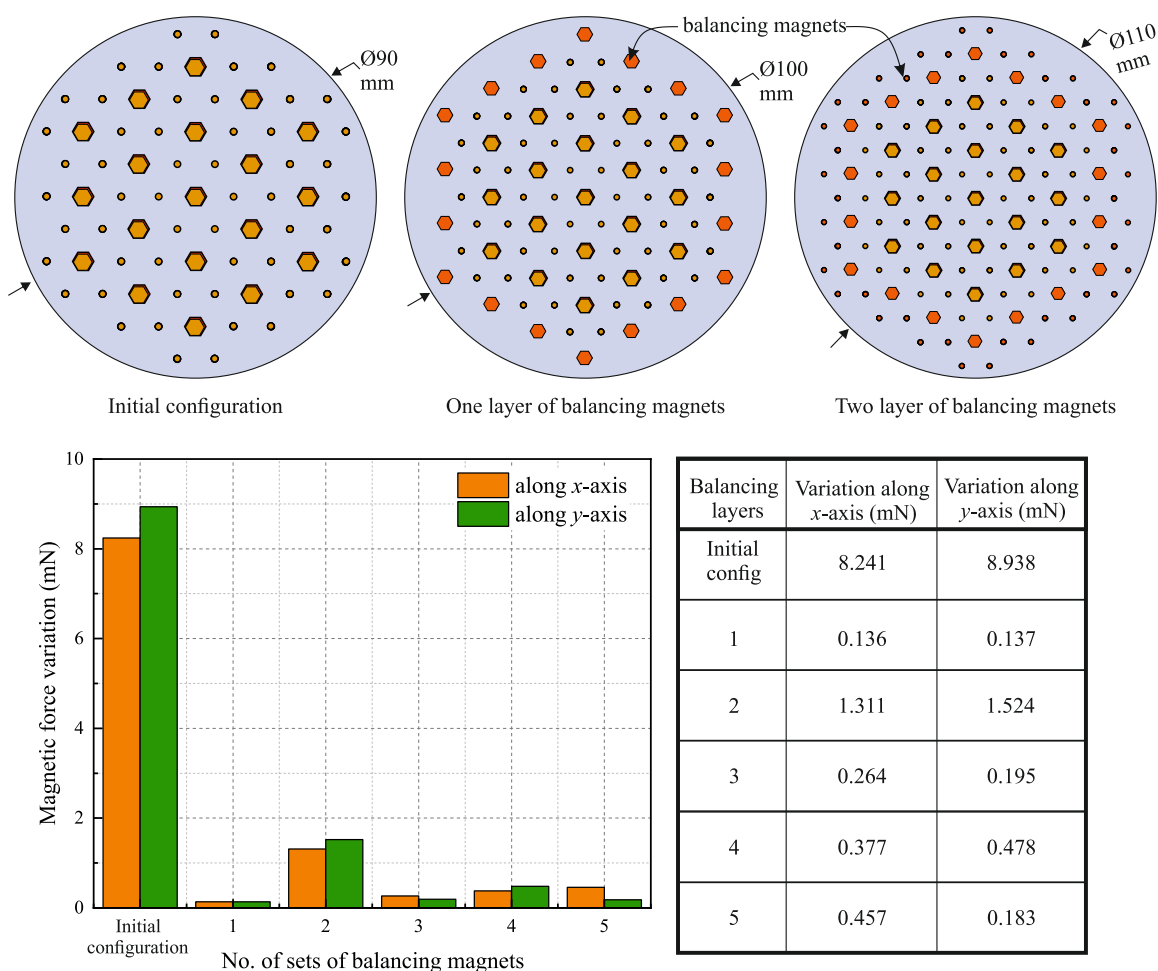


FIGURE 4.20: Representation of magnetic force variation for different configuration.

Radia. Huge variation in magnetic forces has been observed and is presented in Fig. 4.20. This variation represents 8.24 mN along x -axis and 8.93 mN along y -axis that induces a non homogenous behavior for the array. To reduce this variation, sets of balancing PMs (indicated by orange colour) are placed around the array as shown in figure. These sets reduce the variation but increases the HDAA size. Taking both into account, one layer of balancing magnets is used. This layer reduces the magnetic force variation to 0.13 mN both in x - and y -axis. For the previous array composed of seven actuators, the variation represented 0.21 mN and 0.33 mN for x and y -axis, respectively. Compared to this previous version, the obtained variation for this new array is then lower. Fig. 4.21 represents the final proposed HDAA composed of 19 HDAs and the magnetic forces generated on each MPM. The average magnetic force generated along x - and y -axis is 1.15 mN and 1.98 mN, respectively. The negative value for the forces is due to the position of each

mobile part of an array (at position $(-x, -y)$).

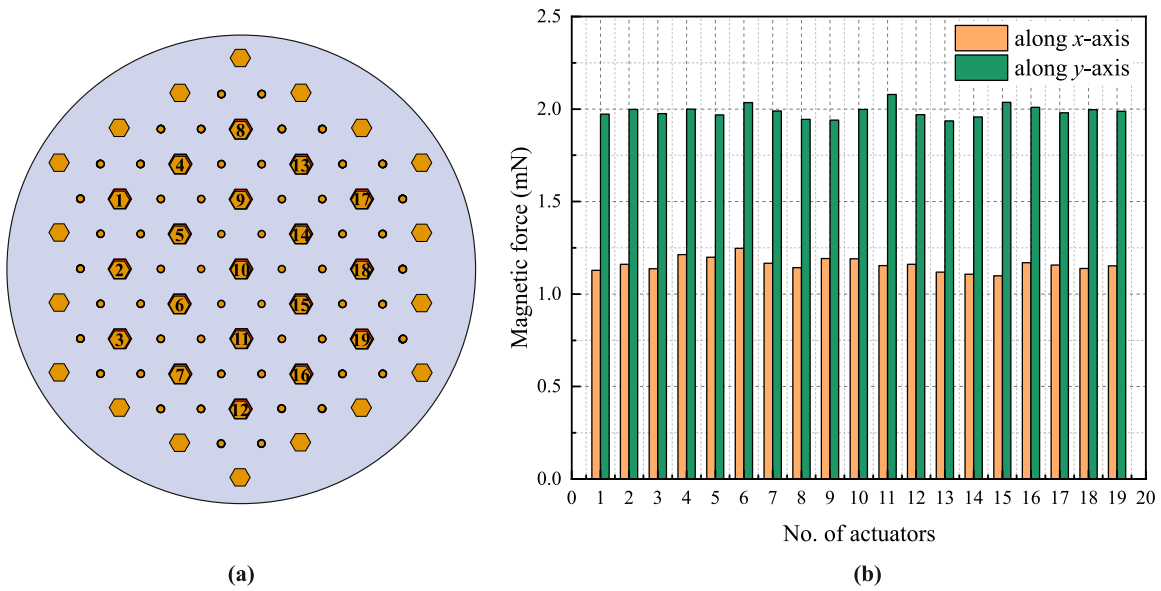


FIGURE 4.21: Representation of the final proposed prototype for 19 HDAA and the generated magnetic forces by each actuator in an array.

A prototype need to be realized to validate the design of this new HDAA and to characterize its performances and to compare the conveyance performances with that of the array composed of seven actuators. This part is in the working phase and it represents a perspective of the presented work.

4.7 Conclusion

This chapter has presented the design, the prototyping and the characterization of a HDAA for conveyance tasks. At first, the design constraints and the requirements have been detailed. The prototype validation was carried out taking into account the discussed constraints. It mainly includes the study of magnetic and electromagnetic force variations to obtain an homogenous behavior of the array. The final proposed design presents a magnetic force variation of 0.21 mN and 0.33 mN along x- and y-axis, respectively. To experimentally validate the conveyance application, initially a rapid prototyping technique has been used. Two different conveyance approaches that are Stick-slip and Lift-mode have been tested with the prototype. To characterize the prototype, several experiments were carried out such as plate displacement, no. of sequences with respect to driving current

values for both the approaches. This characterization permits to validate the proposed concept.

In the second step, a micro-fabricated version of the HDAA has been realized to overcome the manufacturing errors. Several experiments have been performed on the micro-fabricated version to test the ability to realize translation, rotation and planar trajectory. It also helps to validate the main objective of using the HDAA as a conveyance device. The given array is able to rotate a plate with elementary control of each actuator. A total of 36.4° rotation is observed with 33 switching sequences with a average rotation of 1.103° using stick-slip approach. The third experiment includes transition of the plate between HDAs. The Lift-mode is used to avoid the impact and therein to reduce observed disturbances in the plate displacement during transition between HDA. A planar trajectory has also been realised to verify the ability to realize planar motions.

At the end of this chapter, a new design for a HDAA has been proposed and includes 19 more compact HDAs that ensures an increased actuator density. The proposed concept of new HDAA has been designed and a prototype is under process.

Chapter 5

Conclusion and perspective

This chapter provides a conclusion of the work presented in the thesis. It will also present several perspectives of the work in order to optimize the proposed conveyance device in terms of its design, its ability to realize complex conveyance trajectories, etc..

5.1 General conclusion

The general objective of this thesis is to develop a micro-conveyance device, based on digital actuators, that can be used for conveyance tasks in the context of micro-factory. In a literature review, various types of smart conveyance devices have been presented which are either used commercially or in laboratories to realize conveyance and sorting of objects at meso or micro scale levels. A wide variety of actuation principles and device architectures are used to realize such type of conveyance. Based on this state of art, the electromagnetic principle has been considered for the switching operation due to its advantages like high speed, ability to realize wireless mobile part, etc. Moreover, a digital actuation technique has been selected because of its simple control (open-loop) and the possibility to obtain collaborative actuation using an array. Due to the use of electromagnetic principle, the holding operation has been obtained magnetically by using the magnetic properties of the mobile part.

In chapter 2, a digital electromagnetic actuator has been realized based on the electromagnetic switching and magnetic holding functions as explained in state of the art. Due

to the hexagonal architecture of the single actuator, three important strokes are defined: Short- x -stroke (0.50 mm), Long- x -stroke (1.00 mm) and Stroke- y (0.86 mm). A 3D architecture of the actuator has been selected which gives a mobile part the ability to reach twelve discrete positions. These positions are distributed at two different levels along z -axis. Two different approaches: Stick-slip and Lift-mode, have been presented to realize positioning tasks using this single actuator. To design the digital actuator, the modelling is an essential part. It helps to calculate the forces exerted in the system and then to define the optimal dimensions for the actuator for given characteristics. For the magnetic and electromagnetic force calculation, different magnetic flux models have been presented: an analytical model for cuboidal PMs and numerical models for cylindrical and hexagonal PMs. These models have been implemented using Matlab software. A FEM analysis has also been realized to determine the electromagnetic force generated by the air-core coil. Two CAD models of the actuator have been presented in this chapter based on the cuboidal based and hexagonal based MPM shapes.

In chapter 3, the proposed designs of the single HDA has been experimentally prototyped and characterized and to do so, the design layout and description about the components have been discussed. Initially, the prototype has been fabricated using rapid-prototyping technique and with PMMA material. This version helps to validate the proposed architecture by experimentally determining the possibility to reach twelve discrete positions. However due to high manufacturing tolerances, there is difference in stroke sizes as 21.39 % and 21.76 % along x - and y -axis, respectively. To overcome it, a micro-fabrication technique has been presented which reduces the stroke difference to 4.54 % and 3.13 %, respectively. To characterize these prototypes, two different contactless measuring techniques (HRC and FODS) have been used. An application of the single HDA as a micro-positioning device has been tested and different experiments have been carried out to validate it. The two conveyance approaches, Stick-slip and Lift-mode, have been tested and validated using these prototypes.

In order to obtain a long-range conveyance device several HDA arranged in a form

of an array have been developed. Seven actuators have been considered in an honeycomb architecture as detailed in chapter 4. These HDAs are collaboratively controlled to realize conveyance tasks. To ensure homogeneity in their behavior, magnetic and electromagnetic force interactions have been studied using the semi-analytical software Radia. A very low electromagnetic force interaction has been observed between the actuators and therefore it has been neglected. However, the observed magnetic force variation is very high (7.87 mN & 9.02 mN along x - and y -axis, respectively) and has been reduced by adding a layer of balancing PMs placed around the array. The balancing PMs helps to reduce the magnetic force variation to 0.21 mN and 0.33 mN, for x - and y -axis, respectively.

The design and working principle of the HDAA has then been explained and various conveyance possibilities have been shown. Two different prototypes of the array have been realized: one using rapid-prototyping technique and other using silicon micro-fabrication. The experimental characterization of both the prototypes have been realized. Four different conveyance abilities have been shown using this version, which includes: translation in xy -plane, rotation in xy -plane, transition between the actuators and forming a square pattern with the help of seven actuators. It has been observed that, the proposed HDAA is able to translate the plate on an average to 1.17 mm for the Long- x -stroke and 0.89 mm for the stroke- y . It is also able to rotate the plate on an average to 1.10° for each switching sequences.

A new array design based on nineteen actuators has then been proposed. The modelling of this new actuator array has been described and its design has been presented but it has not been tested yet.

5.2 Perspectives

In this section, several perspectives of the presented thesis work are proposed. This will improve the design or the possibilities proposed by the different designs and prototypes presented in this previous chapters.

5.2.1 Micro-fabricated Hexagonal casing

In chapter 3, a comparison has been made between the theoretical and experimental stroke values. It has been observed that the micro-fabricated version provides more precision for the required strokes. The remaining stroke error is mainly due to the manufacturing tolerances of the MPM. This tolerance is difficult to be controlled in the MPM manufacturing. Therefore, a hexagonal casing can be fabricated using micro-fabrication

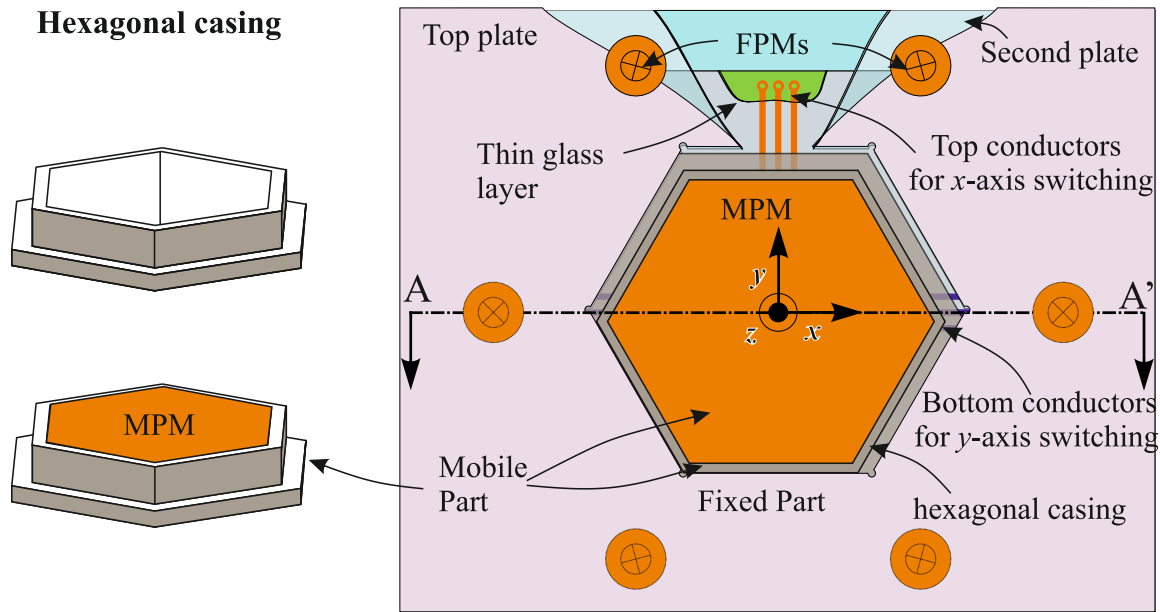


FIGURE 5.1: CAD view of hexagonal casing and its assembly

technique as shown in Fig. 5.1 in which the MPM can be inserted. The casing will also integrate the z -axis retainer at the bottom. The MPM will be fixed inside the casing as shown and the final stroke values will be the difference between the hexagonal cavity and the casing. This will also help to reduce the stroke error along z -axis due to the use of micro-fabricated retainer. Apart from that, the hexagonal casing will also help to overcome the geometrical errors of the MPM.

5.2.2 HDA capable to reach multiple z -axis

A 3D displacement HDA is presented in this thesis work however, the mobile part is having only two levels along z -axis. Multi z -axis displacement can be a perspective for this work, as it will help to elevate the conveyance object on different levels along z -axis and

thus, will further increase the flexibility of the proposed conveyance device. Fig. 5.2, represents an concept of a multi z -axis displacement HDA. The switching along z -axis could

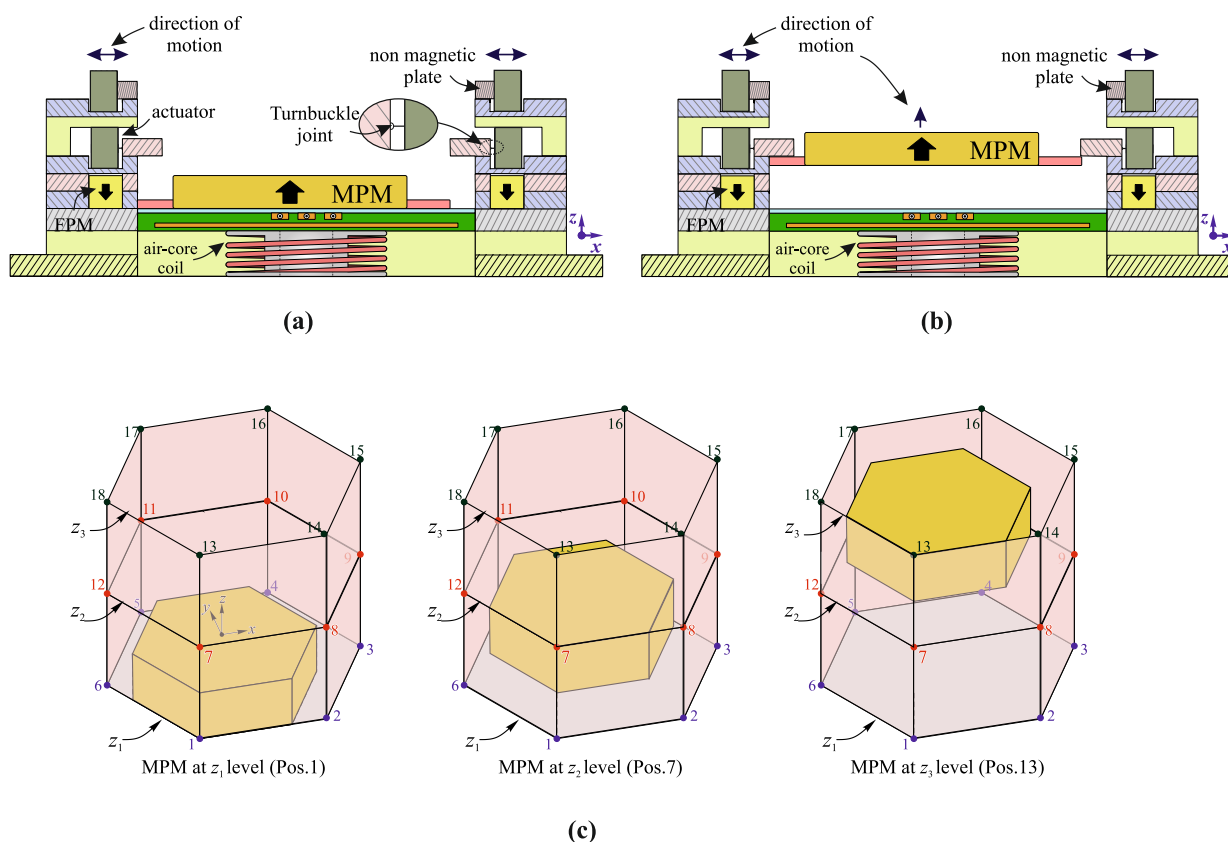


FIGURE 5.2: Representation of multi z -axis displacement for an HDA

be achieved with the help of an electromagnetic air-core coil. Moreover to obtain different levels along z -axis, an locking arrangement can be realized using miniaturized locking actuators. If the actuator needs to reach the second level along z -axis [see Fig. 5.2(b)], the two locking actuators need to be activated to release the mobile part. The plate acts as a barrier for the mobile part and also helps to define the stroke along z -axis. In the similar fashion, to achieve third level along z -axis, the bottom locking actuators will hold the plate whereas, the top actuators will release the plate to set next barrier.

5.2.3 Realisation and characterization of the array composed of 19 actuators

In chapter 4, an array composed of nineteen miniaturized actuators has been presented and designed. A direct perspective is to realize a prototype of this array and to characterize it as a conveyance device. The obtained results can be compared with the ones obtained using the array composed of seven actuators. Parameters like sliding effect, energy consumption, conveyance velocity, planar trajectory formation can be compared. As shown in Fig. 5.3, this new array integrates more elementary actuator therefore, it can also be used to convey multiple plates at a time as each actuator in an array is independently controlled.

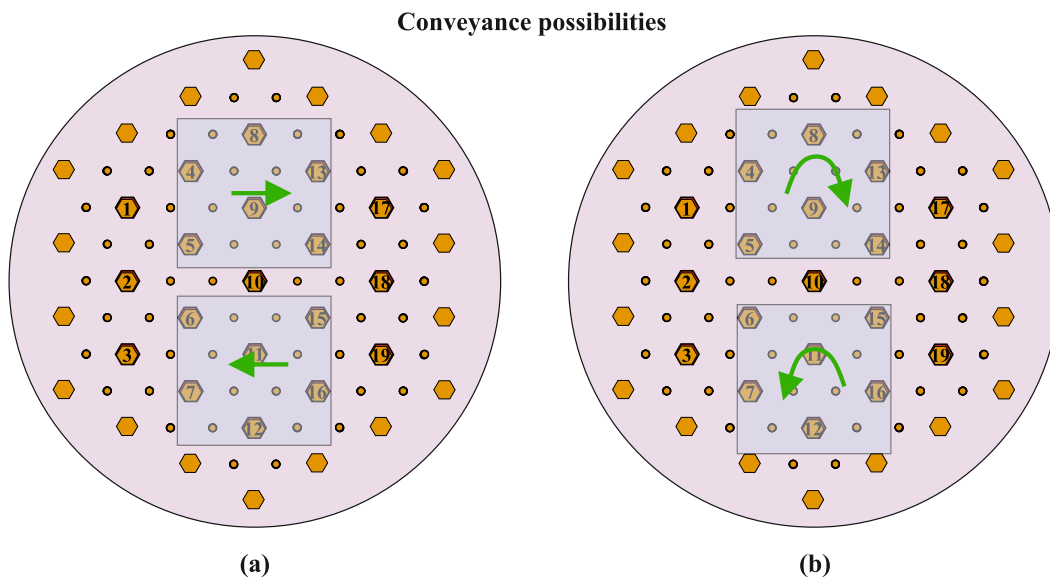


FIGURE 5.3: Representation of different conveyance possibilities using 19 actuator array

5.2.4 Modular Design concept

A long range application has already been explained in the thesis using an array composed of seven actuators. An optimised version using nineteen actuators is also mentioned. However, to realize long range conveyance tasks, these designs are limited. To solve this problem, a modular HDAA design can be adapted to attach and detach multiple arrays to realize long range conveyance possibilities. Fig. 5.4 represents a modular design concept

Modular Design

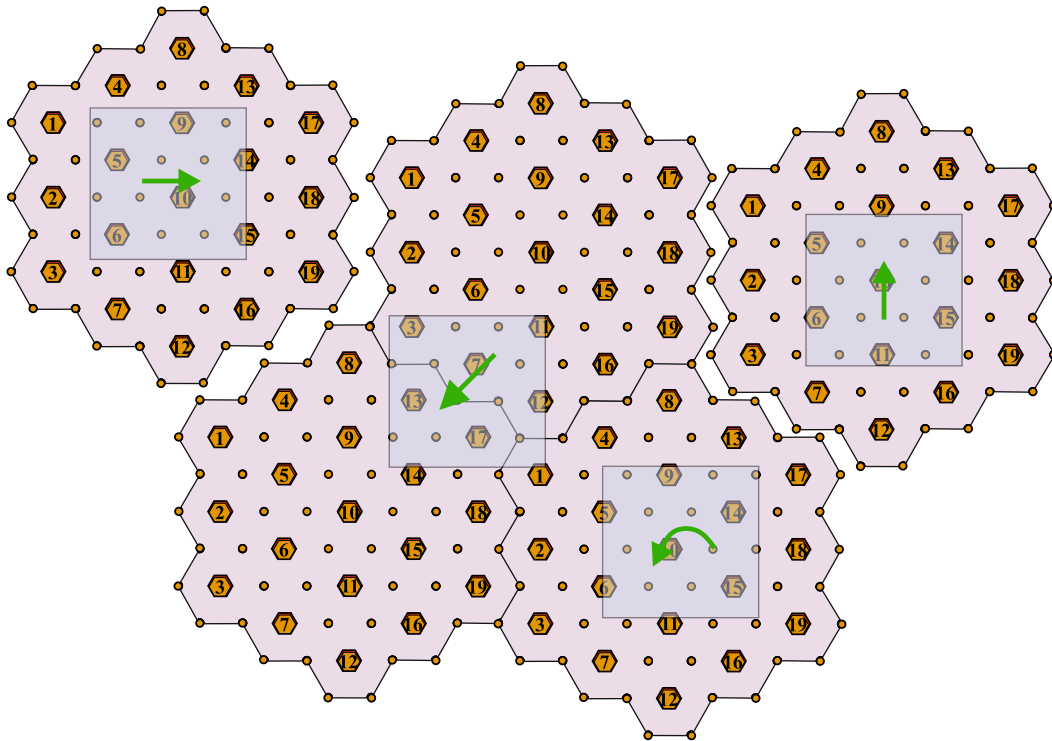


FIGURE 5.4: Representation of modular design concept for long range application

based on the HDAA composed of 19 HDAs. The modules have a geometry that permits the assembly of several modules to cover a large surface.

Appendix A

List of publications

The work presented in this thesis has been published and presented in the following international journals and international conferences.

- **A. Deshmukh**, L. Petit, M. Khan, F. Lamarque, C. Prella, “A Novel 3-D Electromagnetic Digital Actuator with 12 Discrete Positions”, IEEE/ASME Transactions on Mechatronics, Vol. 23(4), pp. 1653-1661, 2018.
- **A. Deshmukh**, L. Petit, M. Khan, F. Lamarque, C. Prella, “An Introduction to Micro-conveyance device based on Digital Principle”, Elsevier, sensors and actuators A physical (submitted).
- **A. Deshmukh**, L. Petit, C. Prella, “A Digital Electromagnetic Conveyance Device: Design, Modeling and Experimentation”, International Conference on Mechatronics “ICM 2019”, 18 au 20 mars, Ilmenau, Germany, 2019.
- **A. Deshmukh**, L. Petit, M.U. Khan, C. Prella, “A Micro-fabricated Hexagonal Digital Electromagnetic Actuator”, IEEE/ASME International Conference on Advanced Intelligent Mechatronics “AIM 2019”, 8 au 12 July, Hong-Kong, 2019.
- **A. Deshmukh**, L. Petit, M. Khan, F. Lamarque, C. Prella, “Stick-Slip Conveyance Device based on a Hexagonal Digital Electromagnetic Actuator”, MECHATRONICS, pp. 174-179, 10 au 12 September, Tsu, Japan, 2018.
- **A. Deshmukh**, L. Petit, M. Khan, F. Lamarque, C. Prella, “Hexagonal Digital Actuator array for Micro Conveyance Application”, IEEE International Conference on System of Systems Engineering “SoSE”, 19 au 22 June, Paris, France, 2018.
- **A. Deshmukh**, L. Petit, M. Khan, F. Lamarque, C. Prella, “Development of a six positions digital electromagnetic actuator”, IEEE/ASME International Conference on Advanced Intelligent Mechatronics “AIM 2017”, 3 au 7 July, Munich, Germany, 2017

Bibliography

- [Abad 09] J. Abadie, N. Chaillet, and C. LExcellent. “Modeling of a new SMA micro-actuator for active endoscopy applications”. *Mechatronics*, Vol. 19, pp. 437 – 442, 2009. Robotics and Factory of the Future, New Trends and Challenges in Mechatronics.
- [Al J 19] A. Al-Jodah, B. Shirinzadeh, M. Ghafarian, T. K. Das, and W. Wei. “Development and Analysis of a Novel Large Range Voice Coil Motor-driven 3-DOF XY? Micro-positioning Mechanism”. In: *2019 International Conference on Manipulation, Automation and Robotics at Small Scales (MARSS)*, pp. 1–6, July 2019.
- [Albe 05] P. Albertos, A. Sala, and M. Chadli. “Book reviews: Multivariable control systems-an engineering approach”. *Automatica (Journal of IFAC)*, Vol. 41, pp. 1665–1666, 09 2005.
- [Andr 14] P. Andrada, B. Blanqué, E. Martínez, M. Torrent, J. García-Amorós, and J. I. Perat. “New linear hybrid reluctance actuator”. In: *2014 International Conference on Electrical Machines (ICEM)*, pp. 585–590, Sep. 2014.
- [Aror 19] N. Arora, M. U. Khan, L. Petit, F. Lamarque, and C. Prella. “Design and Development of a Planar Electromagnetic Conveyor for the Microfactory”. *IEEE/ASME Transactions on Mechatronics*, Vol. 24, No. 4, pp. 1723–1731, Aug 2019.
- [Baz 12] D. E. Baz, V. Boyer, J. Bourgeois, E. Dedu, and K. Boutoustous. “Distributed part differentiation in a smart surface”. *Mechatronics*, Vol. 22, No. 5, pp. 522 – 530, 2012. Special Issue on Distributed Intelligent MEMS: from hardware to software.
- [Bout 10] K. Boutoustous, G. J. Laurent, E. Dedu, L. Matignon, J. Bourgeois, and N. Le Fort-Piat. “Distributed control architecture for smart surfaces”. In: *2010 IEEE/RSJ International Conference on Intelligent Robots and Systems*, pp. 2018–2024, Oct 2010.

- [Cai 17] K. Cai, Y. Tian, F. Wang, D. Zhang, X. Liu, and B. Shirinzadeh. “Design and control of a 6-degree-of-freedom precision positioning system”. *Robotics and Computer-Integrated Manufacturing*, Vol. 44, 04 2017.
- [Chai 06] J. Y. Chai, Y. W. Lin, and C. M. Liaw. “Comparative study of switching controls in vibration and acoustic noise reductions for switched reluctance motor”. *IEEE Proceedings - Electric Power Applications*, Vol. 153, No. 3, pp. 348–360, May 2006.
- [Chin 13] C. S. Chin and C. Wheeler. “Sliding-Mode Control of an Electromagnetic Actuated Conveyance System Using Contactless Sensing”. *IEEE Transactions on Industrial Electronics*, Vol. 60, No. 11, pp. 5315–5324, Nov 2013.
- [Conr 16] H. Conrad, B. Kaiser, M. Gaudet, S. Langa, M. Stolz, S. Uhlig, K. Schimmanz, and H. Schenk. “A Novel Electrostatic Actuator Class”. *Procedia Engineering*, Vol. 168, pp. 1533–1536, 12 2016.
- [Dao 11] D. V. Dao, P. H. Pham, and S. Sugiyama. “Multimodule Micro Transportation System Based on Electrostatic Comb-Drive Actuator and Ratchet Mechanism”. *Journal of Microelectromechanical Systems*, Vol. 20, No. 1, pp. 140–149, Feb 2011.
- [Deng 16] Z. Deng, M. Stommel, and W. Xu. “A Novel Soft Machine Table for Manipulation of Delicate Objects Inspired by Caterpillar Locomotion”. *IEEE/ASME Transactions on Mechatronics*, Vol. 21, No. 3, pp. 1702–1710, June 2016.
- [Deng 18] J. Deng, Y. Liu, K. Li, Q. Su, and H. Yu. “A novel planar piezoelectric actuator with nano-positioning ability operating in bending-bending hybrid modes”. *Ceramics International*, Vol. 44, pp. S164 – S167, 2018. The 11th Asian Meeting on Electroceramics (AMEC-11).
- [Ding 17] B. Ding, Y. Li, X. Xiao, Y. Tang, and B. Li. “Design and analysis of a 3-DOF planar micromanipulation stage with large rotational displacement for micromanipulation system”. *Mechanical Sciences*, Vol. 8, pp. 117–126, 05 2017.
- [Dong 15] L. Dong, J. Chen, C. Zhang, D. Wu, and G. Yu. “A novel voice coil motor used in nano-positioning device”. In: *2015 18th International Conference on Electrical Machines and Systems (ICEMS)*, pp. 1997–2002, Oct 2015.
- [Dong 16] L. Dong, J. Chen, C. Zhang, D. Wu, G. Yu, and Q. Liu. “Design and comparison of three-type VCMs for nano-positioning system”. In: *2016 IEEE 11th Conference on Industrial Electronics and Applications (ICIEA)*, pp. 1656–1660, June 2016.

- [Dudr 14] M. Dudragne, F. T. Yang, T. Denoix, L. Petit, and C. Prella. “Design of a multiple-stroke digital actuators array”. In: *2014 10th France-Japan/ 8th Europe-Asia Congress on Mechatronics (MECATRONICS2014- Tokyo)*, pp. 139–144, Nov 2014.
- [Ebef 99] T. Ebefors, J. U. Mattsson, E. Kalvesten, and G. Stemme. “A robust micro conveyer realized by arrayed polyimide joint actuators”. In: *Technical Digest. IEEE International MEMS 99 Conference. Twelfth IEEE International Conference on Micro Electro Mechanical Systems (Cat. No.99CH36291)*, pp. 576–581, Jan 1999.
- [Erzi 98] F. Erzincanli, J. Sharp, and S. Erhal. “Design and operational considerations of a non-contact robotic handling system for non-rigid materials”. *International Journal of Machine Tools and Manufacture*, Vol. 38, No. 4, pp. 353 – 361, 1998.
- [Espr 10] A. Espírito Santo, M. Calado, and C. Cabrita. “Design and evaluation of a linear switched reluctance actuator for positioning tasks”. *Turkish Journal of Electrical Engineering and Computer Sciences*, Vol. 18, pp. 925–941, 11 2010.
- [Firv 18] M. B. Firvida, H. Thamer, C. Uriarte, and M. Freitag. “Decentralized omnidirectional route planning and reservation for highly flexible material flow systems with small-scaled conveyor modules”. In: *2018 IEEE 23rd International Conference on Emerging Technologies and Factory Automation (ETFA)*, pp. 685–692, Sep. 2018.
- [Fuku 06] Y. Fukuta, Y. Chapuis, Y. Mita, and H. Fujita. “Design, fabrication, and control of MEMS-based actuator arrays for air-flow distributed micromanipulation”. *Journal of Microelectromechanical Systems*, Vol. 15, No. 4, pp. 912–926, Aug 2006.
- [Furl 01] E. P. Furlani. “Chapter 4 - Permanent Magnet Applications”. In: E. P. Furlani, Ed., *Permanent Magnet and Electromechanical Devices*, pp. 207 – 333, Academic Press, San Diego, 2001.
- [Gao 19] Y. Gao, T. Ema, Z. Cao, S. Ni, E. Y. L. Chan, O. Tabata, T. Tsuchiya, X. Wang, and M. Wong. “A Planar Single-Actuator Bi-Stable Switch Based on Latch-Lock Mechanism”. In: *2019 20th International Conference on Solid-State Sensors, Actuators and Microsystems Eurosensors XXXIII (TRANSDUCERS EUROSENSORS XXXIII)*, pp. 705–708, June 2019.
- [Ghaf 18] M. Ghafarian, B. Shirinzadeh, T. Das, A. Aljodah, and W. Wei. “Design of a novel parallel monolithic 6-DOF compliant micromanipulation mechanism”. pp. 997–1002, 07 2018.

- [Gong 13] Z. Gong, Z. Zhang, L. Zhang, R. Yang, Y. Liu, and H. Huang. “Reliability enhancement test of vertical voice-coil motor on wafer stage of lithography machine”. In: *2013 International Conference on Quality, Reliability, Risk, Maintenance, and Safety Engineering (QR2MSE)*, pp. 991–995, July 2013.
- [Guel 17] V. Guelpa, G. J. Laurent, B. Dahroug, and N. Le Fort-Piat. “Modular Contact-Free Conveyors for Handling Planar Fragile Objects”. *IEEE Transactions on Robotics*, Vol. 33, No. 1, pp. 92–101, Feb 2017.
- [Hadd 13] Y. Haddab, Q. Chalvet, Vincentand Chen, and P. Lutz. *Digital Microrobotics Using MEMS Technology*, pp. 99–116. Springer New York, New York, NY, 2013.
- [Hamz 11] H. Hamzehbahmani. “Modeling and Simulating of Single Side Short Stator Linear Induction Motor with the End Effect”. *Journal of Electrical Engineering*, Vol. 62, pp. 302–308, 09 2011.
- [Hao 15] Y. C. Hao, W. Z. Yuan, H. M. Zhang, and H. L. Chang. “A microgripper with a ratchet self-locking mechanism”. In: *2015 28th IEEE International Conference on Micro Electro Mechanical Systems (MEMS)*, pp. 1106–1109, Jan 2015.
- [Hass 17] A. Hassan, A. Bijanzad, and I. Lazoglu. “Dynamic Analysis of a Novel Moving Magnet Linear Actuator”. *IEEE Transactions on Industrial Electronics*, Vol. 64, No. 5, pp. 3758–3766, May 2017.
- [Hiem 14] D. Hiemstra. *Design of Moving Magnet Actuators for Large-range Flexure-based Nanopositioning*. PhD thesis, 07 2014.
- [Hoso 15] T. Hosobata, A. Yamamoto, and T. Higuchi. “Transparent Synchronous Electrostatic Actuator for Long-Stroke Planar Motion”. *IEEE/ASME Transactions on Mechatronics*, Vol. 20, No. 4, pp. 1765–1776, Aug 2015.
- [Jans 10] J. Janssen, J. Paulides, and E. Lomonova. “3D analytical field calculation using triangular magnet segments applied to a skewed linear permanent magnet actuator”. *COMPEL: Int J for Computation and Maths. in Electrical and Electronic Eng.*, Vol. 29, pp. 984–993, 07 2010.
- [Jeon 07] J. Jeon, K.-Y. Park, and H. Toshiro. “Contactless suspension and transportation of glass panels by electrostatic forces”. *Sensors and Actuators A: Physical*, Vol. 134, pp. 565–574, 03 2007.
- [Ji 10] L. Ji, Y. Zhu, S. O. R. Moheimani, and M. R. Yuce. “A micromachined 2DOF nanopositioner with integrated capacitive displacement sensor”. In: *SENSORS, 2010 IEEE*, pp. 1464–1467, Nov 2010.
- [Khan 14] M. Khan. *Contribution to the design and fabrication of an integrated micro-positioning system*. PhD thesis, 03 2014.

- [Khaz 10] J. Khazaai, M. Haris, M. Khir, H. Qu, and J. Slicker. “Design and Fabrication of a Low Power Electro-thermal V-shape Actuator With Large Displacement”. Vol. 2, 01 2010.
- [Knos 09] C. Knospe and S. Nezamoddini. “Capillary force actuation”. *Journal of Micro-Nano Mechatronics*, Vol. 5, pp. 57–68, 12 2009.
- [Koc 11] M. Koc and T. Ozel. *Fundamentals of Micro?Manufacturing*, pp. 1 – 23. 03 2011.
- [Krh 10] T. Krühn, S. Falkenberg, and L. Overmeyer. “Decentralized control for small-scaled conveyor modules with cellular automata”. In: *2010 IEEE International Conference on Automation and Logistics*, pp. 237–242, Aug 2010.
- [Kuma 12] M. Kumagai and R. L. Hollis. “Development and control of a three DOF planar induction motor”. In: *2012 IEEE International Conference on Robotics and Automation*, pp. 3757–3762, May 2012.
- [Lai 12] L.-J. Lai, G. Gu, and L.-M. Zhu. “Design and control of a decoupled two degree of freedom translational parallel micro-positioning stage”. *The Review of scientific instruments*, Vol. 83, p. 045105, 04 2012.
- [Laur 11] G. J. Laurent, A. Delettre, and N. Le Fort-Piat. “A New Aerodynamic-Traction Principle for Handling Products on an Air Cushion”. *IEEE Transactions on Robotics*, Vol. 27, No. 2, pp. 379–384, April 2011.
- [Le 18] T. A. Le, M. P. Bui, and J. Yoon. “An Optimal Design of an Electromagnetic Actuator for Targeting Magnetic Micro-/Nano-Carriers in a Desired Region”. *IEEE Transactions on Magnetics*, Vol. 54, No. 11, pp. 1–5, Nov 2018.
- [Lin 11] C.-Y. Lin, T.-Y. Tsai, J. C. Chiou, and C.-P. Chien. “Design, fabrication and actuation of 4-axis thermal actuating image stabilizer”. *Micro & Nano Letters, IET*, Vol. 6, 07 2011.
- [Liu 17] G. Liu, X. Zhang, X. Xu, and X. Liu. “Analyzing of a 2-D Magnet Array with Hexagon Magnet based on superposition”. *IOP Conference Series: Materials Science and Engineering*, Vol. 244, p. 012015, 09 2017.
- [Liu 18] Y. Liu, J. Deng, and Q. Su. “Review on Multi-Degree-of-Freedom Piezoelectric Motion Stage”. *IEEE Access*, Vol. 6, pp. 59986–60004, 2018.
- [Mach 19] F. Mach, M. Kurfirt, and I. Dolezel. “Bistable Fully Electromagnetic Valve for High-Speed and Fail-Safe Operations”. *IEEE Transactions on Industrial Electronics*, Vol. 66, No. 1, pp. 349–357, Jan 2019.

- [Mati 10] L. Matignon, G. Laurent, N. Fort-Piat, and Y.-A. Chapuis. “Designing Decentralized Controllers for Distributed-Air-Jet MEMS-Based Micromanipulators by Reinforcement Learning”. *Journal of Intelligent and Robotic Systems*, Vol. 59, pp. 145–166, 08 2010.
- [Medi 17] L. Medina, R. Gilat, and S. Krylov. “Latching in bistable electrostatically actuated curved micro beams”. *International Journal of Engineering Science*, Vol. 110, pp. 15 – 34, 2017.
- [Naka 97] H. Nakazawa, Y. Watanabe, O. Morita, M. Edo, and E. Yonezawa. “The two-dimensional micro conveyer: principles and fabrication process of the actuator”. In: *Proceedings of International Solid State Sensors and Actuators Conference (Transducers '97)*, pp. 33–36 vol.1, June 1997.
- [Naki 16] C. Nakic, J. Bieker, D. Lämmle, T. Winterstein, H. F. Schlaak, G. Schaumann, and T. Abel. “Development of an electrothermal micro positioning platform for laser targets with two degrees of freedom”. In: *2016 International Conference on Manipulation, Automation and Robotics at Small Scales (MARSS)*, pp. 1–5, July 2016.
- [Oda 18] Y. Oda, Y. Ito, K. Okuno, M. Kida, T. Suzuki, T. Narita, H. Kato, and H. Moriyama. “A Study on Edge Supported Electromagnetic Levitation System: Fundamental Consideration on Levitation Performance of Thin Steel Plate”. In: *2018 International Power Electronics Conference (IPEC-Niigata 2018 -ECCE Asia)*, pp. 2324–2328, May 2018.
- [Pere 13] R. Perez, O. Davila, A. Molina, and M. Ramirez-Cadena. “Reconfigurable Micro-Machine Tool Design for Desktop Machining Micro-factories”. *IFAC Proceedings Volumes*, Vol. 46, No. 9, pp. 1417 – 1422, 2013. 7th IFAC Conference on Manufacturing Modelling, Management, and Control.
- [Peti 09] L. Petit. *Contribution aux techniques d'actionnement numerique cas d'un système électromagnétique 2D*. PhD thesis, 07 2009.
- [Pole 15] K. Poletkin, Z. Lu, U. Wallrabe, and V. Badilita. “A New Hybrid Micromachined Contactless Suspension With Linear and Angular Positioning and Adjustable Dynamics”. *Journal of Microelectromechanical Systems*, Vol. 24, No. 5, pp. 1248–1250, Oct 2015.
- [Pote 19] Potekhina and Wang. “Review of Electrothermal Actuators and Applications”. *Actuators*, Vol. 8, p. 69, 09 2019.
- [Prab 18] N. Prabaharan, A. R. A. Jerin, E. Najafi, and K. Palanisamy. “6 - An overview of control techniques and technical challenge for inverters in micro grid”. In: A. H. Fathima, N. Prabaharan, K. Palanisamy, A. Kalam, S. Mekhilef, and J. J.

- Justo, Eds., *Hybrid-Renewable Energy Systems in Microgrids*, pp. 97 – 107, Woodhead Publishing, 2018.
- [Prel 06] C. Prella, F. Lamarque, and P. Revel. “Reflective optical sensor for long-range and high-resolution displacements”. *Sensors and Actuators A: Physical*, Vol. 127, pp. 139–146, 02 2006.
- [Prus 10] T. Prusi, A. Vuola, N. Siltala, R. Heikkilä, and R. Tuokko. “Robots for micro and desktop factories: examples and experiences”. In: *Proceedings of the joint conference of the 41st International Symposium on Robotics, ISR 2010, and 6th German Conference on Robotics, ROBOTIK 2010, 7-9 June, 2010, Munich, Germany*, pp. 1088–1094, 2010. Contribution: organisation=tte,FACT1=1.
- [Rako 14] M. Rakotondrabe, A. G. Fowler, and S. O. R. Moheimani. “Control of a Novel 2-DoF MEMS Nanopositioner With Electrothermal Actuation and Sensing”. *IEEE Transactions on Control Systems Technology*, Vol. 22, No. 4, pp. 1486–1497, July 2014.
- [Rava 08] R. Ravaut, G. Lemarquand, V. Lemarquand, and C. Depollier. “Analytical Calculation of the Magnetic Field Created by Permanent-Magnet Rings”. *IEEE Transactions on Magnetics*, Vol. 44, No. 8, pp. 1982–1989, Aug 2008.
- [Ravi 17] B. V. Ravi Kumar, K. Sivakumar, Y. Srinivas Rao, and S. Karunanidhi. “Design of a New Electromagnetic Brake for Actuator Locking Mechanism in Aerospace Vehicle”. *IEEE Transactions on Magnetics*, Vol. 53, No. 11, pp. 1–6, Nov 2017.
- [Reza 17] M. M. Reza, A. Ahmad, P. Kumar, and R. K. Srivastava. “Semi-analytical model for triangular skewed permanent magnet axial flux machine”. In: *2017 IEEE Transportation Electrification Conference (ITEC-India)*, pp. 1–5, Dec 2017.
- [Roth 18] P. Rothmund, A. Ainla, L. Belding, D. Preston, S. Kurihara, Z. Suo, and G. Whitesides. “A soft, bistable valve for autonomous control of soft actuators”. *Science Robotics*, Vol. 3, p. eaar7986, 03 2018.
- [Rube 13] C. Rubeck, J. Yonnet, H. Allag, B. Delinchant, and O. Chadebec. “Analytical Calculation of Magnet Systems: Magnetic Field Created by Charged Triangles and Polyhedra”. *IEEE Transactions on Magnetics*, Vol. 49, No. 1, pp. 144–147, Jan 2013.
- [Sain 09] L. Sainiemi. “Cryogenic deep reactive ion etching of silicon micro and nanostructures”. 01 2009.
- [Sang 12] A. Sangster. *Fundamentals of Electromagnetic Levitation: Engineering Sustainability Through Efficiency*. *Circuits and Devices*, Institution of Engineering and Technology, 2012.

- [Sari 11] I. Sari and M. Kraft. “A micro electrostatic linear accelerator based on electromagnetic levitation”. In: *2011 16th International Solid-State Sensors, Actuators and Microsystems Conference*, pp. 1729–1732, June 2011.
- [Shut 05] M. Shutov, E. Sandoz, D. Howard, T. Hsia, R. Smith, and S. Collins. “A micro-fabricated electromagnetic linear synchronous motor”. *Sensors and Actuators A: Physical*, Vol. 121, pp. 566–575, 06 2005.
- [Sohr 16] S. Sohr, T. Krühn, , and L. Overmeyer. “Mechanical feasibility and decentralized control algorithms of small-scale, multi-directional transport modules”. *Logistics Research*, Vol. 9, No. 1, p. 16, Aug 2016.
- [Staa 11] M. Staab and H. F. Schlaak. “Novel electrothermally actuated magnetostatic bistable microrelay for telecommunication applications”. In: *2011 IEEE 24th International Conference on Micro Electro Mechanical Systems*, pp. 1261–1264, Jan 2011.
- [Tang 17] C. Tang, M. Zhang, and G. Cao. “Design and testing of a novel flexure-based 3-degree-of-freedom elliptical micro/nano-positioning motion stage”. *Advances in Mechanical Engineering*, Vol. 9, p. 168781401772524, 10 2017.
- [Tell 15] M. C. Tellers, J. S. Pulskamp, S. S. Bedair, R. Q. Rudy, I. M. Kierzewski, R. G. Polcawich, and S. E. Bergbreiter. “Piezoelectric actuator array for motion-enabled reconfigurable RF circuits”. In: *2015 Transducers - 2015 18th International Conference on Solid-State Sensors, Actuators and Microsystems (TRANSDUCERS)*, pp. 819–822, June 2015.
- [Tisn 19] S. D. Tisnés, Z. Shi, L. Petit, C. Prella, and F. Lamarque. “Characterization of a micro-fabricated digital actuator array as a micro-factory conveyor device”. In: *2019 IEEE/ASME International Conference on Advanced Intelligent Mechatronics (AIM)*, pp. 382–387, July 2019.
- [Tuok 13] R. Tuokko, E. Järvenpää, R. Heikkilä, and A. Nurmi. “Micro and Desktop Factories for Micro/Meso-Scale Manufacturing Applications and Future Visions”. *Applied Mechanics and Materials*, Vol. 289, pp. 1–12, 02 2013.
- [Uria 15] C. Uriarte, H. Thamer, and M. Freitag. “Fördertechnik aus der Zelle - Hochflexibles Fördersystem aus kommunizierenden und kooperierenden Modulen”. *Hebezeuge Fördermittel*, p. 3, 2015.
- [Vand 05] V. Vandaele, P. Lambert, and A. Delchambre. “Non-contact handling in micro-assembly: Acoustical levitation”. *Precision Engineering*, Vol. 29, No. 4, pp. 491 – 505, 2005.

- [Vand 11] T. L. Vandoorn, B. Renders, L. Degroote, B. Meersman, and L. Vandeveld. “Active Load Control in Islanded Microgrids Based on the Grid Voltage”. *IEEE Transactions on Smart Grid*, Vol. 2, No. 1, pp. 139–151, March 2011.
- [Vero 17] M. Verotti, A. Dochshanov, and N. Belfiore. “A Comprehensive Survey on Modern Microgrippers Design: Mechanical Structure”. *Journal of Mechanical Design*, Vol. 139, p. 060801, 05 2017.
- [Vero 18] A. Veroli, A. Buzzin, F. Frezza, G. Cesare, M. Hamidullah, E. Giovine, M. Verotti, and N. Belfiore. “An Approach to the Extreme Miniaturization of Rotary Comb Drives”. *Actuators*, Vol. 7, p. 70, 10 2018.
- [Walt 03] C. Waltham, S. Bendall, and A. Kotlicki. “Bernoulli levitation”. *American Journal of Physics*, Vol. 71, No. 2, pp. 176–179, Feb 2003.
- [Wang 09] D.-A. Wang, H.-T. Pham, and Y.-H. Hsieh. “Dynamical switching of an electromagnetically driven compliant bistable mechanism”. *Sensors and Actuators A: Physical*, Vol. 149, No. 1, pp. 143 – 151, 2009.
- [Wang 99] D. Wang and Y. Alayli. *Conception et réalisation d’un minicapteur de déplacement à fibres optiques de résolution nanométrique*. PhD thesis, 03 1999.
- [Wu 18] Z. Wu and Q. Xu. “Survey on Recent Designs of Compliant Micro-/Nano-Positioning Stages”. 2018.
- [Xiuy 15] Xiuyuan Li, Yulong Zhao, and Tengjiang Hu. “Design of a novel electrothermal actuator for integrated MEMS safety-and-arming devices”. In: *10th IEEE International Conference on Nano/Micro Engineered and Molecular Systems*, pp. 63–66, April 2015.
- [Xu 14] Q. Xu. “Design and Development of a Compact Flexure-Based XY Precision Positioning System With Centimeter Range”. *IEEE Transactions on Industrial Electronics*, Vol. 61, No. 2, pp. 893–903, Feb 2014.
- [Xu 16] J. Xu. *Design of a conveyance device based on a digital actuators array and structured plate*. PhD thesis, Université de Technologie de Compiègne, May 2016.
- [Zamo 10] R. Zamora and A. K. Srivastava. “Controls for microgrids with storage: Review, challenges, and research needs”. *Renewable and Sustainable Energy Reviews*, Vol. 14, No. 7, pp. 2009 – 2018, 2010.
- [Zhic 16] Zhichao Shi, B. Bélier, E. Martincic, J. Moulin, E. Lefeuvre, L. Petit, J. Terrien, C. Prella, and F. Lamarque. “Development of an elementary micromachined

- electromagnetic digital actuator for microdisplacements”. In: *2016 Symposium on Design, Test, Integration and Packaging of MEMS/MOEMS (DTIP)*, pp. 1–4, May 2016.
- [Zhon 17] W. Zhong, X. Gu, K. Xu, F. Liu, X. Li, and T. Kagawa. “Modeling and verification of a contactless air film conveyor using a viscous traction principle”. *International Journal of Precision Engineering and Manufacturing*, Vol. 18, No. 12, pp. 1763–1772, Dec 2017.
- [Zhou 19] Y. Zhou, B. Kou, h. Zhang, L. Zhang, and L. Wang. “Design, Analysis and Test of a Hyperbolic Magnetic Field Voice Coil Actuator for Magnetic Levitation Fine Positioning Stage”. *Energies*, Vol. 12, p. 1830, 05 2019.
- [Zhu 15] L. Zhu, D. El-Baz, and H. Ning. “Survey on Air Levitation Conveyors with Possible Scalability Properties”. In: *2015 IEEE 12th Intl Conf on Ubiquitous Intelligence and Computing and 2015 IEEE 12th Intl Conf on Autonomic and Trusted Computing and 2015 IEEE 15th Intl Conf on Scalable Computing and Communications and Its Associated Workshops (UIC-ATC-ScalCom)*, pp. 802–807, Aug 2015.